

**MICROFLUIDIC-MICROSTRUCTURE INTERACTION STUDY
UNDER OSCILLATING FLOWS: DESIGN, MODELING, TESTING
AND VERIFICATIONS**

MD Shakhawat Hossain

A Thesis

in

the Department

of

Mechanical and Industrial Engineering

Presented in Partial Fulfillment of the Requirements for the
Degree of Master of Applied Science (Mechanical Engineering) at
Concordia University
Montreal, Quebec, Canada

April 2010

© MD Shakhawat Hossain, 2010



Library and Archives
Canada

Published Heritage
Branch

395 Wellington Street
Ottawa ON K1A 0N4
Canada

Bibliothèque et
Archives Canada

Direction du
Patrimoine de l'édition

395, rue Wellington
Ottawa ON K1A 0N4
Canada

Your file Votre référence
ISBN: 978-0-494-71094-4
Our file Notre référence
ISBN: 978-0-494-71094-4

NOTICE:

The author has granted a non-exclusive license allowing Library and Archives Canada to reproduce, publish, archive, preserve, conserve, communicate to the public by telecommunication or on the Internet, loan, distribute and sell theses worldwide, for commercial or non-commercial purposes, in microform, paper, electronic and/or any other formats.

The author retains copyright ownership and moral rights in this thesis. Neither the thesis nor substantial extracts from it may be printed or otherwise reproduced without the author's permission.

In compliance with the Canadian Privacy Act some supporting forms may have been removed from this thesis.

While these forms may be included in the document page count, their removal does not represent any loss of content from the thesis.

AVIS:

L'auteur a accordé une licence non exclusive permettant à la Bibliothèque et Archives Canada de reproduire, publier, archiver, sauvegarder, conserver, transmettre au public par télécommunication ou par l'Internet, prêter, distribuer et vendre des thèses partout dans le monde, à des fins commerciales ou autres, sur support microforme, papier, électronique et/ou autres formats.

L'auteur conserve la propriété du droit d'auteur et des droits moraux qui protègent cette thèse. Ni la thèse ni des extraits substantiels de celle-ci ne doivent être imprimés ou autrement reproduits sans son autorisation.

Conformément à la loi canadienne sur la protection de la vie privée, quelques formulaires secondaires ont été enlevés de cette thèse.

Bien que ces formulaires aient inclus dans la pagination, il n'y aura aucun contenu manquant.


Canada

ABSTRACT

Microfluidic-Microstructure Interaction Study under Oscillating Flows: Design, Modeling, Testing and Verifications

MD Shakhawat Hossain

In microsystem applications, many MEMS devices are submerged in fluid and their responses and performances are directly influenced by the microfluid-microstructure interactions. Recent developments in microfluidic devices such as micro pumps, micro valves, micro viscometer, biomedical related micro fluidic chips, have necessitated investigations on fluid-structure interactions at the micro levels. A microcantilever submerged in microfluidic channel forms the simplest model for such investigations. The study of such interactions however necessitates systematic developments in suitable experimental methods.

In this dissertation, a polymer base micro-fabrication process called "soft-lithography" is adopted to fabricate microcantilever integrated microfluidic channels. An experimental setup is designed to characterize the dynamic behavior of the submerged microcantilever using a new method called DVIP (Deflection using Video Image Processing) method. The DVIP method is used to estimate the deflection or dynamic responses of microcantilever under different flow conditions. The flow behaviors could also be characterized from the response of the microcantilever. A finite element model of the microstructure is developed and results obtained from this model are validated using the experimental results. The finite element model also provides considerable potential to investigate the influence of fluid viscosity on the dynamic responses of the

microcantilever. A microcantilever integrated within the microfluidic chip was subsequently tested in the laboratory with fluids of different viscosities. The results obtained are analyzed and discussed in the context of an application development such as a viscometer. An effort is made to visualize the flows near the cantilever tip using the fluids mixed with fluorescent particles. The DVIP method is further extended to estimate the full cantilever beam deflection, which can be applied for determining the mode of vibration. Finally, it is established that the DVIP method is a reliable approach to estimate the dynamic deflections of a microcantilever subject to fluid forces. The concept of the micro viscometer that is developed in the current study can be miniaturized by integrating a miniature camera and an integrated circuit within the microfluidic chip. The current study, however, is limited to square cross-section microfluidic chip, while the proposed methodology would be applicable to study the responses of the microcantilever integrated within channels of different cross-sections. The DVIP method also offers considerable potential to characterize nano-electromechanical devices by integrating a more efficient and faster camera.

ACKNOWLEDGEMENTS

First, I would sincerely like to thank my thesis supervisors Dr. Muthukumaran Packirisamy and Dr. Subhash Rakheja for showing interest in taking me as research student and introducing me to the exciting fields of MEMS and Microfluidics. Their guidance, ideas, encouragement and financial support have been influential in the successful completion of this thesis.

It was a great pleasure for to be a part of the Optical Microsystem laboratory of Concordia University. I also once again like to thank Dr. Muthukumaran Packirisamy to give me the new idea of image processing methods. I am very grateful to Dr. A. K. Waizuddin Ahmed for his support to develop the theoretical background of this dissertation.

I want to acknowledge my colleague Mr. Alberto Qing Fang to help in the development of image processing method for my application. I am also grateful to my colleagues Mr. Arvind Chandrasekaran and Mr. Ashwin Acharya to introduce and train me the fabrication process. It was an excellent experience for me to work at this laboratory in a friendly environment with all other colleagues. My sincere thanks to Danius Juras, technical officer who have helped me with my experimental setups.

I am forever indebted to my parents, sisters, brother in law and friends for their countless support and inspiration.

Dedicated to my parents

Table of Contents

List of Figures	xi
List of Tables	xxi
Nomenclature	xxii
List of Symbols	xxiii
CHAPTER 1 - INTRODUCTION	
1.1 Fluid-structure Interaction in Microsystems	1
1.1.1 Applications in MEMS Device	2
1.1.2 Applications in Biomedical Engineering	4
1.2 Review on Relevant Literature	4
1.2.1 Significance of Microstructure-fluid interactions	4
1.2.2 Excitation Methods	7
1.2.3 Fabrication of Device	10
1.2.4 Experimental Method	12
1.2.5 Theoretical Modeling	16
1.2.6 Results and Analysis	18
1.3 Thesis Objective, Contribution and Overview	27
1.3.1 Thesis Objective	27
1.3.2 Thesis Contribution	28
1.3.3 Thesis Overview	28
CHAPTER 2 - DESIGN AND FABRICATION OF MICROSTRUCTURE INTEGRATED MICROFLUIDIC CHANNEL	
2.1 Introduction	30

2.2	Design of a Microstructure Integrated Microfluidic Chip	31
2.3	Fabrication of Integrated Microcantilever Microfluidic Chips	35
2.3.1	Fabrication of Microchannel by 'Soft Lithography' Technique	35
2.3.2	Fabrication of Microcantilever	40
2.3.3	Integration of the Microcantilever	40
2.3.4	Bonding of Top and Bottom Microchannel Chips	41
2.3.5	The Leak Testing	43
2.4	Summary	43
CHAPTER 3 - EXPERIMENTAL METHOD AND CHARACTERIZATION		
3.1	Introduction	44
3.2	Experimental Setup	45
3.2.1	Flow Lines and Couplers	48
3.2.2	Pressure and Flow Sensors	49
3.2.3	Data Acquisition Board	52
3.2.4	Peristaltic Pump	53
3.3	Measurement of Cantilever Deflection	58
3.3.1	Laser Doppler Velocitymeter (LDV)	59
3.3.2	Estimation of Deflection using Video Image Processing (DVIP) Method	59
3.3.3	Comparison of Deflection Measurement Methods	66
3.4	Experimental Design	68
3.4.1	Experimental Methods and Parameters	68
3.5	Experimental Results at 'Low Flow' Conditions	71
3.5.1	Test 1: Study on a Chip with 3.2 mm Hydraulic Diameter	71
3.5.2	Test 2: Study on a Chip with 2.1 mm Hydraulic Diameter	79

3.6	Experimental Results at High Flow Condition	84
3.6.1	Test 3: Study on a Chip with 3.2 mm Hydraulic Diameter	85
3.6.2	Test 4: Study on a Chip with 2.1 mm Hydraulic Diameter	89
3.7	Comparison and Discussion	95
3.8	Summary	99
CHAPTER 4 - FINITE ELEMENT MODELING AND VALIDATION		
4.1	Introduction of Finite Element Method	100
4.1.1	Microfluidics Mode	101
4.1.2	Structural Mechanics Mode	101
4.1.3	Moving Mesh or Morphing Mesh	102
4.2	Model Geometry	102
4.2.1	Geometry Meshing	105
4.2.2	Boundary Conditions	105
4.3	Boundary Conditions from Testing Conditions for Pulsed Flows	108
4.4	Result Validation for Pulsed Flows	111
4.4.1	Results and Discussion	115
4.5	Finite Element Analysis on the Influence of Fluid Viscosity on Quality Factor using Step Excitation	120
4.5.1	Geometrical Parameters and Boundary Conditions	121
4.5.2	Quality Factor Definition	121
4.5.3	Influence of Fluid Viscosity on 'Q' Factor and Response of Cantilever	122
4.5.4	Results Discussion on Influence of Viscosity over 'Q' factor from FEM	123
4.5.5	Finite Element Analysis of the Influence of Cantilever Geometry over Quality Factor	127

4.5.6	Results and Discussion for the Influence of Aspect ratio on 'Q' Factor	128
4.6	Summary	129
CHAPTER 5 - APPLICATION DEVELOPMENT		
5.1	Introduction to Application Development	130
5.2	Experiment for Viscosity Estimation under Pulsed Flows	130
5.2.1	Experimental Result for Viscosity Variation	131
5.2.2	Experiments with Different Fluids	134
5.2.3	Finite Element Modeling and Validation	137
5.3	Flow Visualization	139
5.4	Deflection of Full Cantilever through Imaging	140
5.5	Summery	144
CHAPTER 6 - CONCLUSION		
6.1	Conclusion	145
6.2	Thesis Contribution	146
6.3	Limitation and Recommendation	147
	References	149

List of Figures

Figure 1.1	Applications involving microfluid-microstructure interactions (a) Nano-flow sensor [3]; (b) AFM cantilever [4]; (c) MEMS based anemometer [5] and (d) Bio-cell (E. Coli Cell) detection by resonating cantilever in bio fluids [6]	1
Figure 1.2	Transduction method for various chemical and biological environments [4]	3
Figure 1.3	Types of excitation considered for fluid-structure interaction.	7
Figure 1.4	(a) Fabrication of cantilever and encapsulation using different wafers, (b) Fabrication of the cantilever and encapsulation in the same wafer [17]	11
Figure 1.5	An Experimental setup of piezoresistor based flow sensor [45]	15
Figure 1.6	(a) Normalized response of rectangular cantilever, for tip deflection (solid) and tip angle (dashed), where the presence of higher mode in tip angle is showed in a zoomed view in the right rectangle, (b) Normalized response of rectangular cantilever, for tip deflection (solid) and tip angle (dashed), where the presence of higher mode in tip angle is showed in a zoomed view in the right rectangle [30]	20
Figure 1.7	Dependence of Brownian noise on fluid density and viscosity: spectrum of combined Brownian and Johnson noise [23]	21
Figure 1.8	Comparison of variation of damping ratios obtained by using different squeeze-film damping models and by extracting them from simulated free vibration response curves of the arbitrary point at the end of a cantilever microstructure after it has been released from its initial deflected position $z = 1 \mu\text{m}$ upwards for the different levels of working air pressure p_0 in the gap with thickness $h = 1 \mu\text{m}$ [1]	22
Figure 1.9	C_{damping} for three types of cross-sections [22]	24
Figure 1.10	Experimental amplitude and phase of deflection for a silicon cantilever ($70\mu\text{m} \times 200\mu\text{m} \times 3000\mu\text{m}$) oscillating in various viscous fluids [11]	25
Figure 1.11	Relation between output voltage and flow rate in the flow sensor developed by Peng and Zhou [45]	26

Figure 1.12	(a) The schematic description of the human pharynx (b) model of the pharynx "the moving part is in black [40]	27
Figure 2.1	(a) An isometric view of the cantilever integrated microfluidic chip and, (b) A close-up view of cantilever and its support	33
Figure 2.2	Flow path of the test spacemen; (a) Top view with possible location of LDV; (b) An enlarged view of cantilever structure	34
Figure 2.3	Detailed design of the mold or master (all dimensions are in mm)	37
Figure 2.4	(a) An isometric view of the mold with bent and straight (b) The mold with rod positioned inside the groove	37
Figure 2.5	Placement of cylindrical rod in the mold for installation of inlet and outlet ports and pressure sensors	38
Figure 2.6	Soft Lithography Steps	39
Figure 2.7	Microcantilever	40
Figure 2.8	(a) A schematic illustration of the cantilever mounting in the microchannel; (b) the groove cut at the middle for clamping of the cantilever; (c) the groove cut created in the flat elastomer block for installation of microcantilever in 2.1 mm hydraulic diameter of microchannel;	41
Figure 2.9	Pictorial view of the block with the cantilever where the top surface was painted with epoxy before bonding	41
Figure 2.10	Pictorial views of bonding of top and bottom chips and cross-section of the microchannel; (a) 3.2 mm hydraulic diameter of channel (b) 2.1 mm hydraulic diameter channel (dimension are presented in mm)	42
Figure 3.1	Schematic of the experimental setup	47
Figure 3.2	A pictorial view of experimental Setup	48
Figure 3.3	(a) Flow lines with different couplers and (b) two different connectors	49
Figure 3.4	(a) Pressure sensors mounted to the test specimen; and (b) Circuit diagram installing a pressure sensor coupled with the capacitors	50
Figure 3.5	Two flow sensing unites built with four pressure sensors	52

Figure 3.6	Circuit diagram showing data acquisition board and sensor connections (DAB- data acquisition board denoted as; MS- microscope mounted with CMOS camera denoted as; LDV- Laser Doppler Velocitymeter; CPU- the central processing unit or personal computer)	53
Figure 3.7	(a) Schematic of the pump head [61] and (b) a pictorial view of the pump head showing rollers mounted on the central disc	54
Figure 3.8	(a) Schematic of the central disc with rollers illustrating squeezed portion of the tube (b) linear representation of the squeezed portion of the tube and the contacting rollers	55
Figure 3.9	Time history of measured flow rate through the 1.2 mm diameter tube with pump operating at 6 rpm	58
Figure 3.10	Frequency spectrum of the flow variation shown in Figure 3.9.	58
Figure 3.11	A Schematic of the Laser Doppler Velocitymeter setup with concave-convex lens	59
Figure 3.12	Specimen positioned in the microscope stage	60
Figure 3.13	The comparison between real image and binary image	61
Figure 3.14	Flow chart to find the Pixel resolution $\mu\text{m}/\text{pixel}$ by comparing the width of the cantilever in pixels and real value of $28 \mu\text{m}$	62
Figure 3.15	The cantilever position in the captured image at different time and estimation of the deflection 'D' by DVIP method	63
Figure 3.16	Flowchart of the algorithm to find the tip position of rest cantilever	64
Figure 3.17	Flowchart of the algorithm to find the deflection of the cantilever	65
Figure 3.18	Image scanning process of MATLAB program. Binary value the of pixels at the tip of the cantilever is shown in a close-up view	66
Figure 3.19	(a) Time history of the measured (a) inlet pressure difference (b) the cantilever tip deflection recorded by LDV at a pump speed of 4 RPM	67
Figure 3.20	(a) Time history of the measured inlet pressure difference (b) the cantilever tip deflection by DVIP method at a pump speed of 4 RPM	67

Figure 3.21	Schematics of the fluid flow paths of the microfluidic chip with 3.2 mm hydraulic diameter channel	70
Figure 3.22	Schematics of the fluid flow paths of the microfluidic chips with 2.1 mm hydraulic diameter channel	70
Figure 3.23	Variation in the inlet and outlet fluid pressure of the 3.2 mm hydraulic diameter of specimen: (a) time history of measured inlet and outlet pressure (b) time history of the measured inlet pressure difference and (c) spectrum of the inlet pressure difference (N= 4RPM)	73
Figure 3.24	(a) Spectrum of the inlet pressure difference (b) Time history of the beam tip deflection (c) Spectrum of the beam tip deflection (N= 4 RPM)	74
Figure 3.25	(a) Spectrum of the inlet pressure difference (b) Time history of the beam tip deflection (c) Spectrum of the beam tip deflection (N= 5 RPM)	74
Figure 3.26	(a) Spectrum of the inlet pressure difference (b) Time history of the beam tip deflection (c) Spectrum of the beam tip deflection (N= 6 RPM)	75
Figure 3.27	(a) Spectrum of the inlet pressure difference (b) Time history of the beam tip deflection (c) Spectrum of the beam tip deflection (N= 7 RPM)	75
Figure 3.28	(a) Spectrum of the inlet pressure difference (b) Time history of the beam tip deflection (c) Spectrum of the beam tip deflection (N= 8 RPM)	76
Figure 3.29	(a) Spectrum of the inlet pressure difference (b) Time history of the beam tip deflection (c) Spectrum of the beam tip deflection (N= 9 RPM)	76
Figure 3.30	(a) Variation of rms of inlet pressure difference and deflection with respect to pump speed (b) Variation of rms of deflection with respect to rms of inlet pressure difference	77
Figure 3.31	(a) Variation of first amplitude of deflection and inlet pressure difference with respect of pump speed (b) Variation of second amplitude of deflection and inlet pressure difference with respect of pump speed	78
Figure 3.32	(a) Spectrum of the inlet pressure difference (b) Time history of the beam tip deflection (c) Spectrum of the beam tip deflection (N= 4 RPM)	80

Figure 3.33	(a) Spectrum of the inlet pressure difference (b) Time history of the beam tip deflection (c) Spectrum of the beam tip deflection (N= 5 RPM)	80
Figure 3.34	(a) Spectrum of the inlet pressure difference (b) Time history of the beam tip deflection (c) Spectrum of the beam tip deflection (N= 6 RPM)	81
Figure 3.35	(a) Spectrum of the inlet pressure difference (b) Time history of the beam tip deflection (c) Spectrum of the beam tip deflection (N= 7 RPM)	81
Figure 3.36	(a) Spectrum of the inlet pressure difference (b) Time history of the beam tip deflection (c) Spectrum of the beam tip deflection (N= 8 RPM)	82
Figure 3.37	(a) Spectrum of the inlet pressure difference (b) Time history of the beam tip deflection (c) Spectrum of the beam tip deflection (N= 9 RPM)	82
Figure 3.38	(a) Variation of rms of deflection and inlet pressure difference with respect of pump speed (b) Variation of rms of deflection with respect to rms of inlet pressure difference	83
Figure 3.39	(a) Variation of first amplitude of deflection and inlet pressure difference with respect to pump speed (b) Variation of second amplitude to deflection and inlet pressure difference with respect of pump speed	84
Figure 3.40	(a) Spectrum of the inlet pressure difference (b) Time history of the beam tip deflection (c) Spectrum of the beam tip deflection (N= 4 RPM)	86
Figure 3.41	(a) Spectrum of the inlet pressure difference (b) Time history of the beam tip deflection (c) Spectrum of the beam tip deflection (N= 5 RPM)	86
Figure 3.42	(a) Spectrum of the inlet pressure difference (b) Time history of the beam tip deflection (c) Spectrum of the beam tip deflection (N= 6 RPM)	87
Figure 3.43	(a) Spectrum of the inlet pressure difference (b) Time history of the beam tip deflection (c) Spectrum of the beam tip deflection (N= 8 RPM)	87
Figure 3.44	(a) Spectrum of the inlet pressure difference (b) Time history of the beam tip deflection (c) Spectrum of the beam tip deflection (N= 9 RPM)	88

Figure 3.45	(a) The rms variation of inlet pressure difference and deflection with respect to pump speed (b) Variation of second amplitude of deflection and inlet pressure difference with respect of pump speed	88
Figure 3.46	Geometrical variation flow path for 2.1 mm hydraulic diameter of specimen	89
Figure 3.47	(a) Spectrum of the inlet pressure difference (b) Time history of the beam tip deflection (c) Spectrum of the beam tip deflection (N= 4 RPM)	91
Figure 3.48	(a) Spectrum of the inlet pressure difference (b) Time history of the beam tip deflection (c) Spectrum of the beam tip deflection (N= 5 RPM)	91
Figure 3.49	(a) Spectrum of the inlet pressure difference (b) Time history of the beam tip deflection (c) Spectrum of the beam tip deflection (N= 6 RPM)	92
Figure 3.50	(a) Spectrum of the inlet pressure difference (b) Time history of the beam tip deflection (c) Spectrum of the beam tip deflection (N= 7 RPM)	92
Figure 3.51	(a) Spectrum of the inlet pressure difference (b) Time history of the beam tip deflection (c) Spectrum of the beam tip deflection (N= 8 RPM)	93
Figure 3.52	(a) Spectrum of the inlet pressure difference (b) Time history of the beam tip deflection (c) Spectrum of the beam tip deflection (N= 9 RPM)	93
Figure 3.53	Variation of rms of deflection and inlet pressure difference with respect to pump speed	94
Figure 3.54	(a) Variation of first amplitude of deflection and inlet pressure difference with respect to pump speed (b) Variation of second amplitude of deflection and inlet pressure difference with respect to pump speed	95
Figure 3.55	Variation of rms of deflection with respect to rms of inlet pressure difference for four different test conditions	96
Figure 3.56	Variation of deflection magnitude A_1 with respect of pressure magnitude P_1 for low flow condition	97
Figure 3.57	Variation of deflection magnitude A_2 with respect of pressure magnitude P_2 for low flow condition	97

Figure 3.58	(a)The overall variation of A_1 for four different test conditions, (b)The overall variation of A_2 for four different test conditions	98
Figure 4.1	The subjected geometry for Finite Element Modeling is represented in dashed area where all dimensions are presented in mm. Hydraulic diameter is denoted by \varnothing and cross-section in different section is indicated inside the parentheses	103
Figure 4.2	Sub-domain division	104
Figure 4.3	The overall meshing	105
Figure 4.4	The boundary conditions for fluid mode	106
Figure 4.5	Boundary condition for structural mechanics mode	107
Figure 4.6	Boundary conditions for moving mesh mode	107
Figure 4.7	Boundary conditions for the pump speed of 4 RPM: (a) Time history of inlet flow velocities (b) Time history of outlet pressure representing	109
Figure 4.8	Boundary conditions for the pump speed of 5 RPM: (a) Time history of inlet flow velocities (b) Time history of outlet pressure representing	109
Figure 4.9	Boundary conditions for the pump speed of 6 RPM: (a) Time history of inlet flow velocities (b) Time history of outlet pressure representing	110
Figure 4.10	Boundary conditions for the pump speed of 7 RPM: (a) Time history of inlet flow velocities (b) Time history of outlet pressure representing	110
Figure 4.11	Boundary conditions for the pump speed of 8 RPM: (a) Time history of inlet flow velocities (b) Time history of outlet pressure representing	110
Figure 4.12	Comparison between Finite Element Modeling and Experimental results for the pump speed of 4 RPM: (a) Time history of beam tip deflection (b) Spectrum of the beam tip deflection	111
Figure 4.13	Comparison between Finite Element Modeling and Experimental results for the pump speed of 5 RPM: (a) Time history of beam tip deflection (b) Spectrum of the beam tip deflection	112

Figure 4.14	Comparison between Finite Element Modeling and Experimental results for the pump speed of 6 RPM: (a) Time history of beam tip deflection (b) Spectrum of the beam tip deflection	113
Figure 4.15	Comparison between Finite Element Modeling and Experimental results for the pump speed of 7 RPM: (a) Time history of beam tip deflection (b) Spectrum of the beam tip deflection	114
Figure 4.16	Comparison between Finite Element Modeling and Experimental results for the pump speed of 8 RPM: (a) Time history of beam tip deflection (b) Spectrum of the beam tip deflection	115
Figure 4.17	Comparison between experimental and FEM results: (a) rms of deflection or Y_{rms}	116
Figure 4.18	(a) Front cross-sectional view of test chip where the cross flow is shown in the clearance zone, between the side edge of microcantilever and the wall of microchannel	117
Figure 4.19	Contour plot of fluid velocity at the instant of maximum deflection of cantilever for the pump speed of 4 RPM	118
Figure 4.20	Contour plot of fluid velocity at the instant of maximum deflection of cantilever for the pump speed of 5 RPM	118
Figure 4.21	Contour plot of fluid velocity at the instant of maximum deflection of cantilever for the pump speed of 6 RPM	119
Figure 4.22	Contour plot of fluid velocity at the instant of maximum deflection of cantilever for the pump speed of 7 RPM	119
Figure 4.23	Contour plot of fluid velocity at the instant of maximum deflection of cantilever for the pump speed of 8 RPM	120
Figure 4.24	Q factor definition	122
Figure 4.25	Variation of Quality factor against viscosity for different fluids	123
Figure 4.26	Deflection amplitude spectrum in different liquids	124
Figure 4.27	Comparison of deflection amplitude spectrum between (a) liquids, and (b) gas	125
Figure 4.28	Comparison of transient beam tip deflection in Benzene, Water of 20°C, IPA and Fluid XP. The final static deflection is shown in a close up view, at the right side figure for different fluids	125

Figure 4.29	Comparison of transient beam tip deflection in Air, Water at 100°C and Acetone where deflection in air is presented in a close up view in right side figure, response in air is approximately 100 times lesser than liquids	126
Figure 4.30	Variation of the final tip deflection of cantilever (when, $t=0.5$ s) with respect to different viscosities of different liquids	127
Figure 4.31	Pressure difference distribution across the cantilever with respect to different viscosities of different liquids (after solving only Microfluidics mode)	127
Figure 4.32	Variation of Quality factor with respect to aspect ratio	128
Figure 5.1	Time histories of the cantilever beam tip deflection in Water at 48 RPM of pump speed	131
Figure 5.2	Time histories of the cantilever beam tip deflection in IPA at 48 RPM of pump speed	132
Figure 5.3	Time histories of the cantilever beam tip deflection in Fluid Xp at 48 RPM of pump speed	132
Figure 5.4	Time histories of the cantilever beam tip deflection in Corn Oil at 48 RPM of pump speed	132
Figure 5.5	Spectrum response of the cantilever tip at 48 RPM in (a) Water, (b) IPA, (c) Fluid Xp and (d) Corn Oil	133
Figure 5.6	(a) The variation of amplitudes of cantilever beam tip deflection with respect to viscosity of fluid; (b) The variation of rms of cantilever beam tip deflection with respect to viscosity of fluid;	134
Figure 5.7	Comparison of beam tip deflection between (a) water and (b) Fluid XP	135
Figure 5.8	(a) Variation in experimental quality factor Q_1 at frequency ω_2 with respect to viscosity; (b) Variation in second experimental factor Q_2 at the frequency ω_1 with respect to viscosity; and (c) Overall variation in the normalized quality factor	136
Figure 5.9	Boundary conditions from testing for finite element modeling with different fluid (N= 48 rpm)	137
Figure 5.10	Comparison of between experimental and FEM results of deflection against viscosity: (a) rms of cantilever beam tip deflection (b) Deflection amplitude A_1 (c) Deflection amplitude A_2	138

Figure 5.11	Comparison of flow visualization between FEM modeling and testing at 8 RPM pump speed	140
Figure 5.12	Full cantilever beam	141
Figure 5.13	Time history of pressure difference between two inlets	141
Figure 5.14	Time history of cantilever tip deflection (full beam deflection over the same interval presented in Figure 5.13 and full beam deflection shape for the marked point is presented in Figure 5.15)	142
Figure 5.15	Full deflection shape of cantilever for marked time in Figure 5.14	143
Figure 5.16	Full deflection shape of cantilever between 6 to 8 s	143

List of Tables

Table 2.1	The detail configuration of fabricated test chips	42
Table 3.1	Components used in the experimental setup and description of the notations used	47
Table 3.2	Four different test conditions	70
Table 3.3	The Excitation frequency variation with respect to RPM of pump	77
Table 3.4	The detail configurations of four test conditions presented in Figure 3.55	96
Table 4.1	Overall Mesh Statistics	105
Table 4.2	Sub-domain property for different fluid along with resultant response frequency	122
Table 5.1	Property of tested fluid	131
Table 5.2	The Effect of Viscosity on Response Amplitudes A_1 and A_2	134

Nomenclature

AFM	Atomic Force Microscope
CMOS	Complementary Metal–oxide–semiconductor
CPU	Central processing unit (Personal Computer)
DAB	Data Acquisition Board
DNA	Deoxyribonucleic acid
DVIP	Deflection using Video Image Processing
FEA	Finite Element Analysis
FEM	Finite Element Modeling
FFT	Fast Fourier Transform
LDV	Laser Doppler Velocitymeter
LOC	Lab on a Chip
LPCVD	Low-pressure Chemical Deposition
MEMS	Microelectromechanical Systems
MS	Microscope mounted with CMOS camera
MSDS	Material Safety Data Sheet
μ TAS	Micro Total Analysis Systems
PDMS	Polydimethylsiloxane
PP	Peristaltic pump
PSD	Position Sensitive Detector
PVDF	Polyvinylidene Fluoride
rms	Root mean square
RPM	Revolutions per minute

List of Symbols

V_{out}	Output voltage of pressure sensors
V_s	Supply voltage of Pressure sensor
α	static sensitivity
β	zero drift
e_p	Pressure error due to thermal sensitivity shift
e_t	Temperature change
Q	Flow rate
ΔP	Pressure difference between two point in a channel
μ	Viscosity of fluid
d	Diameter of the tube
L	Spacing between the two pressure sensors
t	Time
f_1	Fundamental frequency of the flow related to central disc rotation of the pump
f_2	Fundamental frequency of the flow related to central rollers rotation of the pump
ω_1	Fundamental angular frequency of the flow related to central disc rotation of the pump
ω_2	Fundamental angular frequency of the flow related to rollers rotation of the pump
N	Pump speed in RPM
D	Deflection Matrix
Δp	Pressure loading or pressure difference across the cantilever
P_o	Mean pressure

P_1	Magnitudes of the pressure loading corresponding to ω_1
P_2	Magnitudes of the pressure loading corresponding to ω_2
y	Deflection of the cantilever
Y_o	Mean Deflection of cantilever
A_1	Magnitudes of the deflection of cantilever corresponding to ω_1
A_2	Magnitudes of the deflection of cantilever corresponding to ω_2
Y_{rms}	rms value of cantilever beam tip deflection
P_{rms}	rms value of inlet pressure difference
\vec{u}	Velocity field or vector
p	Pressure
ρ	Density of fluid
η	Dynamic viscosity of fluid
v_1	Inlet velocity 1
v_2	Inlet velocity 2

1.1 Fluid-structure Interaction in Microsystems

Microfluid-microstructure interaction issue draws a great interest as the performance of many micro devices with microstructures submerged in fluid is potentially influenced by fluid interactions. In the field of microsystems, significant attention has been recently directed towards fluid-structure interactions due to its application in micro flow sensors, bio-microsystems, bio-sensors, chemical sensors, micro-valves, micro-pumps, drug delivery micro devices, diagnosis, lab on a chip (LOC), microswitches, atomic force microscope (AFM), micro total analysis Systems (μ TAS), etc. There are several energy dissipating mechanisms that affect the performance of MEMS devices, such as, losses due to acoustic radiation, losses due to viscous friction, losses due to micro-slips at support (anchor or, clamping losses), and intrinsic losses due to the material damping [1]. Among these sources, viscous damping is the most significant source of energy dissipation in MEMS devices [2]. Some of the applications that involve microfluid-structure interactions are shown in Figure 1.1.

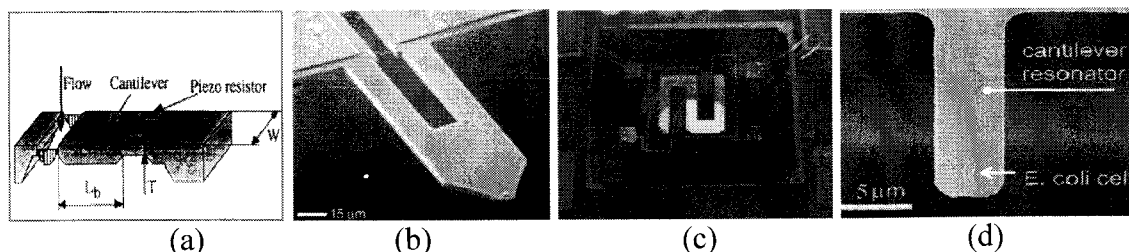


Figure 1.1: Applications involving microfluid-microstructure interactions (a) Nano-flow sensor [3]; (b) AFM cantilever [4]; (c) MEMS based anemometer [5] and (d) Bio-cell (*E. coli* Cell) detection by resonating cantilever in bio fluids [6]

During late 80's, the field of Microfluidics evolved as another subfield of MEMS with the innovation and development of different devices such as micropumps, micro valves, micro viscosity sensors and bioassays. The nature of these devices motivated researchers to investigate the complex fluid-structure interactions at the micro level. A simple microcantilever structure is presently explored to study its interactions with the fluids since microcantilevers are most commonly used as the elastic sensing elements in microflow sensors, micro valves, microswitches, microactuators, etc.

1.1.1 Applications in MEMS Device

Many MEMS devices such as cantilever based micro flow sensors, micro valves, micro switches, and actuators are influenced by fluid interactions. The applications of microfluid-microstructure interactions in such MEMS devices are briefly discussed in this section.

a. Flow Sensors: In a typical cantilever based flow sensor, the flow is sensed by the deflection or the stress developed in the cantilever due to force acting on it [3]. The stress developed in cantilever is usually measured by piezoresistive method by embedding piezoresistor inside the cantilever. In similar line, inviscid fluid-structure interaction such as air-structure interaction also plays an important role in MEMS based anemometer [5]. The MEMS based air speed sensors also use the same working principle as that of the MEMS flow sensor, with only difference being the design and the packaging method.

b. Micro Valves: In BIOMEMS field, development in cantilever-based micro valves have motivated studies in fluid-cantilever interactions [7-9]. Such types of valves are widely used in micropumps used in drug delivery systems.

c. Bio Chemical Sensors: Fluid-cantilever, interactions have been studied for different micro-bio sensing devices packaged as micro-fluidic chips [10]. Microchannel integrated cantilever transducers have been recognized as promising platforms for the next generation of chemical and biological sensors, as it is anticipated that microcantilevers can provide a versatile platform for real-time, in situ measurements of physical, chemical, and biochemical properties of physiological fluids [4]. The mechanisms involving the sensing or conversion of various chemical and biological environments into different physical parameters are shown in Figure 1.2.

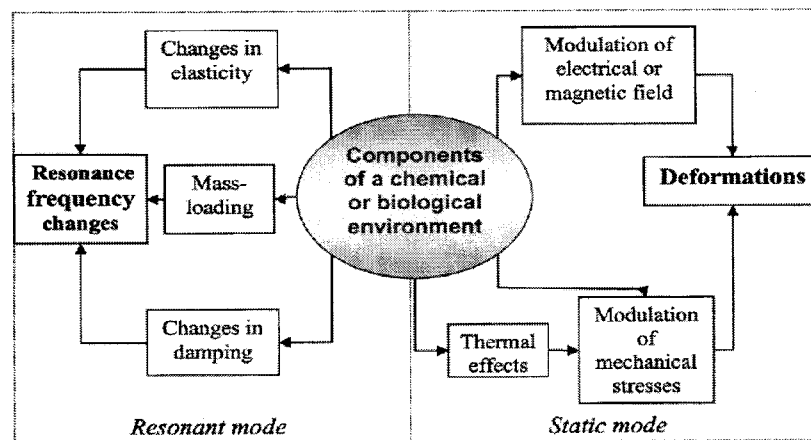


Figure 1.2: Transduction method for various chemical and biological environments [4]

d. Micro Viscometers: The amplitude and frequency of the response of a cantilever is extremely biased by viscosity of the fluid around it. A micro-viscometer is developed by applying this phenomenon. In a typical micro viscometer, the cantilever is excited electromagnetically [11] or by using piezoelectric material [12] and changes in vibration behavior are considered as the indicative of the viscosity.

e. Liquid Level Sensors: The micro-cantilever partially submerged in fluid is used as a liquid level sensor by relating the viscous damping effect on cantilever vibration, when

the cantilever is excited externally by an actuator [13]. Therefore, the response of the cantilever changes with the level of immersion of the cantilever in the liquid.

f. Others Applications: Many MEMS sensors including cantilever based MEMS capacitors, AFM cantilevers, switches, and actuators are affected by the squeeze film damping of the viscous fluid surrounding the device. The fluid-structure interaction studies would help enormously with the performance validation of these devices.

1.1.2 Applications in Biomedical Engineering

The fluid-solid interaction theories also help to explore the issues related to the biomechanics of human snoring. The response of a cantilever submerged in fluid depends upon its resultant loading condition that is dependent on the position of the cantilever with respect to the fluid flow. A cantilever in an axial fluid flow vibrates due to difference in the fluid pressure across the cantilever. With this type of fluid loading, two distinct types of instabilities emerge, namely the ‘static divergence’ and the ‘dynamic instability’ or ‘flutter’ [14]. A divergence type instability occurs, when the applied force due to fluid pressure is greater than the cantilever’s internal force. Similarly, instability can also occur in dynamic condition leading to flutter. In the context of biomechanics of snoring, Huang [15] showed that the linear theories would be sufficient to predict this type of instability.

1.2 Review on Relevant Literature

1.2.1 Significance of Microstructure-fluid interactions

The performance characterization of MEMS devices submerged in fluid together with application developments is the major motivation to study the microfluid-

microstructure interactions. The cantilever based micro-fluidic chips are becoming eminent due to their high sensing accuracy, reduced size for portability, easy fabrication, and low cost. To translate the bio-chemical environment, the common sensing parameter is the stress developed in the cantilever due to the bio-interaction on its surface, which results in the cantilever deflection or change in the elastic property of the structure. However, depending on the measured parameter, such as, cantilever deflection or resonance frequency, the mode of cantilever operation can be referred to as either static or dynamic [4]. Thaysen et al. [16] and Yang et al. [10] implemented the piezo-resistor to sense the stress in the cantilever, while Aubin et al. [17] and Vancura et al. [18], applied external optical interferometric technique with a laser beam and parasitic capacitances, respectively, to sense the cantilever frequency response in dynamic characterization.

The quality factor 'Q' of microcantilever-based sensors that work with fluid is immensely influenced by fluid damping. Hirai et al. [19] presents resonance characteristics of a microcantilever in various viscous fluids. The energy dissipation effects of microcantilever due to interaction with the environment (fluid) and potential applications of microcantilever in atomic force microscopy motivated Bhiladvala and Wang [20] to study the relation between quality factor of cantilever beam and the fluid pressure. High Q factor is the result of sharp change in different resonant parameters such as resonant frequency, amplitude or phase [21]. Zhang and Turner [22] investigated the issues that dominate the damping of the resonators and their consequence on 'Q' factor. Furthermore, Sukuabool and Sood [23] showed that the cantilever dimension has a significant affect on the damping and miniaturization increases the performance of microcantilever-based sensors in viscous fluids. While most of the studies concentrate on

the cantilever behavior, an exceptional study is carried out by Dareing et al. [24] as they highlighted not only cantilever behavior but also the fluid flow pattern around the cantilever.

In the case of bio chemical sensing, the fluid-structure interactions have been emphasized for cantilever based MEMS sensors. Initially, Gass et al. [3] and Peng et al. [25] introduced a single cantilever based flow sensor. Later Chen et al. [26] developed a multi cantilever based two-dimensional flow sensor array. Along with flow sensing, microcantilever has also been implemented to measure the viscosity of fluid. Quist et al. [25] developed piezoresistive nanoflow sensor and viscosity sensor to characterize nanoflows. The viscous damping effect, however, substantially alter the resonance frequency response of a cantilever. By applying this mechanism, a few viscosity meters have been developed [11]. The microcantilever based viscosity meters have been prominent not only in the industrial fluid monitoring applications [12] but also in biochemical as well as in biomedical engineering fields [27].

The performance evaluations of microcantilevers in AFM (Atomic Force Microscope) operating in viscous fluids have also motivated considerable studies on fluid-structure interactions at micro levels [28-35]. Most of these studies have concentrated on natural frequency shift of the cantilever, under viscous environment and an external excitation. However, a few studies have also been carried out at the nano level, focusing energy dissipation and response behavior of nanocantilevers under fluid-structure interactions [36, 37]. Beside this, squeeze film damping properties have also been discussed, which significantly influence the performance of cantilever based micro actuators and switches [38]. On the other hand, the studies on fluid-structure interactions

have also facilitated developments in micro-liquid level meters [13] and micro valves for biomedical applications [7-9]. In macro level, studies on fluid-structure interactions have been motivated by the issue of biomechanics in human snoring [14, 15, 39, and 40]. In addition, several studies have been carried out focusing the application of fluid-structure interaction theory in different macro devices [41-44].

1.2.2 Excitation Methods

A review of reported studies on microstructure-fluid interactions suggested that a wide range of excitation methods could be considered for applications at the micro level. These include the excitations due to fluid flows and other sources, as shown in Figure 1.3 and discussed below.

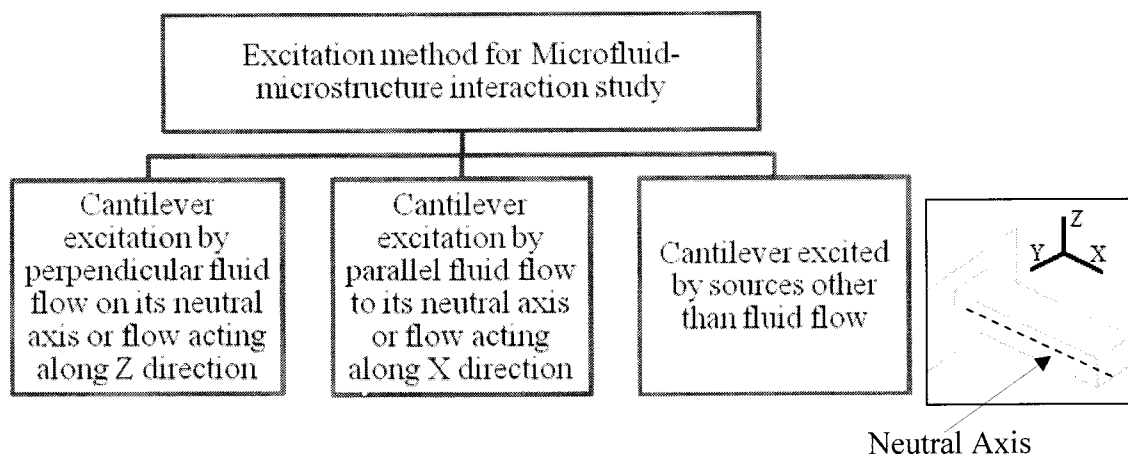


Figure 1.3: Types of excitation considered for fluid-structure interaction.

I. Cantilever Excitation by Perpendicular Fluid Flow (Flows along Z-axis)

The most prominent applications of this type of excitation could be observed in microflow sensors, where the cantilever is excited by flows acting perpendicular to its neutral axis. The cantilever beam was introduced in the fluid flow by Gass et al. [3] and excited by drag force due to viscosity of fluid passing through the tip of the cantilever.

However, Peng and Zhou [45] introduced another micro-cantilever based flow sensor where fluid flow exerts drag force on the surface of the cantilever that is perpendicular to its neutral axis. Quist [25] et al. used the same principle to develop a flow sensor used to detect not only the flow but also the viscosity. Chen et al. [26] used multi dimensional cantilever array to introduce two dimensional flow sensors. Another application of this type of model is the micro valve developed by Koch et al. [7-9] for biomedical applications.

II. Cantilever Excitation by Parallel Fluid Flows (Flows along X-axis)

The structure responses to parallel flows have been extensively investigated at the macro level while only limited studies could be found with applications involving microstructures. In MEMS applications, the dynamic characterizations of microstructures, subjected to parallel flows offer considerable potentials. Such a model has been mostly investigated for MEMS based biochemical sensors applications. Thaysen et al. [16] introduced a MEMS based biochemical sensor for DNA detection where a piezoresistor-integrated cantilever was applied to readout, which enabled measurements in non-transparent liquids, such as blood. In this case, the stress was developed in the cantilever due to the molecular adsorption of blood on the cantilever surface. Yung et al. [10] followed the same principle to develop a bio chemical sensor that was optimized through FEM simulations.

Huang et al. [39] developed a similar model at the macro level to explain the mechanics of human snoring. This occurs due to the fluttering behavior of soft palate, which is considered as a cantilever working in a closed channel of human neck subject to

excitation due to airflows along the axial direction. This study was followed by several more investigations [14, 15, 40, 46], focusing on different experimental and analytical methods, which will be explained later in this chapter. This model is explored in this thesis to study the dynamic microfluid-microstructure interactions.

III. Cantilever Excitations by Others External Sources

This type of model has been studied for two primary purposes: (i) developments of sensors for measuring fluid properties and contents; and (ii) to increase the performance of MEMS actuators, switches and sensors that are submerged in fluids.

In a traditional micro-viscometer, the cantilever, submerged in the fluid is excited by an external source and the change in the resonance frequency is observed due to the viscous damping effect of the surroundings fluid. Hausler et al. [27] introduced a micro-viscometer, which consists of either a tube or a rod oscillating torsionally at a resonance frequency with amplitudes in the micro and nanometer range. A fluid flowing through the tube or surrounding the rod dampens the torsional oscillations. The damping effect due to the viscosity of fluid is used to determine viscosity. Jungwirth [12] used the same principle to develop not only experimental setup but also a finite element model of the micro-viscometer. Here the cantilever is excited by piezoelectric actuation. The limitation of all these typical micro viscometer is that the fluid may prevent the resonant state from occurring due to large viscous losses for higher viscous fluids. To improve upon this limitation, Belmiloud et al. [11] proposed to widen the viscosity measurement range by studying the entire frequency spectrum of a microcantilever immersed in a Newtonian liquid, instead of focusing solely on the resonant frequency shift.

The performance characteristics of MEMS devices operating in fluidic environment are strongly affected by the viscous damping force of fluid. Hirai et al. [19] investigated the change in resonant frequency of microcantilevers due to changes in the surrounding fluidic environment. This study provided significant knowledge to understand the behavior of the microcantilevers used in the atomic force microscope, when operated in biological fluidic environments. They used a bimetal (Si_3N_4 , and Au) as a cantilever, excited by a laser thermal actuation system while the influence of geometry of cantilever probes was not investigated. Bhiladvala and Wang [20] investigated the same issue in different sizes of beams subject to different fluid pressures. Zhang and Kimberly [22] investigated the quality factor Q of microcantilevers of varying geometries operating in a fluid. The geometric parameters included ranges of widths, thicknesses and cross-sections.

1.2.3 Fabrication of Device

Provision of precision and minimum obstacle to the flow, enough facility to detect the structural response, leak proofing of the microchannel, and enough instruments to estimate fluid parameters during experiments, are the major requirements to fabricate these devices. Implementations of all these conditions at the same time, makes the fabrication process more challenging. Thaysen et al. [16] carried out the fabrication by selective reactive ion etching of a sandwiched silicon wafer where layer of silicon nitride and polysilicon is deposited by low-pressure chemical vapor deposition (LPCVD) to fabricate cantilever based biochemical sensor integrated with microfluidic handling system. Chen et al. [26] used both conventional micro-fabrication processes such as, surface micromachining and deep reactive ion etching to fabricate cantilever based flow

sensor. The simple way to fabricate this type of model is, by deep etching of cantilevers followed by encapsulation and bonding as carried out by Gass et al. [3].

However, two different interesting fabrication methods are carried out by Aubin et al. [17], which are presented, in Figure 1.4. In the first method, cantilever and microchannel were fabricated in two separate wafers. The cantilever was fabricated by surface micromachining and channel was fabricated in a 500 μm thick borosilicate glass wafer by reactive ion etching. A silicon oxide layer was used as a sacrificial layer, which was deposited on a silicon wafer. To define the cantilever anchor a trench was made in the sacrificial layer and the silicon nitride, which was the structural layer of the cantilever, was deposited on the oxide layer by low-pressure chemical vapor deposition (LPCVD). The cantilever was defined by photolithography and reactive ion etching on the structural layer. At the end, cantilever was released by removing the sacrificial layer. Both wafers (microchannel and cantilever wafer) were anodically bonded using a commercially available bonder. In the second method, channels were defined on both wafers and were aligned and bonded together by applying pressure (~ 20 kPa) at 200°C for 30 minutes.

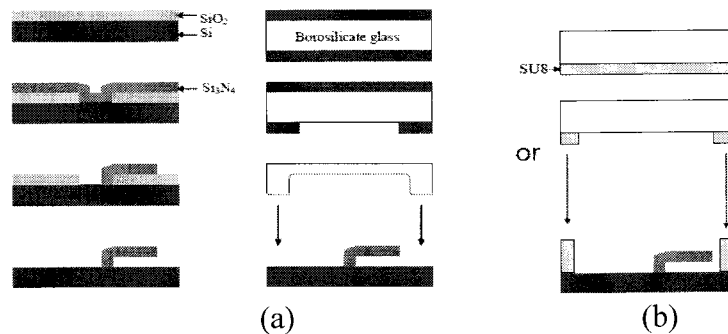


Figure 1.4: (a) Fabrication of cantilever and encapsulation using different wafers, (b) Fabrication of the cantilever and encapsulation in the same wafer [17]

Between these two fabrications, the later process is more suitable for better optical access to the devices as the glass wafer does not undergo a wet chemical etch. Since, in the fabrication of micro valve the optical access is not necessary so Koch et al. [8] fabricated the cantilever by surface micromachining and the channel by bulk micromachining in two different wafers and bonded them using IR aligner. However, in this fabrication process the channel and cantilever were fabricated in the same wafer so that the cantilever was aligned with the channel of second wafer.

1.2.4 Experimental Method

An experiment method includes some input accessories and an output and feedback characterization processors, which consist of instrumentation and measurement equipment. Based on the characterization method of structural interaction with fluid, the fluid-structural interaction experimental method can be classified into the following categories.

a. Optical Characterization

Laser Doppler Velocitymeter (LDV) and Position Sensitive Detector (PSD) are the most common devices that are used for optical characterization of structural interaction with fluid. LDV estimates the frequency response by measuring the phase difference between an internal reference beam and a test beam, whereas Position Sensitive Detector (PSD) is an optical position sensor (OPS), that can measure the position of a reflected light spot on one or two-dimensional detector surface.

In the case of external excitation, laser is sometimes used to excite the cantilever in a definite frequency. Hirai et al. [19] excited the cantilever by laser and at the same

time, the frequency response of microcantilever with respect to different fluid was characterized by a PSD, with a FFT analyzer.

Aubin et al. [17] followed the same process to excite the NEMS (Nano-Electro-Mechanical System) resonator by laser in microfluidic channel. However, they used LDV to characterize the vibration behavior of cantilever in microchannel where, the laser excited the cantilever thermally. In their experiment, fluid is pumped by a syringe pump and pressure was monitored during the test. However, Zhang and Turner [22] characterized the damping effect of fluid on micro resonators with respect to different geometry of those resonators by LDV but they excited the structure with piezoelectric shaker.

Naik et al. [44] used piezoelectric actuation to excite the cantilever and the response of the cantilever is sensed by LDV with vector analyzer. They characterize the resonance of the cantilever with respect to different types of fluids as well as different gaps between wall of the channel and cantilever. They studied the influence of wall distance under the cantilever. They can vary the gap height from 0-2.5 mm. Belmiloud et al. [11] also use optical characterization but they excited the cantilever in the fluid by electromagnetic actuation to study the entire frequency spectrum of a microcantilever immersed in a Newtonian liquid, instead of focusing solely on the resonant frequency shift.

The main advantage of optical characterization is that, this method is very precise to detect the high frequency response of structure interaction in fluid. Conversely, the main disadvantage of this read-out technique is that, it requires external devices for

deflection measurements. Therefore, their continuous alignment and calibration are very time consuming. Optical techniques are sensitive to changes in the optical density of the sample and can be affected, by changes in the optical properties of the medium surrounding the cantilever [47]. However, Lechuga et al. [48] remove this disadvantage by introducing a new novel bio sensing chip where the microcantilever was deflected due to reaction with bio-chemical and the cantilever was itself an optical waveguide which coupled with another one. This optical read out method is not suitable for the cantilevers surrounded by opaque fluid.

b. Piezoresistive Characterization

The piezoresistor changes its resistance when any kind of stress is applied on it. Therefore, if a piezoresistor is embedded inside a cantilever that is interacting with fluid then the response of that cantilever can be sensed as change in the resistance of the piezoresistor with the deflection of that cantilever. Typically, a piezoresistor is connected to a Wheatstone bridge to sense the change of resistance. Piezoresistance based transduction is mostly used in flow sensors and biochemical sensors. As described earlier Gass et al. [3] used this arrangement for flow sensing by measuring the drag force. This drag force is proportional to the flow of the fluid. In the case of piezoresistor based micro biochemical sensors, the stress is produced due to the molecular interaction with cantilever surface. Figure 1.5 illustrates a piezoresistor based flow sensor calibration experimental setup, which Peng and Zhou [45] introduced in their study.

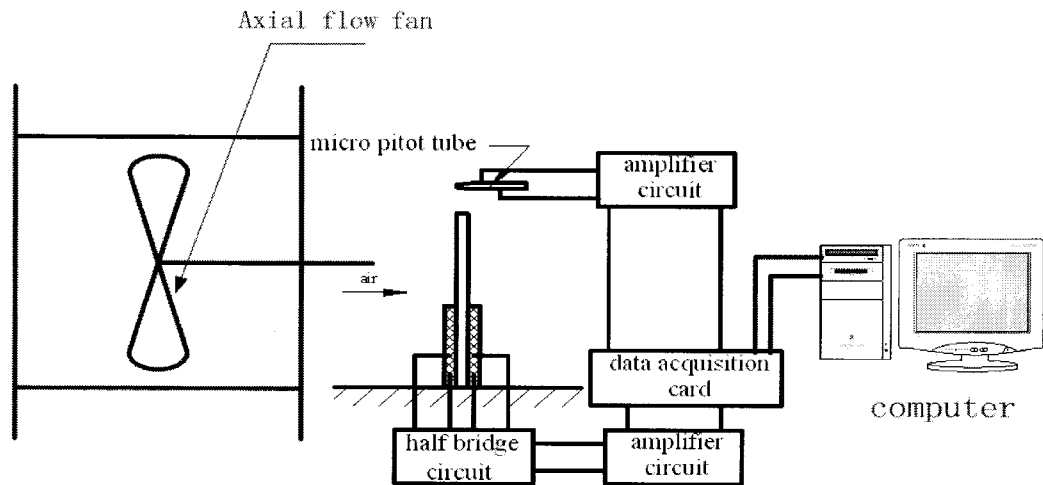


Figure 1.5: An Experimental setup of piezoresistor based flow sensor [45]

The piezoresistor-based detection has several advantages comparative to optical detection such as [47],

- Piezoresistive detection can work in non-transparent solutions
- Time consuming laser alignment is not needed
- Readout electronics can be integrated on the same silicon chip
- Temperature control can be easily implemented
- They are compatible with miniaturization and array fabrication

The disadvantage is low resolution and this method is not so much suitable for high frequency response.

c. Piezoelectric Actuation

In Piezoelectric actuation, cantilever is excited by a piezoelectric material embedded inside cantilever. If that cantilever acts as a sensor, such as, viscosity meter or liquid level sensor then it is excited in some certain frequency range to get the resonance response. The impedance is measured with a spectrum analyzer [12, 13]. In macro level,

Auregan and Depollier [40] used piezoelectric cantilever to observe the fluttering behavior of cantilever under axial airflow condition.

d. Imaging Method

In image method, the response of the cantilever is captured by high-speed camera and the video image can be post processed to estimate the deflection as well as resonance spectrum. However, in macro level, Huang et al. [39] use high-speed camera to find the critical flow velocity when a cantilever touch the fluid channel wall. They only noticed the gap between the cantilever and the wall of the channel. However, they did not employ any post processing to capture the response of the cantilever.

As this method in micro level has not been explored yet, this thesis uses this method along with image post processing to characterize the deflection of the cantilever. This method is simpler to implement at the micro level using a microscope.

1.2.5 Theoretical Modeling

The theoretical modeling of the fluid-structure interaction depends on the objective of the study. The boundary conditions are implemented according to the nature of the flow. Most of the studies applied finite element modeling to investigate the fluid-structure interaction in micro level as well as in macro level.

However, for the miniature elastic object, the fluid viscosity dominates the dissipation and the motion due to the bombardment of fluid molecules dominates the fluctuation in the deflection of the structures. Sader [49] developed the Finite Element Model of microcantilever operating in viscous fluid for the application in Atomic Force Microscope. He applied thermal excitation in his Finite Element Model, which is the

Brownian motion of the molecules in the surrounding fluid. In this model, the potential energy for each mode of the beam must be identically equal to the thermal energy $1/2k_B T$, where k_B is Boltzmann's constant and T is absolute temperature. In another study, Green and Sader [32] presented a theoretical model that is capable of calculating both torsional and flexural frequency response of a cantilever beam immersed in a viscous fluid and vibrating in proximity to a solid surface. Paul et al. [37] followed this investigation of the stochastic dynamics of micron and nanoscale elastic cantilevers in fluid and used finite element numerical simulations to solve a three-dimensional, and time dependent fluid-structure interaction problem. The simulation is initiated with the removal of a step force applied to the tip of the cantilever and it was assumed that all of the dissipation comes from the fluid and that elastic dissipation in the cantilever is negligible. In another finite element simulation, Clark and Paul [50] considered the stochastic dynamics of an array of two closely spaced atomic force microscope cantilevers in a viscous fluid. Therefore, the cantilevers are not driven externally, as is common in applications of atomic force microscopy, and they explored the stochastic cantilever dynamics due to the Brownian motion of fluid particles. Clark and Paul [30] also carried out finite element numerical investigation about the stochastic dynamics of rectangular, v-shaped cantilevers immersed in water, and they considered two-dimensional flow of liquid with the thermal excitation of the beam.

For the development of bio-chemical sensor, Yang et al. [10] also used finite element method to explore the fluid-structure interaction. In the finite element software package CFDRC, they used piezoresistive cantilever with chemo-mechanical boundary condition. To explore the squeeze film damping effect on the microcantilever beam based

switches Ostasevicius et al. [1] carried out finite element modeling based on three different form of Reynolds equation which are linear, nonlinear and linear incompressible. However, Jungwirth [12] presents finite element modeling using COMSOL 3.4 software package to validate the developed viscosity meter consisting of piezoelectric excitation on a partially submerged cantilever. Koch, et al. [9] developed a sequential finite element model of microcantilever-based valve for biomedical application. The performance of MEMS cantilever based micro wind speed sensor is characterized by Du et al. [5] with the finite element software package, ANSYS. Peng and Zhou [45] characterized their developed flow sensor in a finite volume numerical model by CFD software called FLUENT, to analyze the flow. However, in macro level, Balint and Lucey [14] present a finite element model to solve the fluttering behavior of soft palate in human throat.

1.2.6 Results and Analysis

The results from relevant literature can be classified in to two categories, namely

- I. Results from Theoretical Study
- II. Results from Experimental Study

I. Results from Theoretical Studies

Most of the theoretical studies focus on the performance of AFM cantilever in viscous fluid. In analytical modeling of AFM cantilever in fluid, Sader [49] showed that there is dramatic shifting and broadening of the fundamental resonance for gases compared to the inviscid fluid. He also explored significant coupling between the fundamental mode and its first harmonic. Overall, he found that the peak frequencies of both the fundamental mode and its first harmonic occur at significantly lower frequencies

than that predicted by the inviscid fluid model. The study indicates that the viscous effect is strongly dependent on the dimensions of the beam, as decreasing these dimensions (length or width) enhances viscous effects, resulting in increased broadening and shifting of the resonant peak from its value in vacuum.

Similar result is found by Martin and Houston [36] for nano level resonator, since their numerical model indicates that the cantilever operating in liquid is a largely damped system, with a large shift in the resonant frequency away from the natural frequency of the cantilever. The quality factor in air is typically orders of higher magnitude than the estimated quality factor in water for the same resonator,

The consideration of thermal noise lowers down the quality factor as represented by Paul et al. [37]. Clark and Paul [50] considered an array of two cantilevers placed opposite with their tips located with a certain gap. When one cantilever was excited by a step force, the other one was also excited due to fluid motion. The other cantilever had more dynamic response than the forced cantilever. However, the gap also influenced the response, as the increase in gap reduced the deflection of the free cantilever. In the closer inspection of fluid flow of a single cantilever they found that, the fluid flow over the cantilever tip is greater than the fluid flow around the sides of the cantilever. This suggests that an elastic object located to the side of the cantilever will exhibit less fluid coupling than an object placed at the same distance of the tip from the cantilever. In another study, Clark and Paul [30] applied step torque and step force to rectangular and V-shaped cantilevers submerged in fluid. They also applied thermodynamic approach in this study. Their study showed that, at short time intervals the influence of higher modes exist for the tip-angle measurements, however, this does not exist for the tip deflection

measurement of both shapes of cantilevers. This existence of higher modes is shown in the Figure 1.6, with the close up view at the right most corner box.

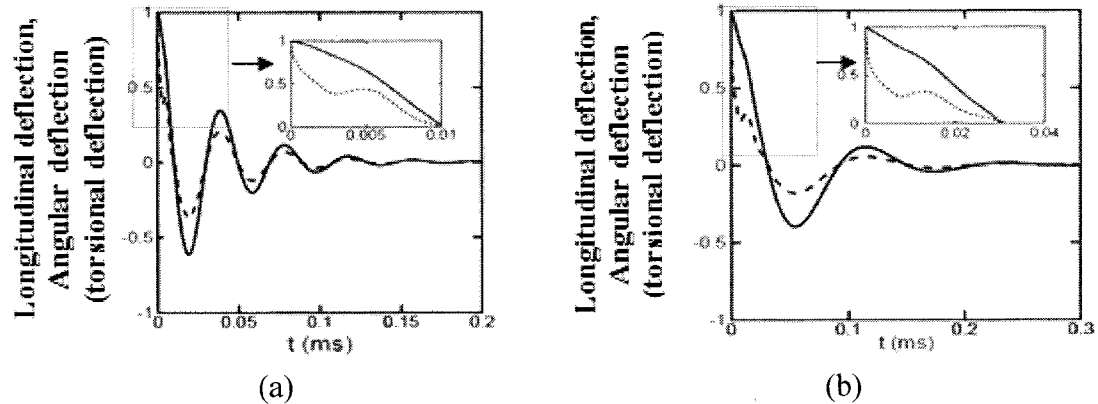


Figure 1.6: (a) Normalized response of rectangular cantilever, for tip deflection (solid) and tip angle (dashed), where the presence of higher mode in tip angle is showed in a zoomed view in the right rectangle, (b) Normalized response of rectangular cantilever, for tip deflection (solid) and tip angle (dashed), where the presence of higher mode in tip angle is showed in a zoomed view in the right rectangle [30]

The effect of Brownian noise is particularly studied by Sukuabool and Sood [23] to characterize the performance of cantilever based biosensors. The effect of Brownian noise increases with the increase of length or width and decreases with the increase of thickness of cantilever. In considering Brownian noise spectrum, the signal amplitude increased and bandwidth decreased when the cantilever length is increased. In the case of Brownian noise spectrum, as the cantilever width is increased, the bandwidth increases due to the increased influence of damping. However, as the cantilever width continues to increase, the bandwidth reaches the steady value and then begins to drop. However, this study showed that the effects of liquid on the frequency response are more dramatic than the effects of gas. The acetone, CCL_4 and water have much sharper resonance peaks than other fluids, which is presented in Figure 1.7. The air and 1-Butanol have a lower resonance peak than the rest. Shift and broadening of the peak are increased with further increase in fluid density and viscosity.

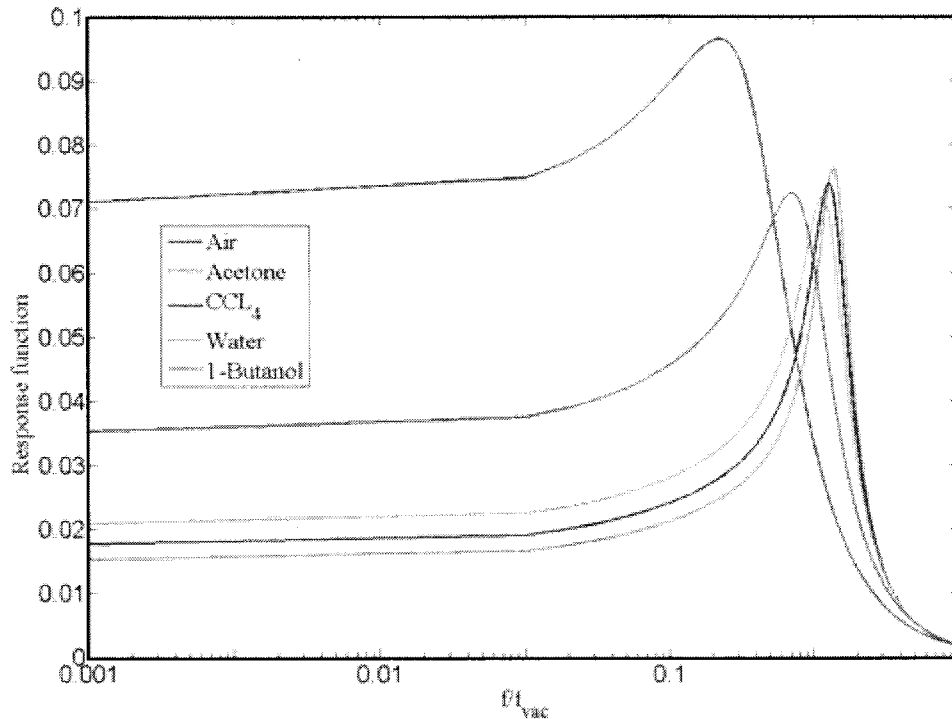


Figure 1.7: Dependence of Brownian noise on fluid density and viscosity: spectrum of combined Brownian and Johnson noise [23]

Finite element analysis of Ostasevicius et al. [1] shows the influence of squeeze film air damping on free vibrations of microstructures. Increase in damping factor was noticed with increase of pressure in the gap and decrease of air film thickness. From their study, it was found that the damping factors estimated using simulations carried out with different squeeze-film damping models showed minor differences between results from nonlinear and linear Reynolds equation (NRE and LRE) based models, which were higher than that of linear incompressible Reynolds equation (LIRE) based model, as presented in Figure 1.8. Their study on the influence of sinusoidal excitation frequency of small-amplitude forced vibrations of microstructure indicates that air compressibility effects become more pronounced with increase in excitation frequency. This is not observed in the case of FE model coupled with LIRE.

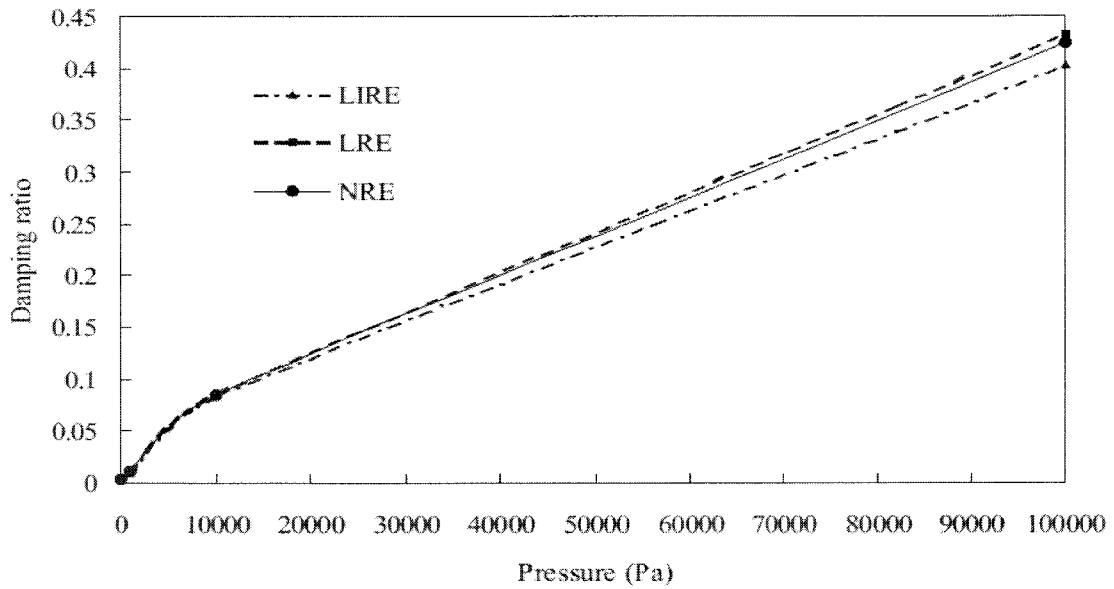


Figure 1.8: Comparison of variation of damping ratios obtained by using different squeeze-film damping models and by extracting them from simulated free vibration response curves of the arbitrary point at the end of a cantilever microstructure after it has been released from its initial deflected position $z = 1 \mu\text{m}$ upwards for the different levels of working air pressure p_0 in the gap with thickness $h = 1 \mu\text{m}$ [1]

It is found from numerical analysis that LIRE oversimplifies the phenomenon of squeeze-film damping, particularly in the case of large-amplitude vibrations of microstructure. Therefore, they suggest the use of NRE or LRE for the modeling of air damping effects in the microdevices.

Jungwirth [12], presents online fluid monitoring system with electromechanical cantilever immersed into water at five different levels (20%, 40%, 60%, 80%, and 100%). The tendency of lower resonance frequency at higher depth of immersion was observed in both simulation and measurements.

In FEM model of MEMS based wind speed sensor, Du et al [5], showed that the maximum deflection and maximum stress of cantilever are proportional to square of the mean flow speed. The fluid-structure interaction numerical model developed by Balint

and Lucey [14] in macro level shows some dramatic result. The model consisted of two channels where the cantilever was placed in between those inputs. Their study indicates that, when both upper and lower channels (airways) are open, the plate loses its stability through flutter. Instability sets in at a speed beyond a critical Reynolds number when the energy transfer exceeds the rate of plate-energy dissipation. When one airway is blocked, the principal means of destabilization is divergence, which sets in at a flow speed, beyond which the magnitude of the fluid-pressure force exceeds the restorative structural forces in the plate. Structural damping promotes pure divergence by facilitating the formation of a critical deformation shape. However, for very low values of damping, at the flow speed below that of divergence onset, flutter may exist. At higher flow speed, a combination of flutter and divergence instability mechanisms can be responsible for oscillatory growth. In such cases, the plate deformation largely comprises fluctuating combinations of both first and second modes of plate deformation.

II. Results from Experimental Studies

Experimental studies have been carried out to investigate the resonance behavior of microcantilever in viscous fluid. With optical characterization of MEMS structure in fluid Hirai et al. [19] indicate that the resonances in water are modulated to lower frequencies compared to in air. These were also confirmed by the theoretical calculations taken into account of the drag force in the viscous fluid.

Aubin et al. [17] characterized the quality factor of NEMS resonator with respect of different pressure of air inside the microchannel and the study shows that lower operating pressures inside the channels eliminated viscous damping effects which would

degrade the quality factor of resonance and thus reduce the mass sensitivity of the sensor if operated in air. This was confirmed by measuring the quality factor of a resonating structure while monitoring the pressure at the vacuum pump and the system was allowed to slowly leak to atmospheric pressure. However, the study of Zhang and Turner [22] characterized the damping effect of MEMS resonator with respect of different widths and different resonance frequencies, different cross-section and different width/thickness ratios. Their investigation indicates that, damping of the cantilevers varies with both resonant frequencies and width of the device. The damping coefficient is linearly dependent on the width for each resonant frequency. They also found, after comparing the damping effect of different cross section such as trapezoid and circular cross-sections with respect to the parameter λ , where $\lambda = \text{width} / \sqrt{(2 \times \text{viscosity}) / (\text{density of fluid} \times \text{natural frequency})}$, the relative differences among them are less than 5%. However, circular cross sectional shows relatively higher damping effect, which is presented in Figure 1.9.

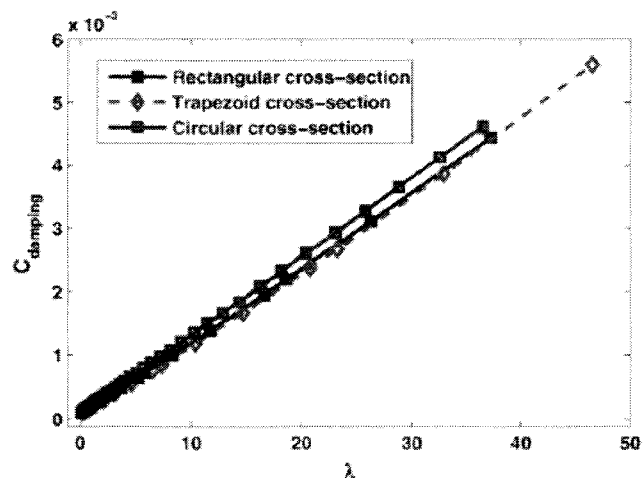


Figure 1.9: C_{damping} for three types of cross-sections [22]

Naik et al. [44] found that the resonance amplitude decreases with increasing viscosity of the liquid. However, damping is generally associated with the flatness or

broadness (bandwidth) of the resonance spectrum. The stronger damping broadens in a given peak in the resonance spectrum. As the gap height between cantilever and wall decreases, the resonance amplitude decreases, and the bandwidth increases.

The study of Belmiloud et al. [11] opens a new window to measure the viscosity, as they showed that even if no resonant phenomenon occurs, viscosity measurement is possible by studying the entire frequency spectrum of a microcantilever immersed in a Newtonian liquid, instead of focusing solely on the resonance frequency shift. They measure the amplitude of vibration and the phase as functions of frequency on a range of 10 to 10000 Hz. The beam is immersed in oils of known viscosities ranging from 20 cP to 30000 cP. Both experimental and numerical simulation showed that no resonant peak occurs for viscosities above the critical limit of 96.5 cP because of the excessive damping that occurs as shown in Figure 1.10.

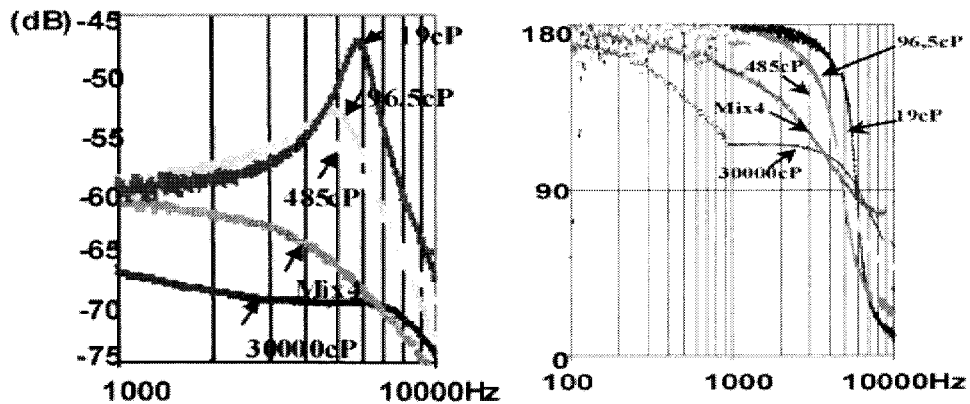


Figure 1.10: Experimental amplitude and phase of deflection for a silicon cantilever ($70\mu\text{m} \times 200\mu\text{m} \times 3000\mu\text{m}$) oscillating in various viscous fluids [11]

The flow sensor developed by Gass et al. [3] has the easy integration with other microfluid elements. This flow sensor can quantify the displaced volumes in the order of

a few nanoliters. The experimental results from the flow sensor developed by Peng and Zhou [45] is shown in Figure 1.11 where the relationship between flow and voltage output is presented.

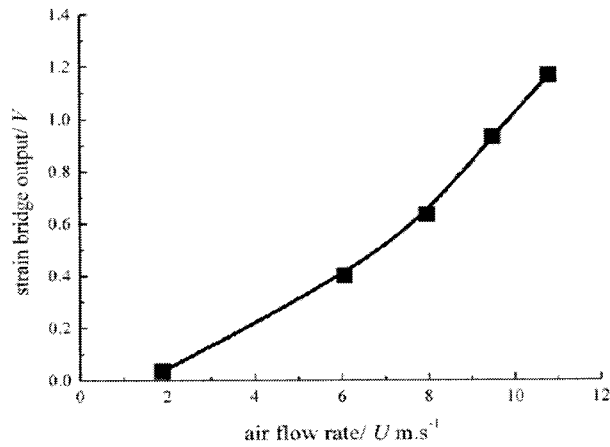


Figure 1.11: Relation between output voltage and flow rate in the flow sensor developed by Peng and Zhou [45]

The Campbell and Mutharasan [13] showed the linear relationship between the resonance frequency shift and depth of immersion of microcantilever in liquid in their liquid level sensor. The shift in first resonance is inversely proportional to the depth of immersion and on the other hand, the shift in second resonance is proportional to time when the liquid is continuously evaporated. However, higher volatile liquid showed higher rate of change in resonant frequency when cantilever is immersed in evaporating liquid.

In macro level, as shown in Figure 1.12 human snoring caused by fluttering behavior of cantilever type soft palate in human throat is a good example of fluid-structure interaction where cantilever is clamped in between the inlet of two channels. To model the human snoring Depollier and Auregan [40] showed that, when both channels

are open, the instability occurs very abruptly just before the amplitude of the motion is weak and just after the beam hits at least one of the wall.

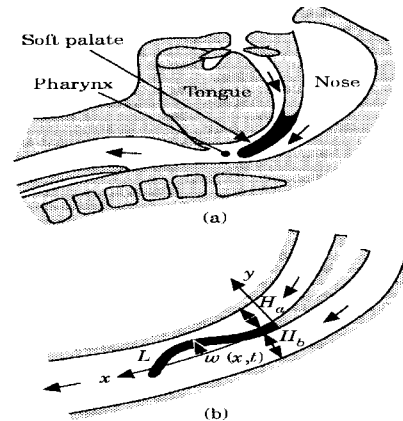


Figure 1.12: (a) The schematic description of the human pharynx (b) model of the pharynx "the moving part is in black [40]

Overall investigation of both theoretical and experimental results of relevant literature shows that resonance frequency and quality factor of cantilever is significantly influenced by viscosity of fluids. In addition, there are also possibilities of divergence and fluttering instabilities depending upon the strength of non-linearity of fluid interaction with cantilever. This type of study bringing development on the performance evaluation of micro devices working in surrounded fluid.

1.3 Thesis Objective, Contribution and Overview

1.3.1 Thesis Objective

The main objective of this thesis is to study the fluid-structure interaction of a microcantilever in a microchannel through experiments and finite element modeling. Another aim is to develop a new experimental method to detect the micro-structural

response in fluid. Final goal is to develop an application such as viscometer for biomedical application.

1.3.2 Thesis Contribution

This thesis makes the following contributions-

1. To perform the experiment on a microcantilever integrated microfluidic chip that is fabricated by the polymer based fabrication method. PVDF film was integrated as the cantilever inside the microfluidic channel.
2. A new experimental method is introduced to detect the cantilever response by introducing image capturing and processing method with high speed CMOS camera and microscope which is named as DVIP (Deflection using video image processing)
3. A finite element numerical model is developed and validation is done with experimental results
4. Effect of viscosity on fluid-structure interaction was investigated
5. Finally, an application is developed on the based on theoretical investigation. A viscometer is fabricated and experimental results are obtained from that.

1.3.3 Thesis Overview

Chapter 1: This chapter provides introduction about the application of fluid-structure interaction in micro level. The comprehensive literature review on the microstructure microfluid interaction is discussed. Finally, the thesis objectives, contributions, and overviews are discussed in this chapter.

Chapter 2: This chapter provides the fabrication method of microcantilever integrated microfluidic test chip. However, molding and patterning based soft lithography method was followed to fabricate the test chip.

Chapter 3: This chapter discusses the development of experimental setups. The detail design of experiments is discussed. A new image capturing and processing method is introduced to measure the cantilever response. The algorithm that is developed to detect cantilever response from the image is discussed. This chapter also presents the experimental results. The cantilever tip responses with respect to different flow conditions are provided.

Chapter 4: This chapter narrates the finite element modeling of the current configuration and validation with the experimental results. This chapter also presents the influence of viscosity of fluid and influence of geometry of structure over the quality factor by the finite element modeling.

Chapter 5: This chapter discusses the detail idea about the application development from current theories. A new microcantilever integrated microfluidic chip based viscometer is introduced. The experimental results of viscometer are discussed. Another application is developed by characterizing the flow behavior near the cantilever tip through particle flow visualization. An experimental result on the full arc deflection of cantilever is presented in this chapter as a potential application of image post processing method.

Chapter 6: This chapter provides conclusion and significant contribution of this thesis. This chapter also presents some recommendation for further works.

Design and Fabrication of Microstructure Integrated Microfluidic Channel

2.1 Introduction

Dynamic behavior of microstructures contained within microfluidic channels are strongly affected by their interactions with the flowing fluids. The resulting dynamic responses of the structure further influence the fluid flow properties in the microchannels. Such interactions between the microstructures and the fluid flows within microchannels are widely observed in many biomedical and chemical applications, particularly those involving fluid transport such as drug delivery, micro valves [8], DNA analysis [51], cell detection [6] etc. Although numerous studies have been reported on microflows and their interaction with the microstructures, only minimal effort has been made on characterization of microflows particularly in the presence of flexible microstructures [52, 53]. This is attributable to a number of factors, namely, lack of reliable measurement methods for microfluidic applications and challenges associated with fabrication of microfluidic channels integrating flexible microstructures. Furthermore, the design of microfluidic channels comprising flexible structures involves additional complexities due to the presence of Vander Waals, Electrostatic and steric forces.

The evolutions in microfabrication techniques over the past few decades have greatly facilitated the fabrication of microfluidic channels, microstructures and an array of micro sensors. In the recent year, a few investigators have used silicate glass to fabricate microfluidic channels for studies on microfluid-microstructure interactions, which

facilitated the flow visualization and implementations of optical measurement methods for the dynamic characterizations of microstructures [16, 17]. A review of the relevant studies revealed that vast majority of microcantilever integrated microfluidic chips were fabricated through combinations of several microfabrication processes [3, 16, 26]. The cantilevers were fabricated by either photolithography-based surface micromachining process or reactive ion etching, while the microchannels were fabricated using bulk micromachining either within the same wafer or within different wafers. Such method, however, are known to be costly, poorly suited for patterning only two-dimensional non-planar structures. Furthermore, these methods provide very little control and flexibility over the chemistry of the surface [54]. In this dissertation research, alternate method for fabricating microfluidic channel integrating a microstructure is explored in an effort to reduce the fabrication cost and to enhance the structural surface properties to study dynamic interactions between the fluid flow and the integrated microcantilever. The associated design and fabrication challenges are briefly described and the design of a microfluidic channel with a microcantilever subjected to axial differential flows is realized, since this model has not been explored in microfluidic channel in satisfactory level. A common fabrication process flow is proposed and adopted for the fabrication of both microstructure and microfluidic elements.

2.2 Design of a Microstructure Integrated Microfluidic Chip

The design of a microfluidic channel integrating a flexible microstructure involves many challenges, particularly when controlled flow conditions are required for fundamental studies of dynamic interactions. These challenges primarily arise from the need to maintain the micro level dimensions for microchannel in the order of a few

hundred micrometers, and to integrate a flexible microstructure with adequate clearance. The fabrication of a microstructure also involves challenges in identifying a suitable material with thickness in the order of 20 to 50 μm . Furthermore, the fixation of the flexible structure within the microchannel with desired boundary conditions could be highly complex task, while the implementations of essential instrument may pose further challenges.

In this dissertation, the study of fluid-structure interaction is undertaken for a microcantilever beam subject to controlled differential flows within a microchannel. The primary design requirements for the integrated microfluidic channel and the microcantilever were formulated as;

- a. Conceive a channel geometry so as to minimize the pressure losses attributed to the geometry and the surface conditions;
- b. Ensure the provision for distributed dynamic loading of the microcantilever through controlled differential flows or fluid pressure across the structure;
- c. The design should be capable of handling two different flows using two different microchannels to ensure differential pressure while the flows may merge only after the beam end;
- d. The cantilever support must be designed so as to permit the flows along the direction parallel to the neutral axis of cantilever with minimal obstruction;
- e. The microchannel design should be realized with a transparent material in order to facilitate optical measurements and flow visualizations; and
- f. The design should be adaptable to a controllable flow sources and essential instrumentations for capturing the fluid pressure and beam deflections

In order to overcome the disadvantages associated with the photolithography based microfabrication process and to satisfy the above stated design requirements an elastomeric element, Polydimethylsiloxane, was chosen as the material for the fabrication of the microfluidic channel. The soft lithography process was followed to fabricate the microchannel. The chosen material is a transparent elastomeric material called Polydimethylsiloxane (PDMS), which is relatively less expensive and can be conveniently applied fabrication process. The PDMS fabrication method called 'Soft-lithography' also supports the batch fabrication, where a single mold may be used for fabrication of a large number of specimens in a highly efficient manner. A microfluidic channel with two inlets and one outlet is subsequently designed using the PDMS material, which could permit two different flows. A microcantilever is realized from a 25 μm thick PVDF (Polyvinylidene Fluoride) film for its integration in the microchannel at the junction of the two flow inlets. Figure 2.1 illustrates the overall design layout of the integrated microchannel and microcantilever specimen together with an enlarged view of the microcantilever. Figure 2.2 illustrates the flow path and possible location of an optical instrument system such as LDV.

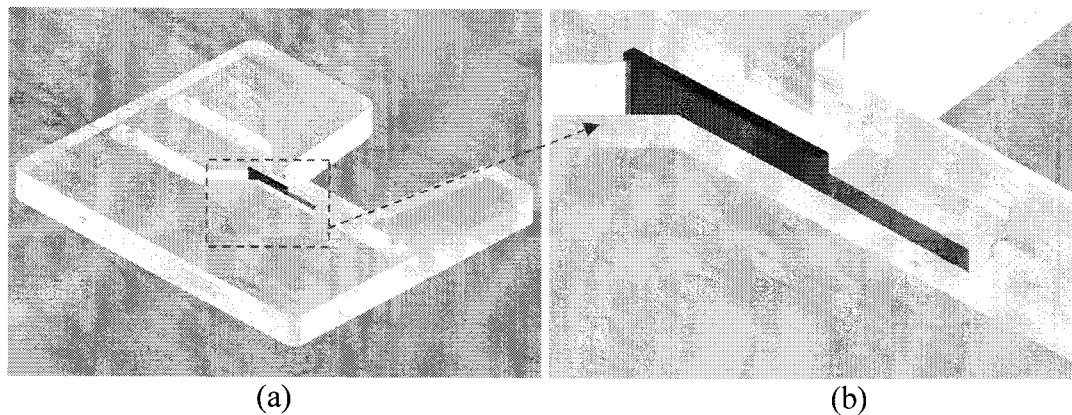
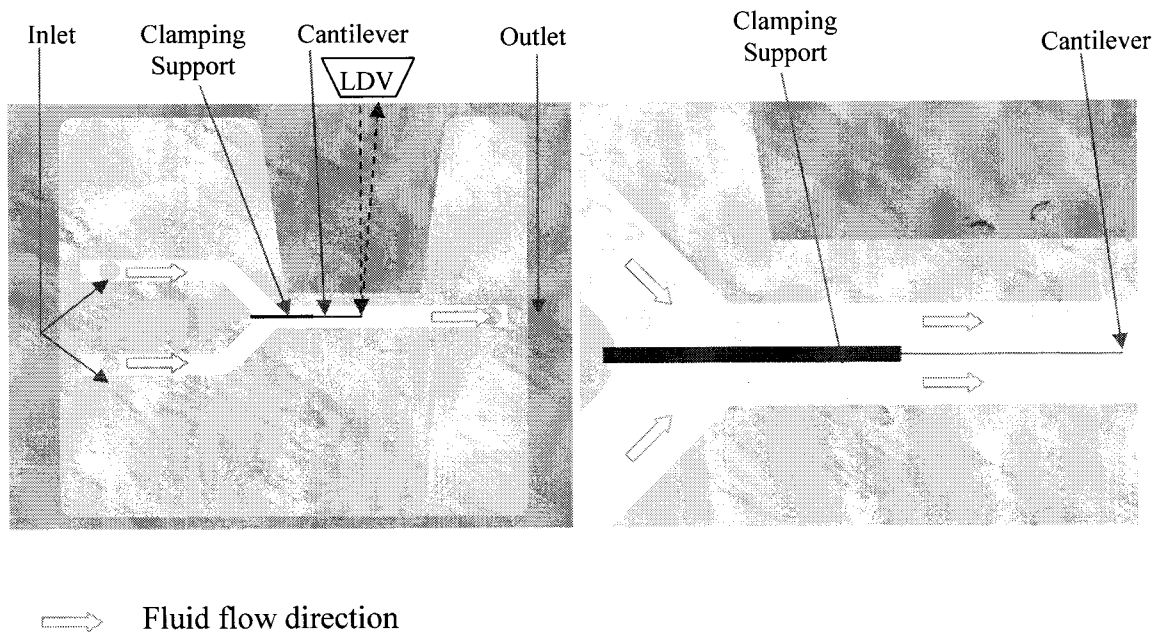


Figure 2.1: (a) An isometric view of the cantilever integrated microfluidic chip and, (b) A close-up view of cantilever and its support



(a)

(b)

Figure 2.2: Flow path of the test specimen; (a) Top view with possible location of LDV; (b) An enlarged view of cantilever structure

The cantilever (red color in Figure 2.2) sandwiched between the two plastic glass plates (blue color in Figure 2.2). The choice of PVDF film as cantilever structure was primarily based on its availability in different sizes and its reflective metal coating, which would permit the use of optical measurement methods such as LDV for the capturing dynamic deflection of the beam. The proposed design comprises of two-inlet ports in order to realize two differential flows. Furthermore, these could be adapted to different sizes of tubes to provide differential flows and fluid pressure distribution across the microcantilever. The specific dimensions of the channel depend on the design of the mold, which is discussed in the subsequent section together with the fabrication processes.

2.3 Fabrication of Integrated Microcantilever Microfluidic Chips

The microcantilever integrated microfluidic chip was realized through various systematic fabrication processes involving; fabrication of microchannel using 'Soft lithography' technique; fabrication of microcantilever from PVDF film; integration of microcantilever within the channel; bonding of top and bottom plates of the specimen and leak testing. The fabrication processes adopted in each task are described in details in the following sub-sections.

2.3.1 Fabrication of Microchannel by 'Soft Lithography' Technique

Soft lithography has been suggested as an alternative to silicon-based micromachining that uses replica molding of non-traditional elastomeric materials for the fabrication of stamps and microfluidic channels [55]. The soft lithography process generally involves fabrication of the master or the mold and patterning of elastomeric element by that mold. The master can be fabricated using either conventional or non-conventional fabrication methods. The primary advantage of this process is that the same mold may be used to produce multiple elastomeric microfluidic specimens. The soft lithography fabrication process however was carried using a number of sequential steps involving; the design and fabrication of master (Mold); mixing and pouring of elastomeric monomer; degasification and baking; and removal of the elastomeric element. These steps are described below.

a. Design and Fabrication of the Master (mold)

Figure 2.3 illustrates the design of the microchannel mold and Figure 2.4 shows the isometric view of the mold. This mold was designed with a 1.6 mm deep and 3.2 mm wide groove as shown in Figure 2.3 and 2.4(a). The groove was considered to provide sufficient flexibility to control the hydraulic diameter of the fabricated channel by placing different shapes and sizes of the rod assembly inside the groove as shown in Figure 2.4. However, the brass was chosen as a material for the mold. Steel rods of chosen size were used to form microchannel of at desired sizes. One of the rods was bent in order to achieve a U-shape for realizing microchannel with two inlets, while a straight other rod served to form the outlet, as shown in Figure 2.4. After fabrication, the rod and mold were coated with gold by electroplating method to prevent the sticking of mold with PDMS. Though in current study the microchannel is fabricated by replicating this 3.2×3.2 mm² square cross-sectional rod, this mold have the flexibility to make more narrow channel by placing thinner rod and also to fabricate cylindrical cross-sectional channel by placing cylindrical rod for further study. In the current experiment, the dimension of the square cross-section rod was used to fabricate two different specimens of two different hydraulic diameters. The hydraulic diameters of these specimens were chosen as 3.2 mm and 2.1 mm. The 3.2×3.2 mm square cross-sectional rod was placed in the 1.6 mm deep groove of the mold to realize the $3.2\text{mm} \times 1.6$ mm cross-sectional channel. Half portion of the rod was inside of the grove. However, by the bonding of this type of two same elastomer blocks, the 3.2 mm hydraulic diameter of channel was made. For the hydraulic diameter of 2.1 mm channel, the one piece of the elastomer block made by the designed mold was bounded with the flat elastomer block made in flat container mold. The

bounding procedure will be discussed later in this chapter. The bottom side of the mold also contained three 1 mm radius ports in order to facilitate the removal of the elastomeric specimen after solidification.

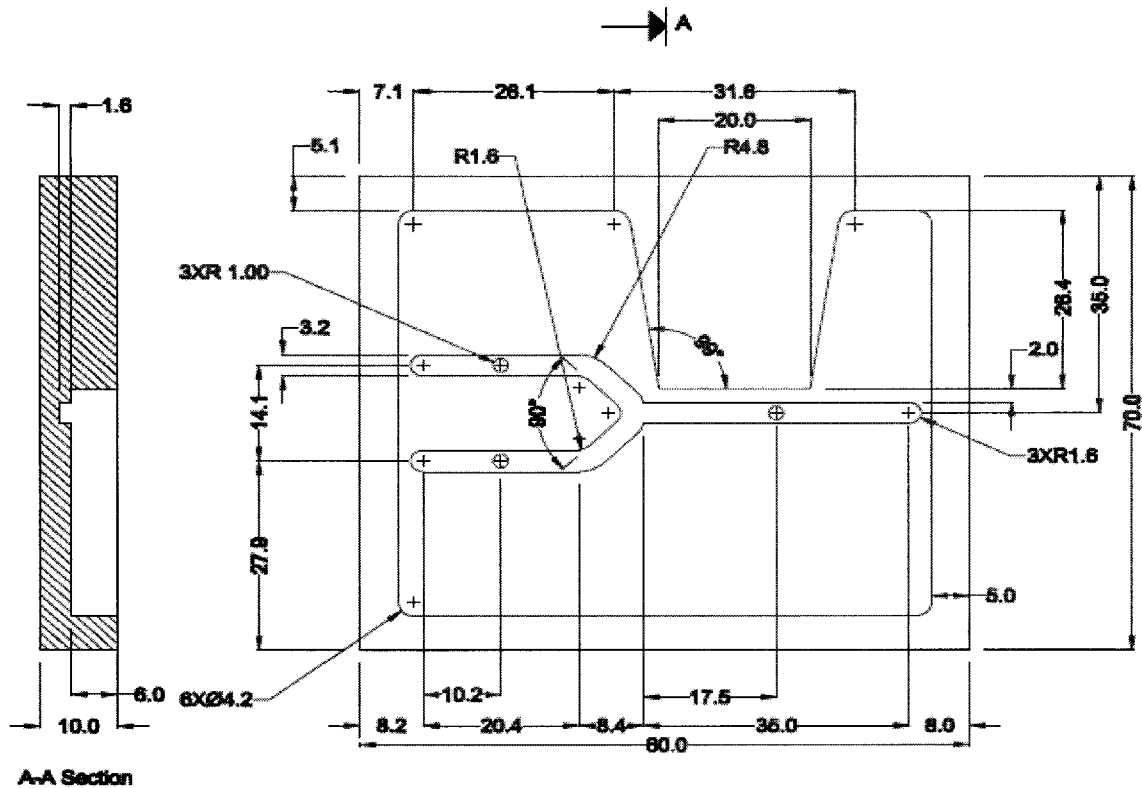


Figure 2.3: Detailed design of the mold or master (all dimensions are in mm)

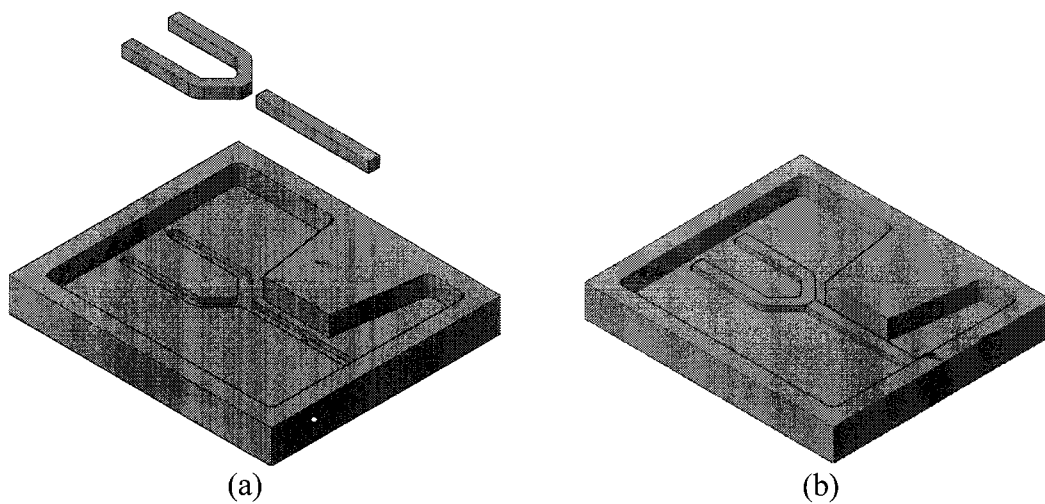


Figure 2.4: (a) An isometric view of the mold with bent and straight (b) The mold with rod positioned inside the groove

The mold design also included provision for flow paths for the installation of flow ports and pressure sensors. For this purpose, the mold was designed to accumulate a total of five cylindrical rods. These rods labeled from 1 to 5 were placed as shown in Figure 2.5. The 3 mm diameter of rods '1' and '2' were positioned to provide access to the two inlets, while the 3 mm diameter rod '5' was positioned over the outlet. The 2.5 mm diameter rods '3' and '4' were positioned to ensure accesses to inlet flows for acquisition of flow pressure via pressure sensors. The entire mold was fabricated using CNC machine and the square rods were positioned in the grooves of the mold, while the remaining voids were filled with china clay. Finally, the entire mold was coated with a thin layer of oil film to facilitate the removal of elastomer specimen after solidification.

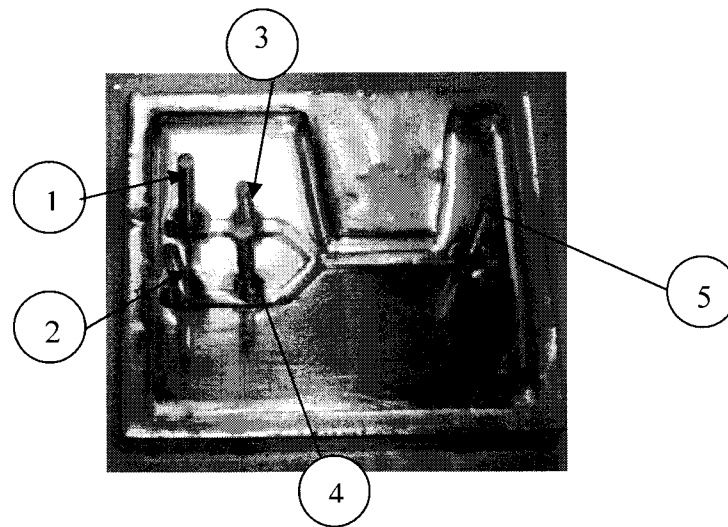


Figure 2.5: Placement of cylindrical rod in the mold for installation of inlet and outlet ports and pressure sensors

b. Mixing and Pouring of Elastomeric Element

Silicon Sylgard 184-silicone elastomer base was chosen as the main material for realizing elastomeric microchannel element. The silicon Sylgard was mixed with curing

agent using a mass ratio of 10:1, as recommended in many published studies [56-58]. The mixture was thoroughly stirred in a beaker and poured in to the mold.

c. Degasification, Baking and Removing the Elastomeric Element

The mold with the mixture was subsequently kept in a degasifying chamber at -60 to -80 kPa gage pressure for 1 hour to remove the air bubbles entrapped in the mixture.

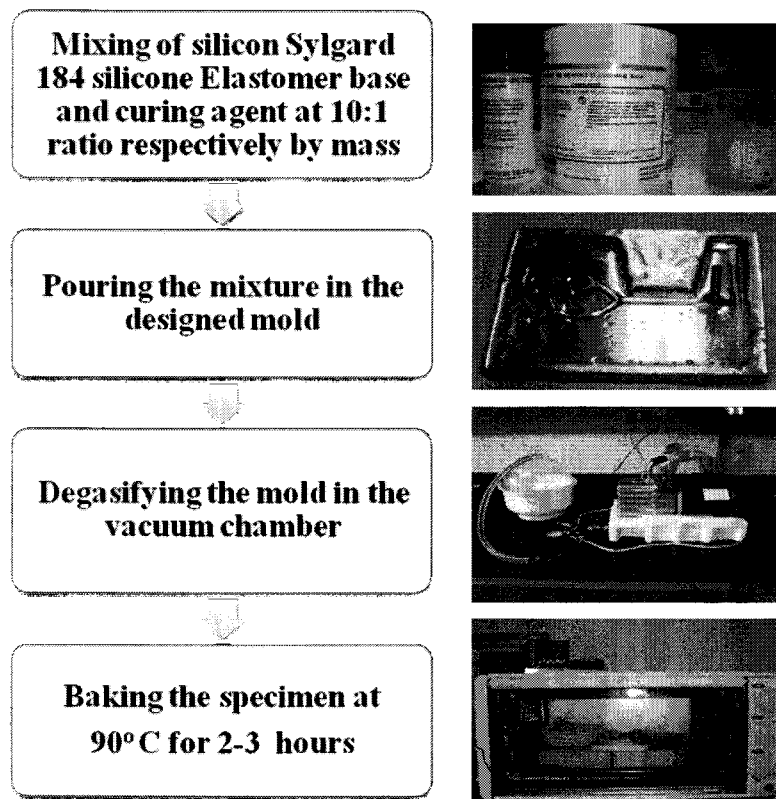


Figure 2.6: Soft Lithography Steps

The mold with the poured solution was baked in a baking oven at 80°C for 2-3 hours to allow solidification of the solution. The mold was subsequently allowed to cool in ambient air and the elastomeric element was released from the mold by pushing through the bottom holes with a 2 mm diameter pin.

2.3.2 Fabrication of Microcantilever

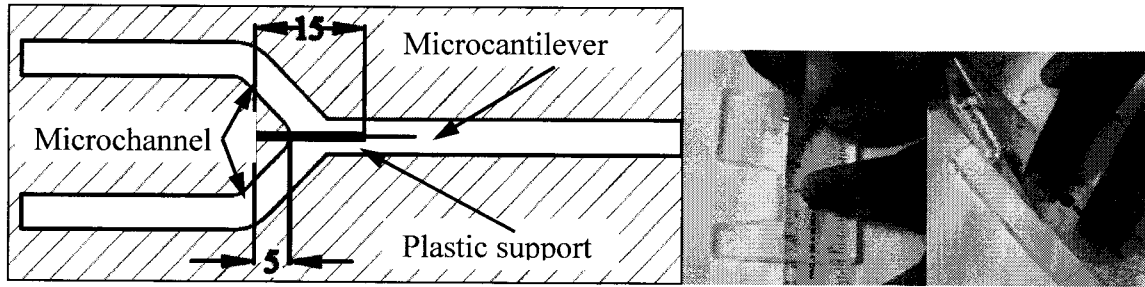
A PVDF film of 25 μ m thin was used to fabricate the micro-cantilever. The PVDF film was cut to the desired size. Different sizes of PVDF film were cut with length varying from 4 to 7 mm and width from 1 to 2 mm. These provided provision for realizing different sizes of the microcantilever structure. The length of each PVDF element was chosen to be slightly larger than that require dimension for the beam, since a portion of the element was clamped within the support as shown in Figure 2.7. The PVDF element was subsequently attached to the plastic cover plate by adhesive to achieve the support condition. The cantilever was sandwiched between the two 0.25 mm thick plastic plates. Upon sandwiching the cantilever between the two cover plates, the total thickness of the clamping portion became 0.5 mm.



Figure 2.7: Microcantilever

2.3.3 Integration of the Microcantilever

Both bottom and top chips were fabricated using mold and they were bonded later. A groove was cut at the middle of the both top and bottom chips as shown in Figure 2.8. The side edge of the plastic support of the cantilever was placed inside that groove of the channel. The Figure 2.9 presents the pictorial views of the microchannel block where the cantilever was positioned by making that groove cut out.



All dimensions are in mm

(a)

(b)

(c)

Figure 2.8: (a) A schematic illustration of the cantilever mounting in the microchannel; (b) the groove cut at the middle for clamping of the cantilever; (c) the groove cut created in the flat elastomer block for installation of microcantilever in 2.1 mm hydraulic diameter of microchannel;

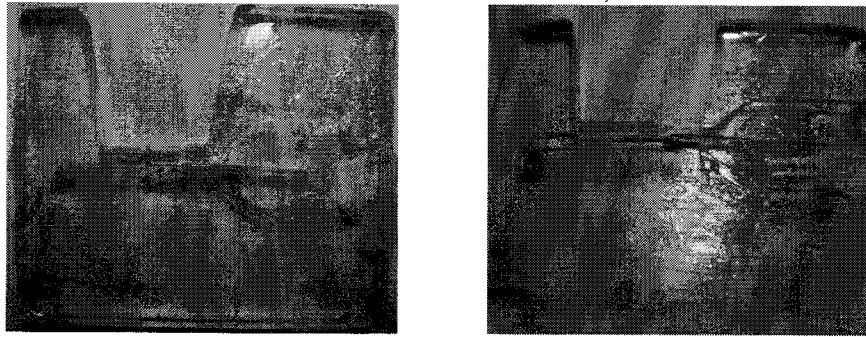
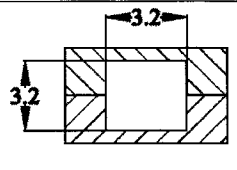
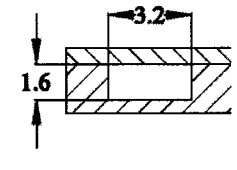


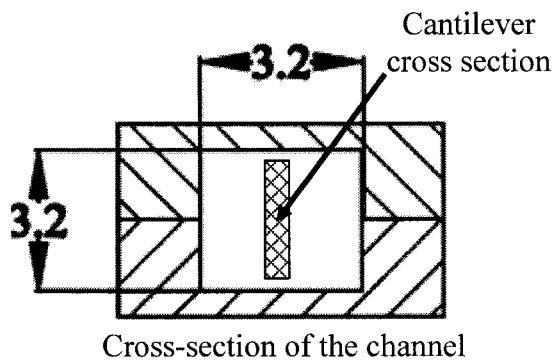
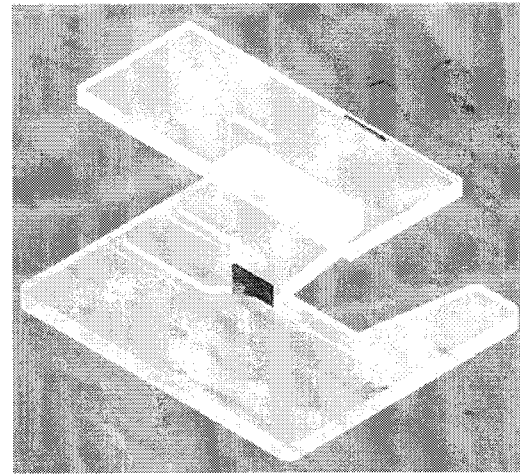
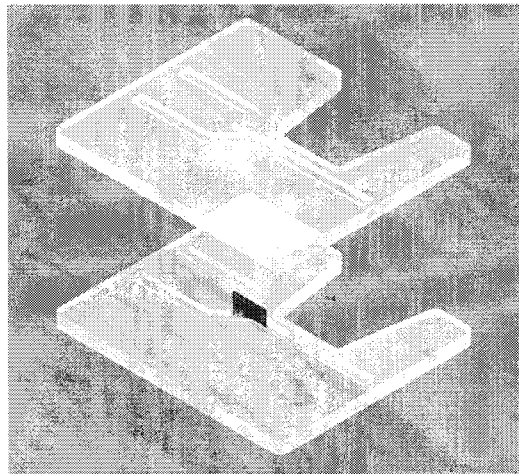
Figure 2.9: Pictorial view of the block with the cantilever where the top surface was painted with epoxy before bonding

2.3.4 Bonding of Top and Bottom Microchannel Chips

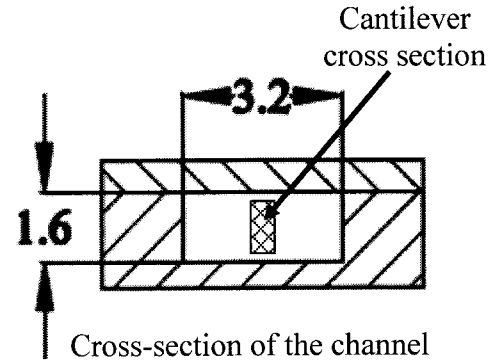
The fabricated microchannel chips were bonded together using Silicon RTV adhesive after placing the PVDF microcantilever structure. The microchannel of 3.2 mm (cross-section of $3.2 \times 3.2 \text{ mm}^2$) hydraulic diameter was realized by bonding of two identical of Chips, fabricated in the designed mold, as shown in Figure 2.10 (a). The microchannel of 2.1 mm hydraulic diameter (cross-section of $3.2 \times 1.6 \text{ mm}^2$) was created by the bonding between bottom chip fabricated using designed mold and a top chip fabricated without channel as shown in Figure 2.10 (b). The Table shows the configuration of two different hydraulic diameters of test chips named chip-1 and chip-2.

Table 2.1: The detail configuration of fabricated test chips

Name of the test chip	Cross-section of the microchannel (height × width)	Hydraulic diameter of the microchannel	Dimension of integrated microcantilever (length × width × thickness)	Cross-sectional view of bonding (dimensions are in mm)
Chip-1: 3.2 mm Hydraulic diameter chip	3.2 mm × 3.2 mm	3.2 mm	7.05 mm × 2.1 mm × 0.028 mm	
Chip-2: 2.1 mm Hydraulic diameter chip	3.2 mm × 1.6 mm	2.1 mm	7.05 mm × 1.1 mm × 0.028 mm	



(a)



(b)

Figure 2.10: Pictorial views of bonding of top and bottom chips and cross-section of the microchannel; (a) 3.2 mm hydraulic diameter of channel (b) 2.1 mm hydraulic diameter channel (dimension are presented in mm)

2.3.5 The Leak Testing

Appropriate flow connections were made to the two inlet ports in order to check each specimen for leaks. For this purpose, each microcantilever-integrated device was connected to a flow source, a peristaltic pump through inlet tubes. The pump supplies the flow by squeezing the tube with rotating rollers attachment integrated in a rotating central disk. Two different flow rates to the channel were realized by inserting two different sizes of the tubes around the rollers. These tubes of the pump were connected to the inlets of the microchannel, while the outlet port of the microchannel was connected to an outlet tube. The outlet tube, partially however, was blocked for the purpose of leak test. Each microchannel specimen was tested under the highest flow supplied by the pump, which was obtained at the speed of 48 RPM. Each specimen revealed small leak during the tests. Silicon RTV adhesive was subsequently applied around the edges and the leak test were repeated. The process was repeated until both the specimen showed no leak.

2.4 Summary

The current chapter narrated the fabrication process of the microcantilever integrated microfluidic test specimen, which was fabricated using polymer based soft lithography method. Characterization of motion of the cantilever in liquids subject to fluid pressure loading, however, necessitates comprehensive developments in measurement systems and test fixtures. In the subsequent chapter, an experimental setup is designed to characterize the dynamic behavior of microcantilever under fluid flows.

Experimental Method and Characterization

3.1 Introduction

The study of dynamic interaction between a microstructure and the fluid flows in a microchannel involves a number of challenges associated with measurements and generation of controlled flow conditions at the micro levels. The experimental characterizations thus require the development of comprehensive experimental setups to address the associated challenges, particularly the instrumentation and the design of the flow sources. Only a few studies have experimentally investigated the fluid-structure interactions in microsystems. These studies suggested that piezoresistive sensors are well-suited for static characterization [3, 45], while the dynamic characterizations may be performed using piezoelectric materials, optical instruments [17, 19, 22] or image-processing methods [39]. The use of piezoelectric sensors would involve some difficulties in their installation in the microstructures, while the optical methods are easy to install as these could be installed externally and they are considered well suited for detecting high frequency response of the structure interacting with the fluid. However, the optical methods require external devices for deflection measurements and this method also reveals considerable difficulties in achieving alignment with vibrating structure, which is very time consuming. In addition, optical techniques are sensitive to variations in optical properties of the sample and that of the medium surrounding the cantilever structure [47]. The image processing techniques on the other hand offer many advantages. This being a direct method of measurement can yield very precise

measurements, where the images could be captured at high sampling rate to obtain high frequency dynamic responses. Furthermore, the image capturing method does not require complex setup and is perhaps well suited for measurements and microsystems. Huang et al. [39] used an image capturing method to determine the critical flow velocity at which the cantilever deflection exceeded the available clearance in the fluid channel while their method was not considered suitable for measuring the deflection of cantilever due to the lack of proper instrumentation facility.

In this study, a test fixture is designed to synthesize controlled flow conditions through the microchannel and an image capture technique is developed to acquire the dynamic deflections of the cantilever structure. The measurements of dynamic deflections were also attempted using an optical method namely Laser Doppler Velocitymeter (LDV). The test fixture is designed to incorporate a flow source to generate differential fluid pressure across the cantilever structure, while a number of micro-pressure sensors were integrated to quantify the flow properties namely the flow rate through the channel, inlet pressure and pressure drop. Finally, an experimental design is formulated and measurements are performed to characterize the dynamic behavior of the microcantilever with respect to different flow conditions of a fluid, namely as Fluid XP. However, the dynamic characterizations of microcantilever are also carried out with fluids of different viscosity and the corresponding experimental results are presented in Chapter 5.

3.2 Experimental Setup

An experimental setup is designed with a flow source, flow lines and couplers, which can accommodate the pressure sensors for characterizing the flow properties. A

peristaltic pump is chosen in this study to supply the fluid flow through two inlets of the integrated microchannel. The flow source is coupled to the test chip through flow lines and a reservoir is used as a fluid storage medium. A total of three pressure sensors are used to measure the fluid pressure at the two inlets and one outlet of the test chip. Additional four pressure sensors, two in each inlet line, are used to measure the flow rates through the two inlets. The output from the pressure sensors are acquired through a data acquisition board. Figure 3.1 illustrates a schematic of the test setup comprising the test chip, flow lines, pressure sensors and data acquisition board connected to the computer (CPU). Table 3.1 further lists the components of the test setup.

The test setup also includes the measurement system for acquiring the dynamic deflection of the microcantilever. For this purpose, two different methods were explored. An optical method employing a LDV was initially used to detect the cantilever deflection, as shown in Figure 3.1. However, the alignment of LDV with the microstructure was found to be quite difficult and time consuming. Alternatively, an image capture process coupled with post processing was developed to measure the deflections, as shown in Figure 3.1. For this purpose, a CMOS Camera was mounted on a microscope and the camera was adequately aligned to capture the images of the cantilever structure. The image file was subsequently processed to estimate the dynamic deflection of the cantilever tip.

From the preliminary experiments, it was concluded that the image capture method could provide more reliable estimate of the deflection in a more convenient manner. This approach was thus implemented during the experiments. Figure 3.2 presents

a pictorial view of the entire test setup. The detailed designs of various components are briefly described in the following subsections.

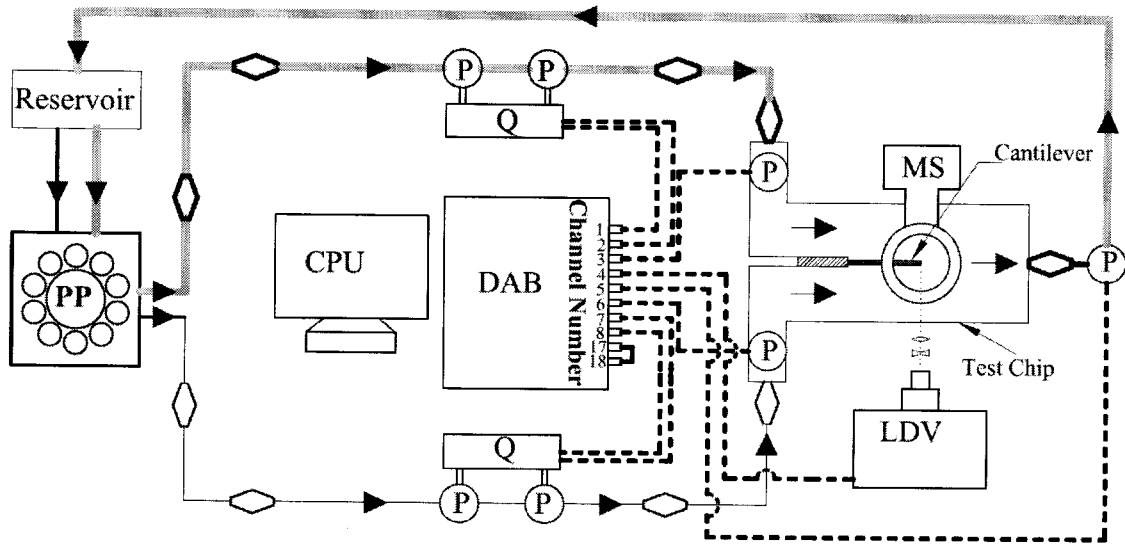






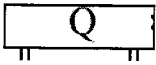


Figure 3.1: Schematic of the experimental setup

Table 3.1: Components used in the experimental setup and description of the notations used

Notations	Components	Symbols	Components
PP	Peristaltic pump		Tube of larger diameter
CPU	Central processing unit (Personal Computer)		Tube of smaller diameter
MS	Microscope mounted with CMOS camera		Electrical Circuit
LDV	Laser Doppler Velocymeter		Tube connectors
DAB	Data Acquisition Board		Fluid flow direction
			Pressure Sensors
			Flow measurement unit

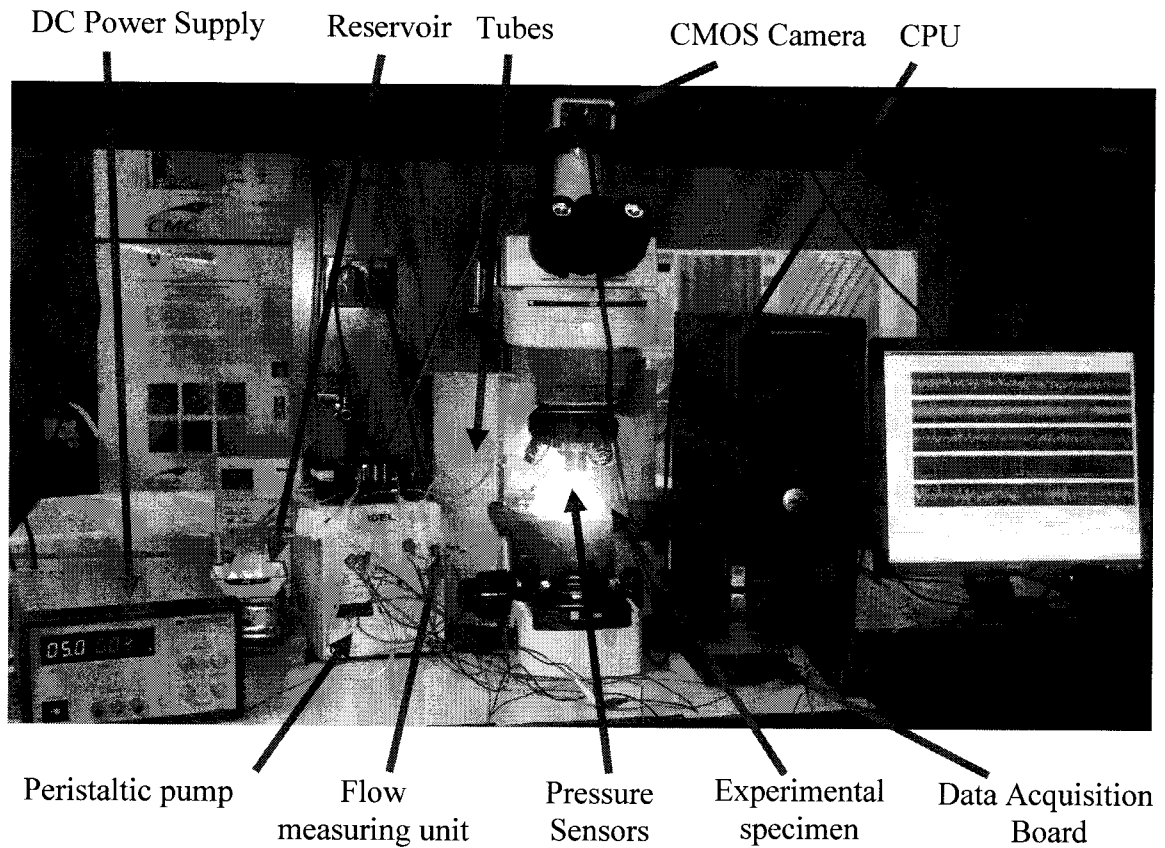


Figure 3.2: A pictorial view of experimental Setup

3.2.1 Flow Lines and Couplers

Flexible and transparent tubes were used as flow lines between the flow source and the test chips. The flow lines were also installed within the peristaltic pump between the rollers mounted in a central disc. The rollers squeezed the tubes to generate the pulsed flow at varying angular speeds. Tubes of different diameters could be installed in the pump to achieve different flow rates and fluid pressure. A total of two tubes could be mounted between the rollers. It should be noted that the rollers produce an oscillatory flow, while the frequency components of the flows are directly related to the angular speed of the rollers and central disc. In the present experimental setup, three different diameters of tubes were chosen to achieve the desired flow conditions as described in the

following sections. These included tubes with inner diameter of 1.2 mm, 2.2 mm and 3.2 mm. Figure 3.3 (a) shows the three tube sizes together with the couplers. The flow lines were coupled to the pump and test chip using two different types of connectors, shown in Figure 3.3 (b). These included an adapter to couple the small diameter tube (1.2 mm inner diameter) with the large size tubes (2.2 mm and 3.2 mm inner diameter), which is denoted as C_S and illustrated in Figure 3.3(b). The second coupler denoted as C_B was used to couple the two large size tubes (3.2 and 2.2 mm inner diameter).

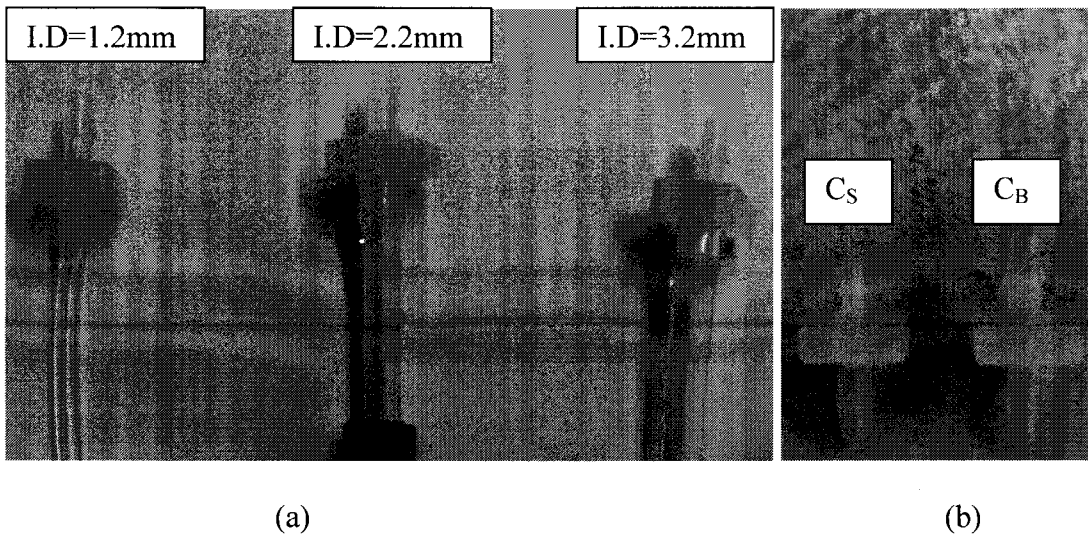


Figure 3.3: (a) Flow lines with different couplers and (b) two different connectors

3.2.2 Pressure and Flow Sensors

The experimental setup was designed to accommodate a number of pressure sensors for characterizing the flow properties. Pressure sensors with integrated signal conditioning were used to measure the inlet and outlet pressures. The sensors were chosen with a pressure range of 25 kPa gauge and were supplied with 5V DC power. Two pressure sensors were mounted at the two inlets using the two holes made in the

specimen during its fabrication as shown in Figure 3.4(a) to measure the fluid pressure at two inlets of the specimen. One pressure sensor was mounted near the outlet through a tubing connection to the small hole in the specimen as shown in Figure 3.4(a). In the fabrication process, it was ensured that, the diameters of the holes were slightly smaller than the diameters of the noses of the pressure sensors such that the sensing noses could be conveniently fastened in to the holes by compression fittings.

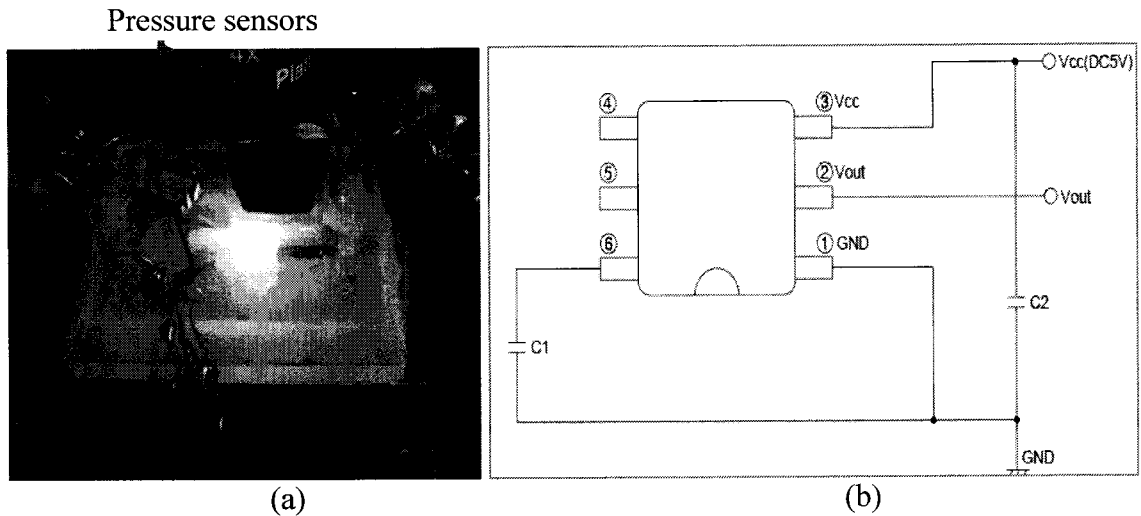


Figure 3.4: (a) Pressure sensors mounted to the test specimen; and (b) Circuit diagram installing a pressure sensor coupled with the capacitors

Figure 3.4 (b) further illustrates the circuit diagram of micro-pressure sensors with connecting pin. A 5 V DC supply was connected to pin 3, while the pin 1 was grounded. The pin 2 provided the signal output, which was connected to the data acquisition board. Two capacitors $C_1 = 680 \text{ pF}$, $C_2 = 0.01 \text{ }\mu\text{F}$ were connected to pins 6 and 3, respectively, as shown in Figure 3.4 (b). The output voltages of the pressure sensor could be related to the flow pressure using the specified static sensitivity, offset and temperature sensitivity drift as [59];

$$V_{out} = V_s \times (P\alpha + \beta) \pm (e_p \times e_t \times \alpha \times V_s) \quad (3.1)$$

Where V_{out} and V_s are output and supply voltages respectively, where $V_s=5V$. P is the flow pressure, α is the static sensitivity in V/kPa per unit supply voltage and β is the zero drift in V, e_p defines the pressure error due to thermal sensitivity shift and e_t is the temperature change with respect to the nominal temperature of 20°C. The manufacturer specifications for the calibrated sensors provided the necessary constants for determining the fluid pressure: $\alpha=0.036V/kPa$ per V input, $\beta=0.04$ V/V, $e_p=0.625$ kPa, where e_t is taken as unity for the laboratory conditions.

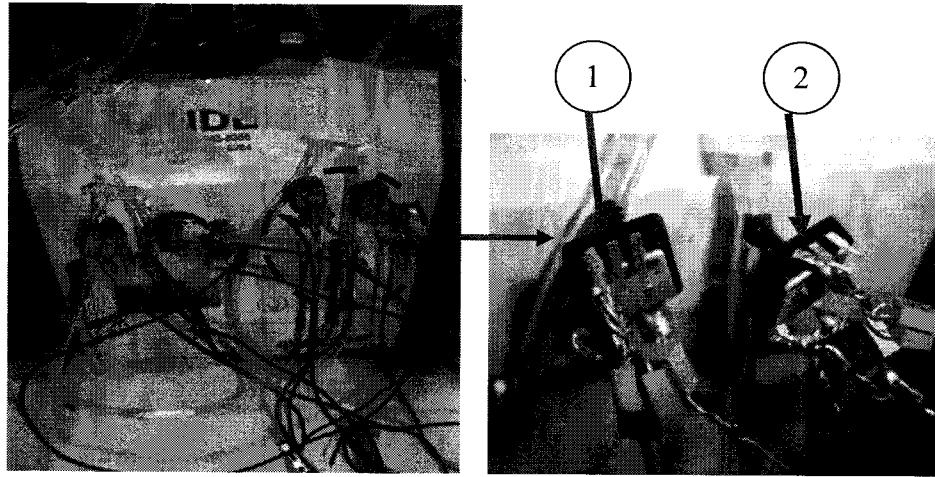
The fluid flow rates through the two inlets were estimated through measurements of pressure drops at the inlets. For this purpose, two micro pressure sensors were placed within each inlet flow tubes as shown in Figure 3.5. The two sensors were spaced by a certain distance along the tube in order to achieve a measurable pressure difference or drop caused by the surface friction. A laminar flow condition was assumed considering the small diameter and larger lengths of the tubes. The Hagen–Poiseuille relation was used to estimate the flow rates through the two inlets such that [60];

$$Q = \frac{\Delta P \pi d^4}{128 \mu L} \quad (3.2)$$

Where Q is the flow rate, μ is the viscosity of fluid, d is the diameter of the tube, L is the spacing between the two pressure sensors. In the above relation ΔP is the pressure difference recorded by the two sensors at locations '1' and '2' such that,

$$\Delta P = P_1 - P_2,$$

Where P_1 and P_2 are fluid pressures measured by sensors located at '1' and '2', respectively as shown in Figure 3.5 (b).



(a) (b)
 Figure 3.5: Two flow sensing unites built with four pressure sensors

3.2.3 Data Acquisition Board

A 16 channel data acquisition board (Data translation multifunction data acquisition module, DT9800 Series) was configured to record the analog voltage outputs from the pressure sensors. The Channel 1, 2, 7 and 8 were used to acquire differential pressure signals from the inlet pressure sensors for estimating the flow rates. Channels 3 and 6 acquired the inlet flow pressures, while the outlet flow pressure was acquired in Channel 5. The LDV signal was also acquired in Channel 4. The circuit diagram of the data acquisition setup is given in Figure 3.6, where the thickest line refers to the positive voltage connections and thin black lines are the negative signal or ground connections. The medium thick line represents the voltage output signals from the pressure sensors and the LDV. The pins 17 and 18 of the data acquisition board served as the ground connections. The data acquisition board was interfaced with a personal computer to store the data using the Measure Foundry software. An 8 band virtual oscilloscope was also configured using the software for online display of the measured signals.

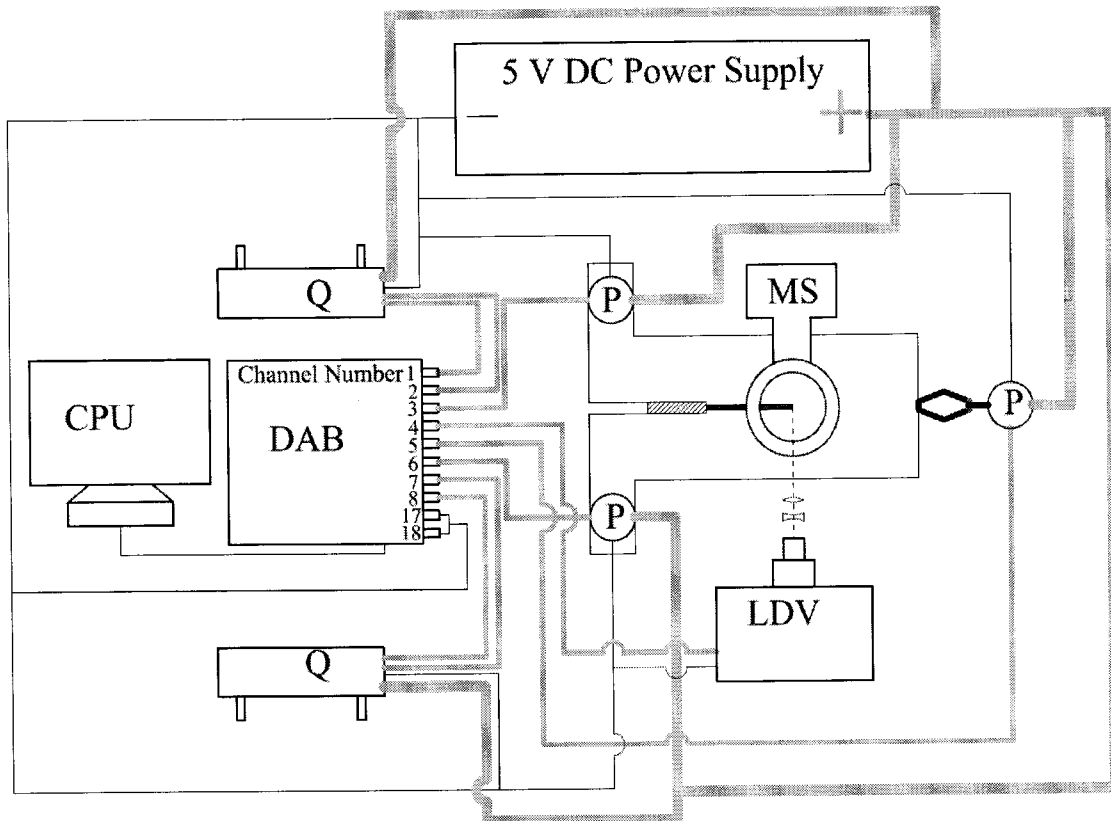


Figure 3.6: Circuit diagram showing data acquisition board and sensor connections (DAB- data acquisition board denoted as; MS- microscope mounted with CMOS camera denoted as; LDV- Laser Doppler Velocimeter; CPU- the central processing unit or personal computer)

3.2.4 Peristaltic Pump

The Peristaltic pump was used to supply the fluid flow from the reservoir to the specimen through the two inlet tubes. The pump produces oscillatory flows, which serve as the dynamic loading of the cantilever. The design and operation of the pump may be divided into two main parts: the controller unit and the head. Figure 3.7 illustrates the schematic and pictorial view of the pump head, which comprises several components such as central disk, rollers, compression cam, locking and trigger key, and jaws for holding the flow lines. The controller unit controls the angular speed of the central disc through a drive and a connecting shaft.

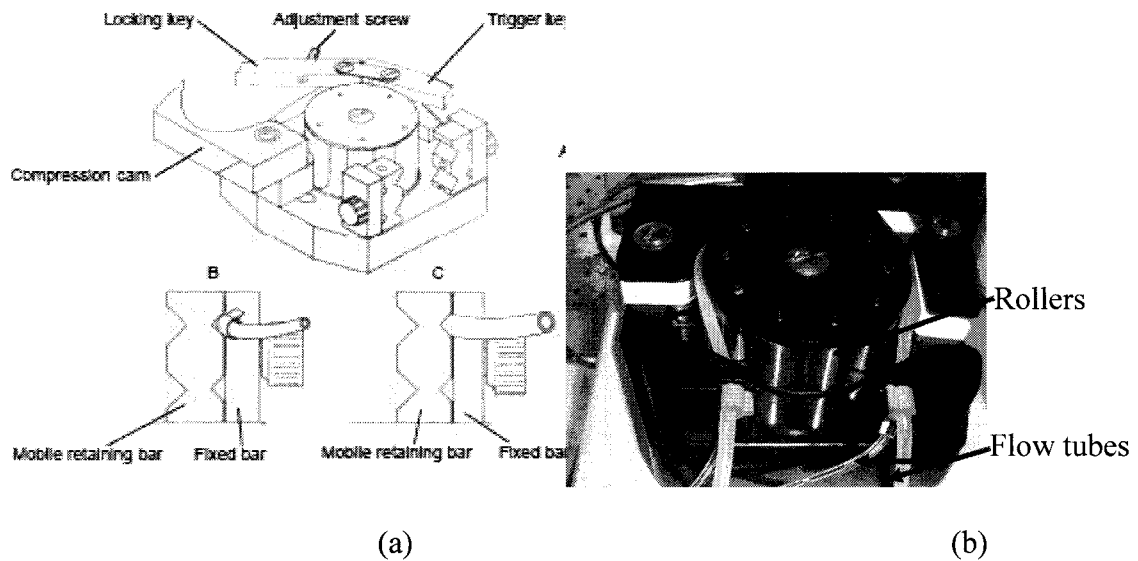
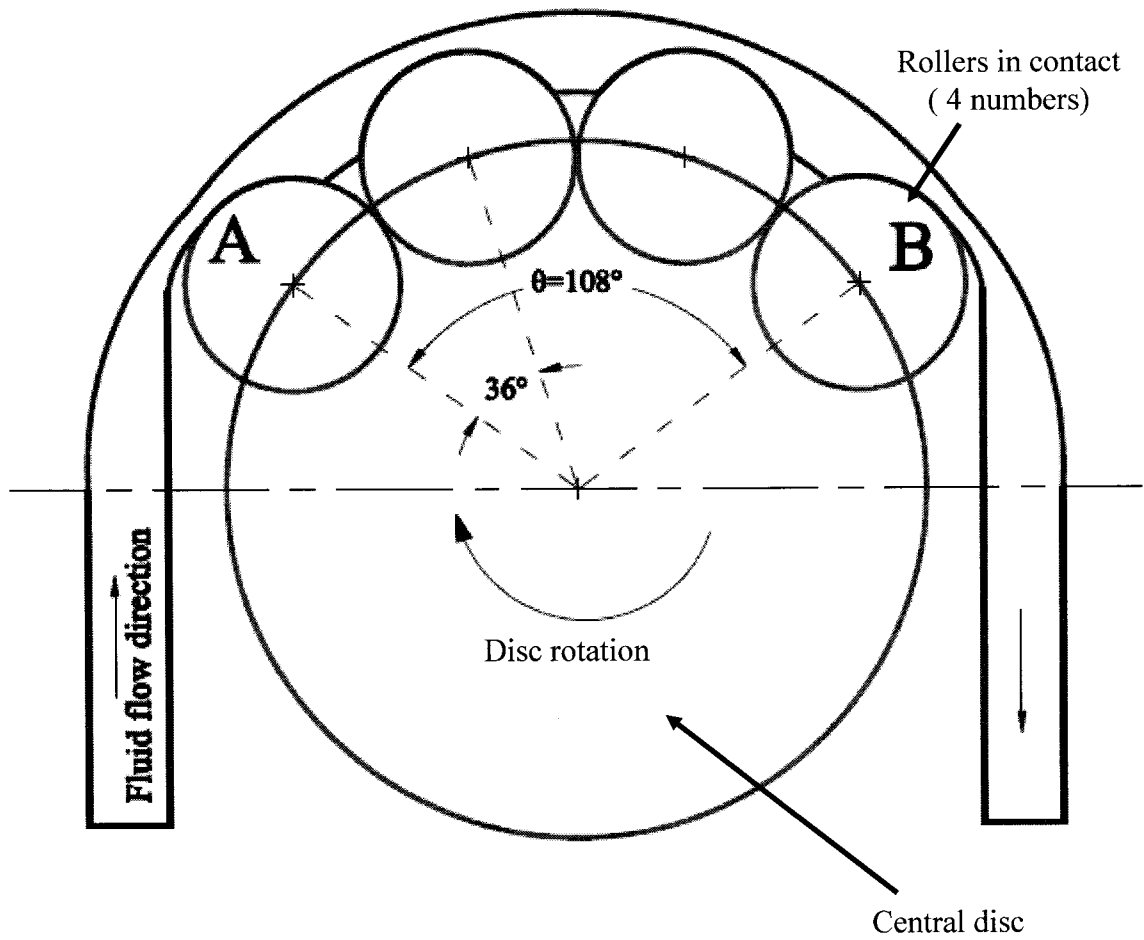
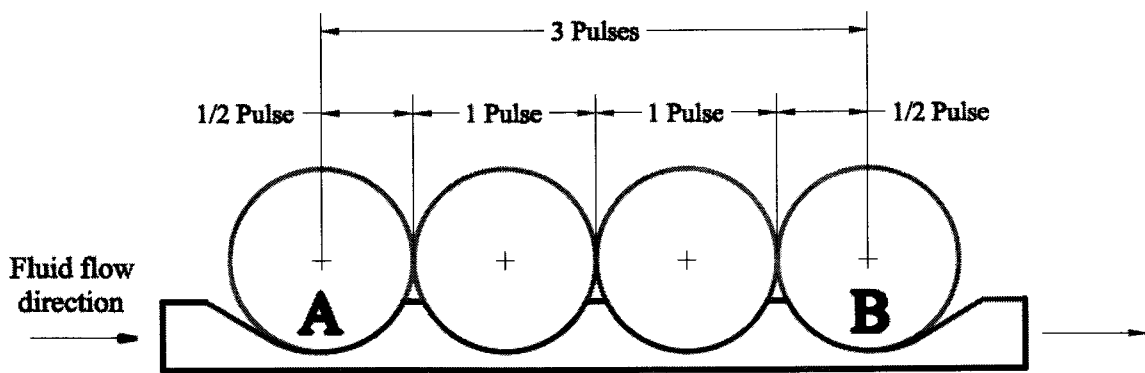


Figure 3.7: (a) Schematic of the pump head [61] and (b) a pictorial view of the pump head showing rollers mounted on the central disc

The central disc comprises of 10 miniature rollers mounted along its perimeter as shown in Figure 3.7(b). The figure also shows two flow tubes mounted around the rollers. Under the rotation of the central disc, the flexible tubes are constantly squeezed by the rollers to generate the fluid flow and pressure. The head also contains holding jaws for mounting of the tubes at the inlet and the outlet. The pump can produce two different flows by using two different diameters of the tubes mounted around the central disk. A glass beaker served as the reservoir for the pump. Flow connections were realized to ensure that the fluid is returned to the reservoir.



(a)



(b)

Figure 3.8: (a) Schematic of the central disc with rollers illustrating squeezed portion of the tube (b) linear representation of the squeezed portion of the tube and the contacting rollers

The fluid flow generated by the pump revealed periodic variation with two distinct harmonic components attributed to angular velocities of the disc and rollers. The angular motion of the central disc induced a low frequency component due to its lower speed, while the rollers caused a relatively higher frequency component. Frequencies of the fluid flow could be determined from the geometries of the disc and rollers, their angular speeds and the number of contacting active rollers. Figure 3.8(a) schematically shows the squeezed portion of the tube and the contacting rollers. The central disc comprises a total of 10 rollers equally distributed over its circumference. Only four of the rollers, however, are actively engaged to squeeze the tube at a given time to produce the flow. As shown in Figure 3.8, the arc angle between the first and the last roller in contact with the tube is 108° , where the first contact point of the tube with the roller center is indicated by 'A', and the contact with the last roller is indicated by 'B'. For the given speed N in RPM of the pump or the central disc, the fundamental frequency of the flow f_1 is directly related to the speed, N ;

$$f_1 = \frac{\omega_1}{2\pi} = \frac{N}{60} \quad (3.3)$$

Where, ω_1 is the angular fundamental frequency of the flow. Figure 3.8 (b) illustrates the contacting rollers and tube arranged in linear manner, which suggests that the squeezing action of 4 rollers will produce three additional pulses in the flow. Assuming that, t as the time taken by the flow particle to travel from initial contact point of the rollers 'A' to the final contact point 'B', the fundamental frequency associated to the pulses f_2 can be expressed as:

$$f_2 = \frac{\omega_2}{2\pi} = \frac{3}{t} \text{ Hz} \quad (3.4)$$

The angular fundamental frequency of the flow attributed to the central disc rotation can also be computed as;

$$\omega_1 = \frac{\theta}{t} \text{ rad / s} \quad (3.5)$$

Where, θ is the angle of the arc described by the initial and final contact points as shown in Figure 3.8 (a). Equation (3.3) and (3.5) yield following relationship between time t and the speed N

$$t = \frac{18}{N} \quad (3.6)$$

Substituting for t from Equation (3.6) in Equation (3.4), for f_2 ;

$$f_2 = \frac{3}{\frac{18}{N}} = \frac{N}{6} \quad (3.7)$$

The above equation suggests that, the fluid flow would exhibit harmonic components corresponding to the speed of the central disc and rollers. Figure 3.9 shows a time record of the flow rate through a 1.2 mm diameter tube while the pump was operating at speed of 6 rpm. Theoretically, lower frequency of the flow should be 0.1 Hz as per Equation (3.3), while the higher frequency should occur at 1 Hz in accordance with Equation (3.7). In order to evaluate its spectral components, Fourier transform of the measured signal was performed. The spectrum of the flow rate signal, shown in Figure 3.10, clearly illustrates two harmonic components centered at 0.1 and 1.0 Hz, as predicted from Equation (3.3) and (3.7), respectively.

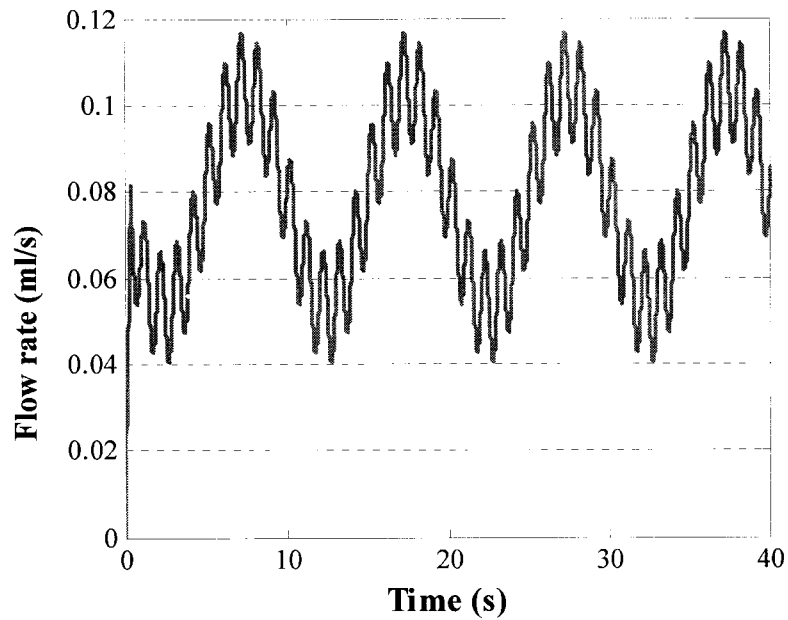


Figure 3.9: Time history of measured flow rate through the 1.2 mm diameter tube with pump operating at 6 rpm

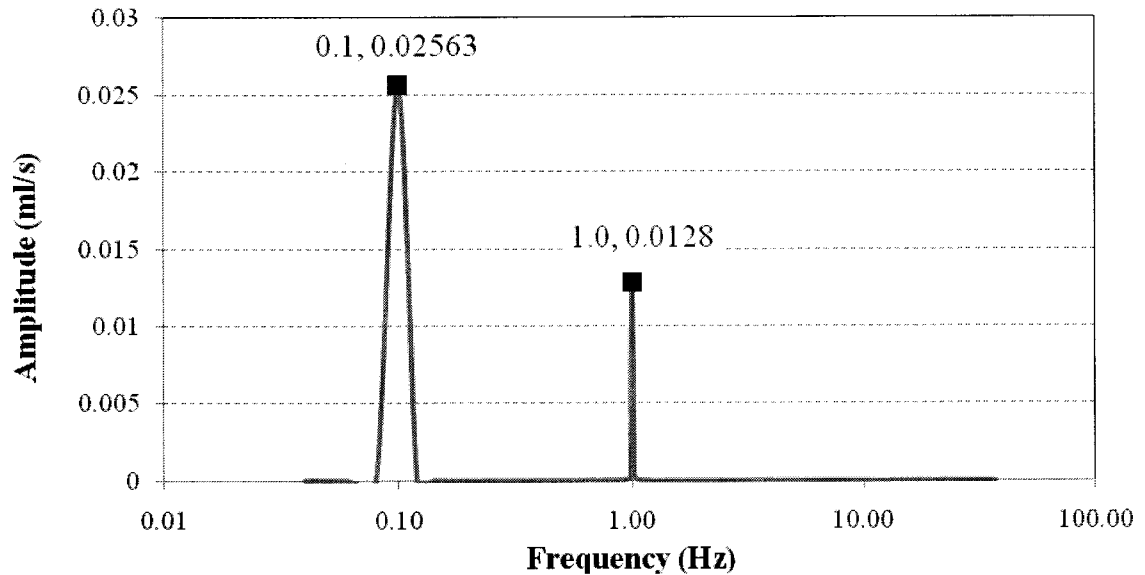


Figure 3.10: Frequency spectrum of the flow variation shown in Figure 3.9.

3.3 Measurement of Cantilever Deflection

Various different techniques were explored to capture the dynamic deflection of the cantilever structure under different flow conditions. These employed a Laser Doppler Velocitymeter (LDV) and image capturing methods, which are described below.

3.3.1 Laser Doppler Velocimeter (LDV)

A Laser Doppler Velocimeter measures the surface velocity of a moving structure at a localized point. In the current experiment, a helium–neon (He–Ne at 632.8 nm wavelength) laser was used as a light source to measure the deflection at the tip of the cantilever. A signal conditioner was used to supply the power to the laser and perform the signal conditioning through an integration network and wide-band filters. The integration network could thus directly yield the deflection of the cantilever. The output of integration network was connected to one of the channel of the DAB. Owing to the small size of the cantilever structure, the diameter of the laser spot was reduced considerably by implementing a combination of concave-convex lenses, which permitted enhanced focus of the laser beam at the tip of the cantilever and thus more reliable measurements. A schematic of LDV setup together with the concave-convex lens and the specimen is shown in Figure 3.11. The LDV was placed on an optical bench with x-y-z aligner to achieve desired distances and alignment.

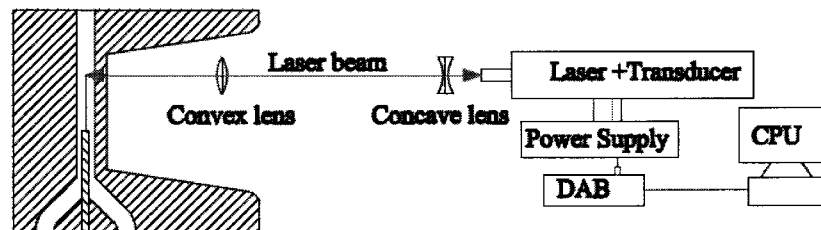


Figure 3.11: A Schematic of the Laser Doppler Velocimeter setup with concave-convex lens

3.3.2 Estimation of Deflection using Video Image Processing (DVIP)

Method

The DVIP (Deflection Using Video Image Processing) method using a CMOS camera was developed to estimate the deflection of cantilever. A high-speed CMOS

camera (Infinity-1) was mounted on a Nikon microscope to capture the beam deflection in a video file format. The target area around the cantilever tip was magnified by the Nikon microscope. The specimen was placed horizontally on the stage of the microscope and the cantilever surrounding area was highlighted by a light source focused on the target area through a number of lens arrangements. Figure 3.12 pictorially illustrates the specimen position on the microscope stage.

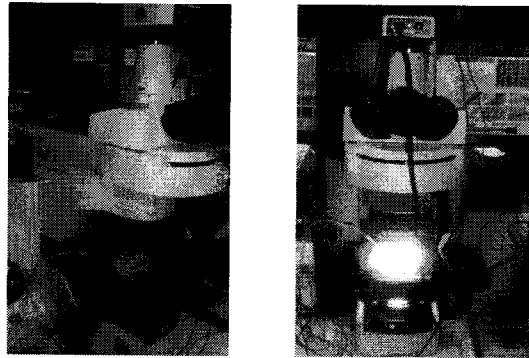


Figure 3.12: Specimen positioned in the microscope stage

The captured video was post processed to obtain time-histories of the cantilever deflection using a processed code developed in MATLAB script. Initially all the frames were extracted from the video file using Avi4Bmp software those were saved as image files. The image files were labeled by the frame number and thus corresponding to the time of capture. The coordinates of the beam in its static equilibrium were defined in code, while the beam was graphically displayed in a bold color different from the surroundings. Each image file was subsequently imported in the MATLAB code in sequential manner and processed to estimate the deflection response of the cantilever. The code developed in this study was used to convert real image to its binary image, where the cantilever coordinates were indicated by black pixels with a binary value of '0', while the surroundings were indicated by white pixels with a binary value of '1'. Figure

3.13 illustrates a comparison of the true captured image and generated binary image of the beam at its static equilibrium position.

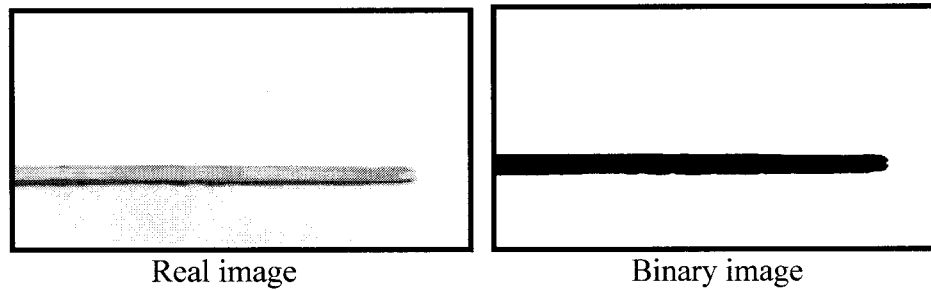


Figure 3.13: The comparison between real image and binary image

The binary image is a combination of $X \times Y$ pixels, where X is the number of columns or length of the binary image in pixels and Y is the number of rows or width of the binary image in pixels. In the current experimental setup, the video resolution was taken as 800×600 pixels, which means that each binary image is generated by 800 pixels along the length and 600 pixels along the width. The resolution of the pixels was calibrated in μm was further computed in the code. For a given $X \times Y$ pixels in the x - y axis system, the resolution of each pixel could be determined by the known dimension of current specimen. For instance, the width of the beam, which is $28 \mu\text{m}$, in the binary image, could be used to calibrate pixels by scanning the image using the MATLAB program. Finally, the ratio corresponds to the width in μm and pixels, yields pixel resolution. Figure 3.14 illustrates the flow chart of the code that was used to determine the pixel resolution in μm . In Figure 3.14, the variable $w1$ and $w2$ scan the left most coordinate of the image or left most column of the image with y increment of 1 for the first loop and y decrement of 1 for second loop. Therefore, m is the value of first column in y 'th row matrix element. The figure 3.18 illustrates the scanning process to find the cantilever width in pixel.

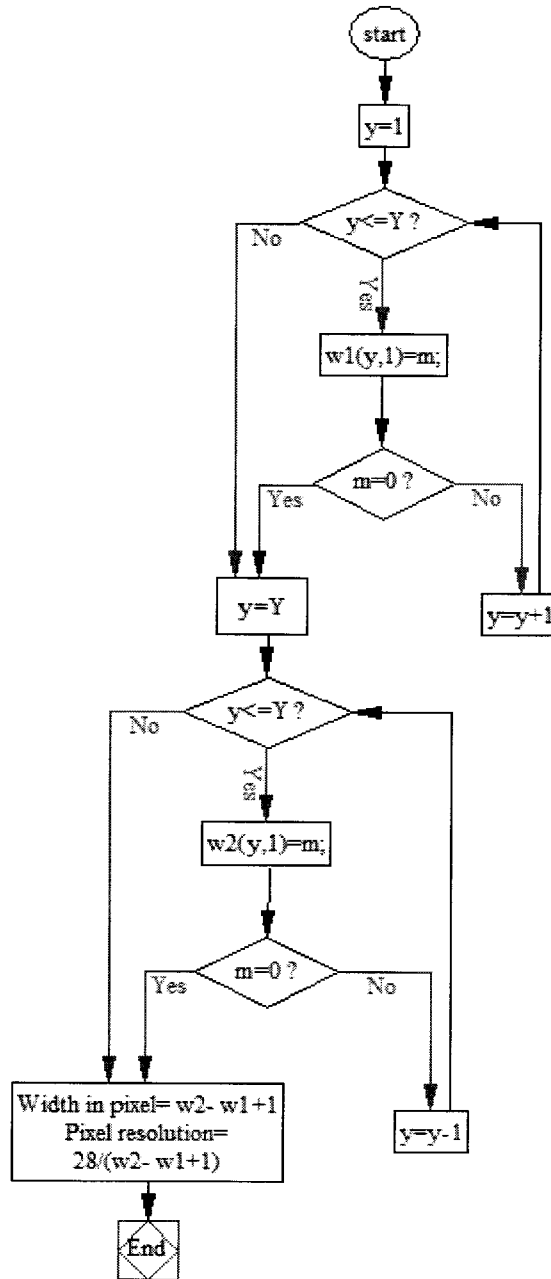


Figure 3.14: Flow chart to find the Pixel resolution $\mu\text{m}/\text{pixel}$ by comparing the width of the cantilever in pixels and real value of $28 \mu\text{m}$

The camera was started to take image few minutes before switching on the pump when there was no circulation of flow in the tube and the cantilever was in its static equilibrium position surrounded by the stagnant fluid. Hence, the second part of the program scans only the first image of the video file, in which cantilever was in initial

position with no flow. The program estimates the distance of tip of the cantilever from top edge of the taken image, which is denoted as y_0 in Figure 3.15. The third part of the program scans entire video file in which the cantilever moved to a new position due to the fluid flow. The program estimates the distances of the moving cantilever tip from the top edge of the images correspond to different time steps. In Figure 3.15 the $y_0, y_1, y_2, \dots, y_n$ are the distances of the tip of the cantilever in pixel from the top edge of the images for time $t_0, t_1, t_2, \dots, t_n$ seconds respectively. Hence, the multiplication of pixel resolution with $(y_0 - y_0), (y_0 - y_1), (y_0 - y_2), \dots, (y_0 - y_n)$ values gives the actual cantilever deflection in μm corresponding to different time $t_0, t_1, t_2, \dots, t_n$ second.

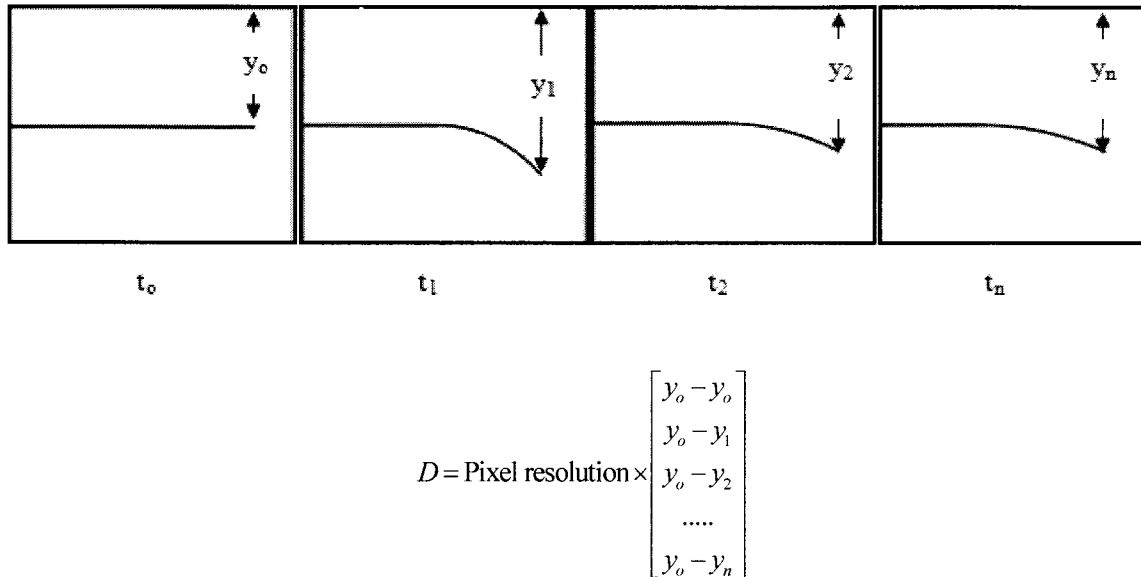


Figure 3.15: The cantilever position in the captured image at different time and estimation of the deflection 'D' by DVIP method

The Figure 3.16 illustrates the flow chart of the program to calculate distance of tip of the cantilever from the top edge of the captured image at no fluid flow condition, where, the variable w_0 scans the image of rest cantilever to find the distance y_0 , between tip of the cantilever and top most boundary of the image.

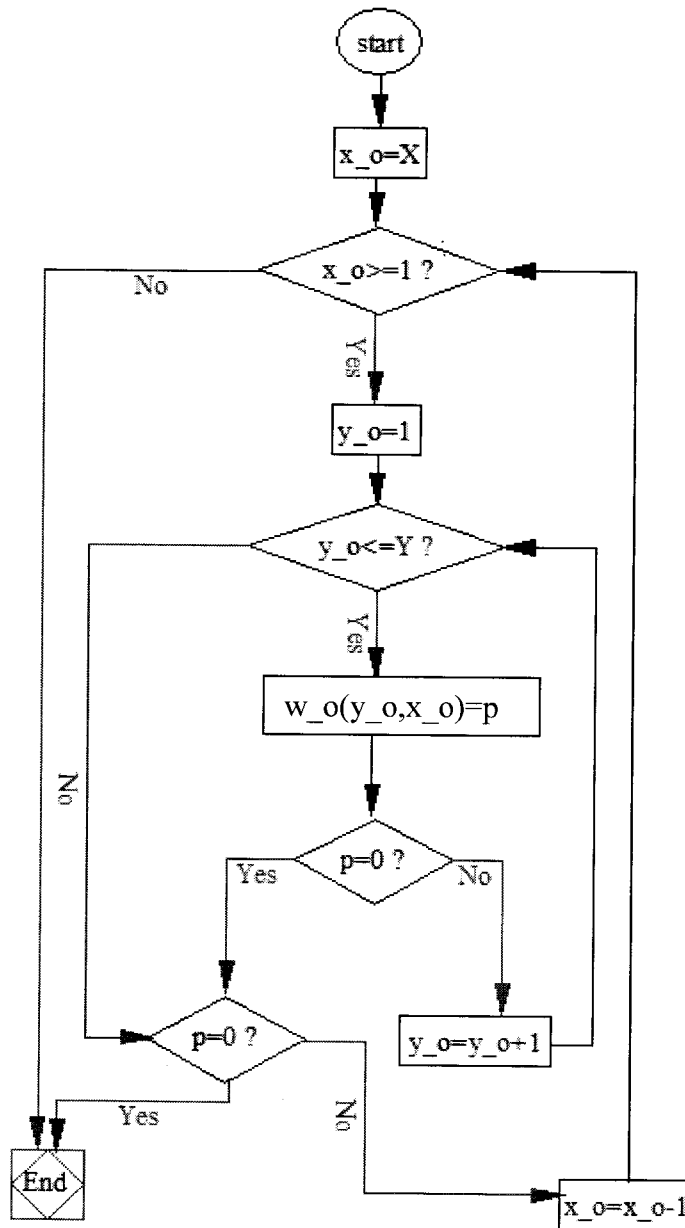


Figure 3.16: Flowchart of the algorithm to find the tip position of rest cantilever

The Figure 3.17 presents the flow chart of the program, which estimates the deflection of the cantilever from the entire video file. In Figure 3.17, N is total number of images and w_n is the variable that scans the n 'th image to find the most right black corner of the cantilever, which is the distance between tip of the moving cantilever and top most boundary of n 'th image. This distance is denoted as y_n . Therefore, the deflection d , in pixel unit is the subtraction value between y_n and y_o . The actual

deflection is represented by 'D', a column vector, obtained by multiplying the difference with pixel resolution.

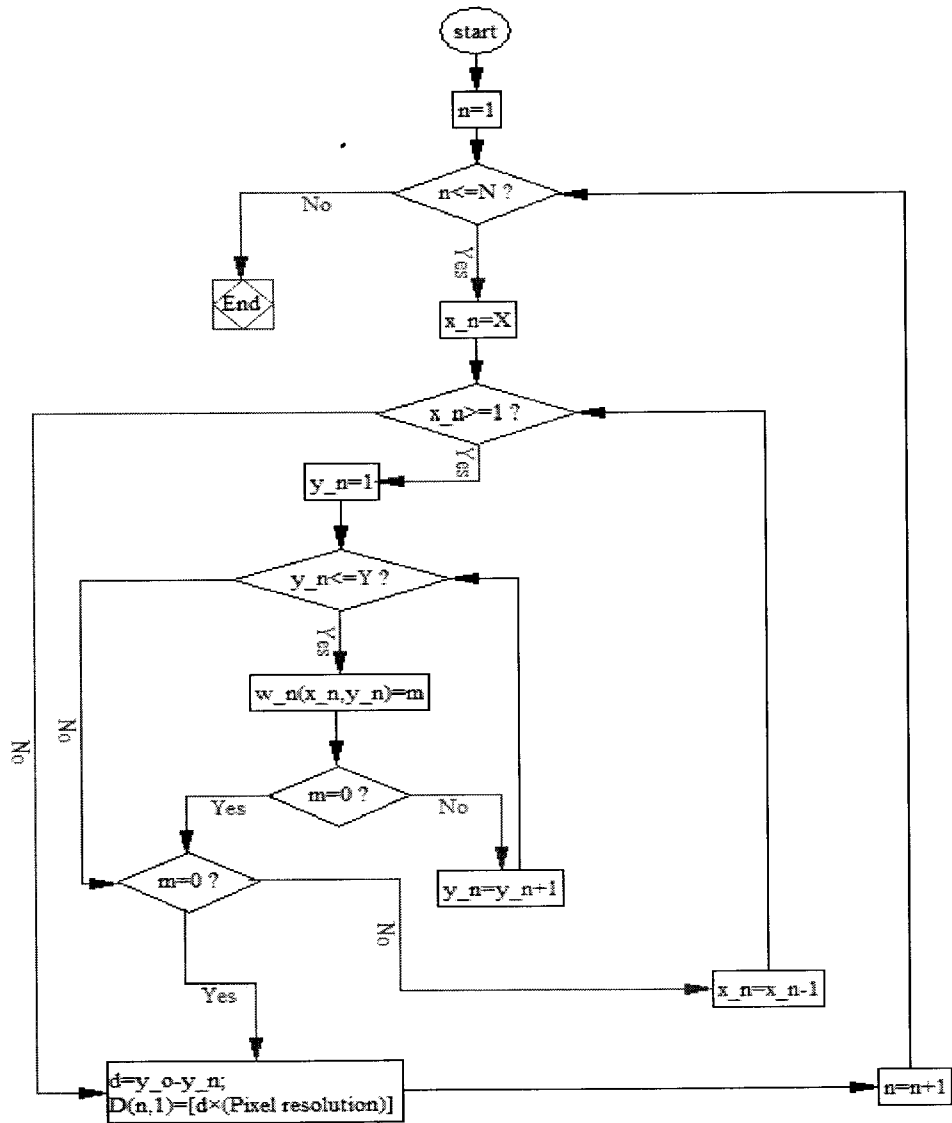


Figure 3.17: Flowchart of the algorithm to find the deflection of the cantilever
 The Figure 3.18 illustrates the pixel values correspond to color variation in the image where black cantilever portion pixels are presented as 0 and other white portion of the image is presented as binary pixel value of 1.

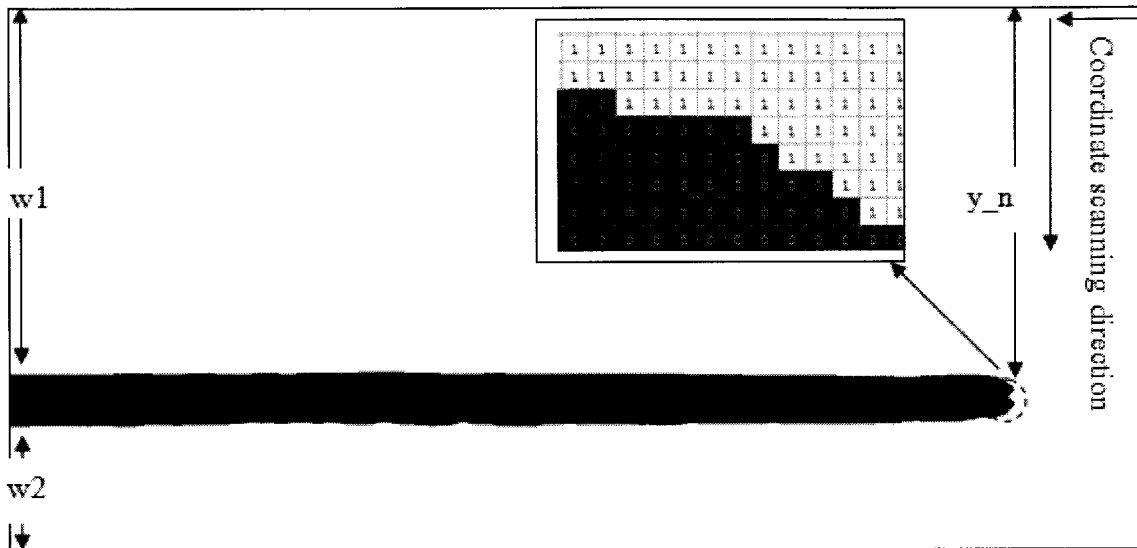


Figure 3.18: Image scanning process of MATLAB program. Binary value the of pixels at the tip of the cantilever is shown in a close-up view

3.3.3 Comparison of Deflection Measurement Methods

The preliminary trials on characterization of the fluid-structure interactions were conducted using a LDV. From these trials, it became apparent that the LDV could not provide reliable measurements of the tip deflection. As an example, Figure 3.19 illustrates the time histories of the inlet flow pressure differential and the resulting cantilever tip deflection. The deflection response does not seem to approach steady state, while deflection peaks approached significantly higher values, in the order of 100 μm . The measured response was thus considered unreliable. The error in the response was attributed to reflections of the laser beam through different media. It was noted that the reflected light was required to pass through three different media such as fluid, PDMS walls of the microchannel and the air, which resulted in considerable refraction of the light and thus the error. Furthermore, the deflection signal does not exhibit steady-state response corresponding to the two harmonic components of the flow (f_1 and f_2), which are clearly evident from the pressure signals.

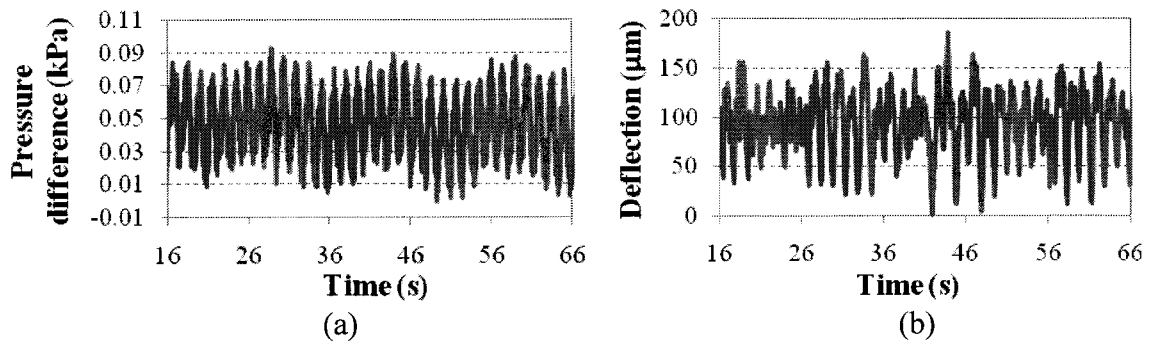


Figure 3.19: (a) Time history of the measured (a) inlet pressure difference (b) the cantilever tip deflection recorded by LDV at a pump speed of 4 RPM

The DVIP method was found to yield satisfactory measurements of the beam deflection. As an example, Figure 3.20 shows the time histories of the differential pressure loading and the measured tip deflection under at 4 RPM. Unlike the response measured using LDV, the beam deflection response approaches steady state and comprises two primary spectral components of the fluid flow. Moreover, the magnitude of the tip deflection is significantly smaller than that observed from the LDV signal. This method was used for further experiments on characterization of dynamic interaction of the microstructure with fluid.

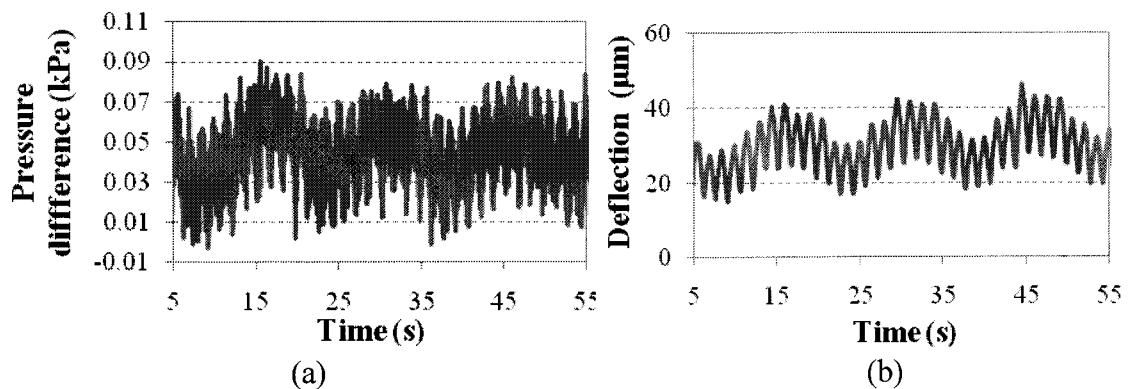


Figure 3.20: (a) Time history of the measured inlet pressure difference (b) the cantilever tip deflection by DVIP method at a pump speed of 4 RPM

3.4 Experimental Design

The experiments were designed to characterize microcantilevers responses under different fluid flows within the fabricated microfluidic chips. The static and dynamic responses of the microstructures are related to several fluid parameters. Naik et al. [44], Hirai et al. [19] and Belmiloud et al. [11] experimentally characterized the resonant microcantilever response under interactions with fluids of different viscosity. The studies showed important effects of fluid viscosity on the dynamic response of structure. Furthermore, Aubin et al. [17] demonstrated the influences of air pressure inside the microchannel on the response of a cantilever. A few studies on development of microcantilever based flow sensors have also reported the effects of flow rate on the structure response [3, 5].

An experiment is designed to characterize fluid-structure interaction under different conditions namely the fluid flow rates and flow pressure. The experiments in this section are limited to a single fluid named Fluid Xp, due to its non-conductive property. The density of Fluid XP was 1029 kg/m^3 and viscosity was $4.5 \times 10^{-3} \text{ Pa.s}$. The effects of fluid viscosity on the cantilever response are also investigated in this study, which is described in Chapter 5. The deflection responses of the cantilever in these experiments are characterized by image capture and post-processing method.

3.4.1 Experimental Methods and Parameters

The experiments were performed under different flow rates realized by selecting different sizes of the inlet tubes and microfluidic chips sizes. The experiments were also performed under different speeds of the pump, to create different harmonic components

of the flow. Prior to each experiment, the pump was operated at its highest speed for a few minutes in order to prime the pump, the flow lines and the test specimen.

The experiments involved specimen with two different hydraulic diameters to achieve two different flow rates, which were realized through different diameters of the tubes in the peristaltic pump. Furthermore, two sets of tubes were employed to achieve low and high flow conditions described below:

- I. Low Flow Condition: This flow condition was achieved by connecting two different diameters of pump tubes to the two different channels of the microfluidic test chips. The one channel of the microfluidic test chips was connected with a medium inner diameter tube of 2.1 mm and the other channel was connected with a smaller inner diameter tube of 1.2 mm.
- II. High Flow Condition: This flow condition was achieved by connecting another two different diameters of pump tubes to the two different channels of the microfluidic test chips. The one channel of the microfluidic test chips was connected with a larger inner diameter tube of 3.2 mm and the other channel was connected with a medium inner diameter tube of 2.1 mm.

Table 3.2 presents four different test conditions using the above combinations together with the 2.1 mm and 3.2 mm hydraulic diameter test chip for realizing the low and high flow conditions.

Table 3.2: Four different test conditions

	Chip 1: 3.2 mm Hydraulic diameter Test chip	Chip 2: 2.1 mm Hydraulic diameter Test chip
<p>Low flow condition</p> <p>Medium diameter tube 1: inner diameter = 2.1 mm</p> <p>Small diameter tube 2: inner diameter = 1.2 mm</p>	Test 1	Test 2
<p>High flow condition</p> <p>Large diameter tube 1: inner diameter = 3.2mm</p> <p>Medium diameter tube 2: inner diameter = 2.1mm</p>	Test 3	Test 4

Figure 3.21 and 3.22 further shows the schematics of the flow channels of 3.2 mm and 2.1 mm hydraulic diameter chips respectively, where for example $\text{Ø } 3.2$ (3.2×3.2) indicates a cross-section of 3.2 mm × 3.2 mm with hydraulic diameter of 3.2 mm.

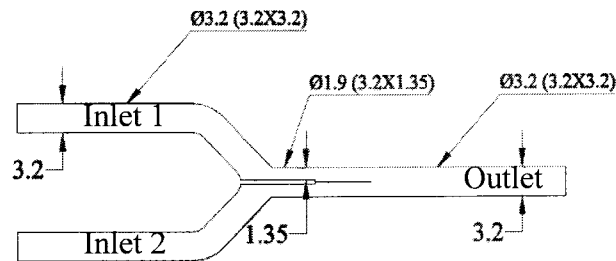


Figure 3.21: Schematics of the fluid flow paths of the microfluidic chip with 3.2 mm hydraulic diameter channel

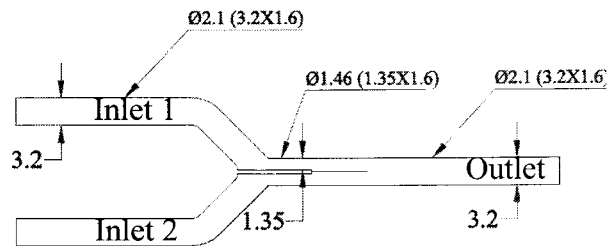


Figure 3.22: Schematics of the fluid flow paths of the microfluidic chips with 2.1 mm hydraulic diameter channel

The dimensions of the PVDF cantilevers were also varied for the two test specimens. The 3.2 mm hydraulic diameter specimen comprised a 7.05 mm long, 2.1 mm wide and 28 μm thick cantilever, while the width of the cantilever was reduced to 1.1 mm for the 2.1 mm hydraulic diameter test chip. The pressure and flow data acquired were analyzed to determine the flow rates and the pressure differential between the two inlet ports, which were considered to represent the excitation to the microcantilever. The frequency spectrum of the pressure signals were also attained to identify the dominate frequencies of the flows. The image files on the other hand were processed to determine the deflection patterns of the microcantilever structure. The results attained from the experiments performed with two test chips are presented in the following section.

3.5 Experimental Results at 'Low Flow' Conditions

The results attained under the low flow condition involving the combination of medium and small diameter tubes within the pump are discussed in the following subsection for two test specimens.

3.5.1 Test 1: Study on a Chip with 3.2 mm Hydraulic Diameter

Figure 3.23, as an example, illustrates the time histories of the inlet and outlet pressure and input pressure difference at low pump speed of 4 RPM. The inlet pressures and pressure difference signal exhibit considerable oscillations, which mostly occur at two distinct harmonic components. These are attributed to the RPM of the main disk and the rollers of the pump as described in Section 3.2.4. The frequencies of oscillations were identified through fast Fourier transform of the measured signals. For this purpose, data segments representing the steady-state values sampled at 100 Hz, were analyzed to

determine the amplitude spectrum of the pressure. While the lengths of the data segments varied for different experiments, the segments of minimum duration of 50 s alone were considered for the analysis. Figure 3.24 (a) illustrates the amplitude spectrum of the measured pressure signal, which clearly shows the presence of two harmonic components at 0.0664 and 0.664 Hz. These frequencies directly correspond with those derived from the speeds of the main disk and rollers of the pump, ω_1 and ω_2 , as presented in Equation (3.3) and (3.7). The amplitudes of the pressure difference at the two frequencies are quite comparable. The pressure loading (Δp) is the difference between the pressures measured upstream to the cantilever, at the inlets as shown in Figure 3.1. The steady-state pressure loading, $\Delta p(t)$ may thus be expressed by:

$$\Delta p(t) = P_0 + P_1 \sin \omega_1 t + P_2 \sin \omega_2 t \quad (3.8)$$

Where, P_0 is the mean pressure, and P_1 and P_2 are the magnitudes of the pressure loading corresponding to ω_1 and ω_2 respectively. The force excitation to the cantilever can thus be expected to excite oscillations at the same frequencies such that:

$$F(t) = F_0 + F_1 \sin \omega_1 t + F_2 \sin \omega_2 t \quad (3.9)$$

Where F_0 is the mean force, F_1 and F_2 and are the amplitudes corresponding to ω_1 and ω_2 . The presence of the harmonic components of the force and pressure is also evident from the deflection response of the cantilever structure as seen in Figure 3.24 (b) and (c). Considering low frequencies of excitations, well below fundamental natural frequency of the beam, the deflection response also exhibits oscillations at the same frequencies ω_1 and ω_2 . This is evident from the amplitude spectrum shown in Figure 3.24 (c). This also suggests that the DVIP technique used in this study can accurately capture

the oscillation of the microstructure. The results also suggest slightly larger deflection at the higher frequency ω_2 than that at ω_1 , although the pressure magnitudes were quit similar at both the frequencies. The measured beam deflection may thus also be expressed by a combination of the responses of two harmonic excitation components such that:

$$y(t) = Y_o + A_1 \sin(\omega_1 t) + A_2 \sin(\omega_2 t) \tag{3.10}$$

The response measured under different pump speeds also revealed two harmonic components while the frequencies varied with the pump speed. The measured signal obtained under different speeds ranging from 5 to 9 RPM, are presented in Figure 3.25 to 3.29 respectively. These figures illustrate the amplitude spectrum of the inlet pressure difference and tip deflection together with time history of the tip deflection.

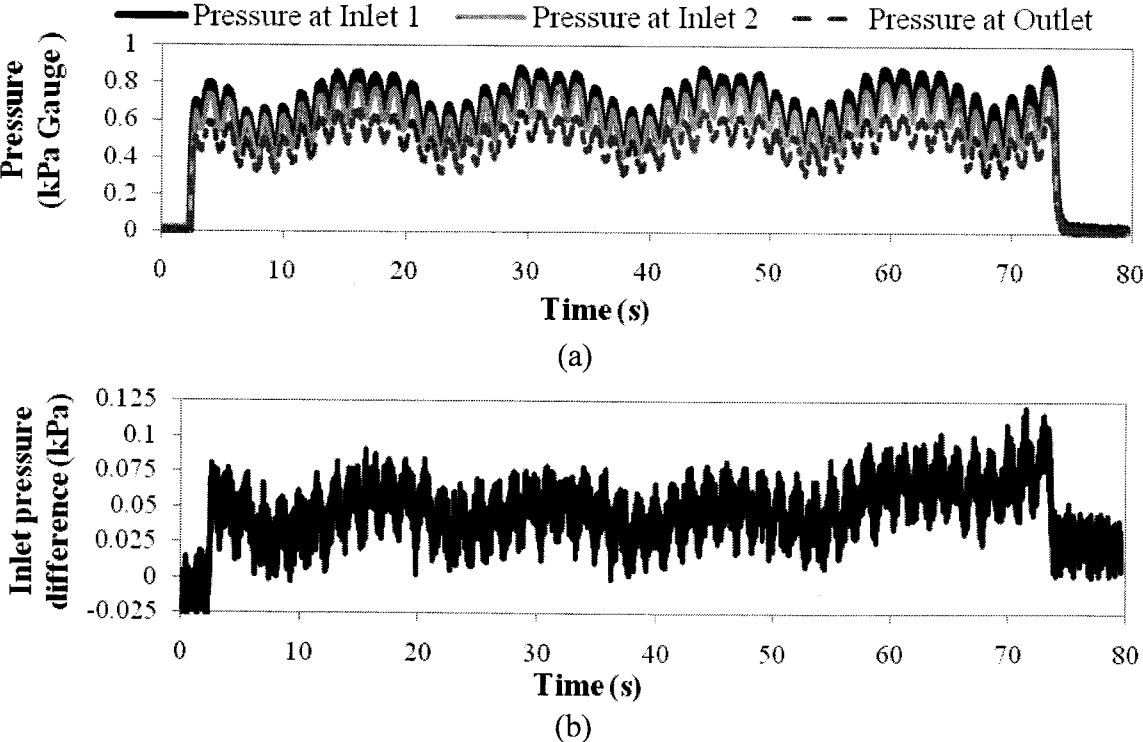
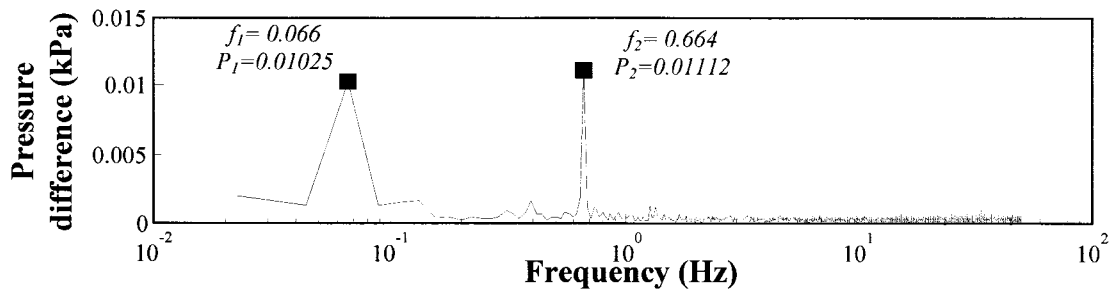
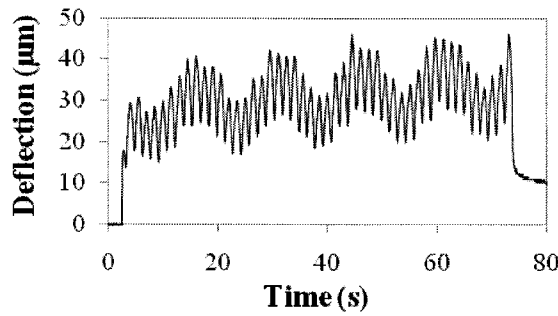


Figure 3.23: Variation in the inlet and outlet fluid pressure of the 3.2 mm hydraulic diameter of specimen: (a) time history of measured inlet and outlet pressure (b) time

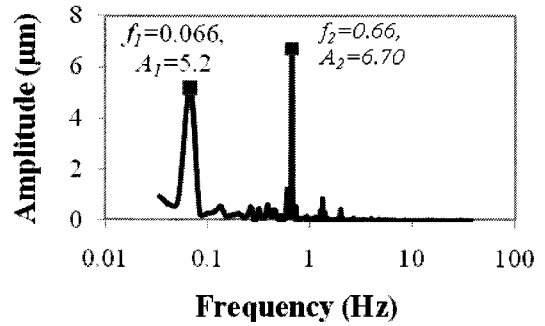
history of the measured inlet pressure difference and (c) spectrum of the inlet pressure difference (N= 4RPM)



(a)

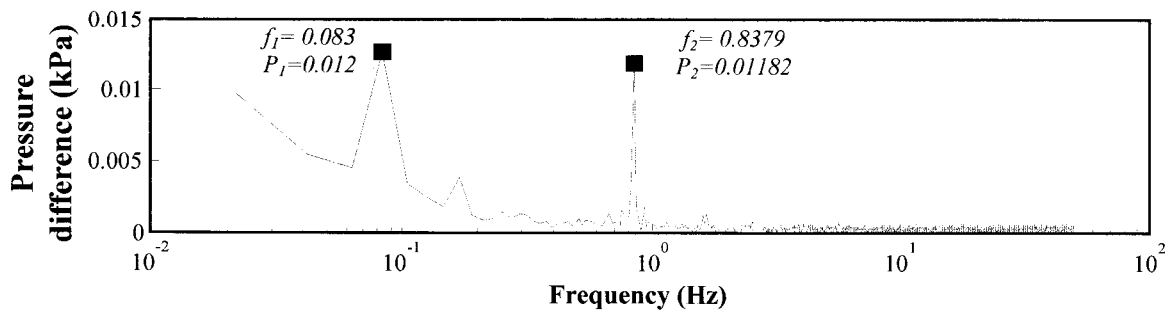


(b)

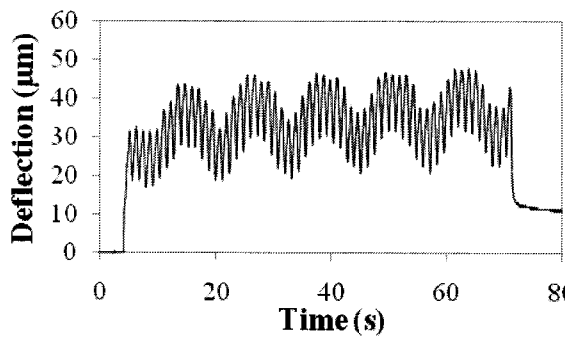


(c)

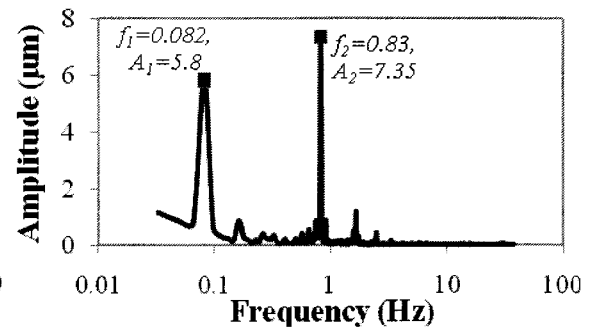
Figure 3.24: (a) Spectrum of the inlet pressure difference (b) Time history of the beam tip deflection (c) Spectrum of the beam tip deflection (N= 4 RPM)



(a)



(b)



(c)

Figure 3.25: (a) Spectrum of the inlet pressure difference (b) Time history of the beam tip deflection (c) Spectrum of the beam tip deflection (N= 5 RPM)

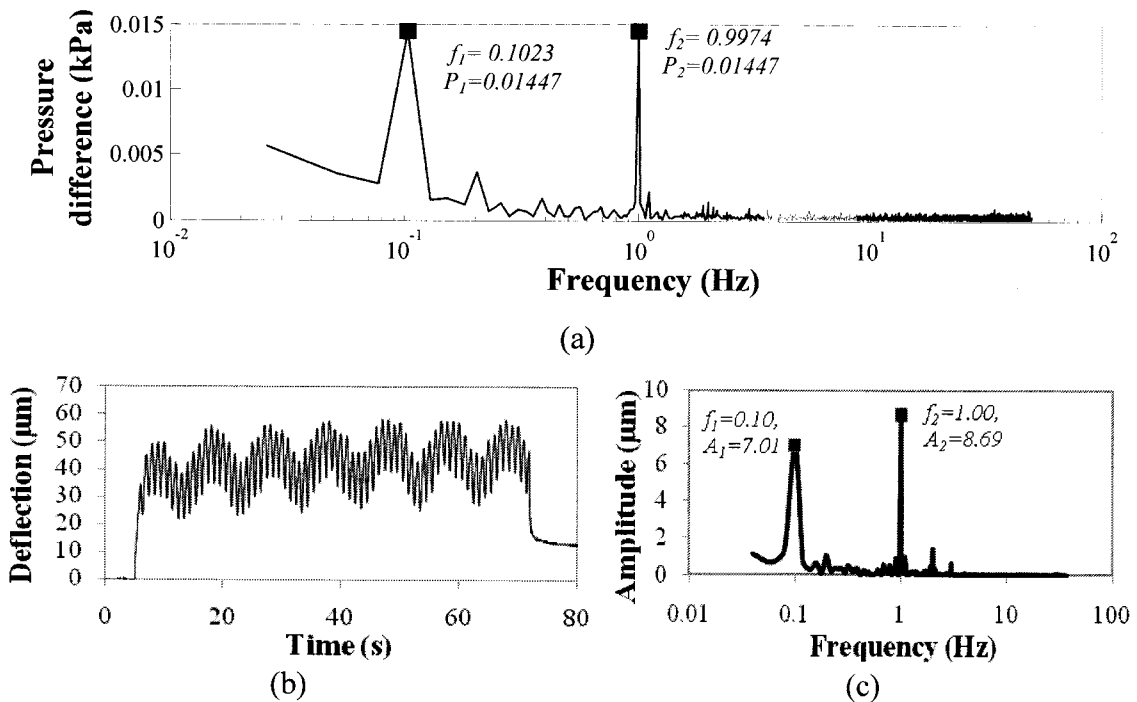


Figure 3.26: (a) Spectrum of the inlet pressure difference (b) Time history of the beam tip deflection (c) Spectrum of the beam tip deflection (N= 6 RPM)

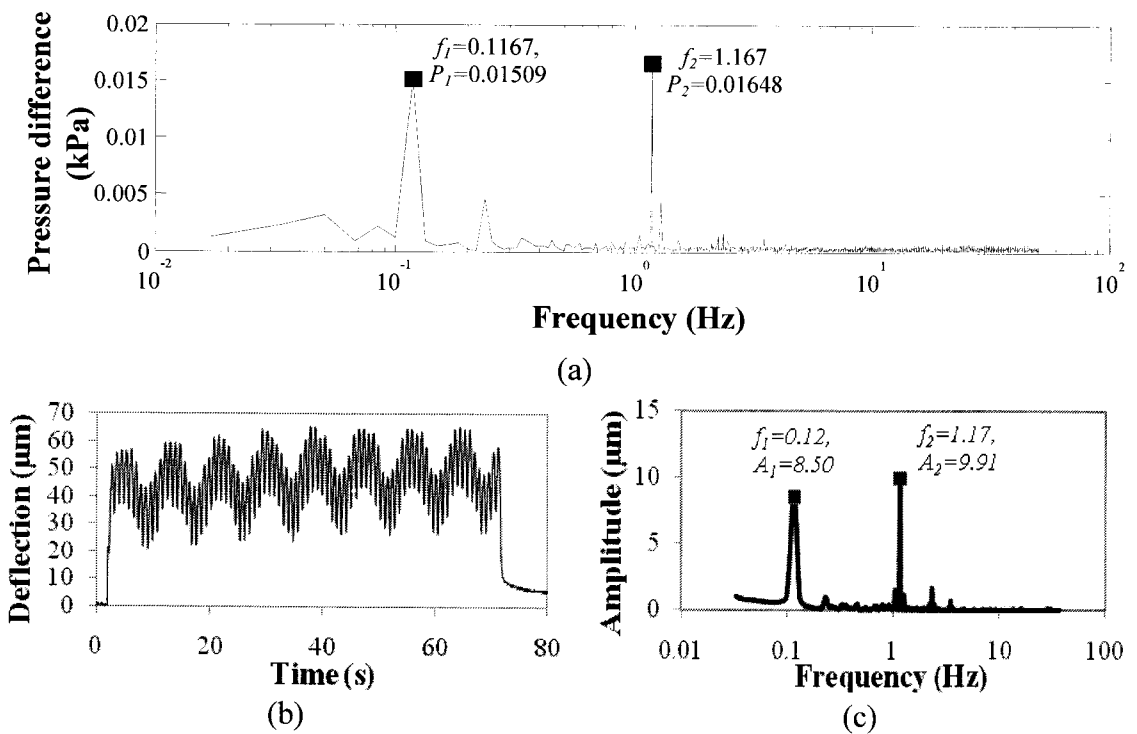
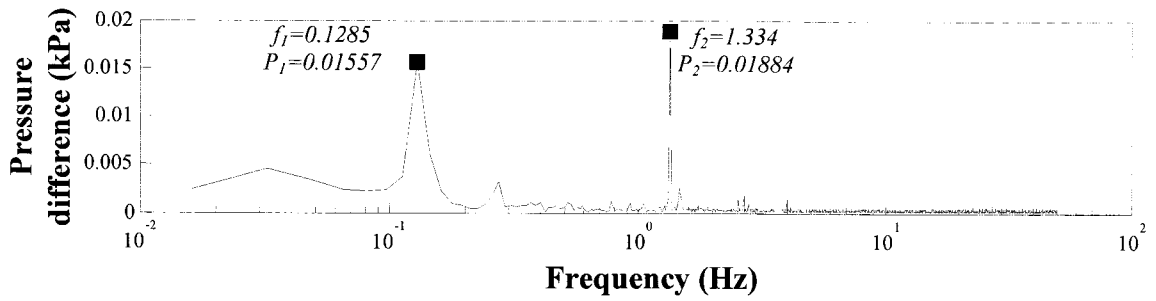
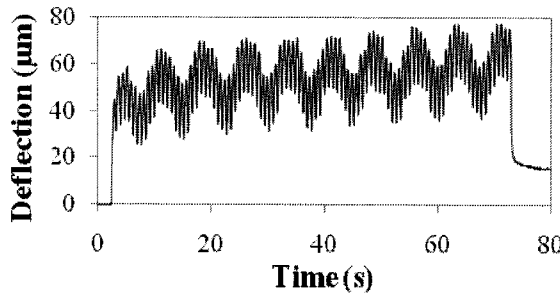


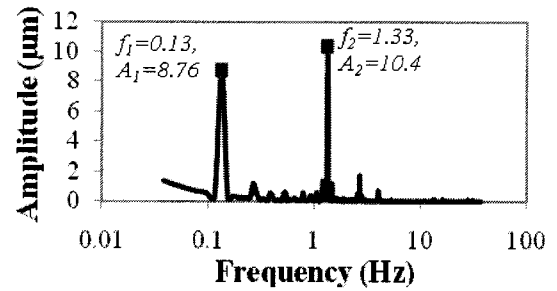
Figure 3.27: (a) Spectrum of the inlet pressure difference (b) Time history of the beam tip deflection (c) Spectrum of the beam tip deflection (N= 7 RPM)



(a)

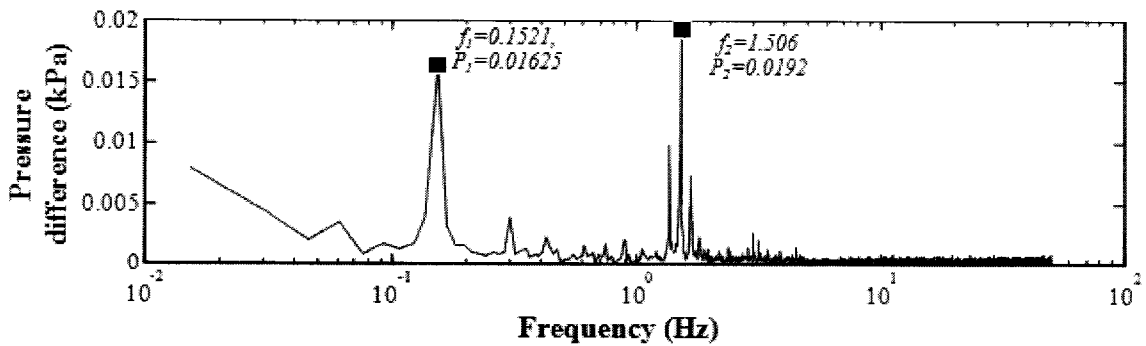


(b)

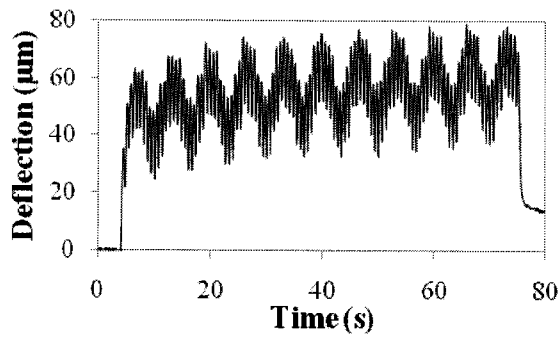


(c)

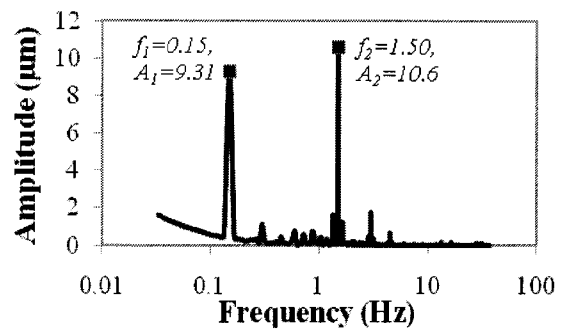
Figure 3.28: (a) Spectrum of the inlet pressure difference (b) Time history of the beam tip deflection (c) Spectrum of the beam tip deflection ($N = 8$ RPM)



(a)



(b)



(c)

Figure 3.29: (a) Spectrum of the inlet pressure difference (b) Time history of the beam tip deflection (c) Spectrum of the beam tip deflection ($N = 9$ RPM)

The theoretical value of the excitation frequencies, f_1 and f_2 for 4, 5, 6, 7, 8 and 9 RPM can be determined from Equation (3.3) and (3.7). The comparison between theoretical and experimental value obtained from the spectrum of beam tip deflection of f_1 and f_2 is presented in table 3.3.

Table 3.3 : The Excitation frequency variation with respect to RPM of pump

RPM	f_1		f_2	
	Theoretical	Experimental	Theoretical	Experimental
4	0.0667	0.0667	0.667	0.667
5	0.083	0.082	0.83	0.83
6	0.1	0.1	1	1.00
7	0.1167	0.115	1.17	1.17
8	0.133	0.133	1.33	1.33
9	0.15	0.15	1.5	1.5

However, table 3.3 indicates DVIP method provides satisfactory result to detect the frequency of response. Figure 3.30 (a) illustrates the change of rms value of inlet pressure difference and deflection with respect to pump speed where the rms value of pressure difference and deflection show a linear relation with pump speed. The Figure 3.30 (b) shows the liner relation between the rms value of deflection and inlet pressure difference.

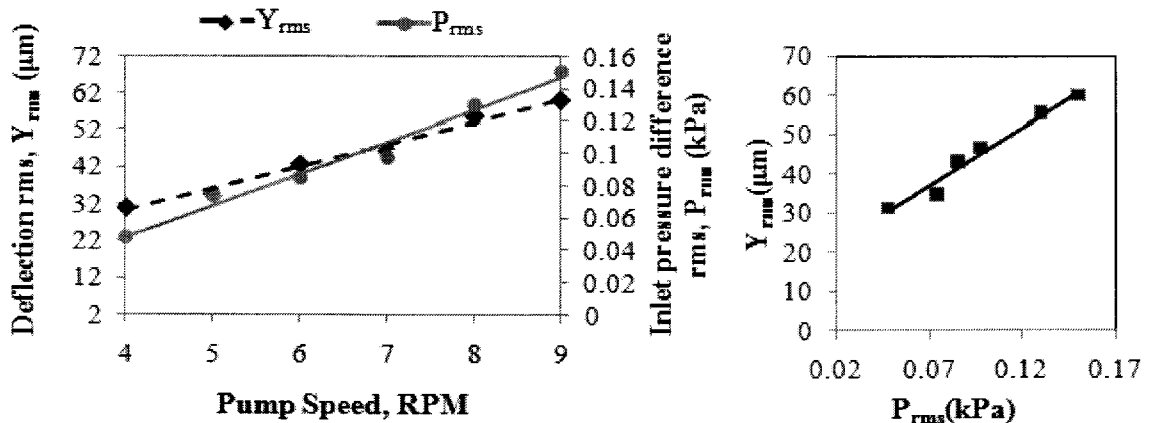


Figure 3.30: (a) Variation of rms of inlet pressure difference and deflection with respect to pump speed (b) Variation of rms of deflection with respect to rms of inlet pressure difference

The Figure 3.31 illustrates the beam tip deflection amplitudes and amplitudes of inlet pressure variation, with respect to the pump speed where it revealed that for both the case of deflection and pressure difference, rate of increment of amplitudes decreases at high RPM of pump speed. Furthermore, the Figures 3.30 (a) and 3.31 show that the output deflection amplitudes and rms follow the input pressure difference amplitudes and rms.

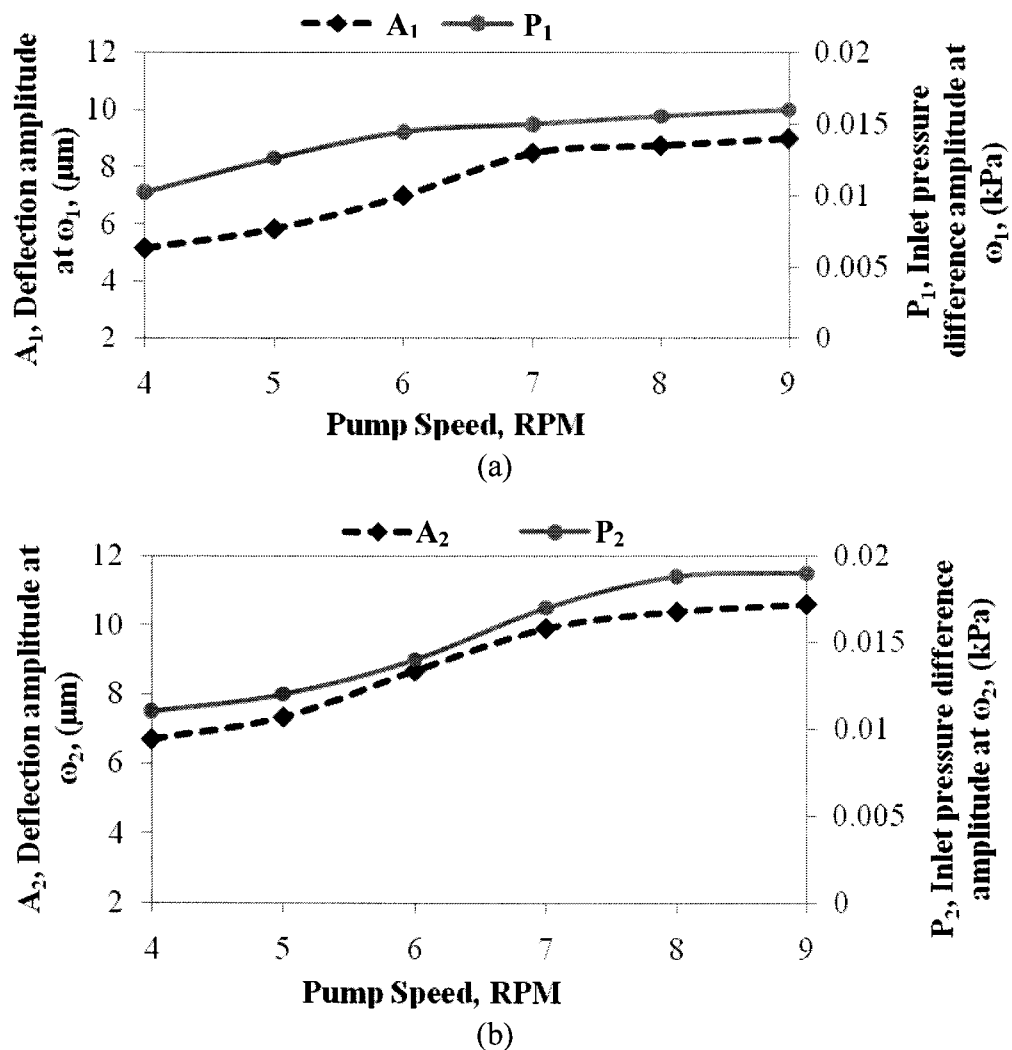


Figure 3.31: (a) Variation of first amplitude of deflection and inlet pressure difference with respect of pump speed (b) Variation of second amplitude of deflection and inlet pressure difference with respect of pump speed

3.5.2 Test 2: Study on a Chip with 2.1 mm Hydraulic Diameter

The measured data obtained by using 2.1 mm hydraulic diameter specimen at low flow condition and with different RPM of the pump are presented in Figures 3.32 to 3.37 where Section (a) of those figures illustrates the spectrum of inlet pressure difference and Sections (b) and (c) represent the time history and spectrum of cantilever tip deflection. However, the spectrum of inlet pressure difference and cantilever tip deflection presented in these figures clearly show the presence of two harmonic components with frequencies directly corresponding to the speeds of the main disk and rollers of the pump, namely ω_1 and ω_2 . These results also suggest that although the pressure magnitudes were quite similar to the previous section but are considerably larger in magnitude at higher frequency ω_2 , due to the change in the hydraulic diameter of specimen. At 2.1 mm hydraulic diameter specimen the cross-section of the flow path changes slightly, as the medium size tube has the same hydraulic diameter, as that of specimen. However, in 3.2 mm hydraulic diameter specimen at low flow condition the dynamic pressure energy was reduced near the inlet port, which is connected with medium size tube, due to the increase of cross-sectional area in the flow path of specimen. Hence, in 2.1 mm hydraulic diameter of specimen the differences between beam tip deflection amplitudes are more significant than the difference of beam tip deflection amplitudes exhibited in the results obtained from 3.2 mm hydraulic diameter of specimen.

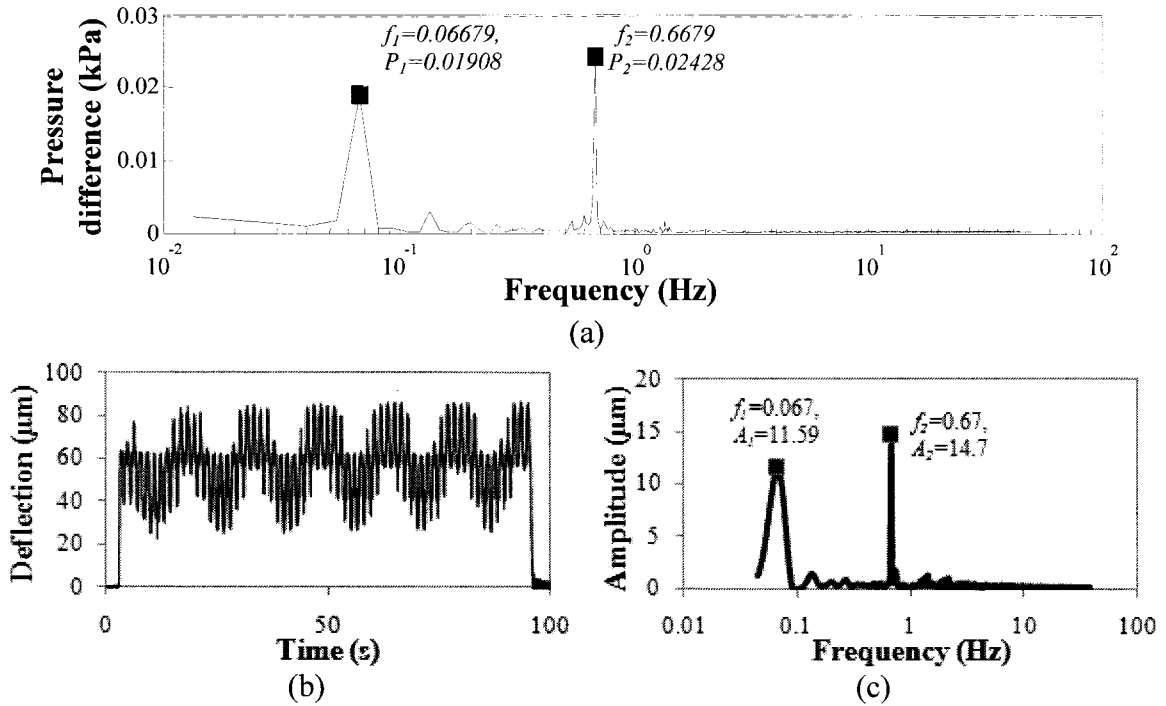


Figure 3.32: (a) Spectrum of the inlet pressure difference (b) Time history of the beam tip deflection (c) Spectrum of the beam tip deflection (N= 4 RPM)

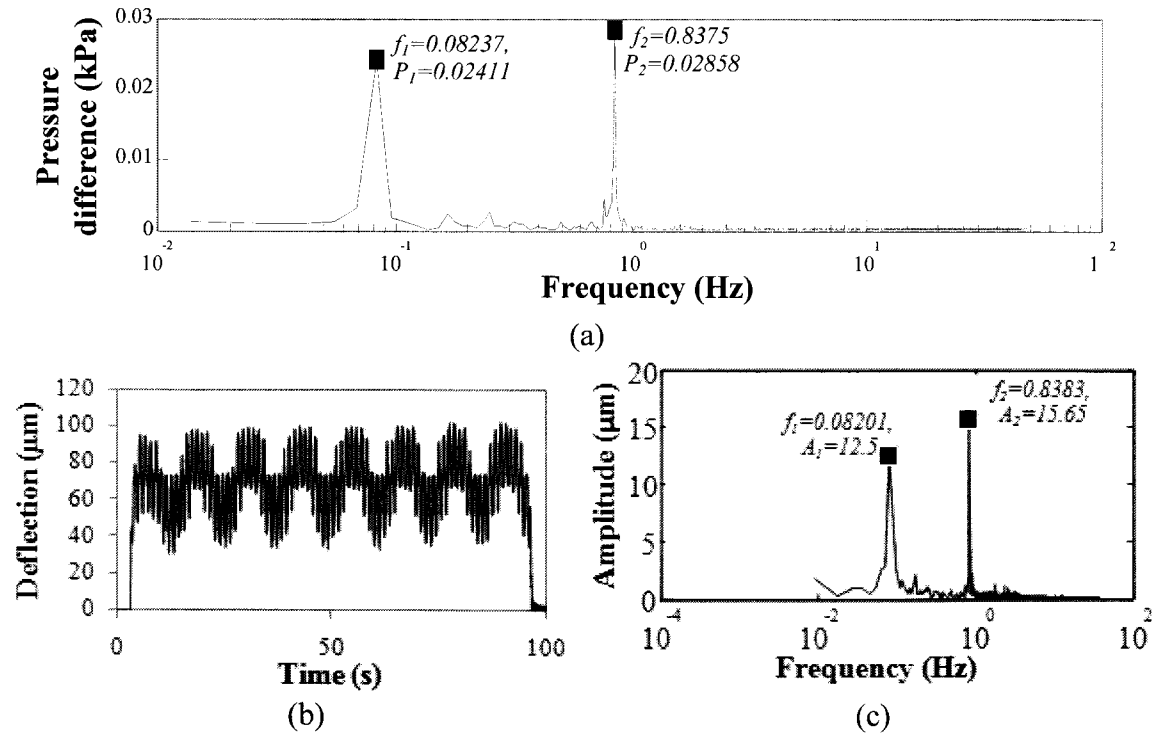


Figure 3.33: (a) Spectrum of the inlet pressure difference (b) Time history of the beam tip deflection (c) Spectrum of the beam tip deflection (N= 5 RPM)

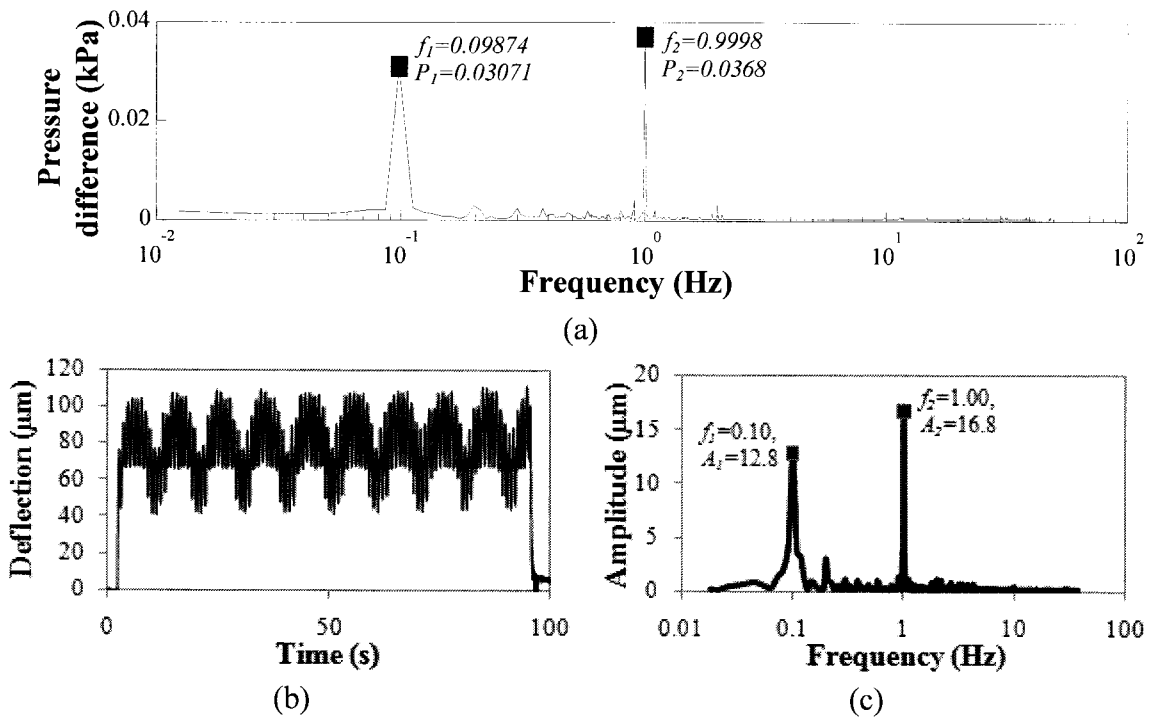


Figure 3.34: (a) Spectrum of the inlet pressure difference (b) Time history of the beam tip deflection (c) Spectrum of the beam tip deflection (N= 6 RPM)

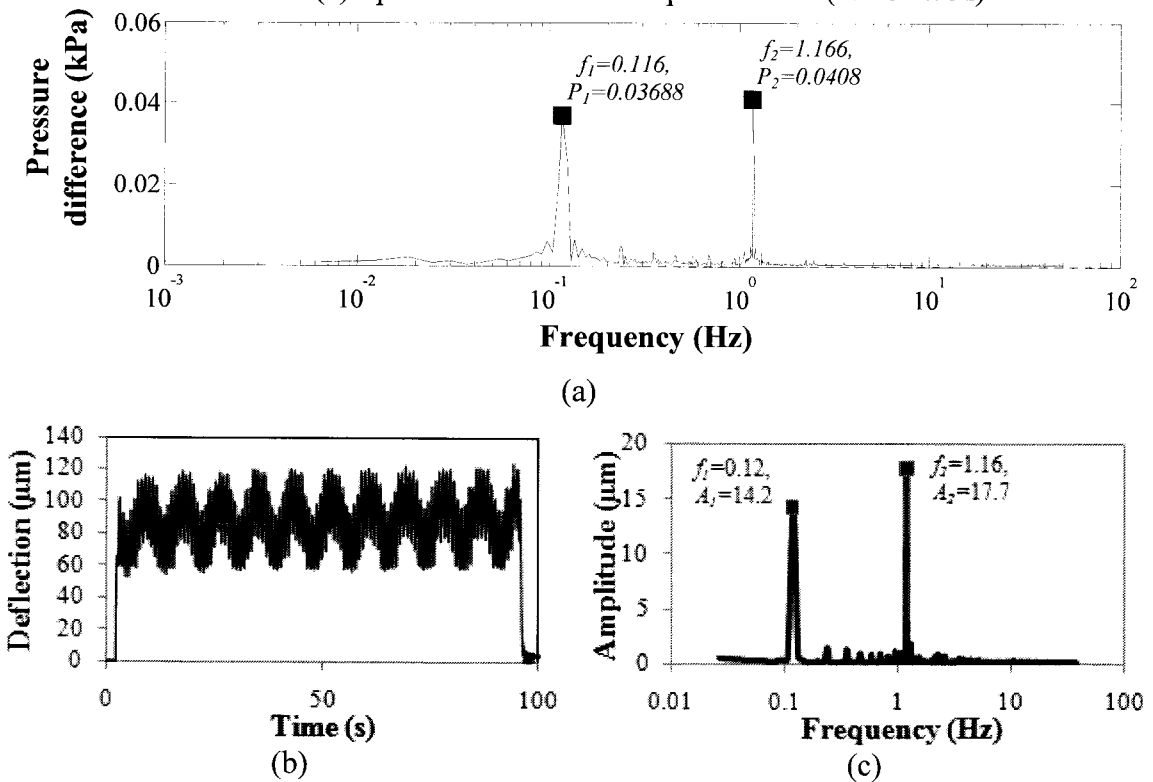


Figure 3.35: (a) Spectrum of the inlet pressure difference (b) Time history of the beam tip deflection (c) Spectrum of the beam tip deflection (N= 7 RPM)

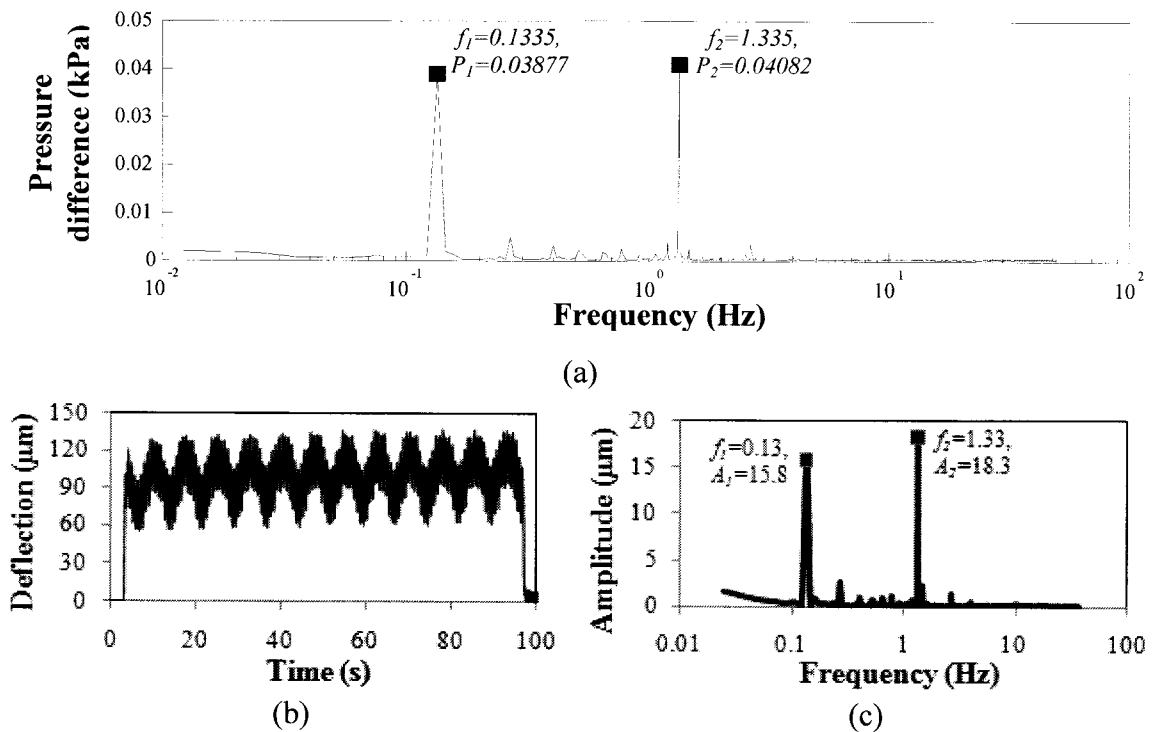


Figure 3.36: (a) Spectrum of the inlet pressure difference (b) Time history of the beam tip deflection (c) Spectrum of the beam tip deflection (N= 8 RPM)

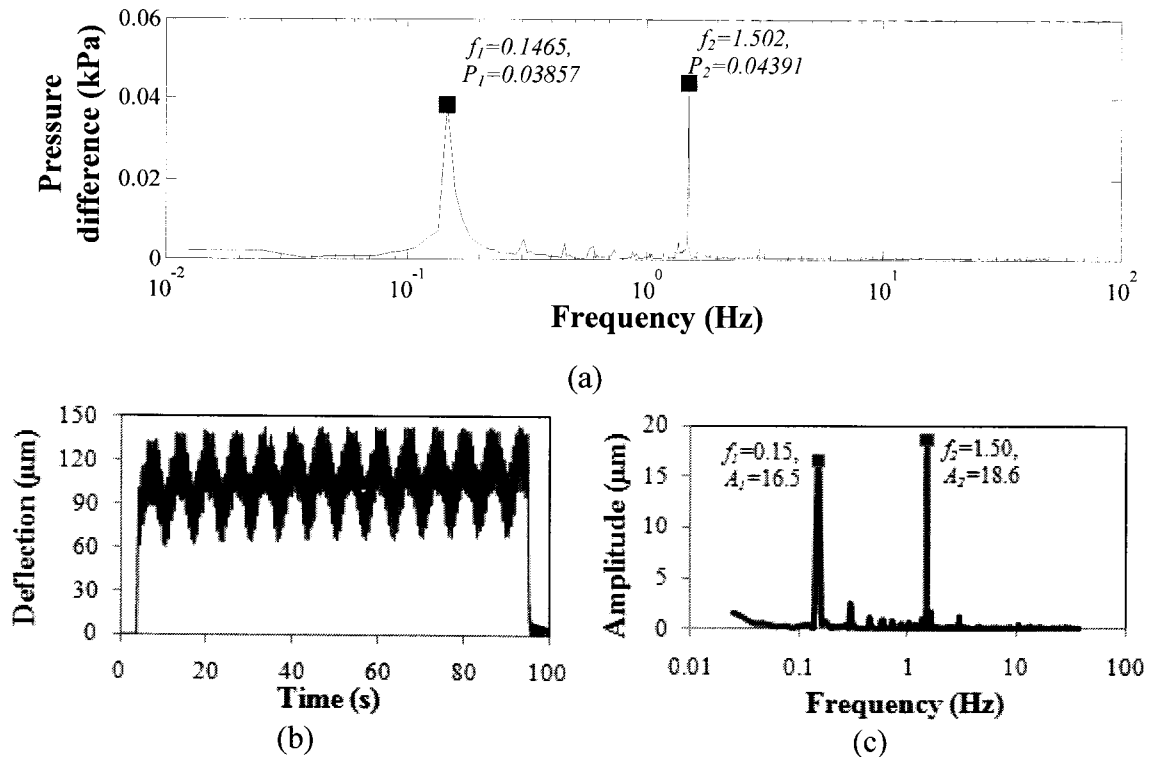


Figure 3.37: (a) Spectrum of the inlet pressure difference (b) Time history of the beam tip deflection (c) Spectrum of the beam tip deflection (N= 9 RPM)

Figure 3.38 (a) illustrates the change of rms of inlet pressure difference and deflection with respect to pump RPM where the rms of pressure difference and deflection shows a linear relation with pump speed. The rms value of deflection revealed a linear relation with the rms value of inlet pressure difference, which is presented in Figure 3.38 (b).

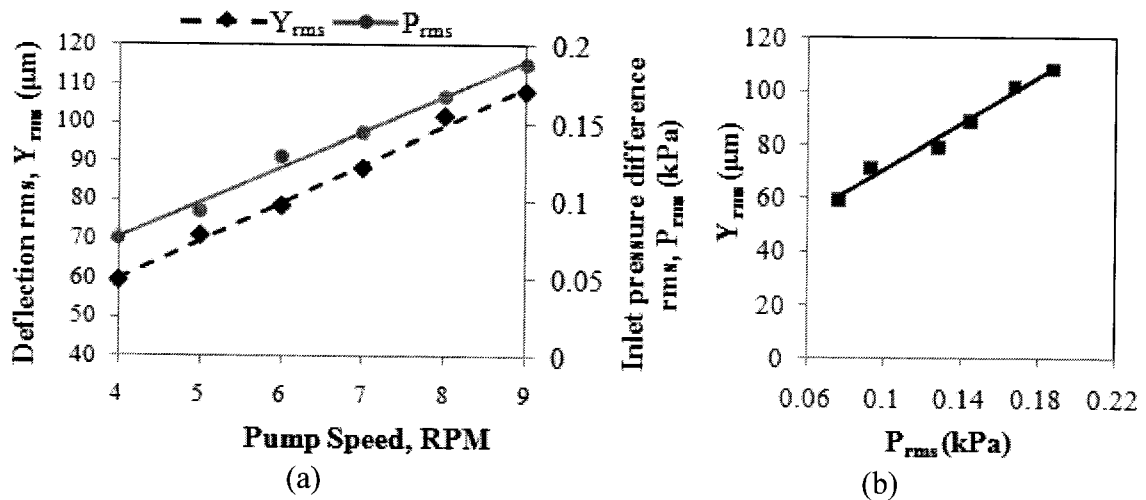


Figure 3.38: (a) Variation of rms of deflection and inlet pressure difference with respect of pump speed (b) Variation of rms of deflection with respect to rms of inlet pressure difference

The Figures 3.39 (a) and (b) illustrate the deflection amplitudes and amplitudes of inlet pressure variation with respect to the pump speed, which is obtained from spectrum of beam tip deflection and inlet pressure difference, respectively. It was found for both the cases of deflection and pressure difference the rate of increment of amplitudes decreases at high RPM of pump. Furthermore, the Figures 3.38 (a) and 3.39 show that the output deflection amplitudes and rms follow the input pressure difference amplitudes and rms.

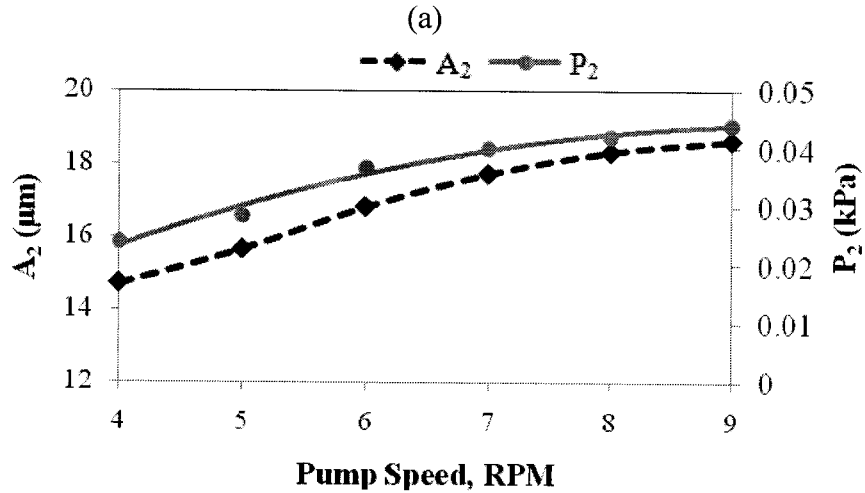
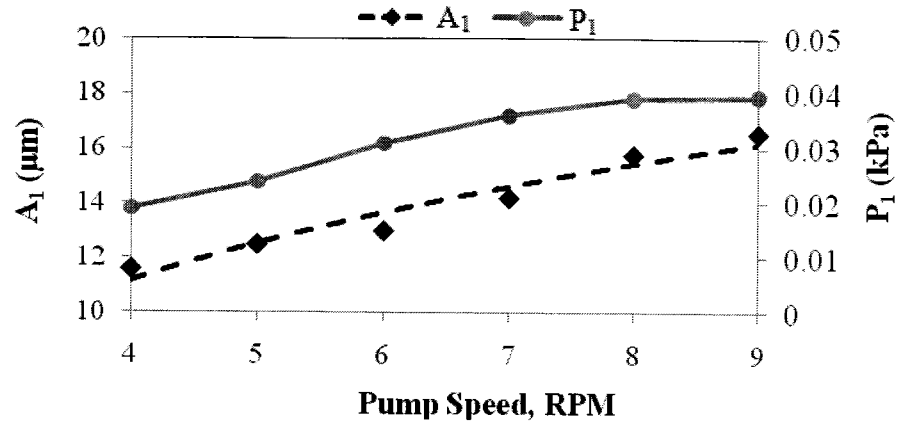


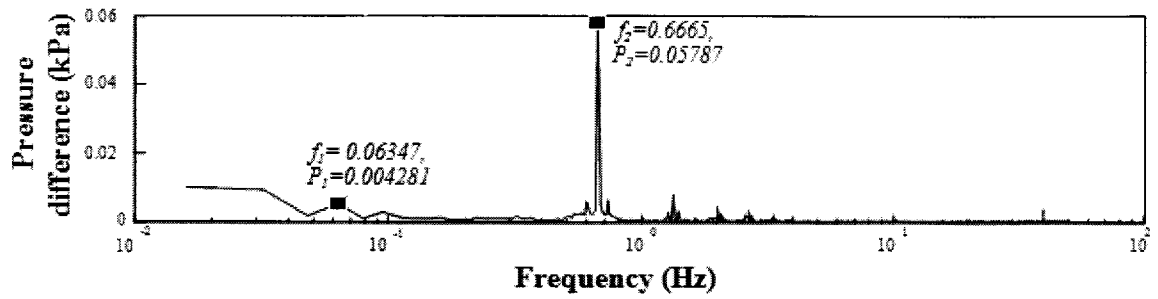
Figure 3.39: (a) Variation of first amplitude of deflection and inlet pressure difference with respect to pump speed (b) Variation of second amplitude to deflection and inlet pressure difference with respect of pump speed

3.6 Experimental Results at High Flow Condition

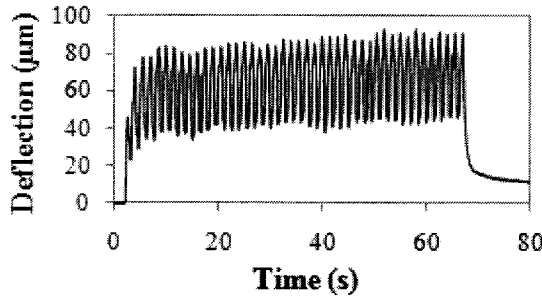
The larger diameter tube of high flow is made of PVC or Polyvinyl chloride, which is less elastic than the medium diameter tube made of silicone elastomer. Therefore, it is expected this property may create a great influence over the excitation pressure as well as the response of cantilever.

3.6.1 Test 3: Study on a Chip with 3.2 mm Hydraulic Diameter

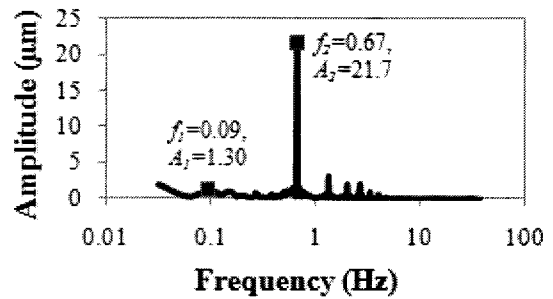
The measured data for the 3.2 mm hydraulic diameter of specimen with high flow supply tube is presented in Figures 4.40 to 4.44. However, these figures suggest that at high flow condition with 3.2 mm hydraulic diameter specimen, A_1 is negligible and significantly smaller than A_2 . The roller rotation of the central disk produce direct influence over tubes, which is greater than the influence of central disk, as it have indirect contact with the tubes. Therefore, the results presented in previous section revealed that A_1 is smaller than A_2 . The excitation pressure pattern on the cantilever is lead by the pressure of larger tube installed in the pump. At high flow condition, the central disk rotation could not produce enough influence to the larger tube of pump because it was made of less elastic material PVC. Therefore, central disk rotation is responsible for lower frequency component as well as A_1 . Hence, A_1 is negligible in the response of the cantilever of 3.2 mm hydraulic diameter of tube at high flow condition of peristaltic pump. On the other hand, for low flow, the medium size tube was made of Silicon elastomer, which was elastic enough to get the influence of central disk rotation as well as roller rotation simultaneously. Therefore, the measured data for low flow condition, which is presented in previous section, shows clearly the existence of both frequency components.



(a)

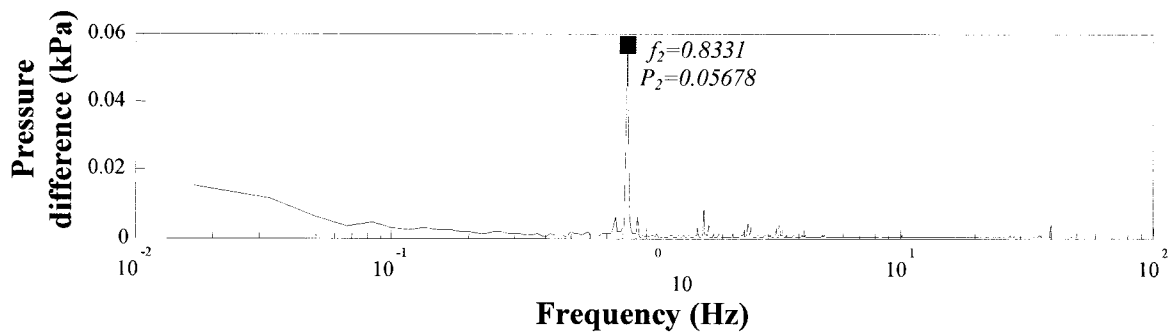


(b)

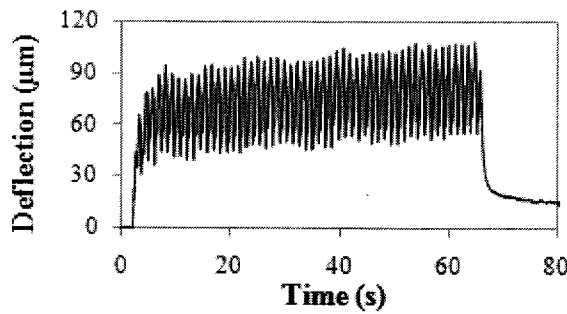


(c)

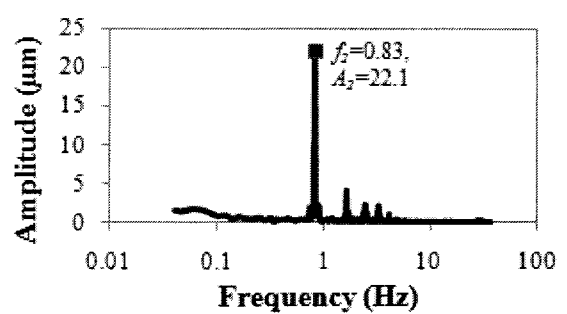
Figure 3.40: (a) Spectrum of the inlet pressure difference (b) Time history of the beam tip deflection (c) Spectrum of the beam tip deflection (N= 4 RPM)



(a)



(b)



(c)

Figure 3.41: (a) Spectrum of the inlet pressure difference (b) Time history of the beam tip deflection (c) Spectrum of the beam tip deflection (N= 5 RPM)

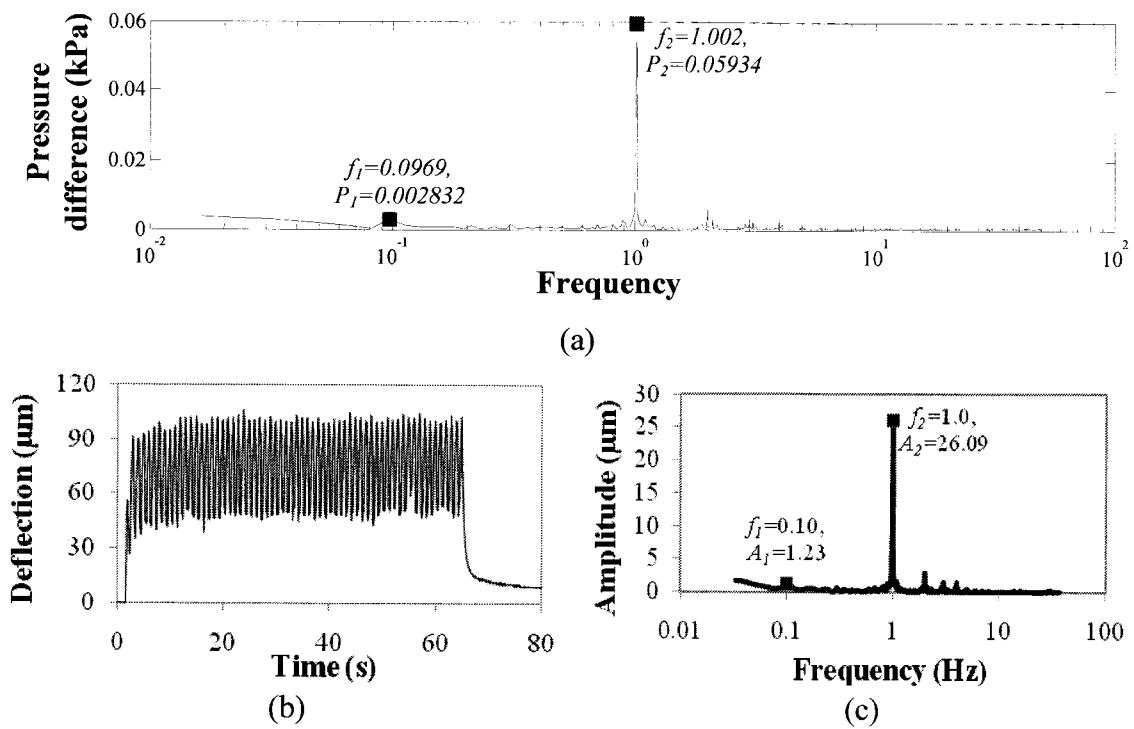


Figure 3.42: (a) Spectrum of the inlet pressure difference (b) Time history of the beam tip deflection (c) Spectrum of the beam tip deflection (N= 6 RPM)

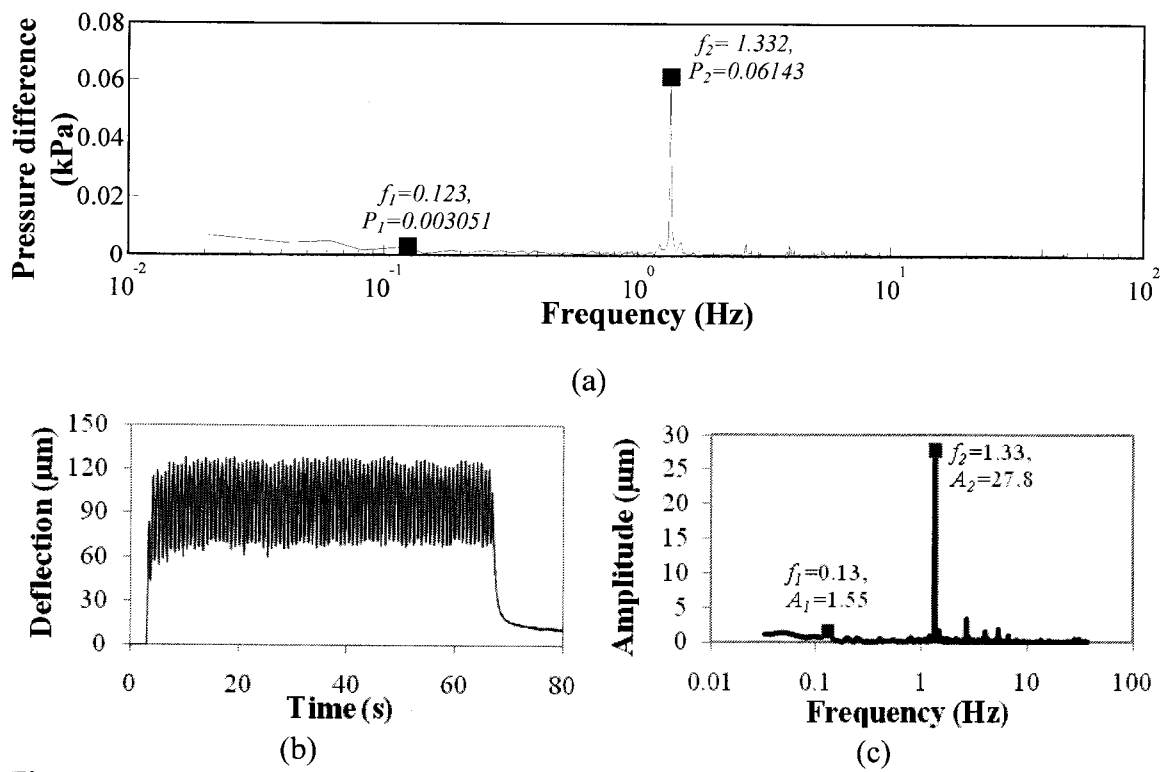


Figure 3.43: (a) Spectrum of the inlet pressure difference (b) Time history of the beam tip deflection (c) Spectrum of the beam tip deflection (N= 8 RPM)

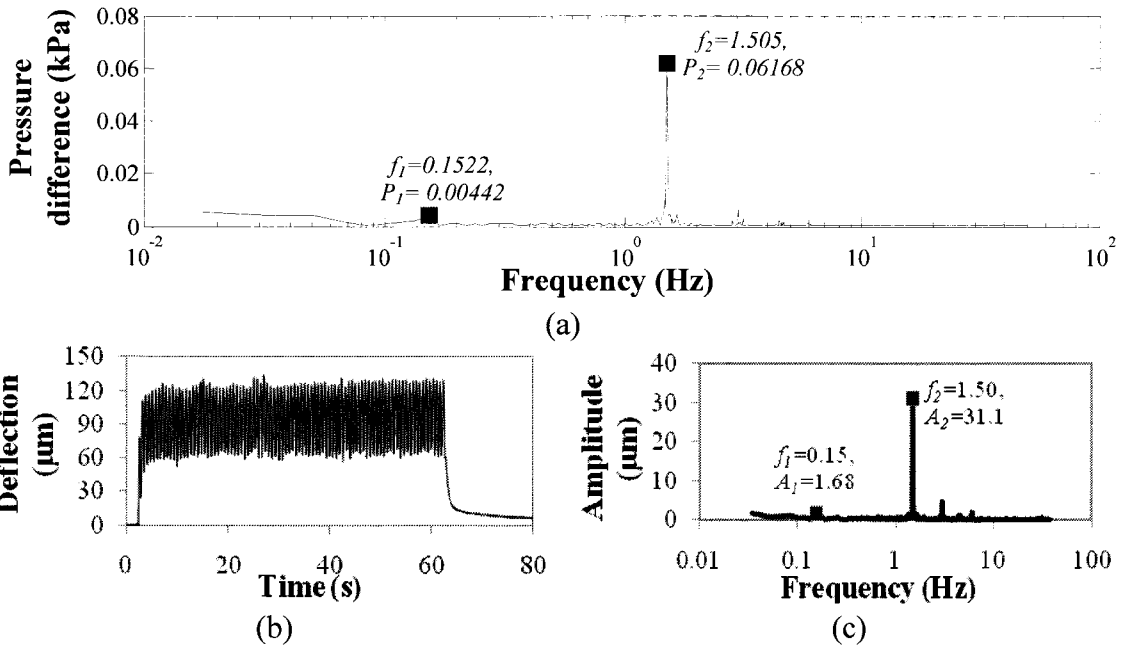


Figure 3.44: (a) Spectrum of the inlet pressure difference (b) Time history of the beam tip deflection (c) Spectrum of the beam tip deflection (N= 9 RPM)

The Figure 3.45(a) presents the liner relation of rms value of deflection and rms value of inlet pressure difference with pump speed. Since the for both inlet pressure difference and beam tip deflection at ω_1 have negligible amplitudes, hence P_1 and A_1 are not plotted here, Figure 3.45(b) illustrates the second amplitude variation of deflection and inlet pressure difference where the output beam tip deflection amplitude increment follows the input pressure difference amplitude.

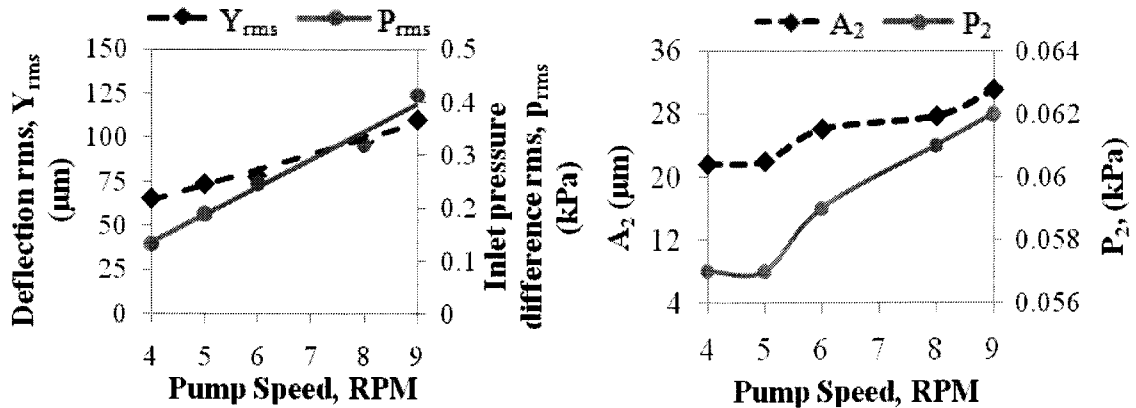


Figure 3.45: (a) The rms variation of inlet pressure difference and deflection with respect to pump speed (b) Variation of second amplitude of deflection and inlet pressure difference with respect of pump speed

3.6.2 Test 4: Study on a Chip with 2.1 mm Hydraulic Diameter

The measured data from 2.1 mm hydraulic diameter of specimen at high flow combination with different pump speed is presented in the Figures 3.47 to 3.52. These results suggest that for the same kind of flow condition (high flow) A_1 is negligible in the spectrum of beam tip deflection for 3.2 mm hydraulic diameter specimen (measured data presented in Section 3.6.1). But A_1 and A_2 both are revealed significant value in the spectrum of beam tip deflection of 2.1 mm hydraulic diameter specimen. Hence, the hydraulic diameter of specimen has a great influence over the cantilever response. The variation of flow path geometry for 2.1 mm hydraulic diameter of specimen connected to high flow configuration tube is presented in Figure 3.46.

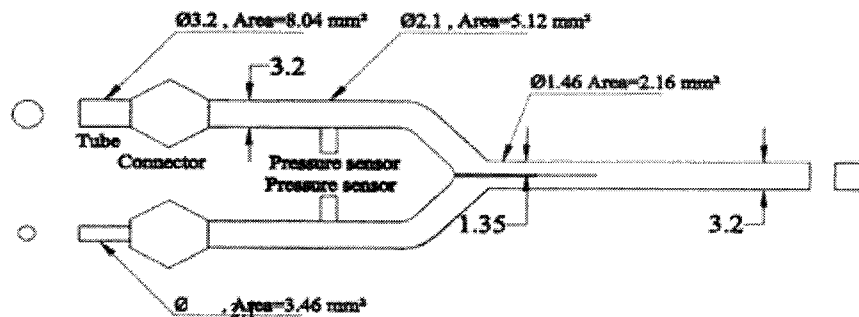
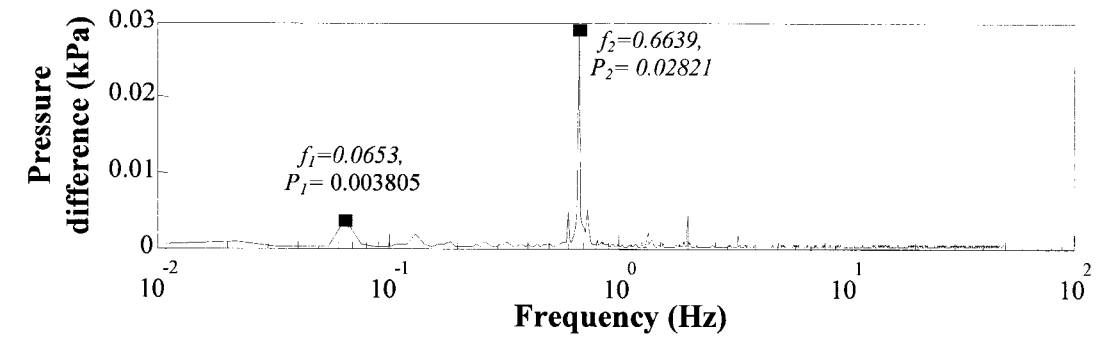


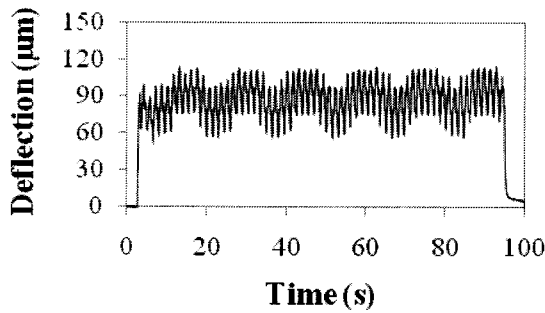
Figure 3.46: Geometrical variation flow path for 2.1 mm hydraulic diameter of specimen

On the larger tube side, the reduction of area is more than the smaller tube side. Since the flow rate is constant until the clamping point of cantilever through the entire flow path therefore, for 2.1 mm hydraulic diameter of specimen, in the larger PVC tube connected portion the velocity of flow gradually increased more than 3.2 mm hydraulic diameter of specimen, which attributed larger amount of dynamic pressure energy. Hence, for 2.1 mm hydraulic diameter specimen the A_2 is revealed larger value comparing to the 3.2 mm hydraulic diameter of specimen. As it was discussed before that

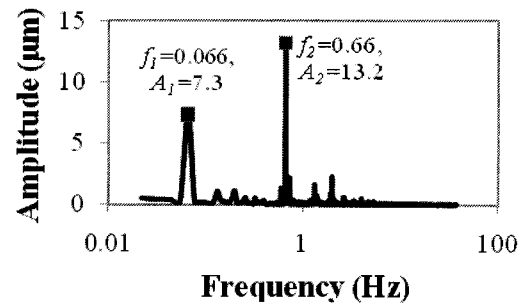
the medium size silicone tube flow have both higher and lower frequency (ω_1 and ω_2) component while, larger PVC tube have only higher (ω_2) frequency component. At high flow condition with 3.2 mm hydraulic diameter specimen the flow, entering from medium size tube faces larger area of cross-section after the inlet port. Hence, here velocity is reduced, which results decrement of dynamic pressure energy in the flow coming from medium size silicon tube. Therefore, in 3.2 mm hydraulic diameter specimen at high flow condition medium size silicon tube could not produce enough influence to attribute the lower frequency component. However, in 2.1 mm hydraulic diameter of specimen at high flow condition the flow coming from medium size tube faced comparatively smaller increment of cross-sectional area which results in less reduction of dynamic pressure energy. Hence, in 2.1 mm hydraulic diameter specimen the medium size tube can attribute enough influence to produce lower frequency component in the response of the cantilever. The result presented in this section also suggest that although pressure magnitude P_1 exhibited comparatively much smaller value than P_2 , the spectrum of beam tip deflection revealed significant value of for both A_1 and A_2 . This type of variation occurs due to the position of pressure sensors at the inlets, which measure the pressure well ahead of the cantilever. The pressure sensors were installed at the bigger cross-sectional area rather than cantilever clamped portion area. Hence, the flow from medium size silicon tube faces smaller area of cross-section near the cantilever-clamping zone, which results in increase of dynamic pressure energy for silicon tube flow. Therefore, at cantilever area the silicone tube flow has more influence in the cantilever zone rather than pressure sensor zone that produce a great influence of lower frequency component over the cantilever response.



(a)

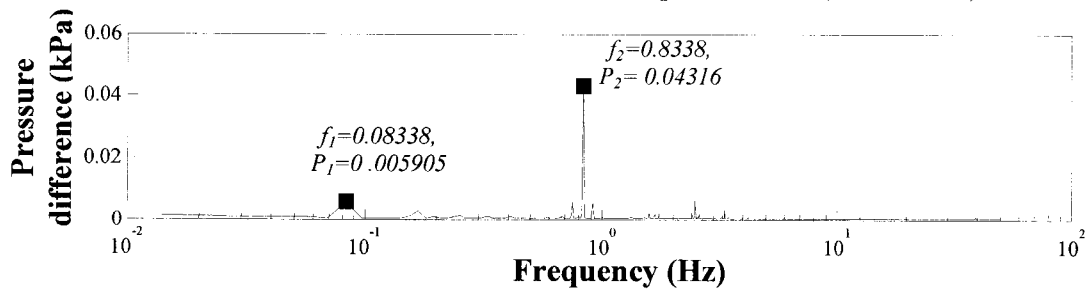


(b)

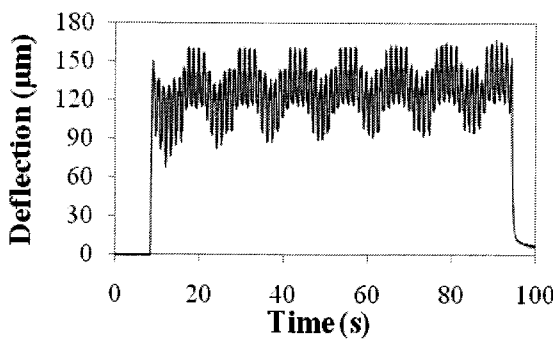


(c)

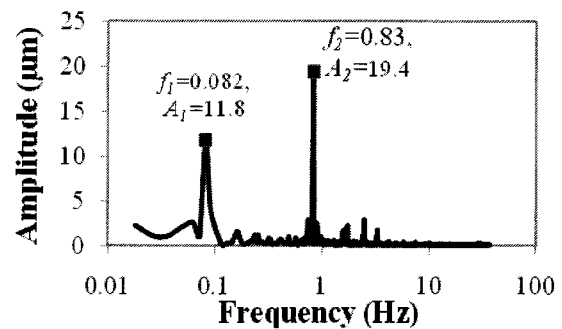
Figure 3.47: (a) Spectrum of the inlet pressure difference (b) Time history of the beam tip deflection (c) Spectrum of the beam tip deflection (N= 4 RPM)



(a)

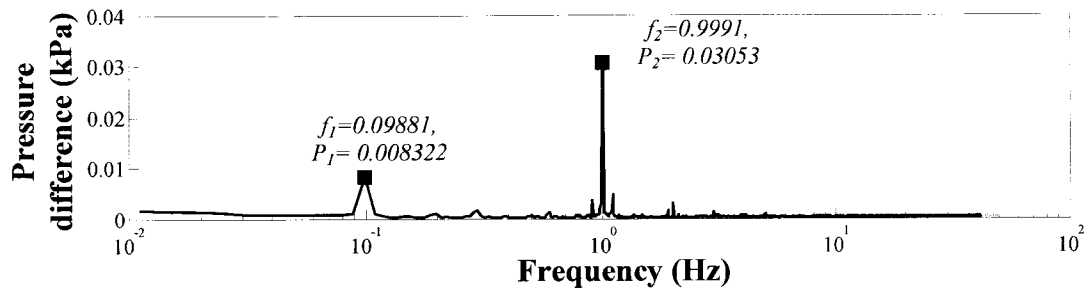


(b)

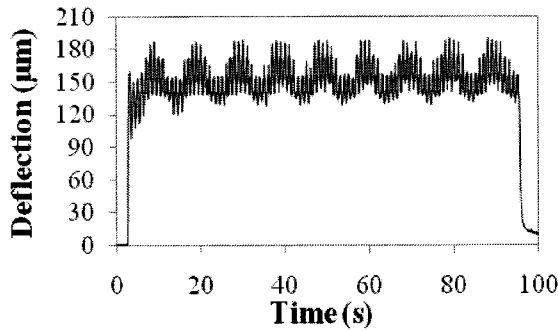


(c)

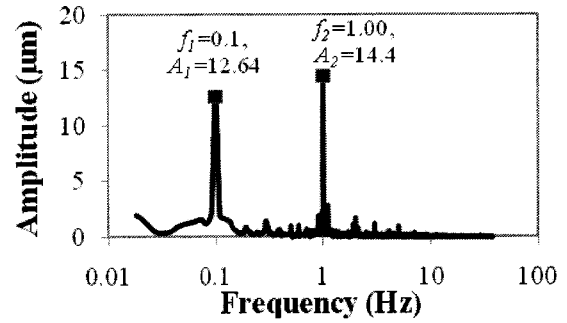
Figure 3.48: (a) Spectrum of the inlet pressure difference (b) Time history of the beam tip deflection (c) Spectrum of the beam tip deflection (N= 5 RPM)



(a)

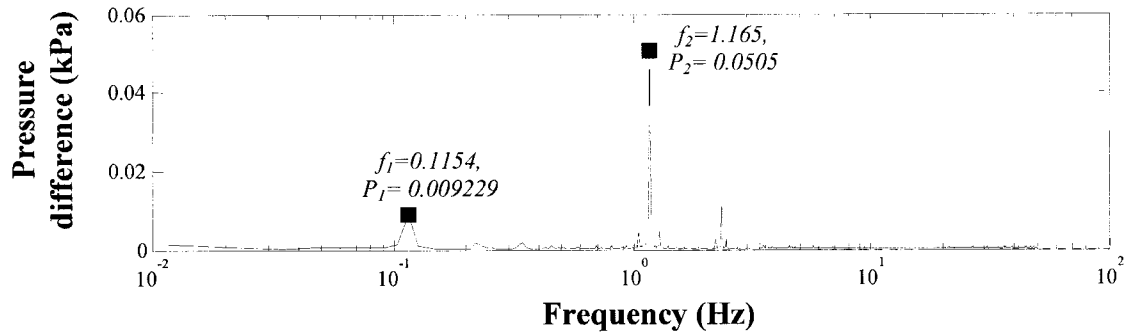


(b)

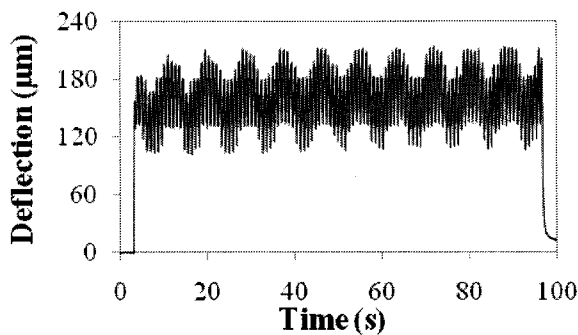


(c)

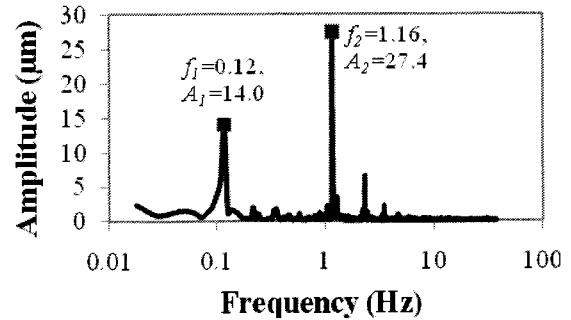
Figure 3.49: (a) Spectrum of the inlet pressure difference (b) Time history of the beam tip deflection (c) Spectrum of the beam tip deflection (N= 6 RPM)



(a)



(b)



(c)

Figure 3.50: (a) Spectrum of the inlet pressure difference (b) Time history of the beam tip deflection (c) Spectrum of the beam tip deflection (N= 7 RPM)

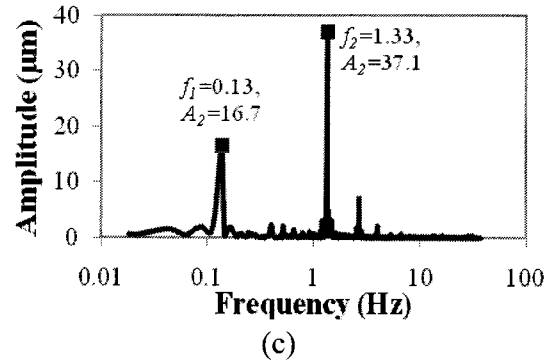
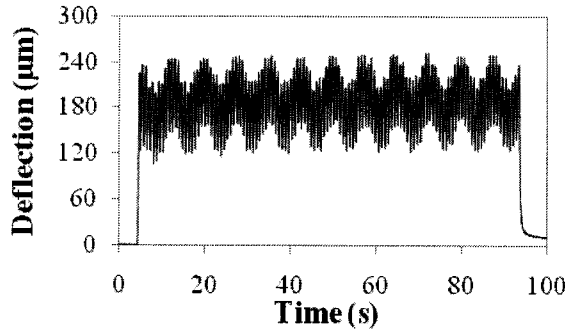
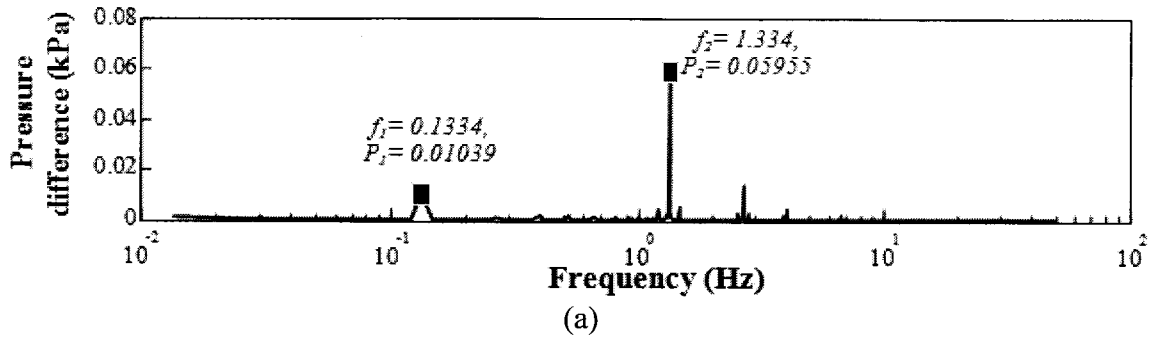


Figure 3.51: (a) Spectrum of the inlet pressure difference (b) Time history of the beam tip deflection (c) Spectrum of the beam tip deflection (N= 8 RPM)

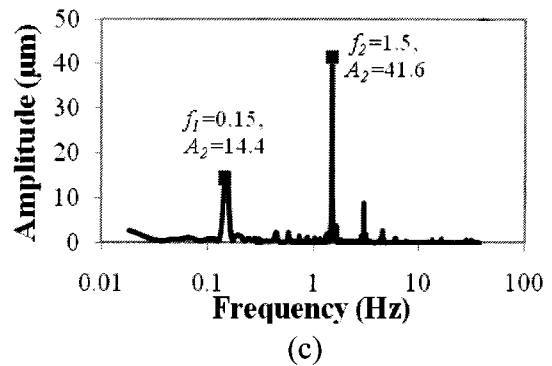
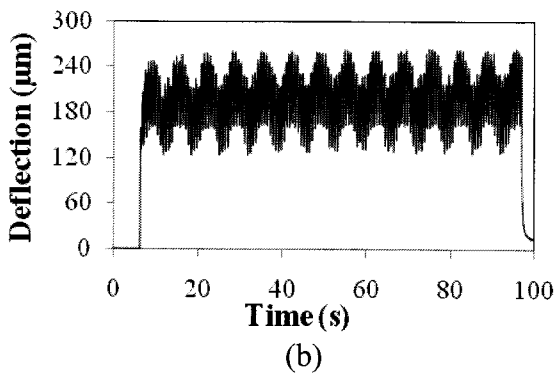
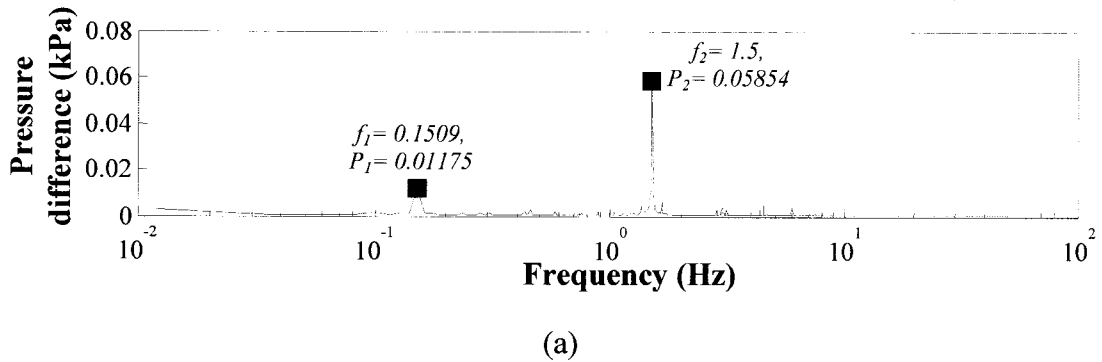


Figure 3.52: (a) Spectrum of the inlet pressure difference (b) Time history of the beam tip deflection (c) Spectrum of the beam tip deflection (N= 9 RPM)

Figure 3.53 illustrates the change of rms of inlet pressure difference and deflection with respect to pump RPM where the rms of pressure difference and deflection shows a linear relation with pump speed.

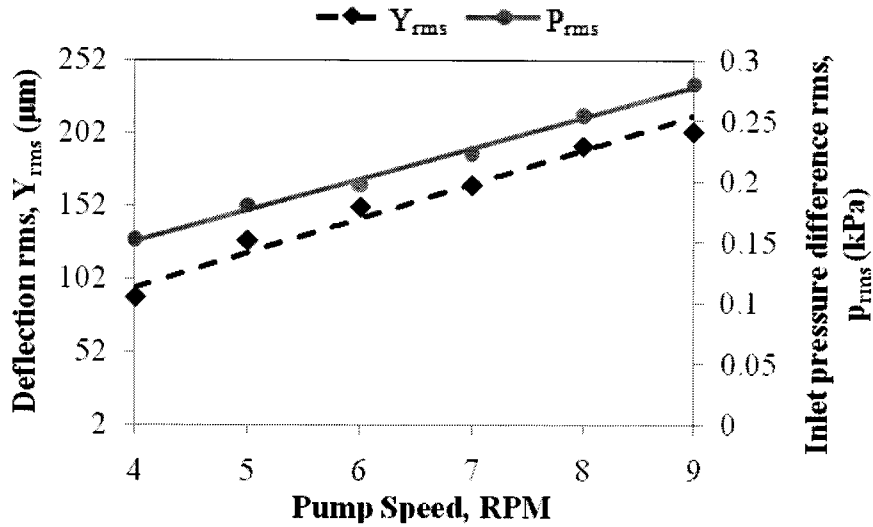


Figure 3.53: Variation of rms of deflection and inlet pressure difference with respect to pump speed

The Figure 3.54 illustrates the deflection amplitudes and amplitudes of inlet pressure variation of with respect to the pump speed where it was found for both deflection and pressure difference that the rate of increment of amplitude decreases at high RPM of pump speed. In Figure 3.54 (b) it was found that the second amplitude of deflection and inlet pressure difference increases initially and then follows with lower rate of increment. Furthermore, the Figure 3.52 and 3.54 shows that the output deflection amplitudes and rms follows the input pressure difference amplitudes and rms.

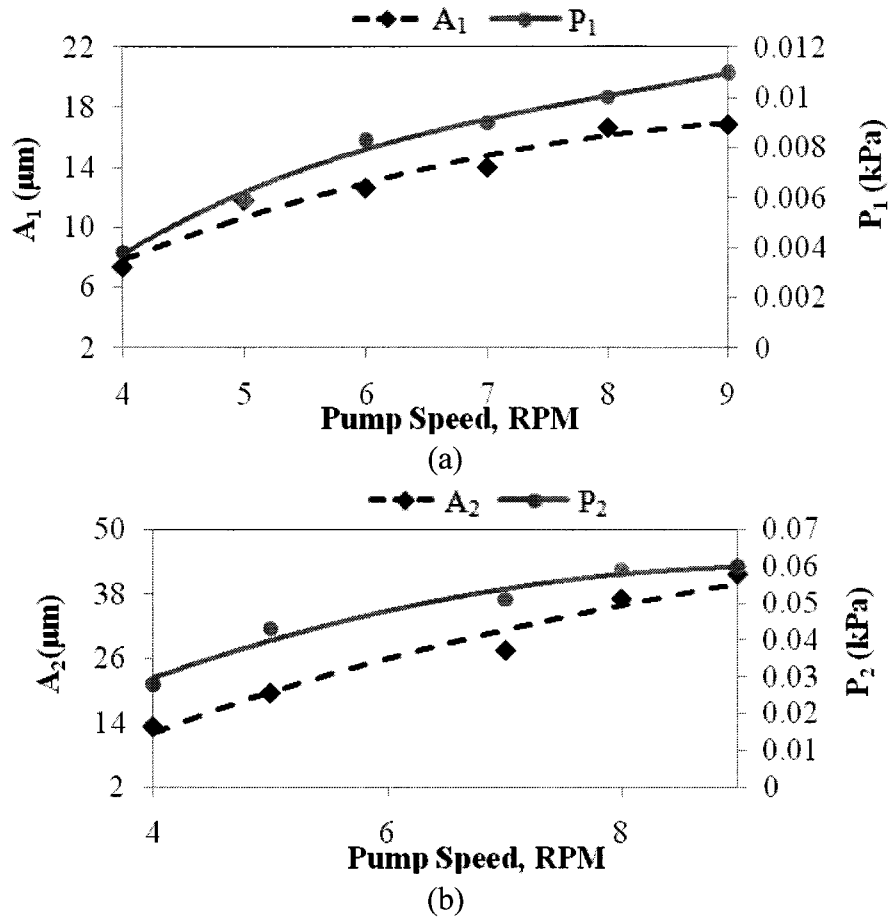


Figure 3.54: (a) Variation of first amplitude of deflection and inlet pressure difference with respect to pump speed (b) Variation of second amplitude of deflection and inlet pressure difference with respect to pump speed

3.7 Comparison and Discussion

The Figure 3.55 illustrates linear relation between the rms of deflection and rms of inlet pressure difference for four test conditions. Hence, this figure indicates the variation of rms of deflection against rms of pressure loading for different chips and flow conditions. However, the Table 3.4 presents the detailed configuration of 4 test conditions presented in Figure 3.55. Different pressure loadings were achieved by changing the pump speeds. The experiments were conducted at the speeds of 4 to 9 RPM for the 4 different test conditions. The rms of deflection increases linearly with rms of

pressure loading and it is strongly dependent on the inlet conditions and geometry. The Figure 3.55 also shows that it is possible to change the loading across the cantilever through speed and fluid flow parameters.

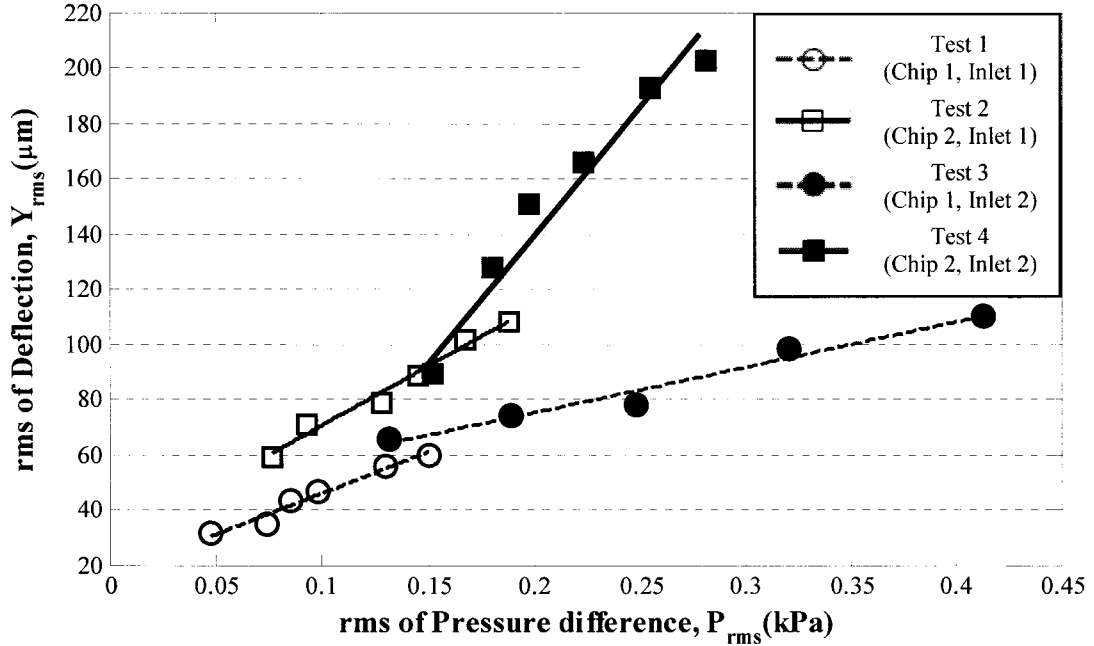


Figure 3.55: Variation of rms of deflection with respect to rms of inlet pressure difference for four different test conditions

Table 3.4: The detail configurations of four test conditions presented in Figure 3.55

Inlet configuration		Chip 1: Hydraulic diameter = 3.2 mm	Chip 2: Hydraulic diameter = 2.1 mm
Inlet 1, low flow condition	Low flow condition Medium diameter tube 1 inner diameter = 2.1 mm Small diameter tube 2 inner diameter = 1.2 mm	Test 1	Test 2
Inlet 2, high flow condition	High flow condition Large diameter tube 1 inner diameter = 3.2mm Medium diameter tube 2 inner diameter = 2.1mm	Test 3	Test 4

The Figures 3.56 and 3.57 show the test results on the effect of harmonic pressure loading at frequencies ω_1 and ω_2 for low flow conditions. Deflection magnitudes are

attributed with respect to inlet pressure difference magnitudes at two different frequencies ω_1 and ω_2 respectively. These figures show that, the deflections magnitudes are comparatively higher for chip 2 than chip 1, which is due to the increased viscous loading in chip-2 due to the modified flow channel geometry. The chip 2 with reduced flow area around the cantilever resulted in higher-pressure loading compare to chip 1 with higher flow cross-sectional area. As a result, the deflection was higher for chip 2. The overall variation of A_1 and A_2 for four different test conditions is presented in Figure 3.58.

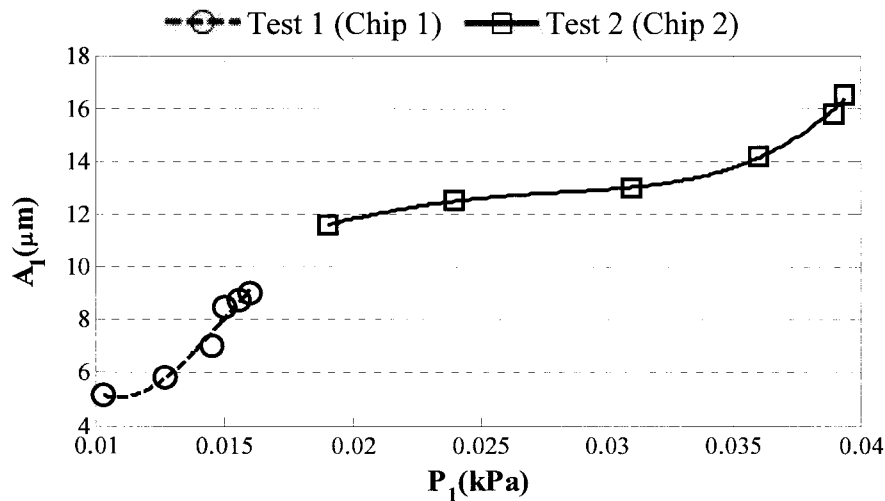


Figure 3.56: Variation of deflection magnitude A_1 with respect of pressure magnitude P_1 for low flow condition

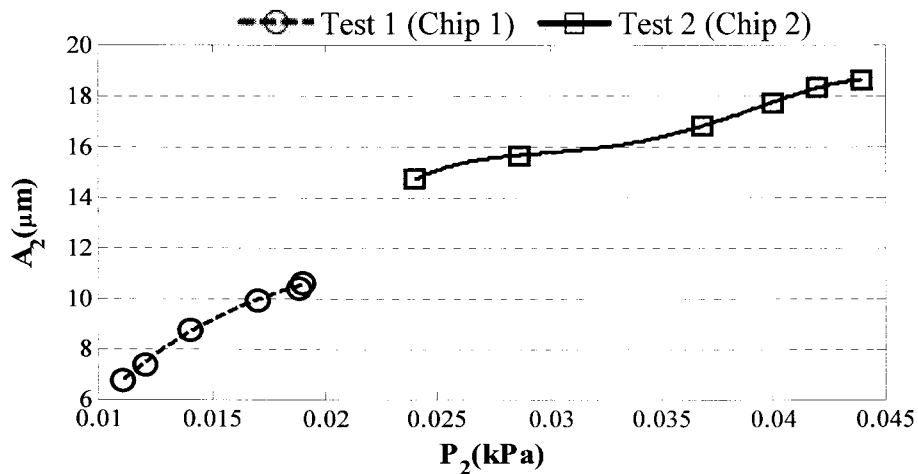


Figure 3.57: Variation of deflection magnitude A_2 with respect of pressure magnitude P_2 for low flow condition

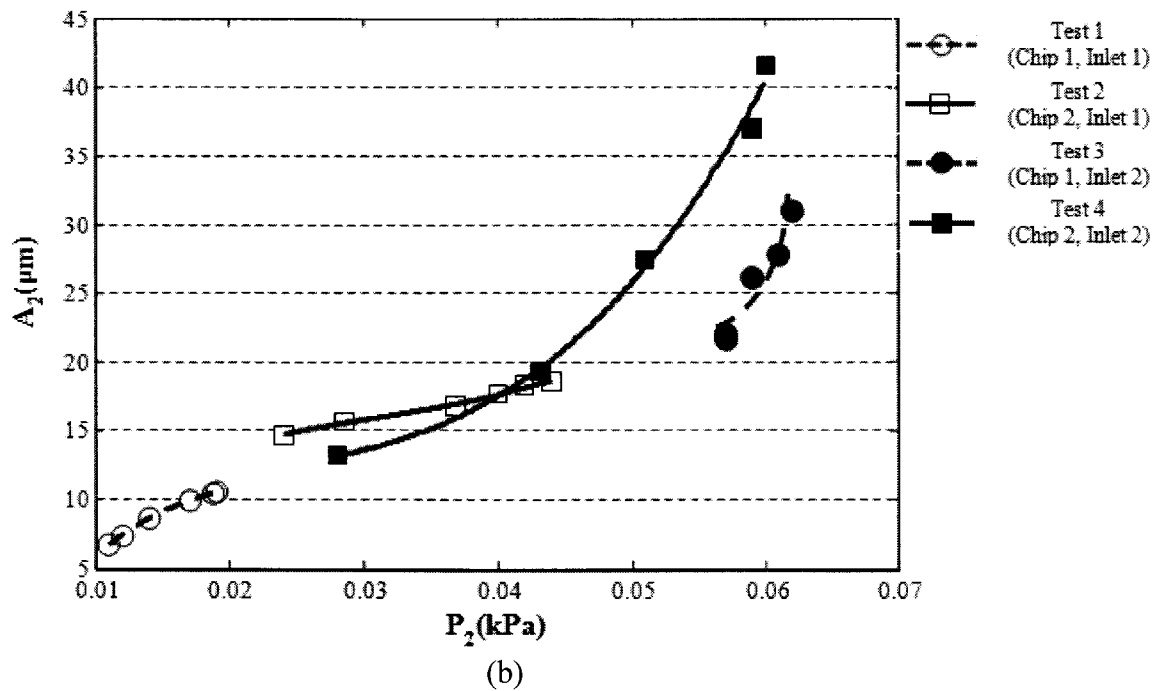
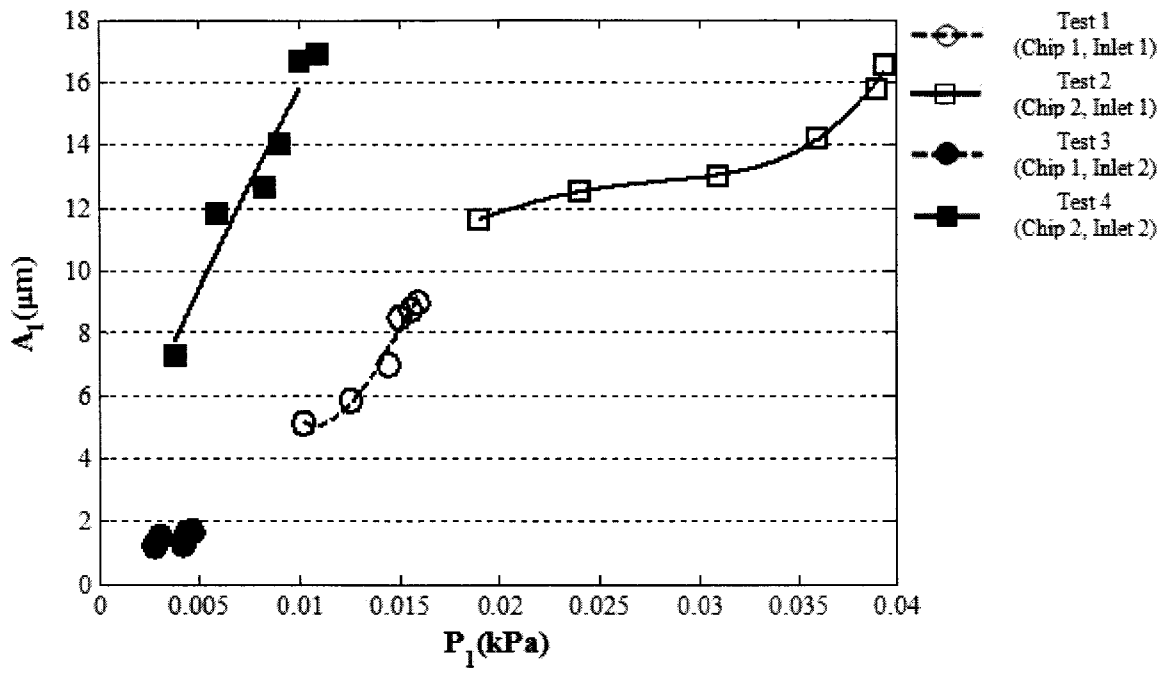


Figure 3.58: (a)The overall variation of A_1 for four different test conditions, (b)The overall variation of A_2 for four different test conditions

3.8 Summary

In the current Chapter, an experimental setup was designed to characterize the dynamic response of microcantilever that was integrated with in the microfluidic chip. A new image post processing method named DVIP method was developed to estimate the deflection of cantilever subjected to fluid forces. The pump supplied the complex harmonic flow with two components of frequencies. However, the spectrum of deflection also shows the existence of these two excitation frequencies. On comparison, it was found at that, DVIP method provided more reliable results than other optical instrument such as LDV. The cantilever response was also characterized with respect to different speeds of pump as well as different pressure difference and flows conditions. The flows and pressures were estimated by using pressure sensors. The current chapter explored experimentally the effects of hydraulic diameter of microfluidic channel on cantilever responses.

Recently, Finite Element Modeling shows satisfactory result in case of microfluid-microstructure interaction [32, 37, 49, and 50]. Therefore, a finite element model has been developed in the subsequent chapter and few results from the current chapter are used to validate that model. Furthermore, the model is used to find the effect of viscous damping over the response of the cantilever.

Finite Element Modeling and Validation

4.1 Introduction of Finite Element Method

The Finite Element Method (FEM) is a numerical technique that provides approximate solutions to differential equations that model problems arising in physics and engineering [62]. In finite element modeling, the domain of interest is subdivided into a finite number of smaller areas or zones called elements. The division of the domain of interest into a number of elements is called meshing. Due to the versatility of the Finite Element Method in handling geometrically arbitrary domains and the availability of sophisticated commercial Finite Element software, this method has become a preferred method for solving engineering problems [63]. Finite Element Analysis (FEA) plays a great role in characterizing the performance behavior of many MEMS devices, particularly those operating in a fluid environment due to its multidisciplinary nature. Some examples include AFM cantilevers [49, 50, and 64], micro-switches and actuators [1], bio-chemical sensors [10], micro viscosity meter [12], micro valves [9], MEMS based anemometer [5] and etc. The COMSOL Multiphysics software, based on Finite Element Analysis, was used to solve the present problem involving fluid-structure interaction. The main objective is to build a fluid-structure interaction model to carry out Finite Element Analysis and validate the results with experimental results. In addition, Finite Element Analysis was carried out to characterize the quality factor of microcantilevers under fluids having different viscosities. In finite element modeling, the following three different application modes of COMSOL were used;

- I. Microfluidics Mode (Incompressible Navier Stokes transient analysis)
- II. Structural Mechanics Mode
- III. Moving mesh (Moving mesh with transient analysis) Mode

4.1.1 Microfluidics Mode

The 2D fluid flow in the channel is described by the Navier-Stokes equations for incompressible flow and transient analysis to solve the velocity field or vector $\vec{u} = (u, v)$, where, u and v are the velocity of fluid in x and y axis direction and the pressure, p in the special (deformed) moving coordinate system [65-67]. The Navier-Stokes equations are represented as;

$$\rho \frac{\partial \vec{u}}{\partial t} - \nabla \cdot \left[-pI + \eta (\nabla \vec{u} + (\nabla \vec{u})^T) \right] + \rho ((\vec{u} - \vec{u}_m) \cdot \nabla) \mathbf{u} = F \quad (4.1)$$

$$-\nabla \cdot \vec{u} = 0 \quad (4.2)$$

Where, I is the unit diagonal matrix, and F is the volume force affecting the fluid, η is the dynamic viscosity of fluid, ρ is the density of fluid and the coordinate system velocity is defined as $\vec{u}_m = (u_m, v_m)$. It was assumed that no gravitation or other volume forces affecting the fluid, with $F = 0$. At the channel entrance, the flow is fully developed laminar with a parabolic velocity profile with its amplitude changing with time.

4.1.2 Structural Mechanics Mode

The structural deformations are solved using an elastic formulation and a nonlinear geometry formulation to cater for large deformations. For boundary conditions,

the cantilever beam is fixed at the one end. The beam is subjected to the load from the fluid, as given by [65-67]:

$$F_T = -n \bullet \left[-pI + \eta (\nabla \bar{u} + (\nabla \bar{u})^T) \right]$$

Where, n is the normal vector to the boundary. This load represents the sum of pressure forces and viscous forces.

4.1.3 Moving Mesh or Morphing Mesh

When the structure deforms due to fluid load the fluid and structure domains, need to be remeshed. The deformed mesh is modeled using Winslow smoothing. The boundary conditions control the displacement of the moving mesh with respect to the initial geometry [65-67]. Therefore, at cantilever boundary, the displacement is the same as the structural deformation and at the exterior boundary of flow path, the deformation is set as zero.

4.2 Model Geometry

The primary objective is to build a fluid-solid interaction model and validate the results with experimental results. Therefore, the geometry considered is that of the experimental specimen that was described in Chapter 2. The specimen with a hydraulic diameter of 2.1 mm is considered for finite element modeling which is illustrated in Figure 4.1. However, the dashed area indicated in Figure 4.1 is used for actual finite element modeling.

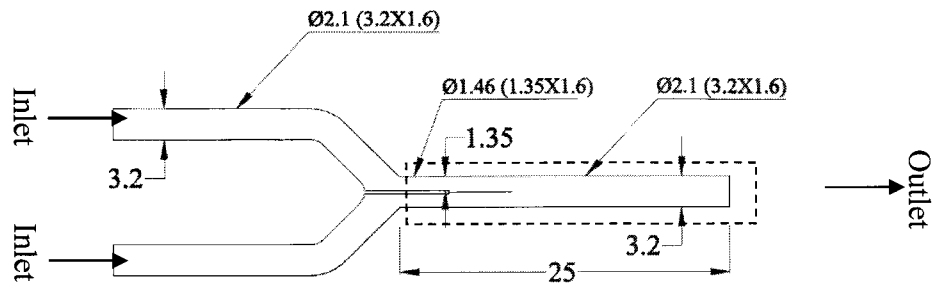


Figure 4.1: The subjected geometry for Finite Element Modeling is represented in dashed area where all dimensions are presented in mm. Hydraulic diameter is denoted by Ø and cross-section in different section is indicated inside the parentheses

In Figure 4.1 the input and output channels are rectangle in cross-section (width 3.2 mm \times depth 1.6 mm) with hydraulic diameter of 2.1 mm. The geometrical parameters of the cantilever are also considered from experimental specimen, where the cantilever was 7.05 mm long, 1.1 mm wide and 28 μm thick. However, the Young's modulus of elasticity of the cantilever was considered from the property of supplied PVDF film in the test specimen, which was 3.5 GPa. The geometry or domain is divided in to two areas or sub-domains, namely Sub-domain 1, and Sub-domain 2. The sub-domains are defined in the following way,

- Sub-domain 1 is active in Micro fluidics Mode but Sub-domain 2 is inactive in this mode
- Sub-domain 2 is active in Structural mechanics mode but Sub-domain 1 is inactive in this mode
- Both Sub-domains 1 and 2 are active in Moving mesh mode

The Sub-domain division is presented in Figure 4.2.

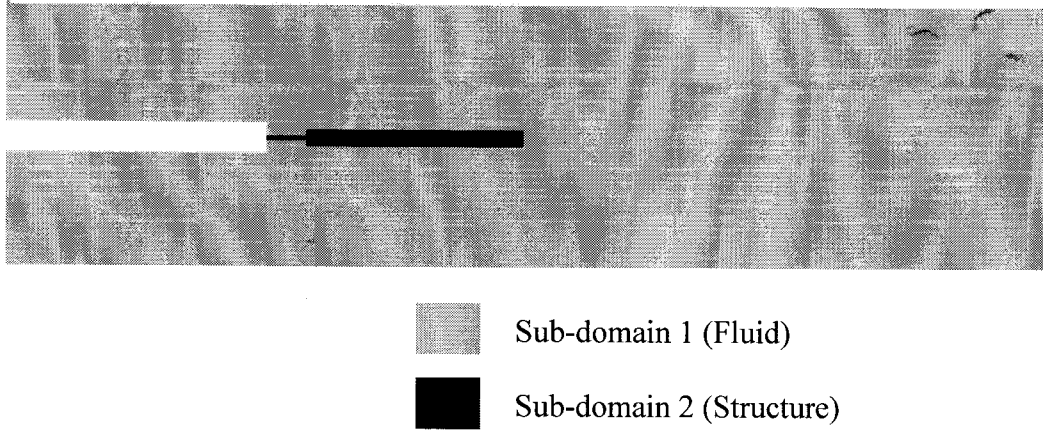


Figure 4.2: Sub-domain division

Sub-domain Settings:

Microfluidics Mode (Sub-domain 1): Since, Fluid-Xp was the supplied fluid during the experiment as described in Section 3.5.3 of Chapter 3, therefore the sub domain property such as density and viscosity were considered same as that of Fluid XP. In Sub-domain 1 of Microfluidics mode, density of Fluid-Xp was set 1029 kg/m^3 and viscosity was set $4.5 \times 10^{-3} \text{ Pa.s}$ according to the supplied Material Safety Data Sheet. However the channel depth was set as 1.6 mm as followed by the test specimen.

Structural Mechanics Mode (Sub-domain 2): The Young's modulus of elasticity of the cantilever was set as 3.5 GPa and density of the material was considered as 1780 kg/m^3 according to the property of supplied PVDF film which was used as cantilever in the test specimen.

Moving Mesh (Moving mesh with transient analysis) Mode: Sub-domain 1 was considered as free displacement and for Sub-domain 2 the displacement of the mesh in x and y directions were provided by the structural displacement.

4.2.1 Geometry Meshing

The complete geometry (approximate total area = 80 mm²) was divided into 3167 number of elements. However, the area of fluid-solid interaction is divided into fine meshes while the other area is divided into coarse meshes. The cantilever sub-domain contains 1176 number of elements and, the fluid sub-domain contains 1991 number of elements. The overall meshing is represented in Figure 4.3.

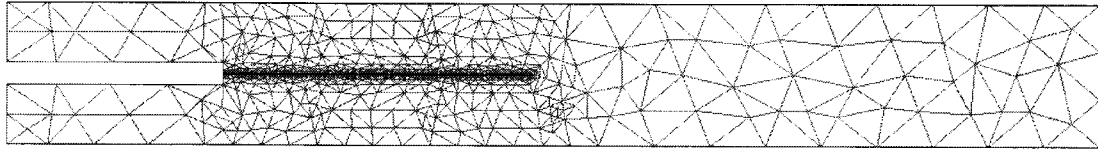


Figure 4.3: The overall meshing

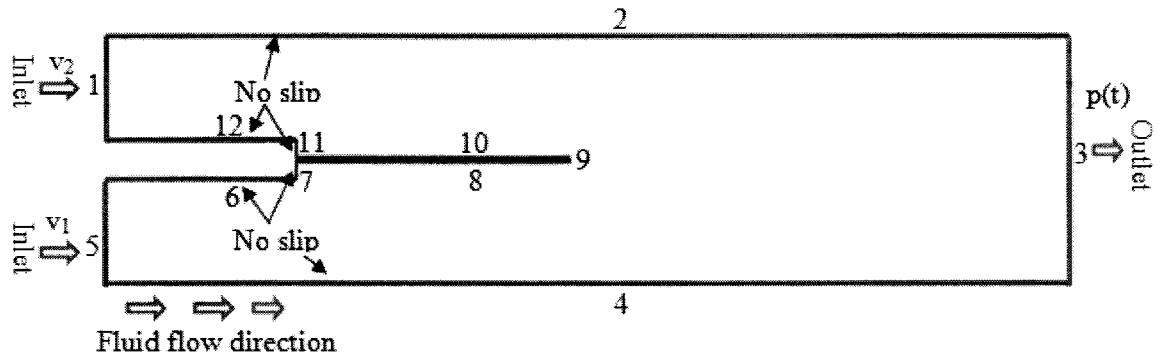
Table 4.1: Overall Mesh Statistics

Number of degrees of freedom	31117
Number of mesh points	1624
Number of elements	3167
Triangular	3167
Quadrilateral	0
Number of boundary elements	667
Number of vertex elements	12
Minimum element quality	0.2599
Element area ratio	7.15E-5

4.2.2 Boundary Conditions

Boundary Conditions for Microfluidics Mode: The boundary conditions for Microfluidics mode are presented in Figure 4.4. The inlet velocities v_1 , v_2 , and the outlet static pressure p that are function of time t are given as boundary conditions. The values are same as that of measured during experiments. The boundary conditions (value of v_1 , v_2 , and p) for Microfluidics mode at different pump speeds are presented in Section 4.3 of

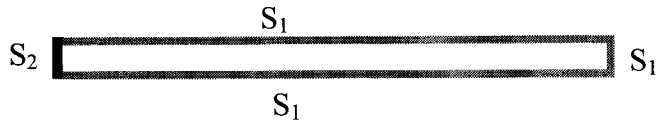
this Chapter. However, No slip condition is assumed for the wall boundaries of the microfluidic channel.



Boundary No.	Boundary Conditions
1	X direction velocity of flow = $v_1(t)$ Y direction velocity of flow = 0
5	X direction velocity of flow = $v_2(t)$ Y direction velocity of flow = 0
8,9,10	X direction velocity of flow = X direction velocity of cantilever Y direction velocity of flow = Y direction velocity of cantilever
3	Pressure = $p(t)$
2,4,6,7,11,12	No slip

Figure 4.4: The boundary conditions for fluid mode

Boundary Conditions for Structure Mode: In the structural mechanics mode, the boundary conditions of cantilever are only activated, while others boundaries are deactivated as those boundaries are related to Microfluidics mode. The boundary conditions for cantilever zone are presented in Figure 4.5. However, in this mode the structural mechanics boundary conditions, the pressure and viscous forces are imported from Microfluidics mode.

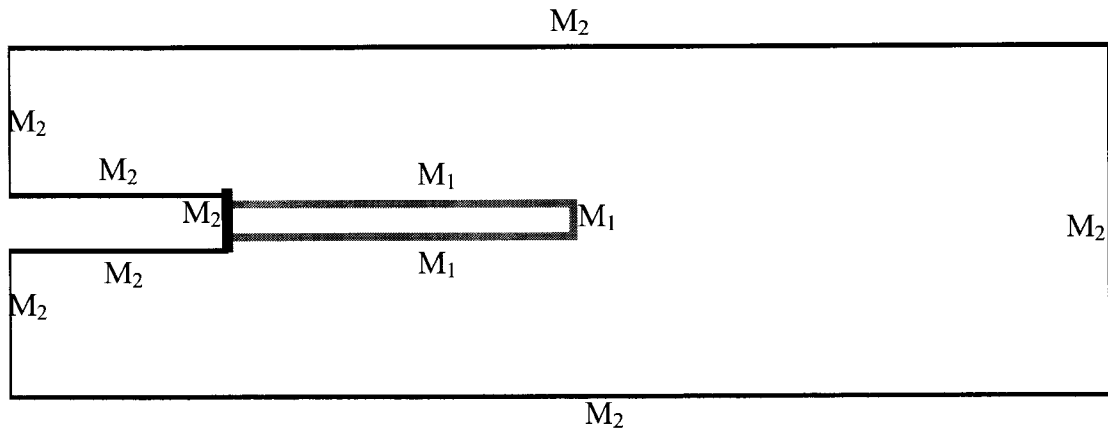


Boundaries	Boundary Conditions
S ₁	Edge load along x direction $F_x =$ Viscous and Pressure force in x direction Edge load along y direction $F_y =$ Viscous and Pressure force in y direction
S ₂	Fixed condition: Displacement in x direction, $R_x = 0$ Displacement in y direction, $R_y = 0$

Figure 4.5: Boundary condition for structural mechanics mode

Boundary Condition for Moving Mesh (Moving mesh with transient analysis)

Mode: The boundary conditions for Moving mesh Mode are presented in Figure 4.6.



Boundaries	Boundary Conditions
M ₁	Mesh displacement in X direction = cantilever displacement X direction Mesh displacement in Y direction = cantilever displacement Y direction
M ₂	Mesh displacement in X direction = 0 Mesh displacement in Y direction = 0

Figure 4.6: Boundary conditions for moving mesh mode

4.3 Boundary Conditions from Testing Conditions for Pulsed Flows

The fluid inlet velocities v_1 and v_2 , and outlet pressure p are duplicated from the test conditions that correspond to test condition 2 where the flow was supplied by the peristaltic pump at low flow condition in the 2.1 mm hydraulic diameter of specimen (Section 3.5.2 of Chapter 3). The flow rate was estimated in testing using the pressure drop across certain tube length and by using Equation 3.2. The inlet velocity for the considered sub-domain was estimated using the actual flow rate and area of cross-section ($1.35 \times 1.6 \text{ mm}^2$) of the channel while the outlet pressure was measured using pressure sensor at the outlet. In order to carry out the simulation with the tested conditions, experimental value of v_1 , v_2 and p are transformed into the spectral components using following equations:

$$v_1(t) = v_{avg1}(t_o) + v_{a1} \sin \omega_1 t + v_{b1} \sin \omega_2 t \quad (4.3)$$

$$v_2(t) = v_{avg2}(t_o) + v_{a2} \sin \omega_1 t + v_{b2} \sin \omega_2 t \quad (4.4)$$

$$p(t) = p_{avg}(t_o) + p_a \sin \omega_1 t + p_b \sin \omega_2 t \quad (4.5)$$

However, the spectral components in the above equation were obtained by performing the Fourier transform of the measured data from the experiments. The time interval of $0 \leq t_o < 0.43$ is the time required to develop the average values v_{avg1} and v_{avg2} and p_{avg} . In this interval the average inlet flows or outlet pressure is linear with the time. However, the total simulation time is considered as 60.49215s with a time step of 0.0134427s which, corresponds to frame capturing rate (74.38 frames/seconds) of video

camera used during the test. Hence the remaining time t after $t_0=0.42s$ was defined as $0.43 \leq t \leq 60.49215$. After substituting the spectral component of the experimental inlet velocities and outlet pressure, such as amplitudes of inlet velocities and outlet pressure and the average of inlet flow velocities and outlet pressure in to the Equations (4.3), (4.4), (4.5) the estimated boundary conditions for different RPM of pump speeds are presented in Figure 4.7 to 4.11. However, the section (a) of those figures represent the inlet boundary conditions such as inlet velocities v_1 and v_2 and the section (b) of those figures represents the outlet boundary condition which is outlet pressure p .

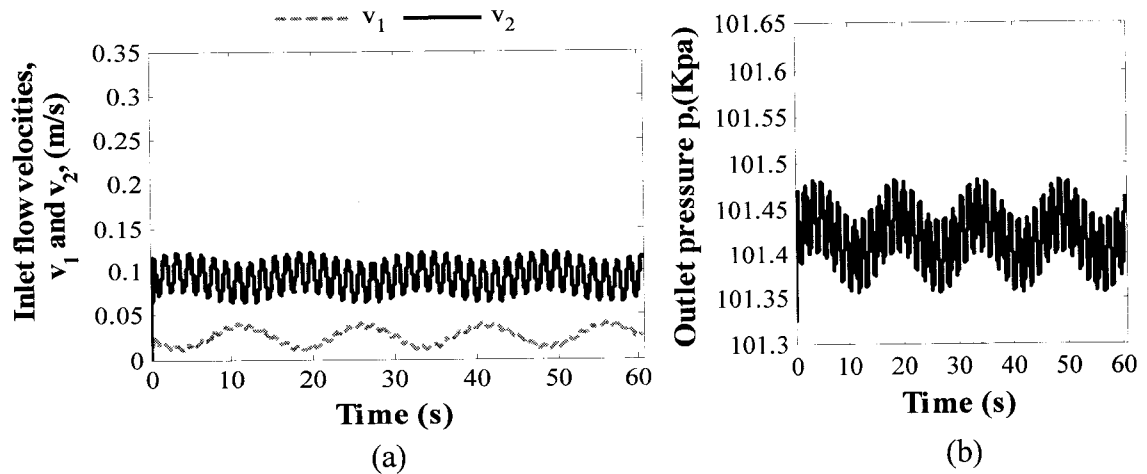


Figure 4.7: Boundary conditions for the pump speed of 4 RPM: (a) Time history of inlet flow velocities (b) Time history of outlet pressure representing

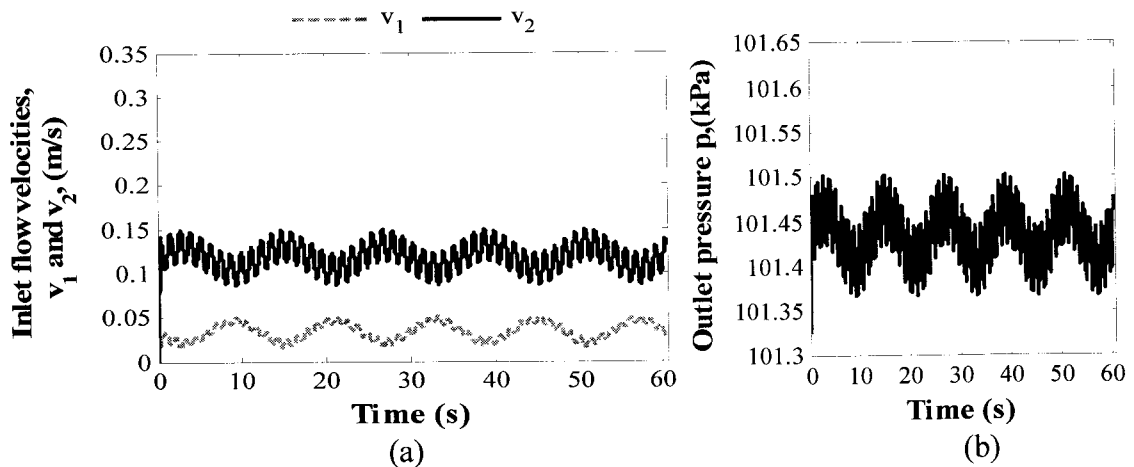


Figure 4.8: Boundary conditions for the pump speed of 5 RPM: (a) Time history of inlet flow velocities (b) Time history of outlet pressure representing

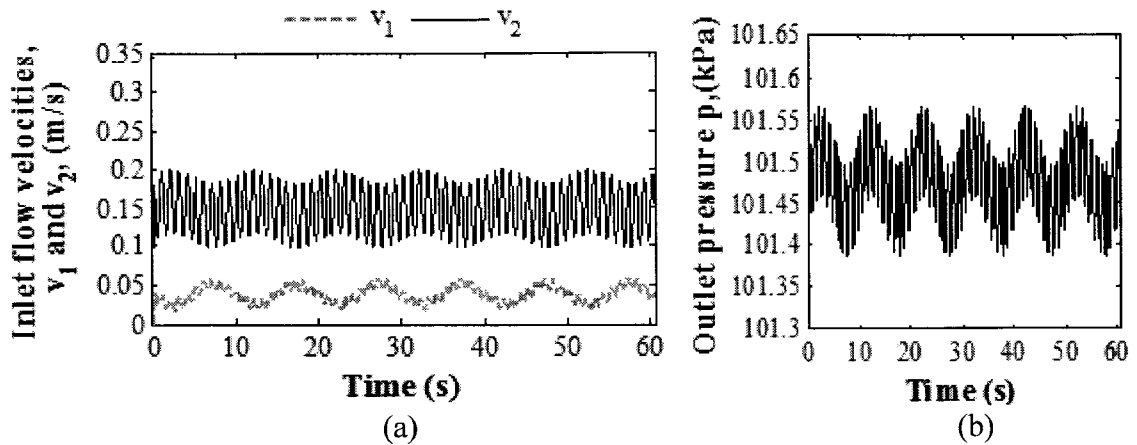


Figure 4.9: Boundary conditions for the pump speed of 6 RPM: (a) Time history of inlet flow velocities (b) Time history of outlet pressure representing

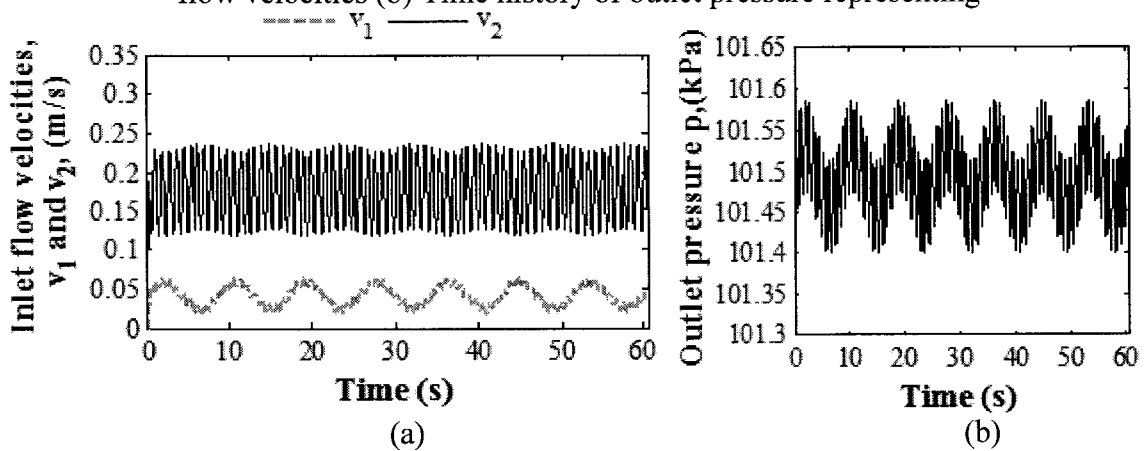


Figure 4.10: Boundary conditions for the pump speed of 7 RPM: (a) Time history of inlet flow velocities (b) Time history of outlet pressure representing

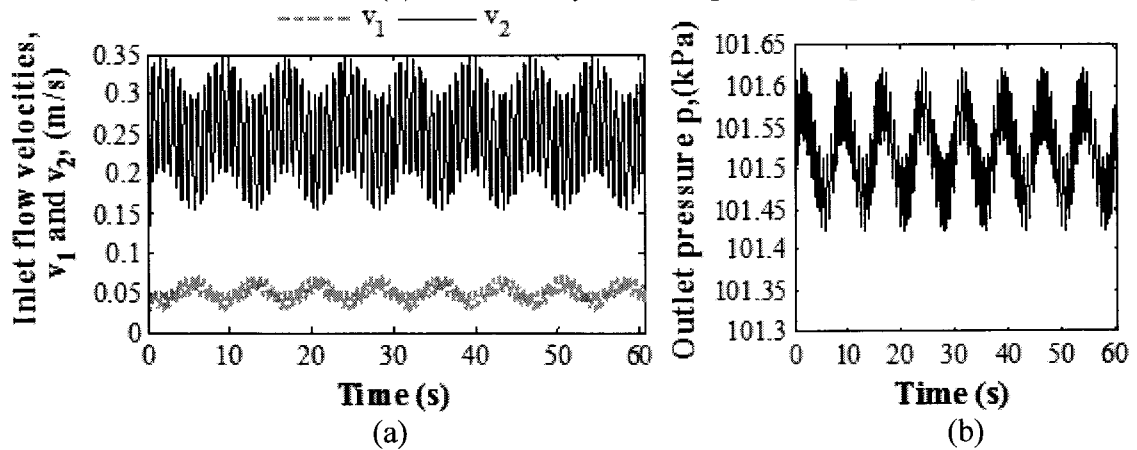


Figure 4.11: Boundary conditions for the pump speed of 8 RPM: (a) Time history of inlet flow velocities (b) Time history of outlet pressure representing

4.4 Result Validation for Pulsed Flows

The most prominent way to validate finite element results is to compare the cantilever tip deflection or response with experimental results. Comparison between Finite Element Modeling results and testing results are presented in Figures 4.12, 4.13, 4.14, 4.15, 4.16 for the pump speeds of 4, 5, 6, 7 and 8 RPM, respectively.

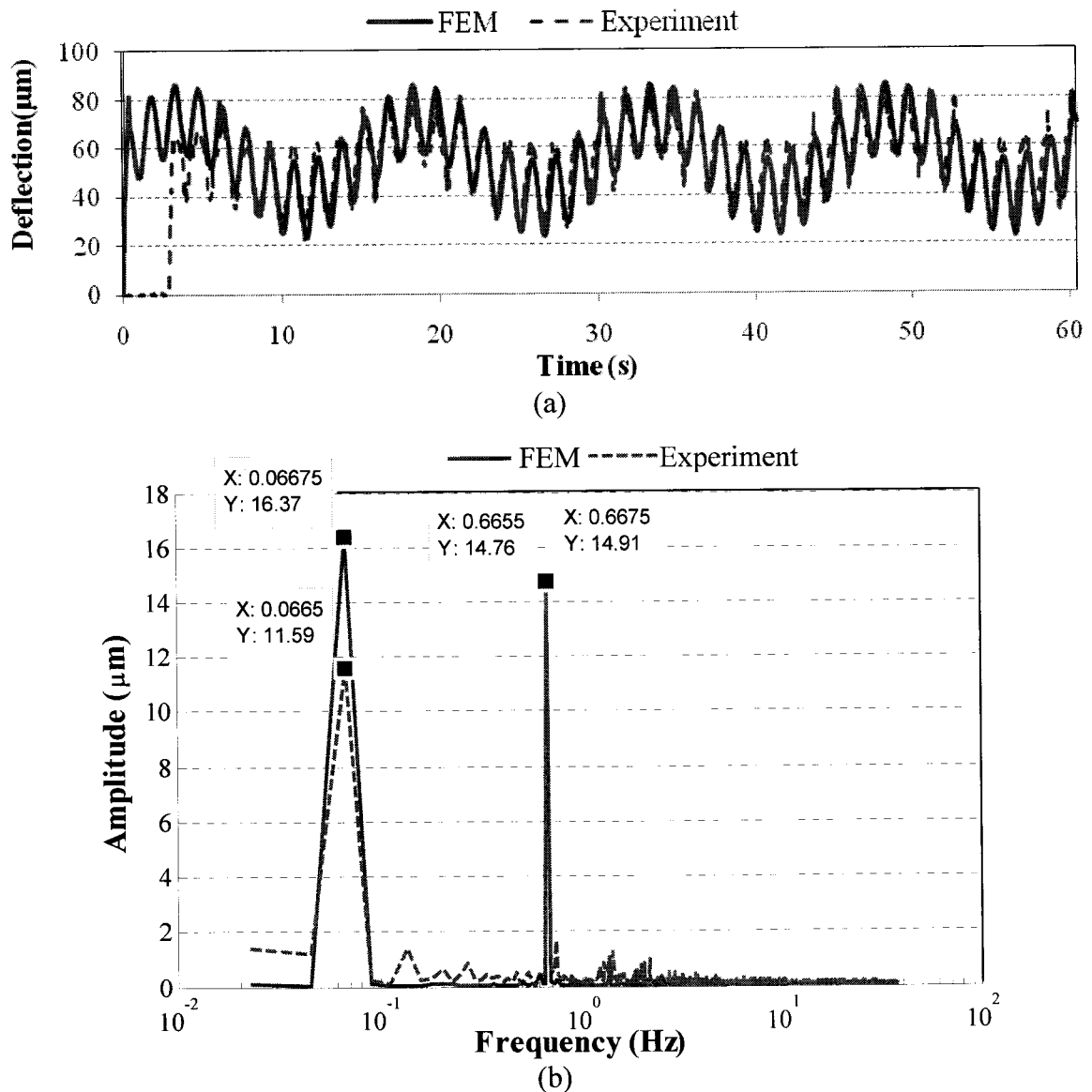
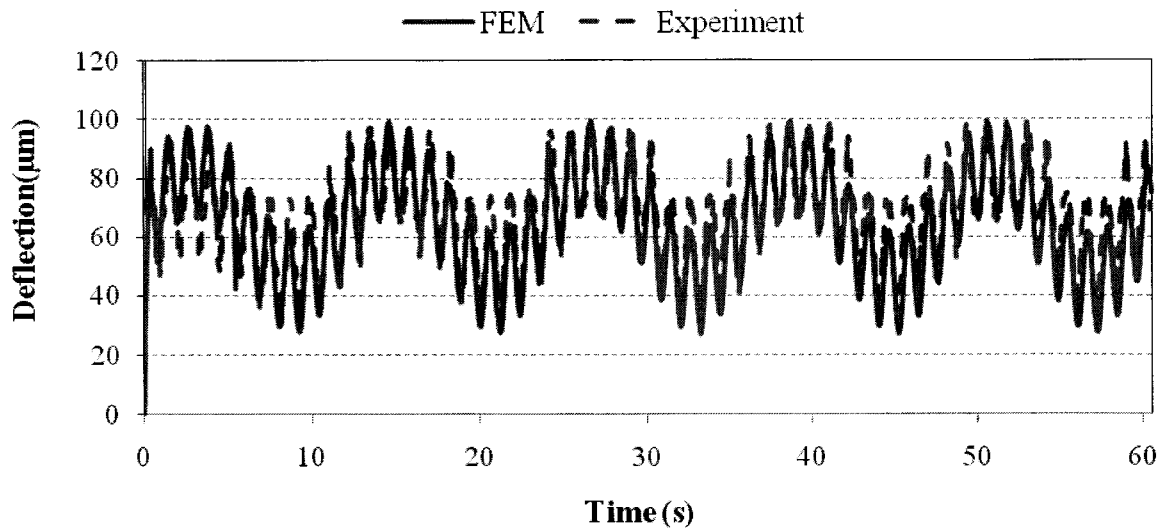
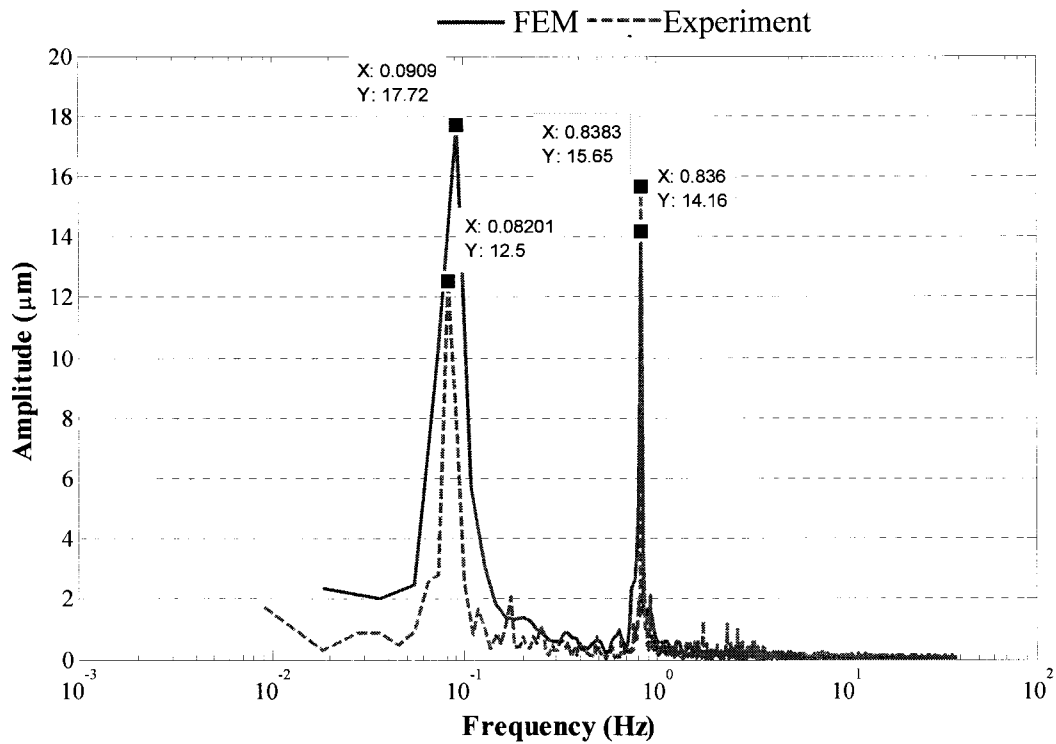


Figure 4.12: Comparison between Finite Element Modeling and Experimental results for the pump speed of 4 RPM: (a) Time history of beam tip deflection (b) Spectrum of the beam tip deflection

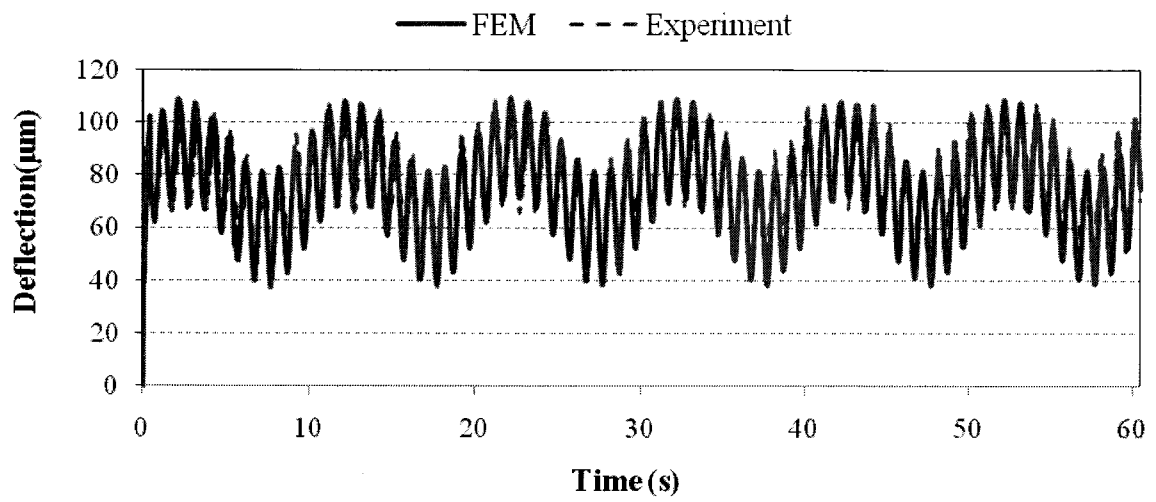


(a)

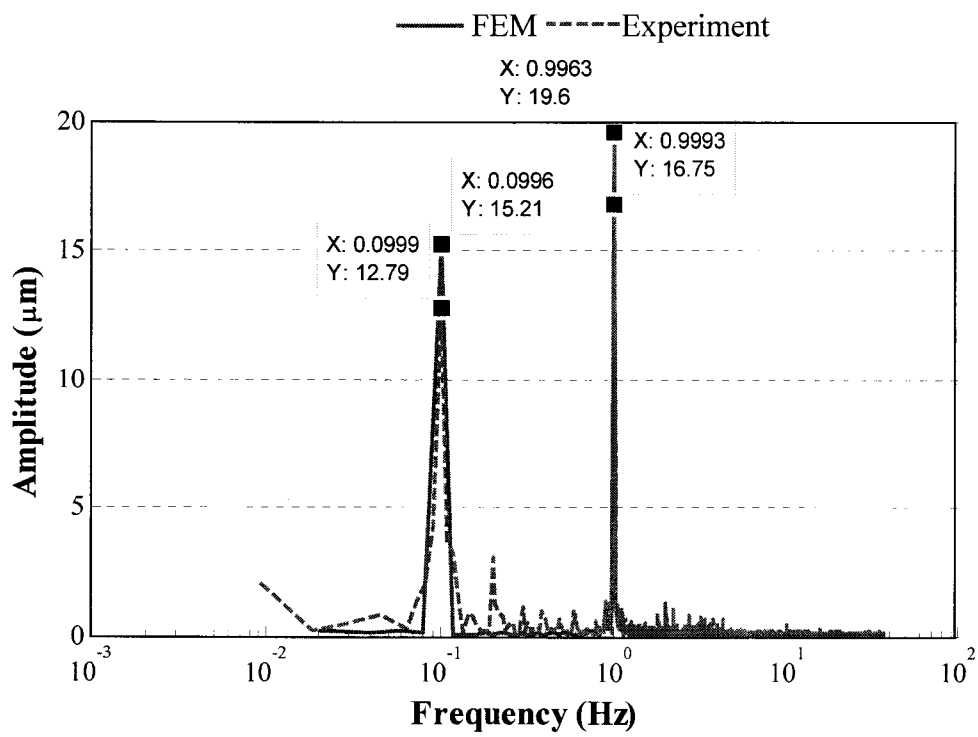


(b)

Figure 4.13: Comparison between Finite Element Modeling and Experimental results for the pump speed of 5 RPM: (a) Time history of beam tip deflection (b) Spectrum of the beam tip deflection

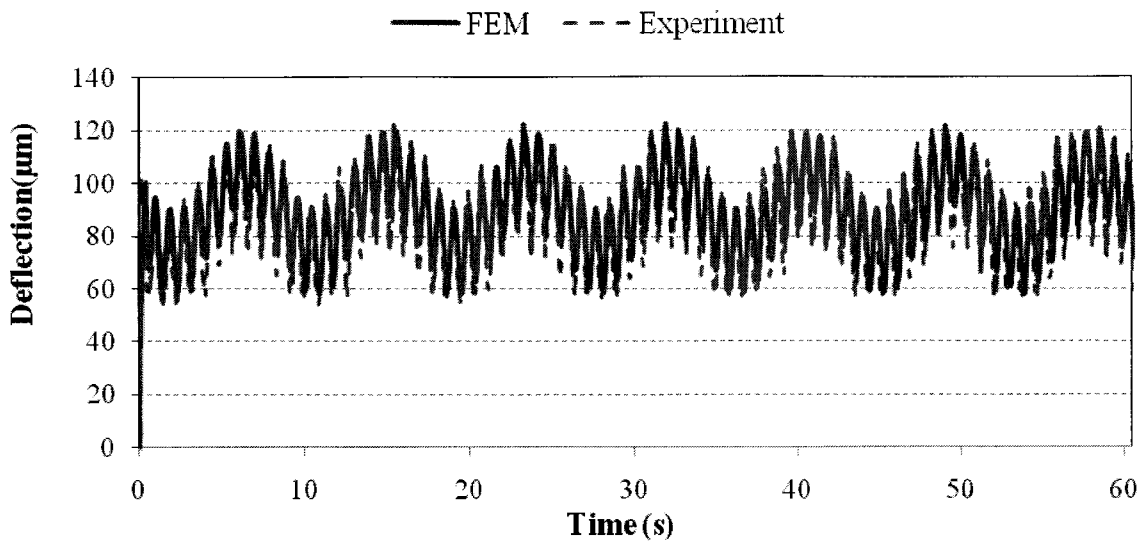


(a)

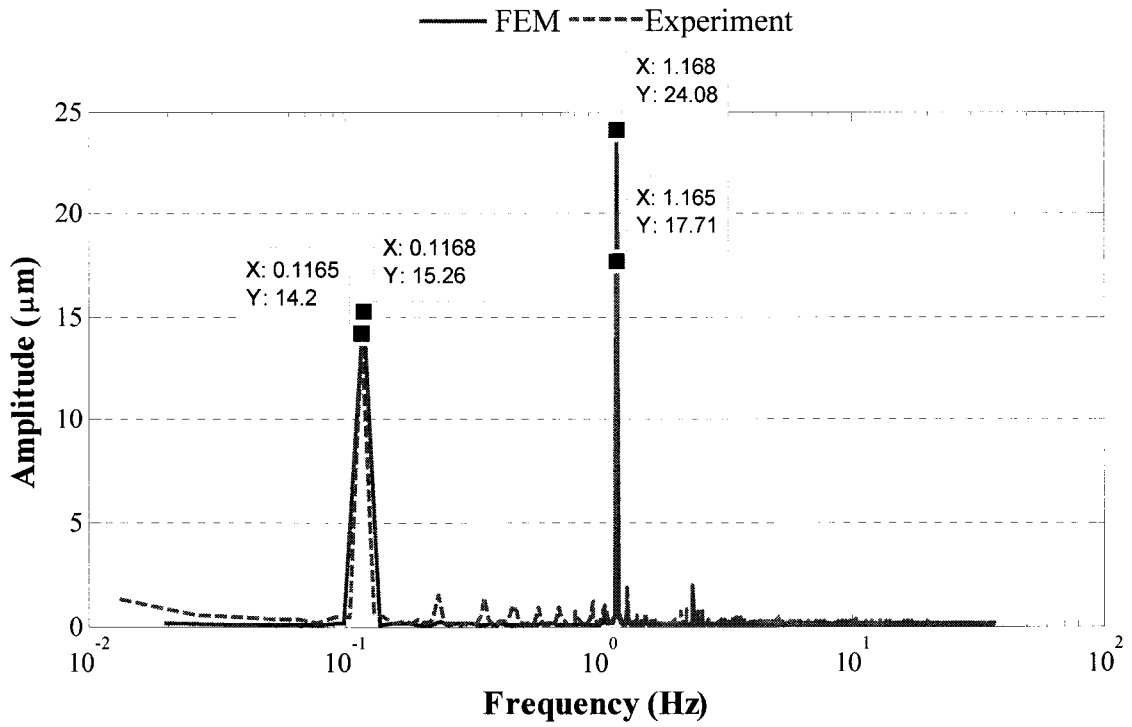


(b)

Figure 4.14: Comparison between Finite Element Modeling and Experimental results for the pump speed of 6 RPM: (a) Time history of beam tip deflection (b) Spectrum of the beam tip deflection

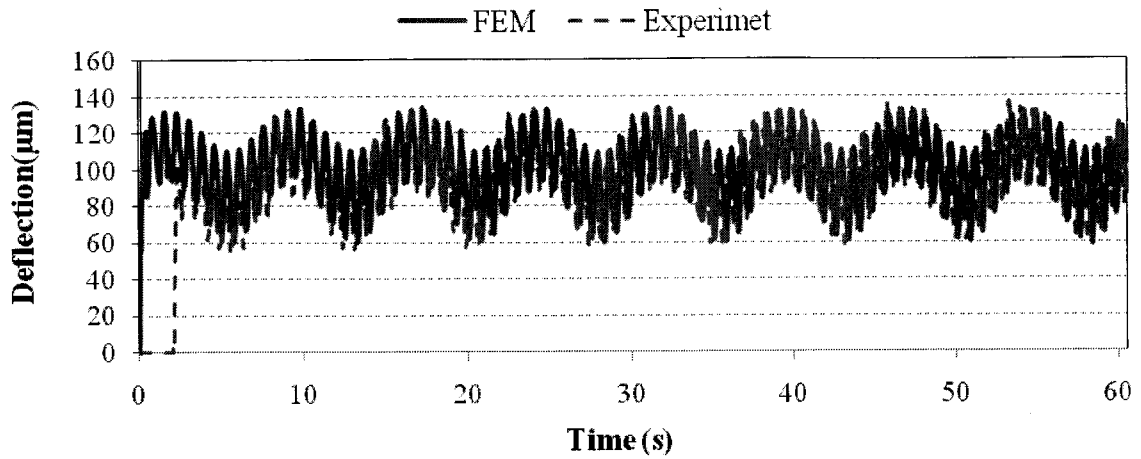


(a)

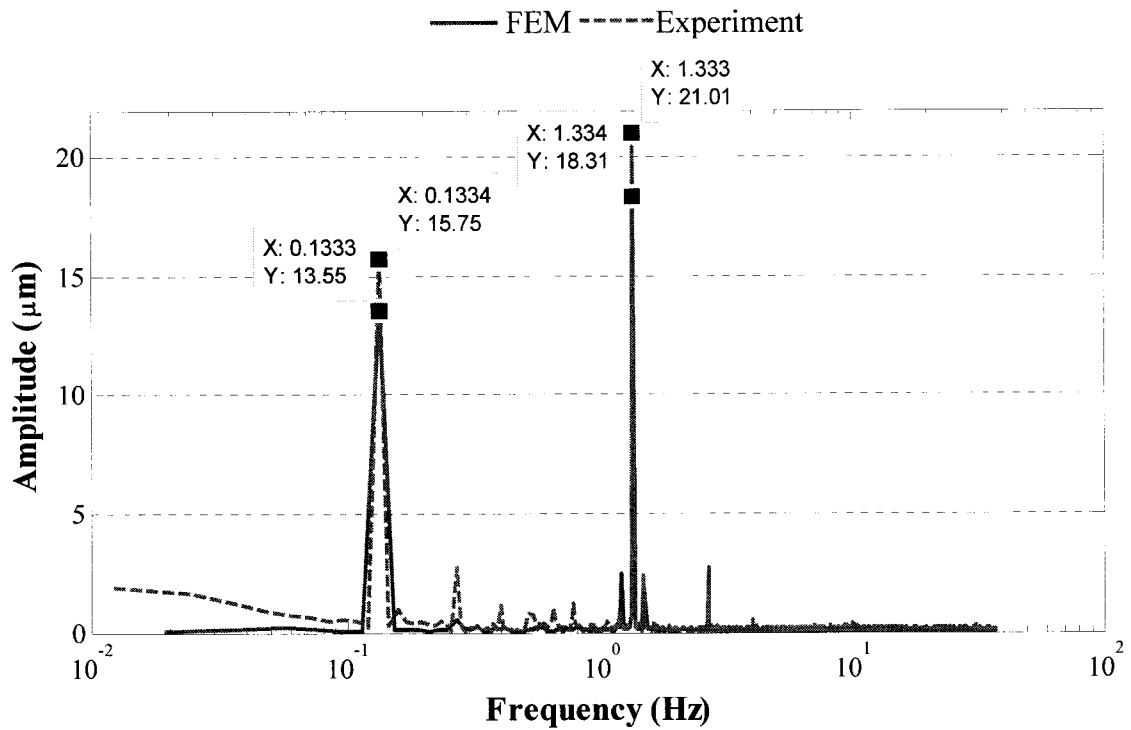


(b)

Figure 4.15: Comparison between Finite Element Modeling and Experimental results for the pump speed of 7 RPM: (a) Time history of beam tip deflection (b) Spectrum of the beam tip deflection



(a)



(b)

Figure 4.16: Comparison between Finite Element Modeling and Experimental results for the pump speed of 8 RPM: (a) Time history of beam tip deflection (b) Spectrum of the beam tip deflection

4.4.1 Results and Discussion

The new DVIP method was successful in capturing the dynamic behavior of cantilever subjected fluid interaction. Comparison between the results of FEM and DVIP method shows good agreement. The comparison of rms values of steady and monotonic

deflections and amplitudes between experiments and finite element modeling is presented in Figure 4.17, which indicates similar trend and agreement.

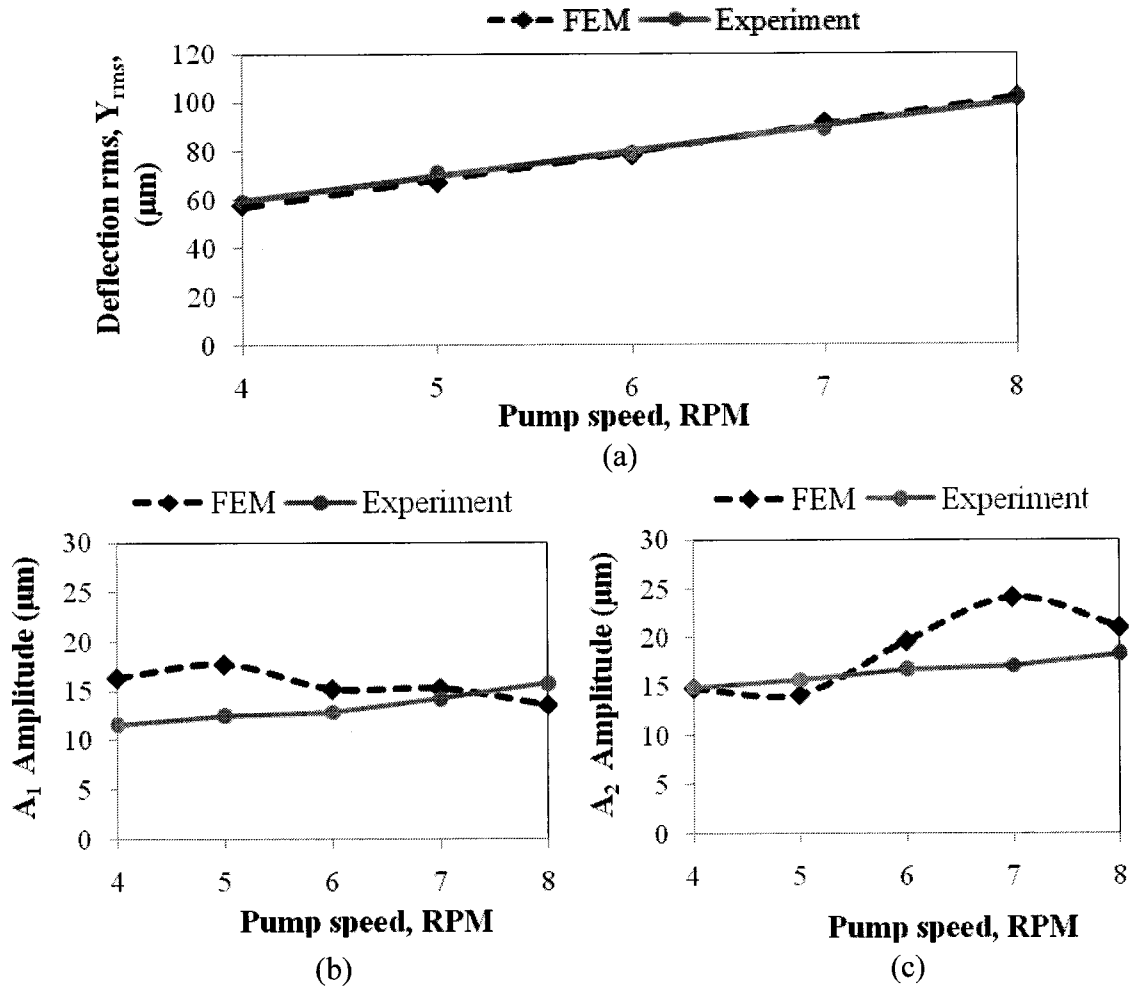


Figure 4.17: Comparison between experimental and FEM results: (a) rms of deflection or Y_{rms} (b) A_1 (c) A_2

In order to ensure the free movement of microcantilever a small clearance of 0.25 mm was provided between the sides of microcantilever and microchannel. As a result, there was a cross leakage flow through this clearance during the experiment, as schematically shown in Figure 4.18. This cross leakage flow through the clearance zone results in pressure equalization across the microcantilever. This leakage flow loss was not considered in two-dimensional finite element modeling. As a result, the prediction from FEM was found to be higher than the experimental results, especially at lower speeds.

The pressure equalization across the cantilever through clearance flow seems to be less dominant at higher oscillation frequency as seen from Figure 4.17.

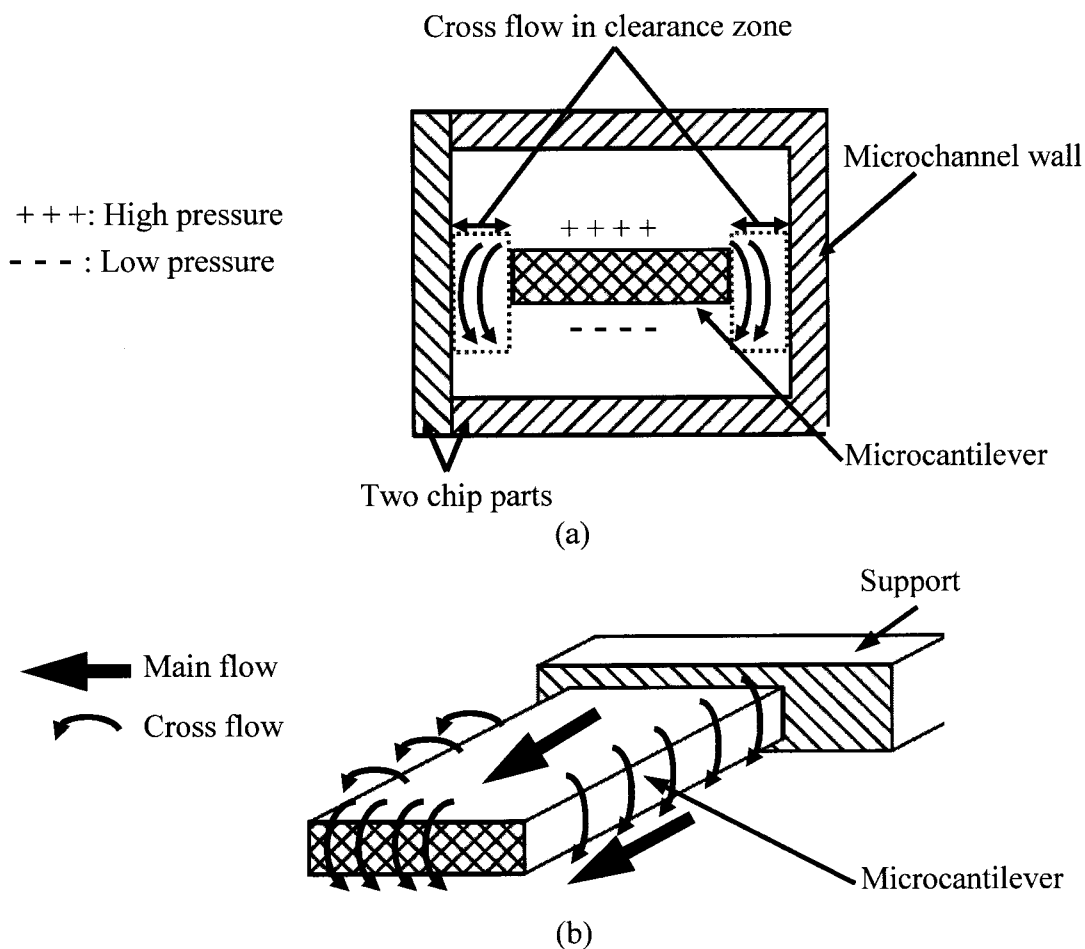


Figure 4.18: (a) Front cross-sectional view of test chip where the cross flow is shown in the clearance zone, between the side edge of microcantilever and the wall of microchannel
 (b) Pictorial view of cantilever where the cross leakage flow is presented as thinner arrow and main flow is presented as thicker arrow

The contour plots of fluid velocity from finite element modeling, at the instant of maximum deflection of cantilever for different pump speeds are presented in Figures 4.19, 4.20, 4.21, 4.22 and 4.23. However, those figures show that the fluid flowing below the cantilever with lower velocities have the tendency to flow towards the opposite

direction of the movement of the cantilever due to the force exerted by the cantilever on the fluid. This mode is equivalent of pumping.

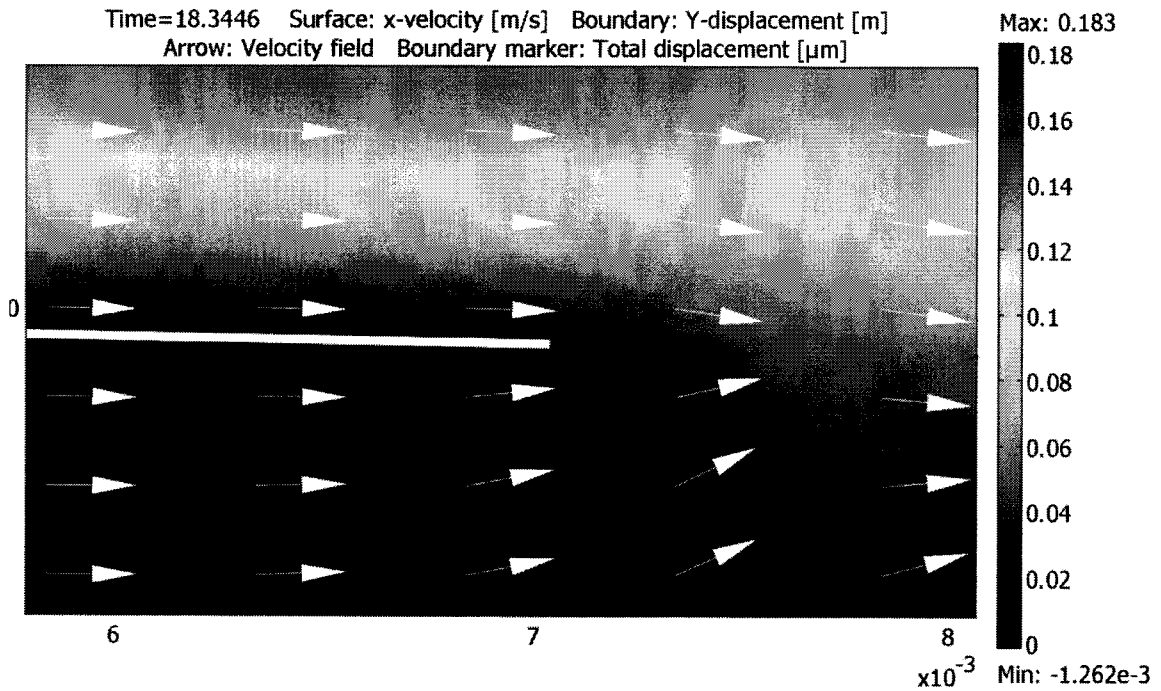


Figure 4.19: Contour plot of fluid velocity at the instant of maximum deflection of cantilever for the pump speed of 4 RPM

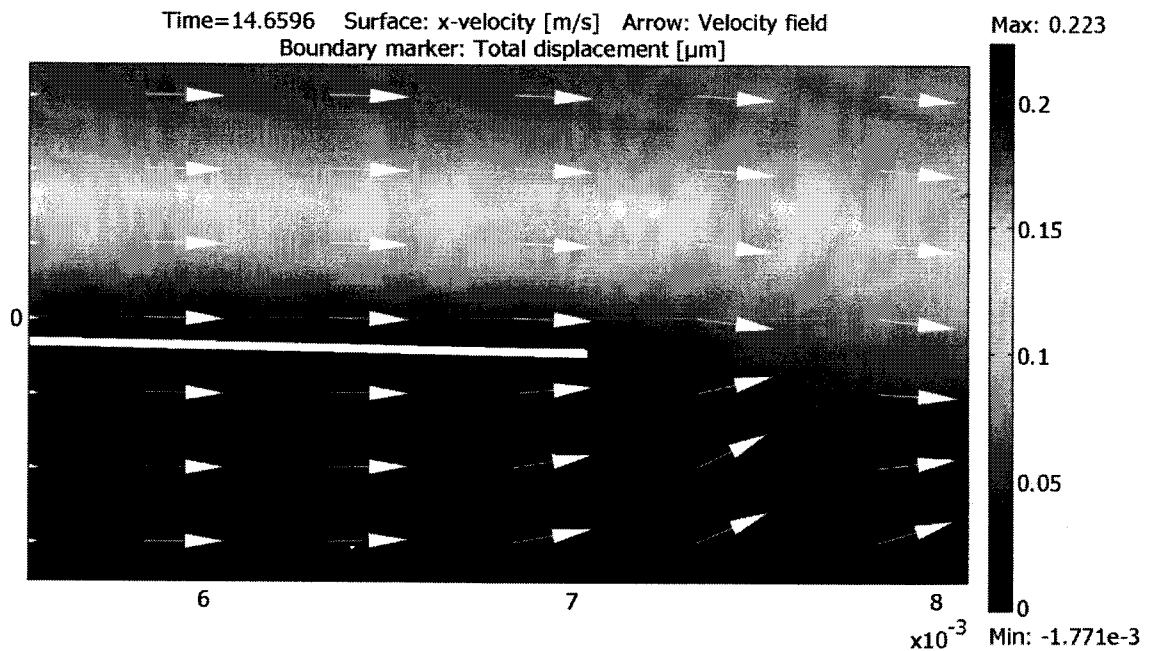


Figure 4.20: Contour plot of fluid velocity at the instant of maximum deflection of cantilever for the pump speed of 5 RPM

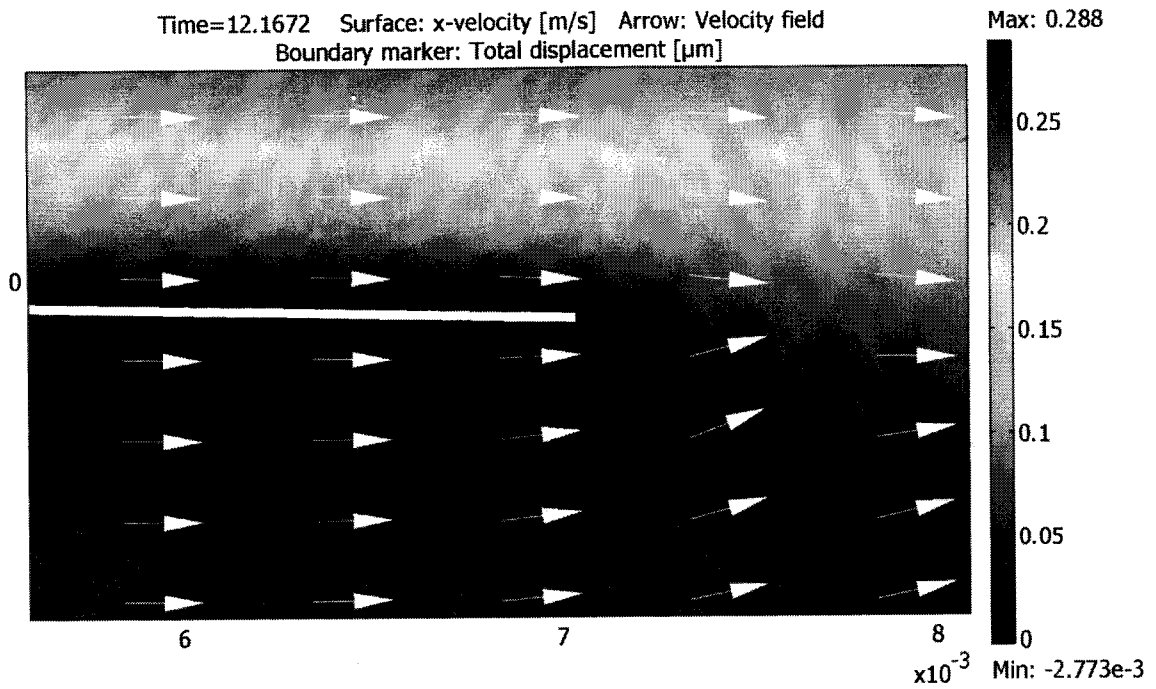


Figure 4.21: Contour plot of fluid velocity at the instant of maximum deflection of cantilever for the pump speed of 6 RPM

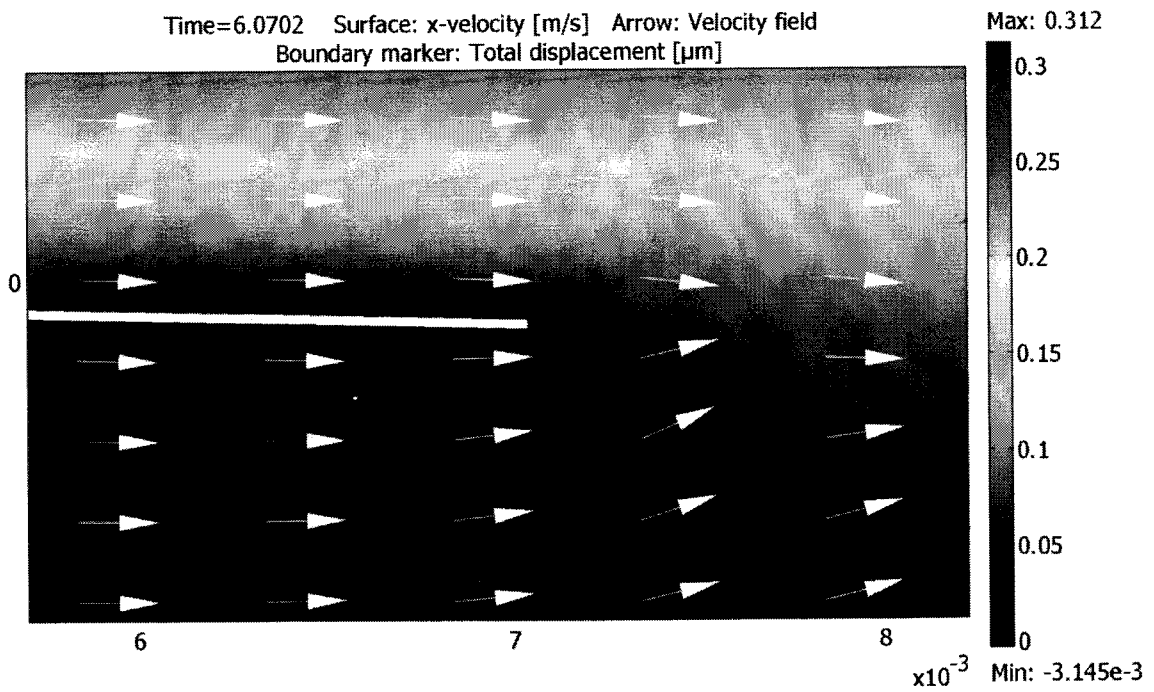


Figure 4.22: Contour plot of fluid velocity at the instant of maximum deflection of cantilever for the pump speed of 7 RPM

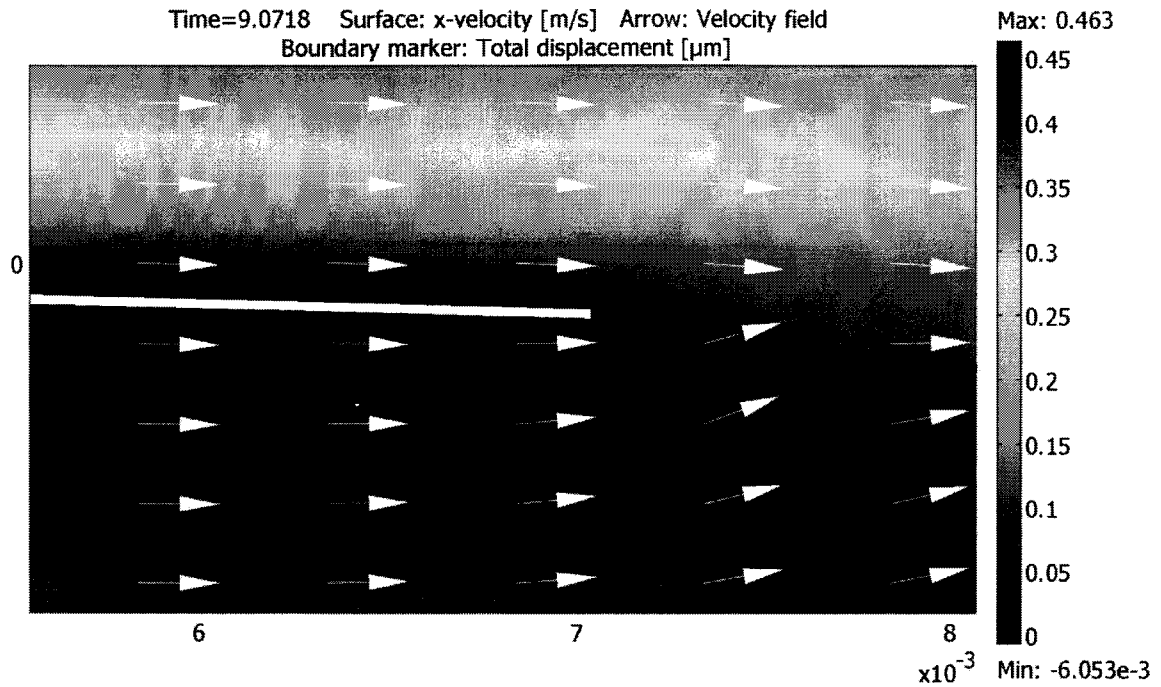


Figure 4.23: Contour plot of fluid velocity at the instant of maximum deflection of cantilever for the pump speed of 8 RPM

4.5 Finite Element Analysis on the Influence of Fluid Viscosity on Quality Factor using Step Excitation

The literature study on both experimental [19] and analytical works [36] of the micro-cantilever in microflow indicates that micro or nano-cantilevers operating in liquid are heavily damped, with a large shift in the resonant frequency away from the undamped natural frequency. If the cantilever is excited by sources other than fluid forces, the quality factor in air was found to be higher than in water for the same resonator. However, lower quality factor is found in air than in liquids when the cantilever is excited by any kind of fluid excitation such as Brownian force [23]. The quality factor of the cantilever is greatly influenced with the pressure loading and viscosity of the fluid.

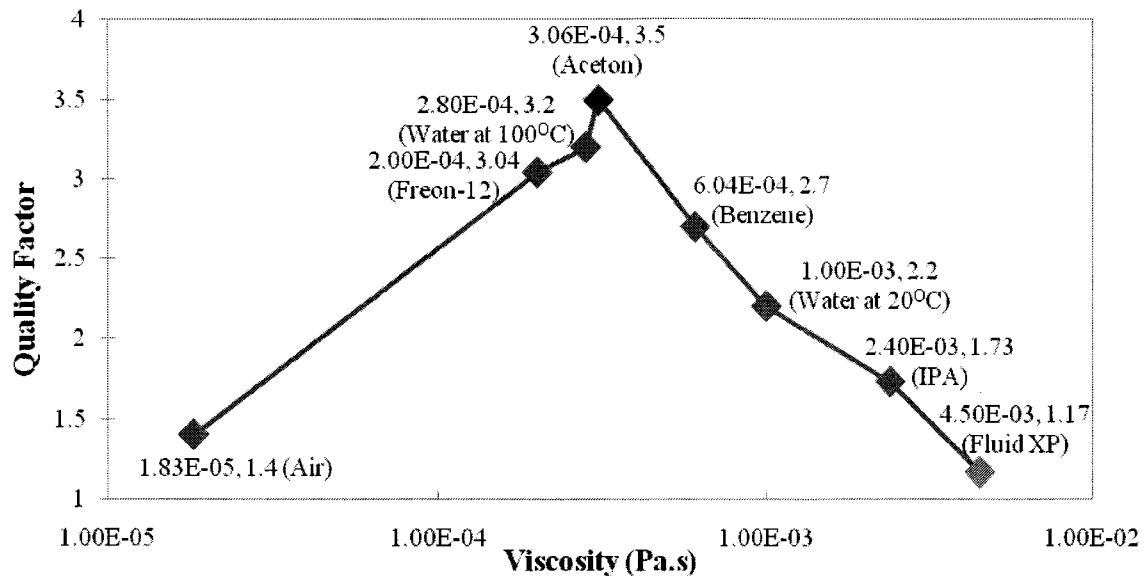


Figure 4.25: Variation of Quality factor against viscosity for different fluids

4.5.4 Results Discussion on Influence of Viscosity over 'Q' factor from FEM

The density and viscosity of fluid influence the quality factor for the fluid surrounded cantilevers. The fluid density is responsible for pressure load, which creates the dynamic motion of cantilever. However, viscosity tries to resist this dynamic motion. Though air has the lower viscosity, which is a good condition of high quality factor but air has very low density compare to the other fluid. This creates lower amplitude where, higher amplitude is another significant condition for higher dynamic behavior or good quality factor. In Figure 4.24, it is clearly shown that highest quality factor is found for the response in Acetone, which has higher density than air but lower than water. The Figure 4.26 and 4.27 illustrate the deflection spectrum of cantilever with respect to different liquids and gases. However, in Figure 4.25 the Acetone shows the sharpest peak, which indicates its highest quality factor. The comparison of amplitude peak

between gases and liquids is presented in Figure 4.27 where the results for liquids shows sharper peak than gasses, hence the liquids have the higher quality factor than gases when the cantilever is excited by the fluid flow. This figure shows that natural frequency is 10 times lower in liquids compare to the air and gases. Similarly, the Figures 4.28 and 4.29 indicate that deflection is 100 times larger in liquid compare to air or Freon-12 due to high viscous loading.

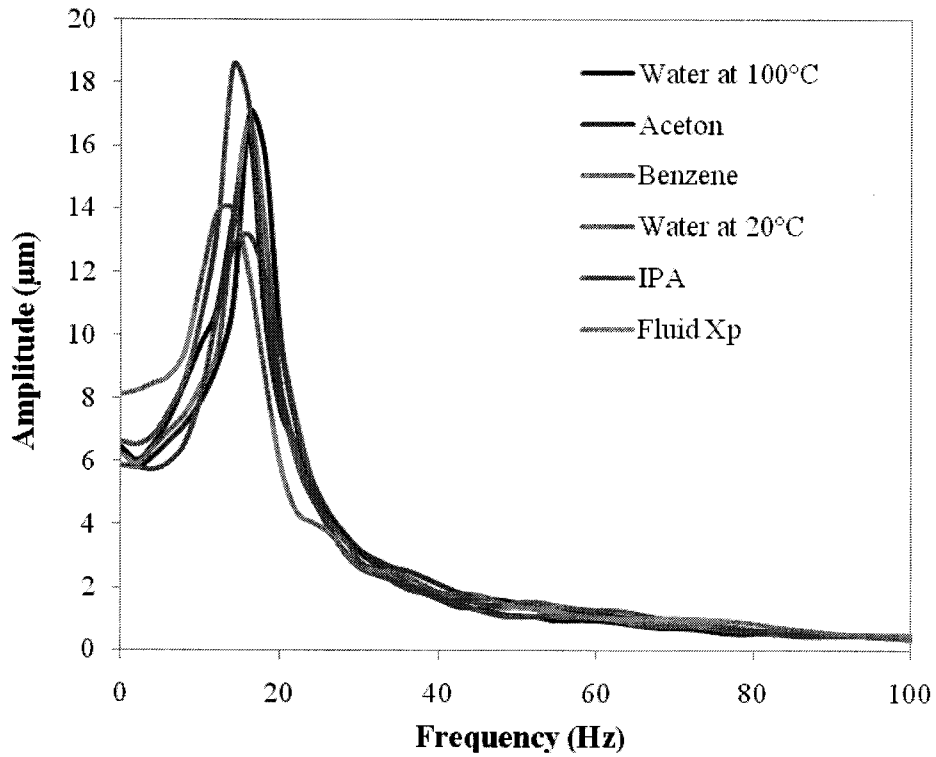


Figure 4.26: Deflection amplitude spectrum in different liquids

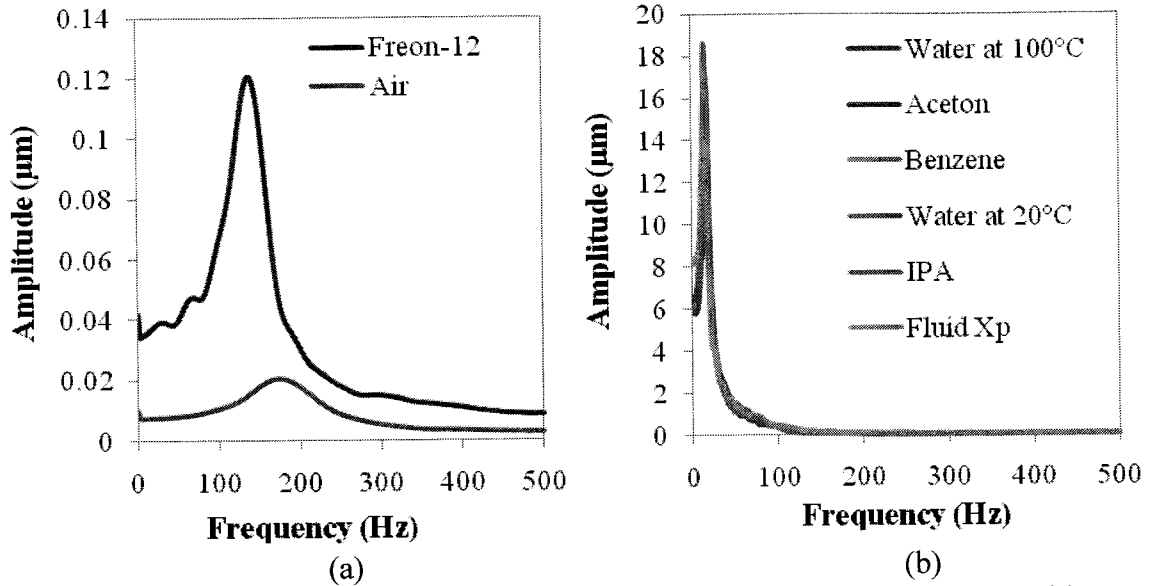


Figure 4.27: Comparison of deflection amplitude spectrum between (a) liquids, and (b) gas

The Figures 4.27 and 4.28 also present the comparison of beam tip deflections in different fluids. These figures suggest that, the cantilever achieved its static equilibrium position faster in high viscous fluid than low viscous fluid due to the viscous damping effect of fluid. These figures also exhibit that fluids with higher viscosity attribute higher static deflection in equilibrium position. The reason of this type of higher static deflection in highly viscous fluid will be explained later of this section.

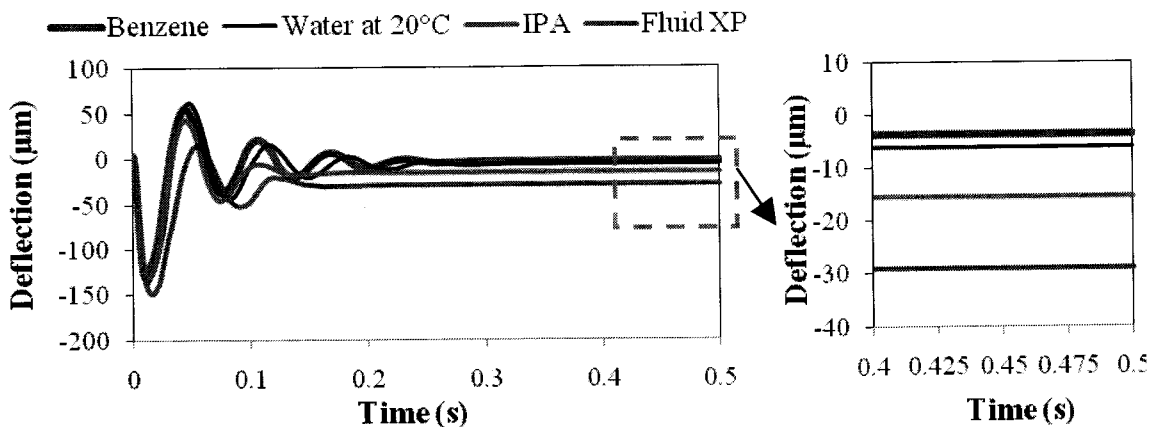


Figure 4.28: Comparison of transient beam tip deflection in Benzene, Water of 20°C, IPA and Fluid XP. The final static deflection is shown in a close up view, at the right side figure for different fluids

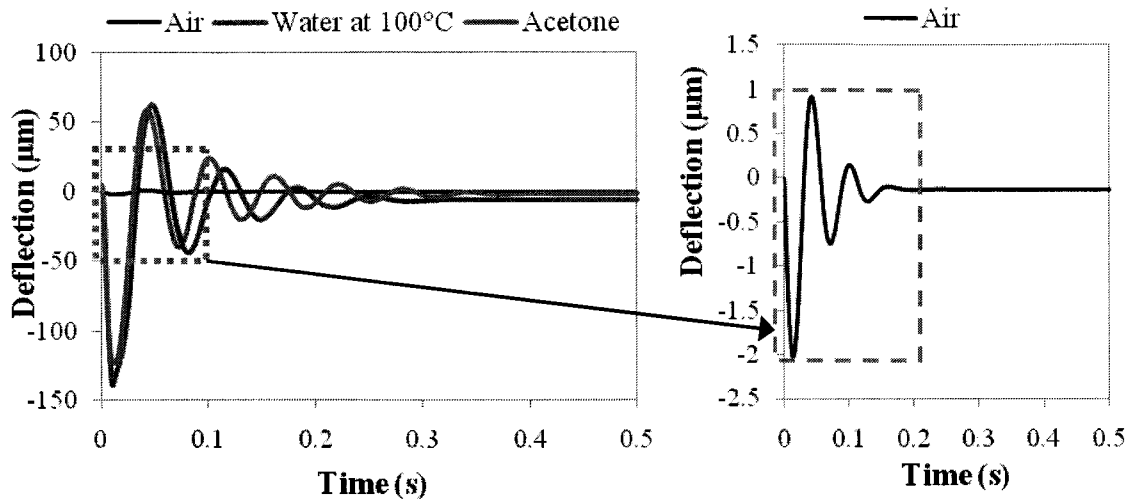


Figure 4.29: Comparison of transient beam tip deflection in Air, Water at 100°C and Acetone where deflection in air is presented in a close up view in right side figure, response in air is approximately 100 times lesser than liquids

The static deflection of cantilever is higher at highly viscous fluid as shown in Figure 4.30, due to high viscous loading. In order to establish the influence of viscosity on the static deflection it is important to estimate the viscous loading under different viscosities. The pressure difference across the cantilever was estimated under no structural interaction that is by solving only the Microfluidic mode of finite element modeling. Pressure difference was computed when flow occurs across the solid cantilever. The predicted pressure difference is shown in Figure 4.31 along the cantilever length. From Figure 4.31 it can be find out that fluid loading increase with the viscosity, leading to higher deflection. Fluid Xp with highest viscosity shows the highest pressure-drop across the length of the cantilever compare to other liquids. Since, the deflection of the cantilever is caused by, the pressure loading due to fluids, the final deflection increases with viscosity of the liquids, which was found in Figures 4.28, 4.29 and 4.30. However, in Figure 4.31, the sudden change in pressure near the support and end-point of the cantilever due to the sudden change of fluid flow direction.

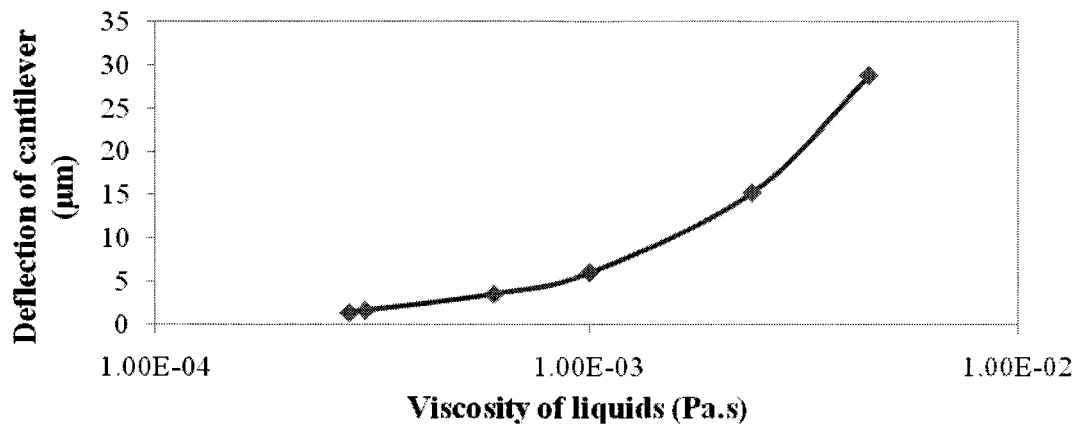


Figure 4.30: Variation of the final tip deflection of cantilever (when, $t=0.5$ s) with respect to different viscosities of different liquids

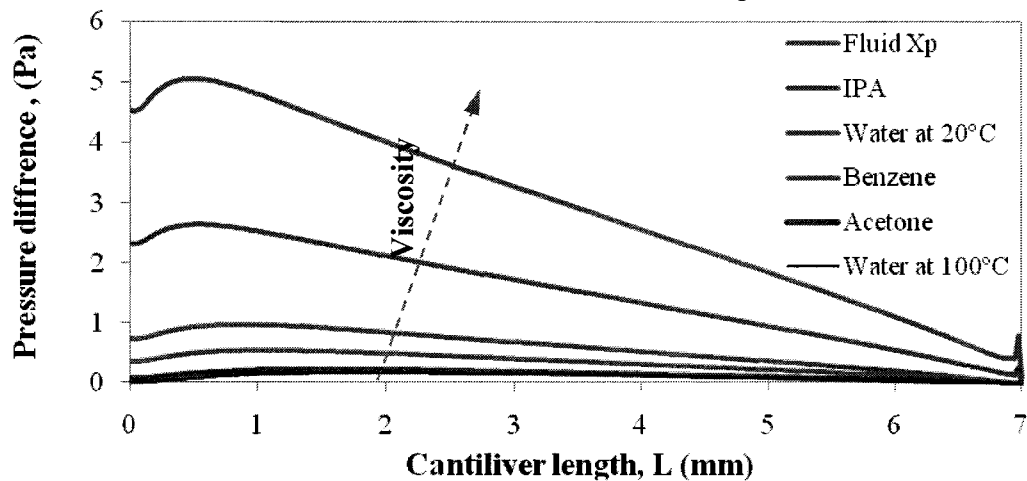


Figure 4.31: Pressure difference distribution across the cantilever with respect to different viscosities of different liquids (after solving only Microfluidics mode)

4.5.5 Finite Element Analysis of the Influence of Cantilever Geometry over Quality Factor

The cantilever property can be defined in terms of aspect ratio, which is the ratio of its length to its width. However, it can be expected that there is some influence of cantilever aspect ratio over quality factor when the interaction surface area of cantilever changes. Hence, a finite element model is developed for cantilever with different length under same flow conditions of $v_2=0.08$ m/s and $v_1=0.001$ m/s. However, the cantilever width and thickness were fixed at 1 mm and 0.030 mm respectively. The length of the

cantilever was varied from 6 to 7.25 mm for 7 different models with a increment of 0.25 mm for each model. Therefore, the aspect ratio varies from 6 to 7.25. The cantilever sub-domain property (density and modulus of elasticity) was identical as shown in previous Finite Element modeling.

4.5.6 Results and Discussion for the Influence of Aspect ratio on 'Q' Factor

The characterization of quality factor with respect to aspect ratio (length/width) is shown in Figure 4.32. However, the peak value was found in near the aspect ratio of 7, that was with a 7 mm long cantilever with 1 mm width.

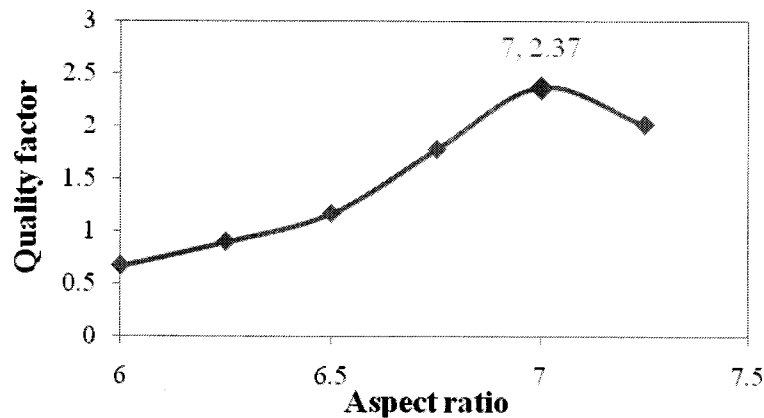


Figure 4.32: Variation of Quality factor with respect to aspect ratio

Increment in the length or aspect ratio of a cantilever leads to more dynamic-interaction as well as higher quality factor. However, increment of length also increases the amount of fluid underneath of cantilever surface area, which resists this dynamic motion of cantilever due to viscous damping. Hence, after certain aspect ratio, the dynamic motion reduces as the amount of fluid under cantilever surface increases which leads to higher viscous damping.

4.6 Summary

The finite element model of microcantilever integrated microfluidic chip provides the satisfactory results and those results were validated in this chapter. The Finite Element Model carried out to estimate the influence of viscosity and cantilever aspect ratio on quality factor. It is essential to validate the modeling through experiments. Hence, the next chapter presents the experimental results.

5.1 Introduction to Application Development

The dynamic behavior of microcantilever in fluid is strongly influenced by the viscosity of the flowing fluid. Such influence can be used to develop Micro-viscometer [11]. In addition, the Finite Element Model in last Chapter showed that micro-structure-micro-fluid interaction could be use for the estimation of fluid property. However, the review of relevant literature shows that most of the microcantilever-based viscometers require huge external system to excite the cantilever [11, 12]. Therefore, the model presented in this work can be used with less complicated system to estimate the fluid viscosity level without any external excitation system, as the fluid flow itself excites the cantilever. The microcantilever-integrated microchannel is tested with different fluids. The current chapter presents the experimental results obtained by testing microcantilever integrated microfluidic chip with different fluids along with flow visualization near the tip of the cantilever. The program used to find the deflection of cantilever beam from image post processing is extended to estimate the deflection shape of entire cantilever. Hence, an experimental result is presented at end of this chapter where the deflection shape of the cantilever is obtained by DVIP method.

5.2 Experiment for Viscosity Estimation under Pulsed Flows

The experimental specimen fabricated with the designed mold is test with respect to 4 different fluids, such as Corn oil, Fluid Xp, Isopropyl alcohol and Water.

Their densities and viscosities are presented in Table 5.1. However, for this experiment, 2.1 mm hydraulic diameter of specimen was used, with a cantilever length, width and thickness of 7.00 mm, 1 mm and 0.030 mm, respectively. In order to establish a similar flow through the specimen the same peristaltic pump was used as described in Chapter 4 with the low flow condition. The response of cantilever is measured by image capturing and post processing method. The result is presented in next section.

Table 5.1: Property of tested fluid

Fluid	Viscosity (Pa.s)	Density (kg/m ³)
Water	1.00E-03	1000
Isopropyl Alcohol	2.40E-03	786
Fluid XP	4.50E-03	1029
Corn Oil	65E-3	921

5.2.1 Experimental Result for Viscosity Variation

The responses of cantilever under different fluids are presented in Figure 5.1, 5.2, 5.3, and 5.4. However, the flow was maintained identical at 48 RPM of pump speed. Therefore, the expected higher and lower frequency components are 0.8 Hz and 8 Hz respectively. The spectral response of the cantilever under different fluids is presented in Figure 5.5.

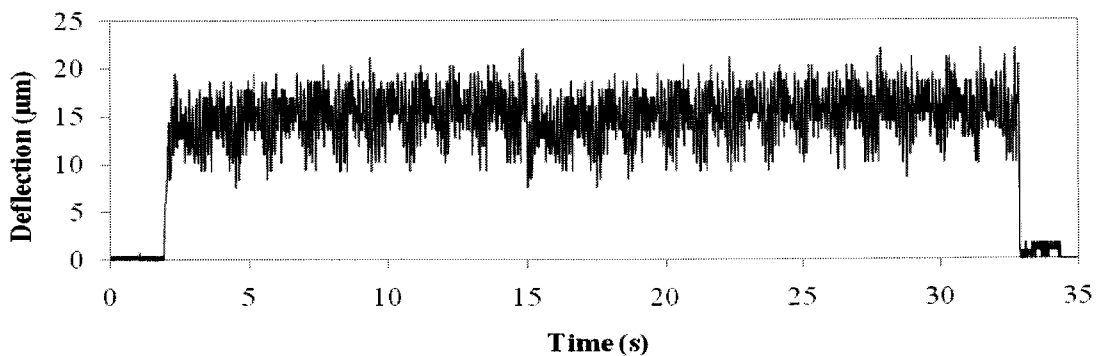


Figure 5.1: Time history of the cantilever beam tip deflection in Water at 48 RPM of pump speed

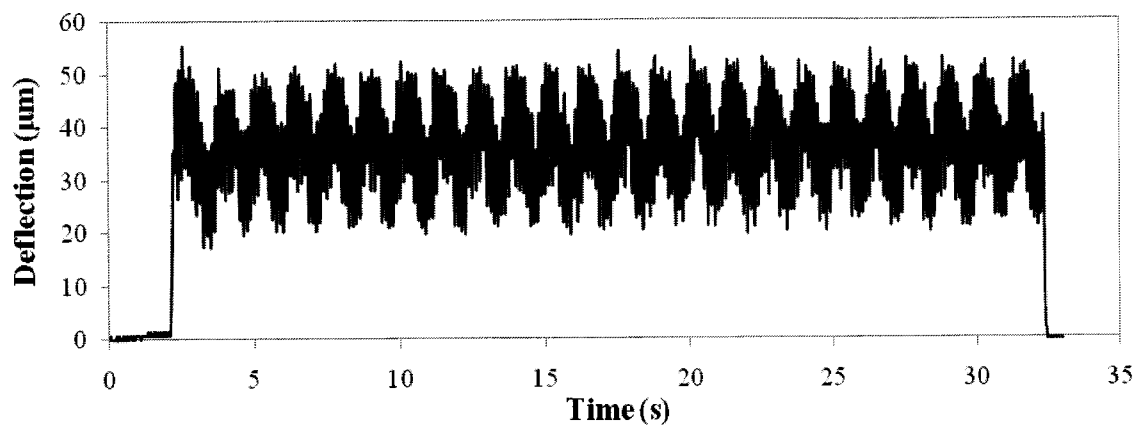


Figure 5.2: Time history of the cantilever beam tip deflection in IPA at 48 RPM of pump speed

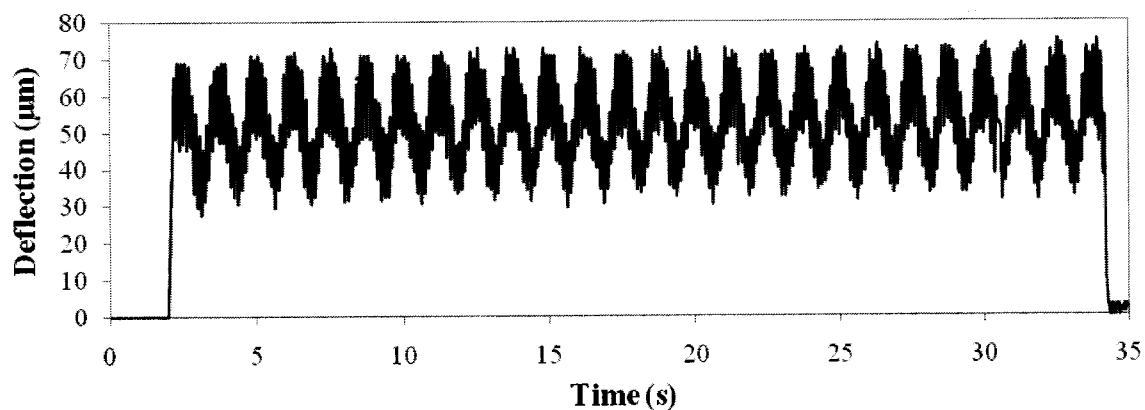


Figure 5.3: Time history of the cantilever beam tip deflection in Fluid Xp at 48 RPM of pump speed

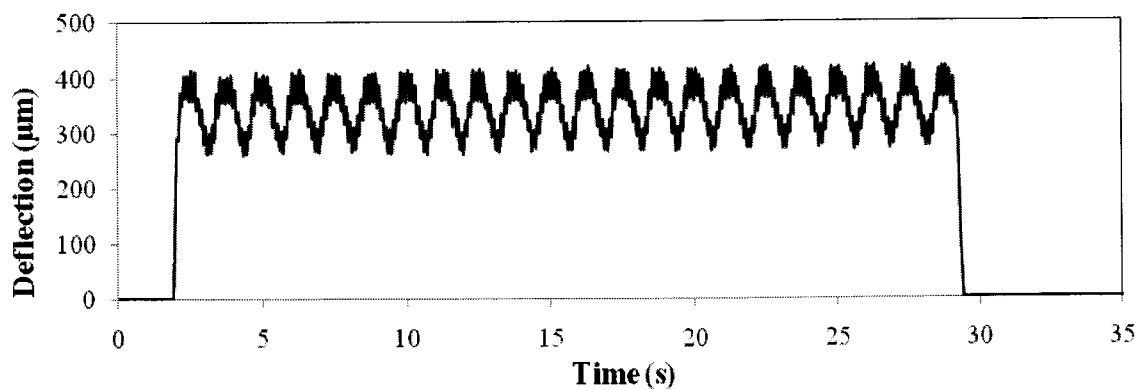


Figure 5.4: Time history of the cantilever beam tip deflection in Corn Oil at 48 RPM of pump speed

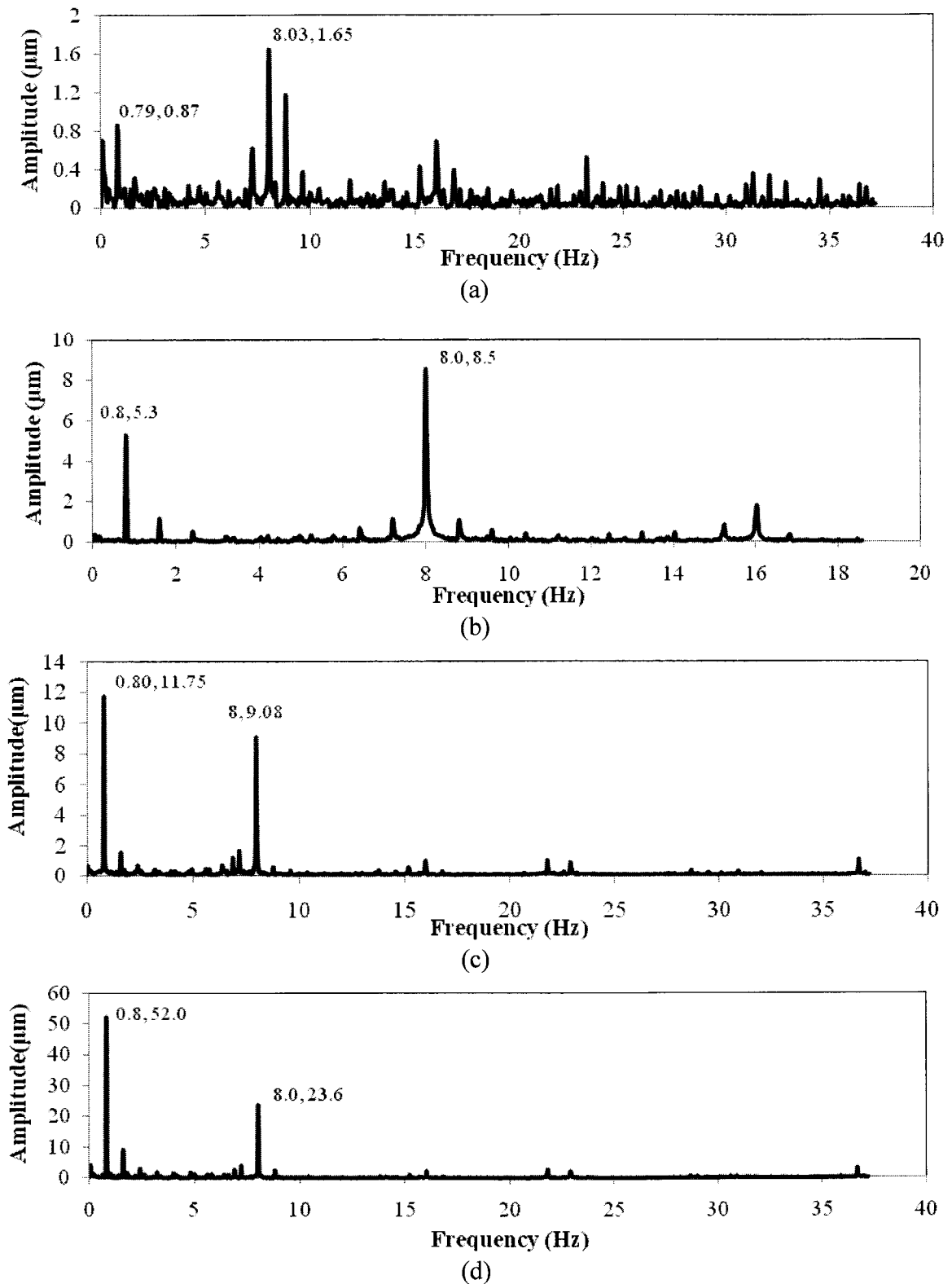


Figure 5.5: Spectrum response of the cantilever tip at 48 RPM in (a) Water, (b) IPA, (c) Fluid Xp and (d) Corn Oil

5.2.2 Experiments with Different Fluids

The Hagen–Poiseuille equation demonstrates [60] that, for a particular flow the pressure drop across a section is proportional to the viscosity of fluid for a given flow. The finite element results presented in Figure 4.29 of last Chapter showed that fluid with higher viscosity produces higher-pressure drop across the cantilever leading to higher loading and higher deflection. In the current experiment deflection magnitudes Y_{rms} , A_1 and A_2 increase with the fluid viscosity as presented in Table 5.2 and in Figure 5.6. Therefore, deflection spectrum analysis can be used as a tool to identify the fluid viscosity.

Table 5.2: The Effect of Viscosity on Response Amplitudes A_1 and A_2

Fluid	Corn Oil	Fluid Xp	IPA	Water
Viscosity (Pa.s)	65E-3	4.50E-03	2.40E-03	1.00E-03
Density (kg/m ³)	921	1029	786	1000
A_1 (μm)	40.9	9.84	5.3	4.58
A_2 (μm)	19.0	9.1	8.5	2.22

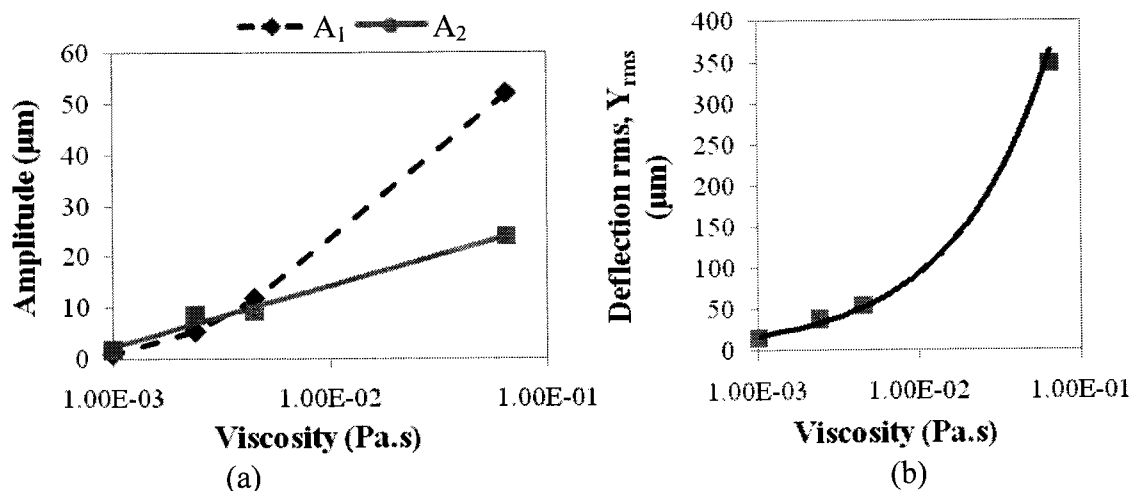


Figure 5.6: (a) The variation of amplitudes of cantilever beam tip deflection with respect to viscosity of fluid; (b) The variation of rms of cantilever beam tip deflection with respect to viscosity of fluid;

The Figure 5.7 represents the comparison of beam tip deflection found in water and fluid XP. However, there were existences of some other frequencies beside the excitation frequency in the beam tip deflection for water as seen in Figure 5.7(a), which are close to the damped natural frequency of cantilever in water. This tendency is noticed to be influenced at lower viscosities.

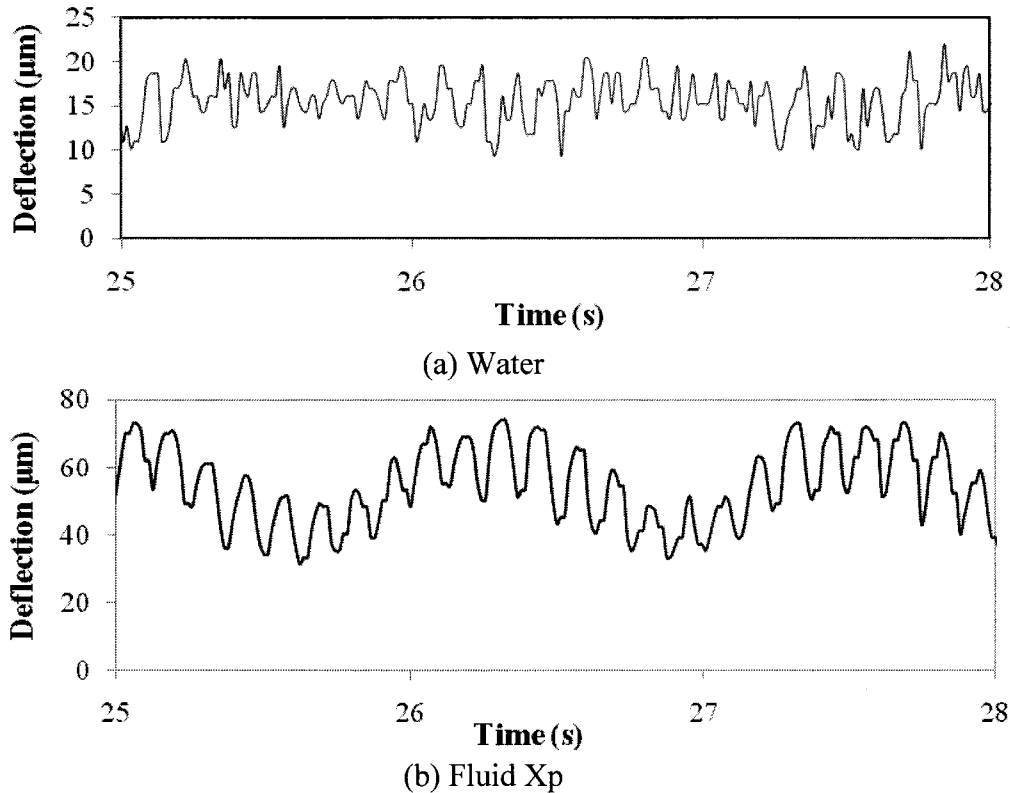


Figure 5.7: Comparison of beam tip deflection between (a) water and (b) Fluid XP

The Figure 5.8 represents the variation of quality factor for oscillatory forced vibration at two distinct frequencies ω_1 and ω_2 , which correspond to passing flow frequencies. Though the finite element modeling of last chapter showed that Fluid XP had lower quality factor than water but Figure 5.8 suggests that highest quality factor was found for Fluid XP. Hence, this result is in opposite trend to FEM results given in Section 4.5. These could be attributed to the following reasons:

- 1) The experimental Q factor was determined at the excitation frequencies ω_1 and ω_2 while, the FEM Q factor was determined at damped natural frequency
- 2) The cantilever was excited with pulse loading in testing while it was excited with step loading in FEM

Even though, these differences could attribute to the estimation between FEM and experiments further study need to be done to explore this in detail.

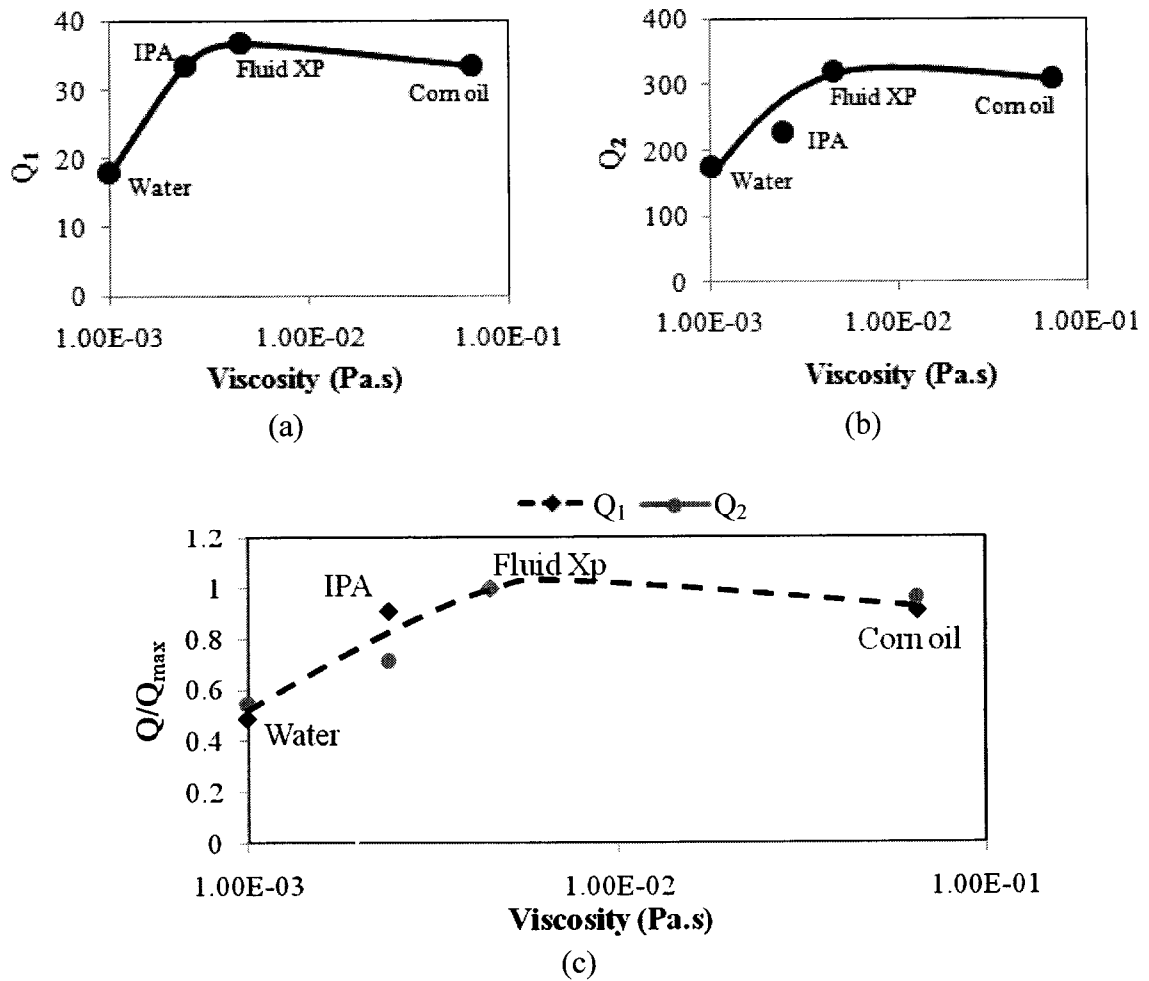


Figure 5.8: (a) Variation in experimental quality factor Q_1 at frequency ω_2 with respect to viscosity; (b) Variation in second experimental factor Q_2 at the frequency ω_1 with respect to viscosity; and (c) Overall variation in the normalized quality factor

5.2.3 Finite Element Modeling and Validation

A finite element model was developed with measured data during the experiment described in previous section. For finite element, modeling same model described in section 4.2 of last chapter was used since the same specimen of 2.1 mm hydraulic diameter was tested with different fluids. The boundary conditions obtained from testing for two different inlets and outlet are presented in Figure 5.9. However, to avoid convergence during the measurement for corn oil the flow velocities were initially reduced by controlling the adjustment screw of locking key of the pump. Hence, these flow velocities were kept identical with that of all other fluids. The boundary conditions illustrated in Figure 5.9 were achieved by the same procedure that was described in Section 4.3 of the last chapter. Though all other boundary conditions were remained same as described in last chapter, the fluid densities and viscosities were varied in the model according to the tested fluid.

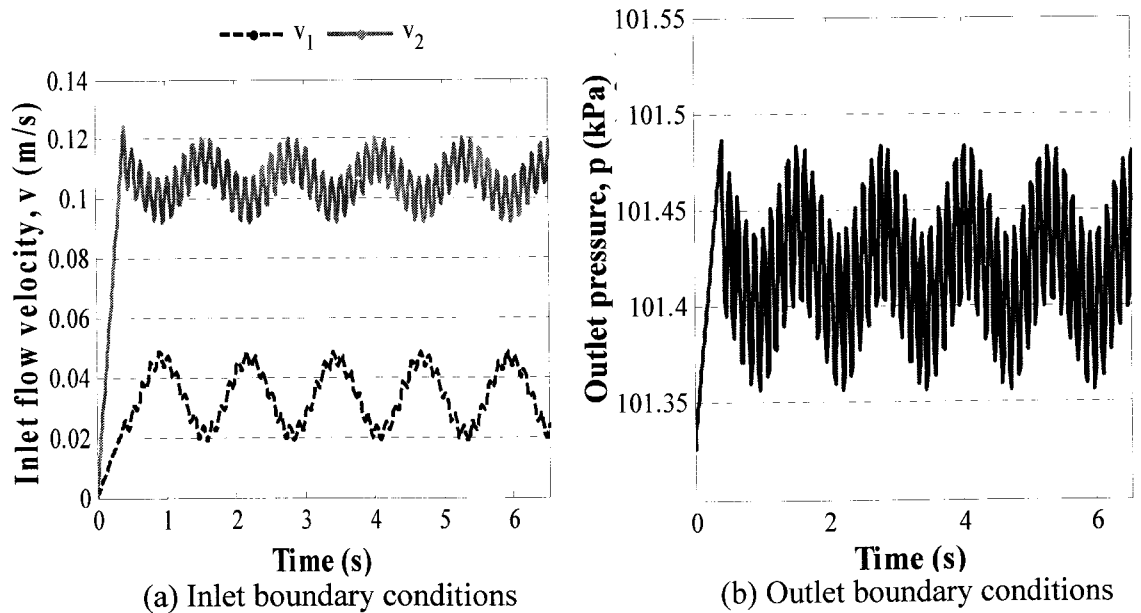


Figure 5.9: Boundary conditions from testing for finite element modeling with different fluid (N= 48 rpm)

The Figure 5.10 illustrates the comparison between FEM and experimental results. The figure shows close agreement between the finite element modeling and experimental results. The higher deflection found at higher viscosities due to loading across the cantilever as discussed in the previous section of this Chapter. The presented results in Figure 5.10 also suggest that, for medium viscous fluids (Fluid XP and IPA) the FEM results are closer to the experimental results compared to high (Corn Oil) and low viscous fluids (water).

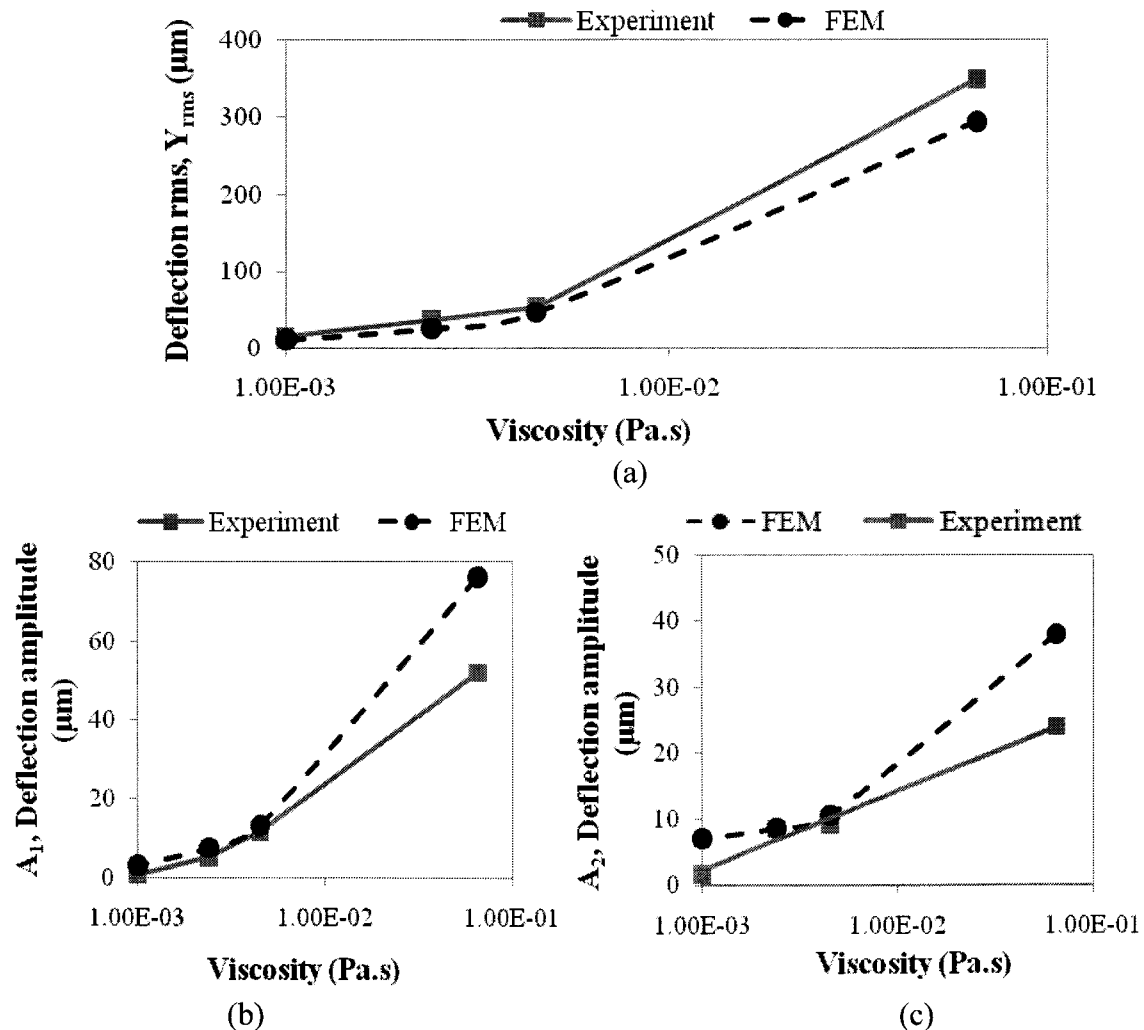
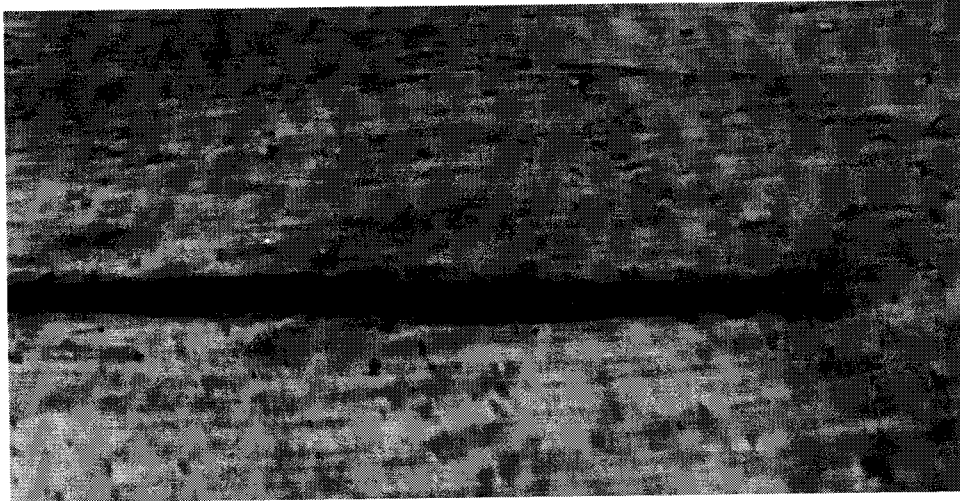


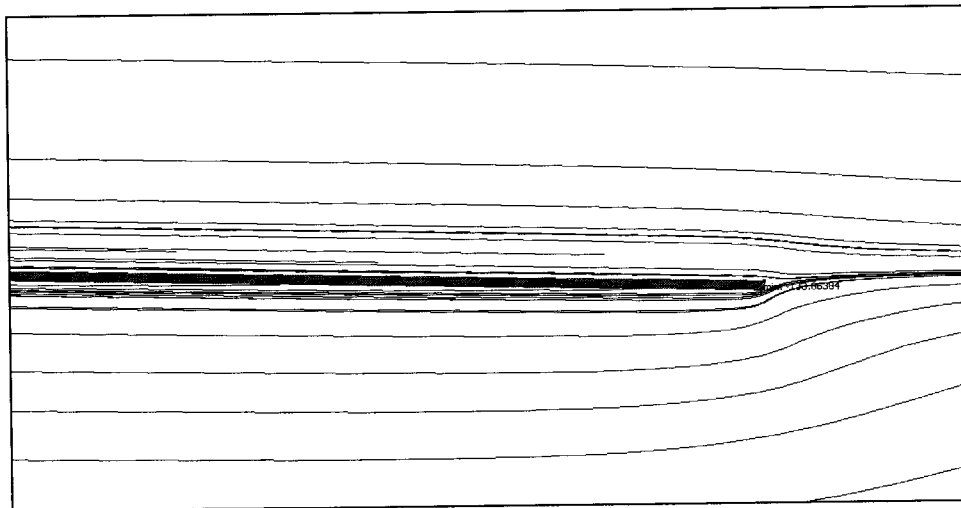
Figure 5.10: Comparison of between experimental and FEM results of deflection against viscosity: (a) rms of cantilever beam tip deflection (b) Deflection amplitude A_1 (c) Deflection amplitude A_2

5.3 Flow Visualization

The device with 2.1 mm hydraulic diameter was tested with fluorescent particles mixed Fluid XP so that the flow can be visualized near the cantilever free end tip. However, the particle movement was captured by the same infinity-1 camera with the resolution of 1280×1024 pixels. In this testing, the pump was run at 8 RPM with low flow configuration tube. The flow parameter were chosen so that captured image can be validated with the result from finite element modeling as explained in the section 4.4 of chapter 4. The streamline plot of FEM model is compared with captured image from flow visualization. The predicted streamlines from the finite element modeling were compared with tested flow visualization during the maximum tip deflection of cantilever, which is shown in figure 5.11. However, the streamline plots from finite element model agree well with the experimental flow visualization results at the maximum deflection position of the cantilever.



(a) Testing



(b) FEM modeling

Figure 5.11: Comparison of flow visualization between FEM modeling and testing at 8 RPM pump speed

5.4 Deflection of Full Cantilever through Imaging

Full cantilever arc deflection imaging is useful to evaluate the mode of vibration and cantilever response. However, for full cantilever beam imaging the same DVIP method was extended. The computer program that calculate the cantilever tip deflection is modified such a way that the variable that initiate the scan from the right-top corner of image can scan the complete image to find the full arc deflection. The length of the cantilever beam was reduced to 4 mm so that it can be viewed in the whole field of view

of the microscope. The pump speed was kept at 48 RPM with high flow configuration of tubes were installed in the pump. The specimen hydraulic diameter was 2.1 mm. Frame rate of the video imaging was 102 frames/s. However, the camera has the limitation with the image resolution. At the increased frame rate of 102 frames/s, the camera can capture images only at maximum image resolution of 640×512 pixels. Figure 5.12 illustrate a sample image that was captured during the experiment and Figure 5.13 shows the variation of pressure difference between two inlets for the time interval of 6 to 8 s.



Figure 5.12: Full cantilever beam

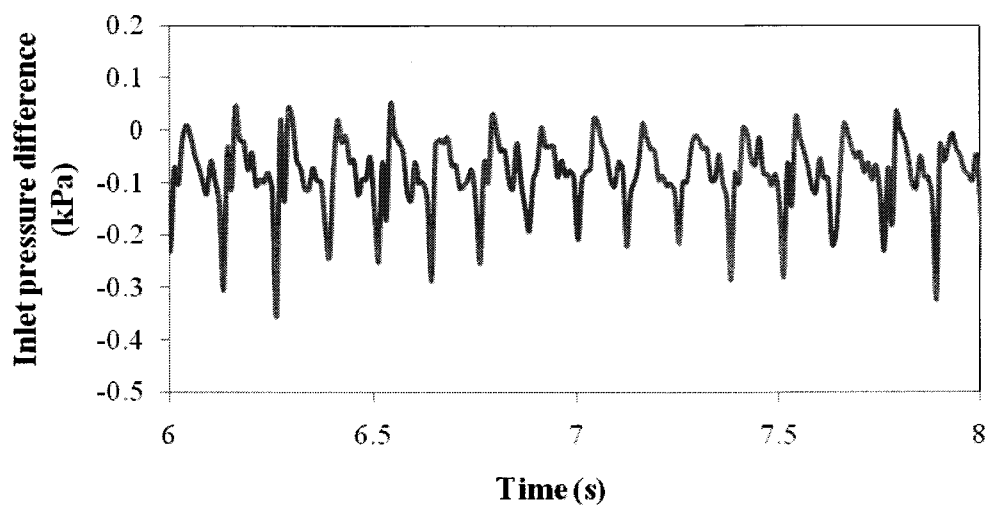


Figure 5.13: Time history of pressure difference between two inlets

The field view of the camera was 640×512 pixels. With this resolution along axial (X-axis) direction 1 pixels of length of the cantilever was correspond to $9.61 \mu\text{m}$ and along transverse direction (Y direction) 1 pixel of deflection was correspond to $1.92 \mu\text{m}$. The video was captured at 102 frames/s where, time interval Δt between two-subsequence frames was 0.0098 s. The time history of cantilever beam tip deflection for 6 to 8 s is presented in Figure 5.14. The full beam deflection of the marked time in Figure 5.14 is presented in Figure 5.15. Figure 5.16 represents the overall full beam deflection pattern for 6 to 8 s. The Figure 5.15 and 5.16 indicate that the dynamic motion of the cantilever was similar to the first mode vibration. Hence, one can estimate the motion parameters such as, deflection, velocity, acceleration with these figures as the time intervals between the positions were clearly known. However, because of low resolution of the image, the deflection arc was not so much smooth. However, this process can be developed for higher frequency, with faster camera.

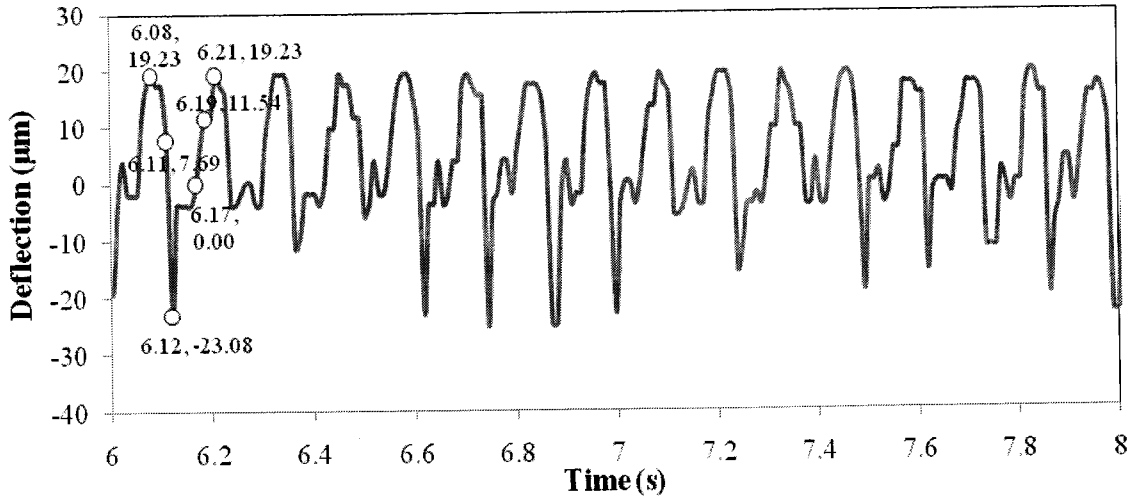


Figure 5.14: Time history of cantilever tip deflection (full beam deflection over the same interval presented in Figure 5.13 and full beam deflection shape for the marked point is presented in Figure 5.15)

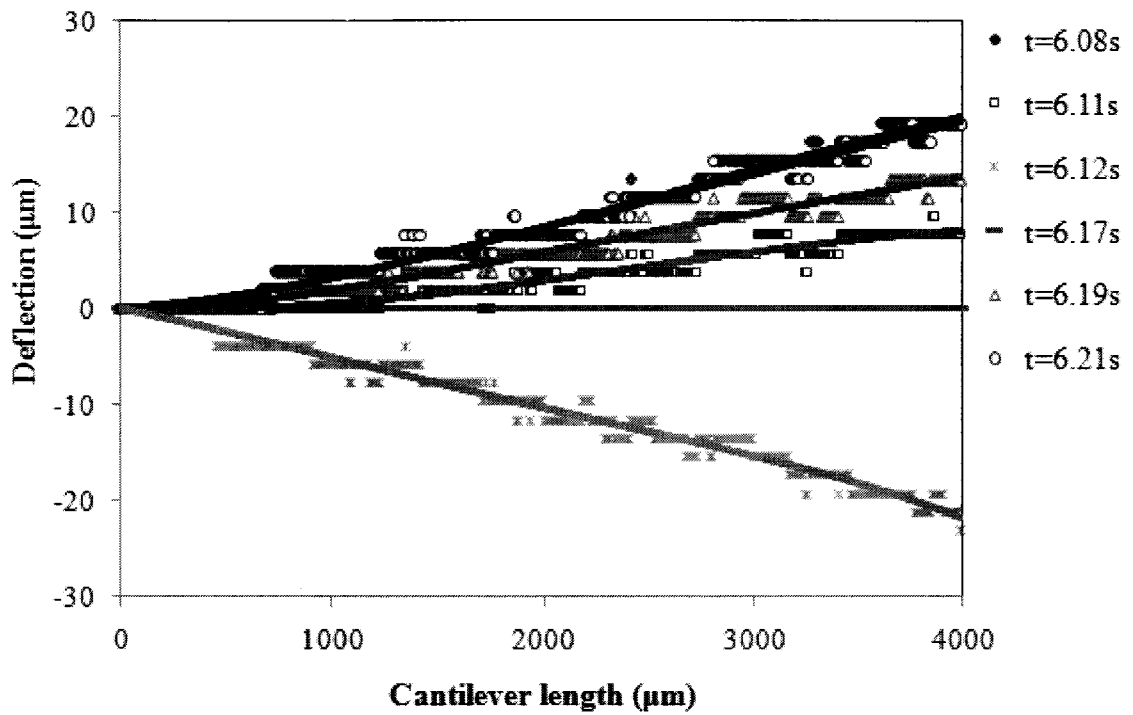


Figure 5.15: Full deflection shape of cantilever for marked time in Figure 5.14

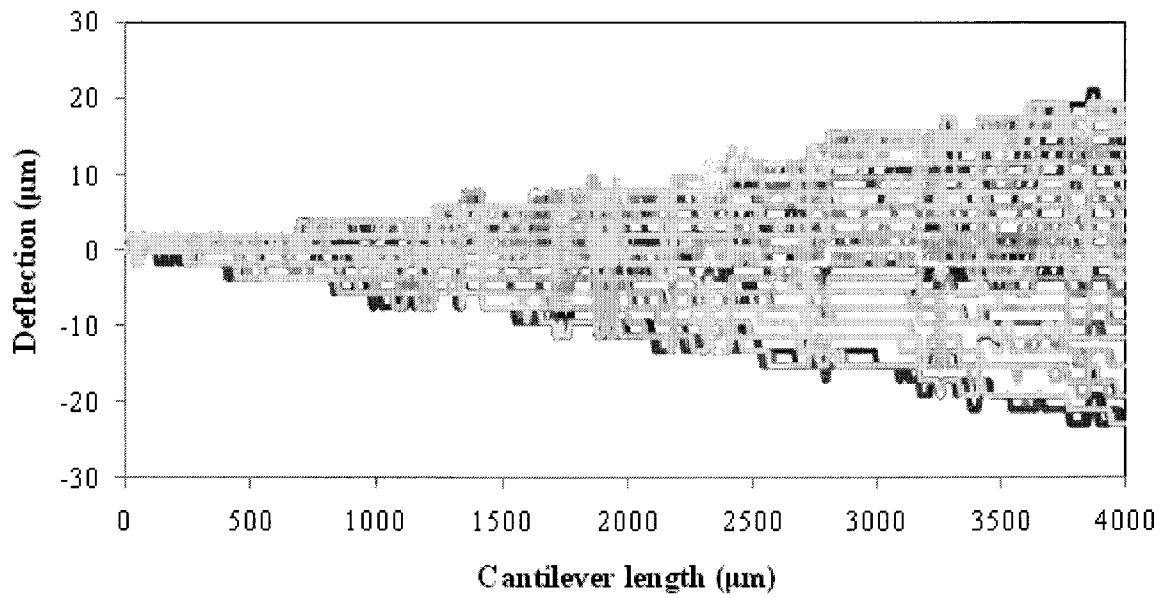


Figure 5.16: Full deflection shape of cantilever between 6 to 8 s

5.5 Summery

The primary objective of this dissertation has been archived by fundamental characterization of dynamic behavior of microcantilever with respect to different flow conditions and different fluid viscosity. The new program developed for image capturing and post-processing method brings a great potential to measure the cantilever response. Still there is further scope to develop this study along with the potential of current study, which is well be described in the next chapter.

Conclusion and Future Work

6.1 Conclusion

The main objective of the current thesis is to develop a model, with which microfluid-microstructural interaction issues can be explored. As, the micro-flow channel mounted with micro-cantilever in the flow path is most prominent and simple to study, the model of microcantilever mounted in between two different flows or pressure is chosen as an experimental model. However, most of the previous study use photolithography based bulk and surface micro machining to fabricate the cantilever. However, those methods are complicated and expensive. Hence, in this current study, polymer based soft-lithography method is used to fabricate the microfluidic chip as, this method is less expensive and simpler. The fabricated specimen is tested and characterized by a new method called DVIP method. However, this method was so much successful that very slide variation of result was found with the theoretical model, which is generated from finite element modeling.

There are several parameters that control the response of the cantilever such as, fluid flow, microchannel geometry, fluid property, cantilever dimension, and its property. It was found that for same input flow the cantilever response is more sensitive at smaller hydraulic diameter of microchannel, which was 2.1 mm. However, the highly viscous fluid creates higher amplitude in the response, which is another great outcome of this current study. The cantilever response is so useful tool to characterize the flow variation of the channel. The finite element model indicate that fluid viscosity and density both

have the great influence over the cantilever response for non transient flow of fluid. This model also indicates the cantilever aspect ratio is a vital parameter in respect of identical flow of fluid. Finally, it can be concluded that micro-fluid-microstructural interaction can be implicated greatly along with this new introduced DVIP method in the field of biochemical sensing.

6.2 Thesis Contribution

The contribution of this thesis work can be highlighted in brief as,

1. Design and modeling of fluid-structure interactions in microfluidic channel
2. Development of soft lithography method for the fabrication of microfluidic chips
3. Development of hybrid fabrication facility for fabricating cantilever integrated microfluidic chips
4. Development of an experimental setup in order to characterize the effect of inlet flows and geometry of different microfluidic chips
5. Characterization of microcantilever responses against variant fluid flow and pressure at two different frequencies associated with the flows supplied by the peristaltic pump
6. Development of a new DVIP method to estimate the deflection of the microcantilever integrated in the microfluidic channel
7. Comparison of results obtained from LDV and DVIP method where DVIP method showed more prominent and reliable results than those derived from the LDV
8. Development of Finite Element Model to validate the experimental results

9. Characterization of Quality factor against the viscosity of different fluids using finite element modeling and analysis
10. Experimental characterization of microcantilever responses and quality factors for fluids of different viscosity using DVIP method and development of finite element model to demonstrate validity of the results
11. Flow visualization near the tip of the microcantilever and comparisons with the FEM results
12. Extension of DVIP method to estimate the full cantilever beam deflection

6.3 Limitation and Recommendation

In the present thesis, the developed image capturing and post-processing method is fully dependent on the instrumentation facility such as capability of the camera. Increase in the sampling rate reduces the capability to capture images with high resolution, while a low-resolution image would yield some errors. However, a high sampling rate is necessary under high frequency excitations of cantilever.

Therefore, beside this small limitation the overall study was successful to evaluate the experimental data with the theoretical result. Hence, this thesis work can be subjected for further study and following ideas can be recommended;

1. However, geometrical shape of the channel has great influence over the cantilever response, hence in future; up to 0.5 mm, hydraulic diameter of specimen can be built for further work
2. The study can be extended with different cross-section of the microchannel such as circular, triangular, or polygonal

3. The image capturing and post processing method could also be greatly beneficial in applications involving nano level deflection
4. By implementing a miniature size of the camera, a micro viscometer chip could be developed using the methods developed in this study. The image post processing method can provide precise data to estimate the fluid viscosity

References

- [1] Ostasevicius, V., Dauksevicius, R., Gaidys, R. and Palevicius, A., "Numerical analysis of fluid-structure interaction effects on vibrations of cantilever microstructure," *Journal of Sound and Vibration*, vol. 308, 3-5, 2007, pp. 660-673
- [2] Lin, R. M. and Wang, W. J., "Structural dynamics of microsystems - Current state of research and future directions," *Mechanical Systems and Signal Processing*, vol. 20, 5, 2006, pp. 1015-1043
- [3] Gass, V., van der Schoot, B. H. and de Rooij, N. F., "Nanofluid handling by micro-flow-sensor based on drag force measurements", *Micro Electro Mechanical Systems, Proceedings An Investigation of Micro Structures, Sensors, Actuators, Machines and Systems. IEEE.*, Fort Lauderdale, FL, USA, 1993, pp. 167-172
- [4] Lavrik, N. V., Sepaniak, M. J. and Datskos, P. G., "Cantilever transducers as a platform for chemical and biological sensors," *Review of Scientific Instruments*, vol. 75, 7, 2004, pp. 2229-53
- [5] Du, L., Zhao, Z. and Pang, C., "Design and fabrication MEMS-based micro solid state cantilever wind speed sensor", *International Conference on Information Acquisition, ICIA 2007, Seogwipo-si, Jeju City, Korea, 2007*, pp. 336-340
- [6] Ilic, B., Czaplewski, D., Zalalutdinov, M., Craighead, H., Neuzil, P., Campagnolo, C. and Batt, C., "Single cell detection with micromechanical oscillators," *Journal of Vacuum Science and Technology B: Microelectronics and Nanometer Structures*, vol. 19, 6, 2001, pp. 2825-2828
- [7] Koch, M., Evans, A. G. R. and Brunnschweiler, A., "Characterization of micromachined cantilever valves," *Journal of Micromechanics and Microengineering*, vol. 7, 3, 1997, pp. 221-3
- [8] Koch, M., Evans, A. G. R. and Brunnschweiler, A., "Simulation and fabrication of micromachined cantilever valves," *Sensors and Actuators A (Physical)*, vol. A62, 1-3, 1997, pp. 756-9
- [9] Koch, M., Evans, A. G. R. and Brunnschweiler, A., "Coupled FEM simulation for the characterization of the fluid flow within a micromachined cantilever valve," *Journal of Micromechanics and Microengineering*, vol. 6, 1, 1996, pp. 112-14
- [10] Yang, M., Zhang, X. and Ozkan, C. S., "Modeling and optimal design of high-sensitivity piezoresistive microcantilevers within flow channels for biosensing applications," *Biomedical Microdevices*, vol. 5, 4, 2003, pp. 323-32
- [11] Belmiloud, N., Dufour, I., Nicu, L., Colin, A. and Pistre, J., "Vibrating microcantilever used as viscometer and microrheometer", *2006 5th IEEE Conference on Sensors, Daegu, Korea, 2006*, pp. 753-756

- [12] Jungwirth, M., "Online fluid-monitoring using an electromechanical cantilever", EuroSimE 2008 - International Conference on Thermal, Mechanical and Multi-Physics Simulation and Experiments in Microelectronics and Micro-Systems, Freiburg im Breisgau, Germany, 2008, pp. 4525008
- [13] Campbell, G. A. and Mutharasan, R., "Sensing of liquid level at micron resolution using self-excited millimeter-sized PZT-cantilever," *Sensors and Actuators, A: Physical*, vol. 122, 2, 2005, pp. 326-334
- [14] Lucey, A. D. and Balint, T. S., "Instability of a cantilevered flexible plate in viscous channel flow," *Journal of Fluids and Structures*, vol. 20, 7, 2005, pp. 893-912
- [15] Huang, L., "Flutter of Cantilevered Plates in Axial Flow," *Journal of Fluids and Structures*, vol. 98, 2, 1995, pp. 127
- [16] Thaysen, J., Marie, R. and Boisen, A., "Cantilever-based bio-chemical sensor integrated in a microliquid handling system", 14th IEEE International Conference on Micro Electro Mechanical Systems, Interlaken, Switzerland, 2001, pp. 401-4
- [17] Aubin, K. L., Seung-Min Park, Jingqing Huang, Craighead, H. G. and Ilic, B. R., "Microfluidic encapsulated NEMS resonators for sensor applications", *Sensors*, 2005 IEEE, Irvine, CA, USA, 2005, pp. 3 pp.
- [18] Vancura, C., Kirstein, K. -U., Li, Y., Josse, F. and Hierlemann, A., "Equivalent-circuit model for CMOS-based resonant cantilever biosensors", 4th International Conference on Solid-State Sensors, Actuators and Microsystems, Lyon, France, 2007, pp. 1733-1736
- [19] Hirai, Y., Mori, R., Kikuta, H., Kato, N., Inoue, K. and Tanaka, Y., "Resonance characteristics of microcantilever in liquid", *International Microprocesses and Nanotechnology Conference*, Kyungju, Korea, 1998, pp. 89-90
- [20] Bhiladvala, R. B. and Wang, Z. J., "Effect of fluids on the Q factor and resonance frequency of oscillating micrometer and nanometer scale beams," *Physical Review E*, vol. 69, 3, 2004, pp. 036307-1
- [21] Yasumura, K. Y., Stowe, T. D., Chow, E. M., Pfafman, T., Kenny, T. W., Stipe, B. C. and Rugar, D., "Quality factors in micron- and submicron-thick cantilevers," *Journal of Microelectromechanical Systems*, vol. 9, 1, 2000, pp. 117-25
- [22] Zhang, W. and Turner, K., "Frequency dependent fluid damping of micro/nano flexural resonators: Experiment, model and analysis," *Sensors and Actuators A (Physical)*, vol. 134, 2, 2007, pp. 594-9
- [23] Sukuabool, S. and Sood, D. K., "Analytical models of resonant rectangular cantilever type chemical sensors for applications in fluids", *ICST 2008*, Tainan, Taiwan, 2008, pp. 604-9

- [24] Dareing, D. W., Tian, F. and Thundat, T., "Effective mass and flow patterns of fluids surrounding microcantilevers," *Ultramicroscopy*, vol. 106, 8-9, 2006, pp. 789-94
- [25] Quist, A., Chand, A., Ramachandran, S., Cohen, D. and Lal, R., "Piezoresistive cantilever based nanoflow and viscosity sensor for microchannels," *Lab on a Chip*, vol. 6, 11, 2006, pp. 1450-4
- [26] Chen, J., Fan, Z., Zou, J., Engel, J. and Liu, C., "Two-dimensional micromachined flow sensor array for fluid mechanics studies," *Journal of Aerospace Engineering*, vol. 16, 2, 2003, pp. 85-97
- [27] Hausler, K., Reinhart, W. H., Schaller, P., Dual, J., Goodbread, J. and Sayir, M., "A newly designed oscillating viscometer for blood viscosity measurements," *Biorheology*, vol. 33, 4-5, 1996, pp. 397-404
- [28] Chon, J. W. M., Mulvaney, P. and Sader, J. E., "Experimental validation of theoretical models for the frequency response of atomic force microscope cantilever beams immersed in fluids," *Journal of Applied Physics*, vol. 87, 8, 2000, pp. 3978-88
- [29] Chou, C. C., Lee, C. W. and Yang, M. H., "Simulation of an Atomic Force Microscopy's Probe Considering Damping Effect", Proceedings excerpt, COMSOL users conference, Taipei, Taiwan, 2007
- [30] Clark, M. T. and Paul, M. R., "The stochastic dynamics of rectangular and V-shaped atomic force microscope cantilevers in a viscous fluid and near a solid boundary," *Journal of Applied Physics*, vol. 103, 9, 2008, pp. 094910-1
- [31] Cole, D. G. and Clark, R. L., "Fluid-structure interaction in atomic force microscope cantilever dynamics and thermal response," *Journal of Applied Physics*, vol. 101, 3, 2007, pp. 34303-1
- [32] Green, C. P. and Sader, J. E., "Frequency response of cantilever beams immersed in viscous fluids near a solid surface with applications to the atomic force microscope," *Journal of Applied Physics*, vol. 98, 11, 2005, pp. 114913-1
- [33] Elmer, F. and Dreier, M., "Eigenfrequencies of a rectangular atomic force microscope cantilever in a medium," *Journal of Applied Physics*, vol. 81, 12, 1997, pp. 7709-14
- [34] Martin, M. J., Fathy, H. K. and Houston, B. H., "Dynamic simulation of atomic force microscope cantilevers oscillating in liquid," *Journal of Applied Physics*, vol. 104, 4, 2008, pp. 044316-1
- [35] Papi, M., Arcovito, G., De Spirito, M., Vassalli, M. and Tiribilli, B., "Fluid viscosity determination by means of uncalibrated atomic force microscopy cantilevers," *Applied Physics Letters*, vol. 88, 19, 2006, pp. 194102-1

- [36] Martin, M. J. and Houston, B. H., "Frequency response of nanoelectromechanical cantilevers operating in fluid", 2008 8th IEEE Conference on Nanotechnology (NANO), Arlington, TX, USA, 2008, pp. 303-6
- [37] Paul, M. R., Clark, M. T. and Cross, M. C., "The stochastic dynamics of micron and nanoscale elastic cantilevers in fluid: fluctuations from dissipation," *Nanotechnology*, vol. 17, 17, 2006, pp. 4502-13
- [38] Atkinson, C. and Manrique, d. L., "The frequency response of a rectangular cantilever plate vibrating in a viscous fluid," *Journal of Sound and Vibration*, vol. 300, 1-2, 2007, pp. 352-367
- [39] Huang, L., Quinn, S. J., Ellis, P. D. M. and Ffowcs Williams, J. E., "Biomechanics of snoring," *Endeavour*, vol. 19, 3, 1995, pp. 96
- [40] Auregan, Y. and Depollier, C., "Snoring: linear stability analysis and in-vitro experiments," *Journal of Sound and Vibration*, vol. 188, 1, 1995, pp. 39-54
- [41] Fernandez, M. A. and Le Tallec, P., "Linear stability analysis in fluid-structure interaction with transpiration. Part II: numerical analysis and applications," *Computer Methods in Applied Mechanics and Engineering*, vol. 192, 43, 2003, pp. 4837-73
- [42] Gorman, D. G., Trendafilova, I., Mulholland, A. J. and Horacek, J., "Analytical modelling and extraction of the modal behaviour of a cantilever beam in fluid interaction," *Journal of Sound and Vibration*, vol. 308, 1-2, 2007, pp. 231-245
- [43] Gosselin, F., Paidoussis, M. P. and Misra, A. K., "Stability of a deploying/extruding beam in dense fluid," *Journal of Sound and Vibration*, vol. 299, 1-2, 2007, pp. 123-142
- [44] Naik, T., Longmire, E. K. and Mantell, S. C., "Dynamic response of a cantilever in liquid near a solid wall," *Sensors and Actuators, A: Physical*, vol. 102, 3, 2003, pp. 240-254
- [45] Peng, J. G. and Zhou, Z. Y., "Numerical simulations and experimental studies on a new type flow sensor," *Journal of Physics: Conference Series*, vol. 48, 1, 2006, pp. 239-44
- [46] Tanida, Y., "Stability of a soft plate in channel flow (aerodynamic aspects of palatal flutter)," *JSME International Journal, Series B (Fluids and Thermal Engineering)*, vol. 44, 1, 2001, pp. 8-13
- [47] Carrascosa, L. G., Moreno, M., Álvarez, M. and Lechuga, L. M., "Nanomechanical biosensors: a new sensing tool," *TrAC Trends in Analytical Chemistry*, vol. 25, 3, 2006, pp. 196-206

- [48] Lechuga, L. M., Zinoviev, K., Fernandez, L., Elizalde, J., Hidalgo, O. E. and Dominguez, C., "Biosensing microsystem platform based on the integration of Si Mach-Zehnder interferometer, microfluidics and grating couplers", Silicon Photonics IV, San Jose, CA, USA, 2009
- [49] Sader, J. E., "Frequency response of cantilever beams immersed in viscous fluids with applications to the atomic force microscope," *Journal of Applied Physics*, vol. 84, 1, 1998, pp. 64-76
- [50] Clark, M. T. and Paul, M. R., "The stochastic dynamics of an array of atomic force microscopes in a viscous fluid," *International Journal of Non-Linear Mechanics*, vol. 42, 4, 2007, pp. 690-96
- [51] Ho, C. M. and Tai, Y. C., "Micro-electro-mechanical-systems (MEMS) and fluid flows," *Annual Review of Fluid Mechanics*, vol. 30, 1, 1998, pp. 579-612
- [52] Jin, W. L., Tung, R., Raman, A., Sumali, H. and Sullivan, J. P., "Squeeze-film damping of flexible microcantilevers at low ambient pressures: theory and experiment," *Journal of Micromechanics and Microengineering*, vol. 19, 10, 2009, pp. 105029 (14 pp.)
- [53] Bidkar, R. A., Tung, R. C., Alexeenko, A. A., Sumali, H. and Raman, A., "Unified theory of gas damping of flexible microcantilevers at low ambient pressures," *Applied Physics Letters*, vol. 94, 16, 2009, pp. 163117 (3 pp.)
- [54] Xia, Y. and Whitesides, G. M., "Soft Lithography," *Annual Review of Materials Science*, vol. 28, 1, 1998, pp. 153
- [55] Unger, M. A., Chou, H., Thorsen, T., Scherer, A. and Quake, S. R., "Monolithic Microfabricated Valves and Pumps by Multilayer Soft Lithography," *Science*, vol. 288, 5463, 2000, pp. 113-116
- [56] Jo, B. H., Van Lerberghe, L., Motsegood, K. and Beebe, D., "Three-dimensional micro-channel fabrication in polydimethylsiloxane (PDMS) elastomer," *Microelectromechanical Systems, Journal of*, vol. 9, 1, 2000, pp. 76-81
- [57] Bhagat, A. A. S., Peterson, E. T. K. and Papautsky, I., "A passive planar micromixer with obstructions for mixing at low Reynolds numbers," *Journal of Micromechanics and Microengineering*, vol. 17, 5, 2007, pp. 1017-1024
- [58] Armani, D., Liu, C. and Aluru, N., "Re-configurable fluid circuits by PDMS elastomer micromachining", Twelfth IEEE International Conference on Micro Electro Mechanical Systems, Orlando, FL, USA, 1999, pp. 222-227
- [59] Data Sheet: Fujikura Pre-amplified, Calibrated, Temperature Compensated Pressure Sensors, Model No.: XFPM, XFHM, 04/11/2010, <http://www.servoflo.com>
- [60] Frank, M. W., *Viscous fluid flow*, McGraw-Hill, New York, 1991

- [61] Minipuls 3 Peristaltic Pump Users Guide, 04/11/2010, <http://www.gilson.com>
- [62] Pepper, D. W. and Heinrich, J. C., The finite element method :basic concepts and applications, Taylor & Francis, New York, 2006
- [63] Bhatti, M. A., Fundamental finite element analysis and applications, John Wiley & Sons, Inc., Hoboken, NJ USA, 2005
- [64] Van Eysden, C. A. and Sader, J. E., "Frequency response of cantilever beams immersed in compressible fluids with applications to the atomic force microscope," Journal of Applied Physics, vol. 106, 9, 2009, pp. 094904 (8 pp.)
- [65] Comsol, A., COMSOL 3.2 multiphysics user's guide, Version: September, 2005
- [66] Avanzini, A. and Donzella, G., "Coupled Fluid-Structural Analysis of Heart Mitral Valve", COMSOL Conference, Hannover, Germany, 2008
- [67] Moondra, S., Upadhyay, A. and Mitra, S. K., "Investigation of fluid structure interaction of an elastic membrane in a microchannel", Excerpt from the Proceedings of the COMSOL Users Conference. Bangalore, Bangalore, India, 2006
- [68] James, H. H., Electric power transformer engineering, CRC Press, Boca Raton, FL, USA, 2004